

SEE-LS: A 4th Generation Synchrotron Light Source for Science and Technology

R. Bartolini, H. Ghasem

Diamond Light Source, Oxfordshire, United Kingdom

Ch. Benabderrahmane, G. Le Bec, J.-C. Biasci, J.-F. Bouteille, J. Chavanne

European Synchrotron Radiation Facility (ESRF), Grenoble, France

D. Einfeld

Consultant at the ESRF for the EBS project

A. Andersson, E. Al-Dmour, P. F. Tavarez

MAX IV Laboratory, Lund, Sweden

D. Fernandez

ITER Organisation, St-Paul-lez-Durance, France

A. Nadji

Synchrotron SOLEIL, Saint-Aubin, France

F. Perez, A. Salom

ALBA Synchrotron, Barcelona, Spain

Ch. Quitmann

MAX IV Laboratory, Lund, Sweden

Lund University, Lund, Sweden

T. Rayment

University of Birmingham, United Kingdom



CERN Yellow Reports: Monographs
Published by CERN, CH-1211 Geneva 23, Switzerland

ISBN 978-92-9083-556-1 (paperback)
ISBN 978-92-9083-555-4 (PDF)
ISSN 2519-8068 (Print)
ISSN 2519-8076 (Online)
DOI <https://doi.org/10.23731/CYRM-2020-001>

Accepted for publication by the CERN Report Editorial Board (CREB) on 27 March 2020
Available online at <http://publishing.cern.ch/> and <http://cds.cern.ch/>

Copyright © CERN, 2020

 Creative Commons Attribution 4.0

Knowledge transfer is an integral part of CERN's mission.

CERN publishes this volume Open Access under the Creative Commons Attribution 4.0 license (<http://creativecommons.org/licenses/by/4.0/>) in order to permit its wide dissemination and use.

The submission of a contribution to a CERN Yellow Report series shall be deemed to constitute the contributor's agreement to this copyright and license statement. Contributors are requested to obtain any clearances that may be necessary for this purpose.

This volume is indexed in: CERN Document Server (CDS)

This volume should be cited as:

SEE-LS: A 4th Generation Synchrotron Light Source for Science and Technology, Dieter Einfeld (ed.)
CERN Yellow Reports: Monographs, CERN-2020-001 (CERN, Geneva, 2020)
<https://doi.org/10.23731/CYRM-2020-001>

Abstract

In 2016 the South East Europe International Institute for Sustainable Technologies was proposed by Herwig Schopper and brought to the political level by Sanja Damjanović, Minister of Science of Montenegro. In this framework two design studies have been completed by two groups of European experts: a South East Europe ‘4th Generation Synchrotron Light Source for Science and Technology’ (SEE-LS) and a ‘Facility for Tumour Hadron Therapy and Biomedical Research’ (SEE-HTR)¹. This report concerns the SEE-LS study, which was completed in October 2018. The proposal is to build a 4th generation light source with a circumference of 350 m and 16 straight sections and with an emittance of 178 pmrad for an energy of 2.5 GeV. In a later stage, the machine could be upgraded to 3 GeV. The estimated budget is roughly €170 million, and the first X-rays should be produced in six years. Readers who are not interested in the details can refer to the Executive Summary.

Keywords South East Europe; synchrotron light source emittance; lattice; accelerator; accelerator components.

Editor: Dieter Einfeld

¹A Facility for Tumour Therapy and Biomedical Research in South-Eastern Europe, editor Ugo Amaldi, CERN Yellow Reports: Monographs, CERN-2019-002 (CERN, Geneva, 2019), <https://doi.org/10.23731/CYRM-2019-002>

Table of contents

SEE-LS: A 4th Generation Synchrotron Light Source for Science and Technology	iv
1 Executive summary	1
2 Synchrotron radiation	5
2.1 Synchrotron radiation facilities	5
2.2 Description of a synchrotron light source	7
2.3 Scientific case and selection of beam lines	10
2.3.1 Considerations of likely scientific fields for SEEIIST	11
2.4 Design parameters of the SEE light source	15
3 Layout of a synchrotron light source	19
4 Lattice considerations	25
4.1 Introduction	25
4.2 Low-emittance lattice design	26
4.3 The synchrotron radiation brilliance	27
4.4 Lattice for the SEE-LS	30
4.4.1 The 7MBA lattice	31
4.4.2 The 3 GeV HMBA I lattice.....	32
4.4.3 The 2.5 GeV HMBA II lattice	33
4.4.4 The 3 GeV 5MBA lattice.....	34
4.4.5 The 3 GeV DTBA lattice	35
4.4.6 The 2.5 GeV S6BA lattice	35
4.4.7 The 3 GeV SLS-2 lattice.....	36
4.4.8 The 2.75 GeV SOLEIL-2 lattice.....	37
4.4.9 Number of magnets.....	37
4.5 Brilliance calculations	37
4.6 Summary	40
5 Beam dynamics and layout of the SEE-LS	43
5.1 Introduction	43
5.2 Beam dynamics of the proposed SEE-LS	43
5.3 Layout of the proposed SEE-LS.....	50
5.4 Specification of the magnets and RF system	50
5.4.1 Specification of the magnet system	51
5.4.2 Specification of the RF system	52
5.5 Lifetime of the stored beam	53
5.5.1 Introduction.....	53

5.5.2	Elastic scattering at the nucleus (Coulomb scattering)	54
5.5.3	Inelastic scattering at the nucleus (bremsstrahlung)	54
5.5.4	Elastic scattering at the shelf electrons	55
5.5.5	Inelastic scattering at the shelf electrons	55
5.5.6	Touschek lifetime.....	56
5.5.7	Conclusions regarding beam lifetime	57
6	Components of the SEE-LS.....	59
7	Magnets of the storage ring	61
7.1	Bending magnets	61
7.2	Combined bending magnets	64
7.3	Medium-gradient quadrupoles	66
7.4	High-gradient quadrupoles.....	67
7.5	Sextupoles	69
7.6	Correctors	70
7.7	Octupoles.....	73
8	Girder system.....	75
8.1	Introduction	75
8.2	General design.....	75
8.3	Girder performance	78
8.4	Locations of magnets on the girders	78
9	Vacuum system.....	81
9.1	The vacuum layout.....	81
9.2	The synchrotron radiation power from bending magnets	86
9.3	The pumping speed needed	86
10	Radio-frequency (RF) system	89
10.1	Introduction	89
10.2	Components of the RF system	90
10.2.1	Cavities	90
10.2.2	Amplifier.....	91
10.2.3	Waveguide system	91
10.2.4	Low-level electronics.....	92
10.2.5	Principle of operation.....	92
10.3	RF system parameters	93
10.4	RF system for the SEE-LS	94
10.5	RF system configuration	95
10.6	Digital low-level RF system.....	100
10.6.1	Introduction.....	100

TABLE OF CONTENTS

10.6.2	Hardware components	100
10.6.3	LLRF firmware description	101
10.6.4	LLRF extra utilities.....	103
11	Power supplies	105
11.1	Requirements of the power supplies	105
11.2	Power distribution	105
11.3	AC/DC rectifier	107
11.4	DC/DC converter.....	108
11.5	Spare power supplies.....	109
11.5.1	Minimum implementation	109
11.6	The AC and DC corrector power supplies driven by the fast-orbit feedback.....	109
11.7	The DC corrector power supplies feeding the sextupole auxiliary coils.....	109
11.8	Earth magnetic field compensation power supplies.....	110
12	Diagnostic system	111
12.1	Introduction	111
12.2	Pre-injector diagnostics	111
12.2.1	Faraday cup (F-cup).....	112
12.2.2	Beam charge monitor (BCM)	112
12.2.3	Beam position monitor (BPM).....	112
12.2.4	Fluorescent screen (FS).....	112
12.2.5	Scraper	113
12.2.6	RF signal distribution system	113
12.3	Transfer line diagnostics	114
12.3.1	Fast current transformer (FCT).....	114
12.3.2	Fluorescent screen (FS).....	114
12.3.3	Beam position monitor (BPM).....	114
12.4	Booster diagnostics	114
12.4.1	Fast current transformer (FCT).....	114
12.4.2	DC current monitor (DCCT).....	115
12.4.3	Fluorescent screen (FS).....	115
12.4.4	Beam position monitor (BPM).....	115
12.4.5	Synchrotron radiation monitor (SRM).....	115
12.4.6	Striplines	116
12.5	Storage ring diagnostics	116
12.5.1	Fluorescent screen (FS).....	116
12.5.2	Fast current transformer (FCT).....	116
12.5.3	DC current monitor (DCCT).....	116

12.5.4	Beam position monitor (BPM).....	117
12.5.5	Beam-based alignment.....	117
12.5.6	Scrapers.....	117
12.5.7	Synchrotron radiation monitor (SRM).....	118
12.5.8	Stripline kicker and tune measurement.....	119
12.5.9	Fast-feedback kickers.....	119
12.5.10	Pinger magnets for turn-by-turn beam dynamics.....	119
12.6	Summary of diagnostic system	120
13	Front end.....	123
13.1	General layout of a front end.....	123
13.2	A particular front-end layout.....	127
13.3	Cooling of front-end components	130
14	Injector.....	131
14.1	Booster synchrotron	131
14.2	Linac.....	133
14.3	Diagnostic beam line.....	135
14.4	Linac-to-booster transfer line (LTB).....	137
14.5	Booster-to-storage ring transfer line (BTS)	138
15	Control system	139
15.1	Introduction.....	139
15.2	Network.....	139
15.2.1	Ethernet connected.....	140
15.2.2	Not Ethernet connected.....	140
15.3	Controls administration.....	142
15.3.1	Development environment and collaborations	142
15.3.2	Standard tool for maintaining versions of software packages installed.....	143
15.3.3	Remote booting.....	143
15.4	The control system centralized sequencer and hardware access manager: the Sardana ‘device pool’.....	144
15.5	IT infrastructure: backups, storage, databases, central management information system, and system administration.....	144
15.6	Naming conventions.....	145
15.7	Equipment, controls, and archiving databases	145
15.8	Fast data logger	145
15.9	Equipment protection system.....	146
15.10	Machine controls	147
15.10.1	Subsystems.....	148

TABLE OF CONTENTS

15.11	Vacuum system.....	149
15.12	Power supplies.....	149
15.13	Radio-frequency (RF) system.....	150
15.14	Diagnostic system.....	151
15.14.1	Beam position monitors	151
15.14.2	Beam loss monitors	151
15.14.3	Fluorescent screens	151
15.14.4	Scrapers and other motions in the machine.....	151
15.14.5	Oscilloscopes.....	151
15.15	Insertion devices	152
15.16	Orbit correction.....	152
15.17	Motor controllers	152
15.18	Timing system	152
15.19	Personnel safety system.....	153
15.20	Alarm handling.....	154
15.21	Organization and economic aspects	154
16	Building, infrastructure, and site.....	157
17	Organization.....	163
18	Project schedule	165
19	Training programme	167
20	Cost estimation.....	169
20.1	Investment cost.....	169
20.2	Laboratory staff.....	170
20.3	Operational budget	170
Appendix A Synchrotron radiation characteristics.....		171
A.1	Introduction	171
A.2	Radiation from a bending magnet	173
A.3	Radiation from a wiggler.....	177
A.4	Radiation from an undulator	182
A.5	Influence of the beam energy spread on the spectral photon flux.....	188

1 Executive summary

S. Damjanović and H. Schopper†*

The South East European (SEE) region is an integral part of Europe but needs the help of other European countries to develop a sustainable economy and social cohesion. The creation of an international institute devoted to sustainable technologies would be an essential element in such endeavours. Scientific and technological cooperation, including knowledge transfer and training of the younger generation, would strengthen innovation, improve information exchange, and enhance human capacity-building.

A large-scale scientific research facility that promotes excellence and engages in internationally competitive activities would provide a significant means of addressing common challenges. Since the development of such a facility cannot be realized by a single country, it requires regional cooperation, and thus the primary mission of attaining scientific excellence would be complemented by peaceful collaboration in a region with a history of considerable political friction.

An initiative to this end was first presented to the World Academy of Arts and Sciences in 2016, and the government of Montenegro, a country which has good relations with its neighbours, was the first to officially support such a proposal regardless of the final location of the scientific facility. Thanks to the engagement of the Montenegrin Minister of Science, Sanja Damjanović, a meeting of Ministers of Science or their representatives took place on 25 October 2017 (see Fig. 1.1), in which a Declaration of Intent was signed to create an international laboratory in the SEE region with the double objective, following the spirit of CERN, of promoting science and technology and improving relations between countries. To demonstrate that all signatory parties are treated on an equal level and have the same rights, the meeting took place at the neutral premises of CERN and was chaired by H. Schopper, a former Director-General of CERN. The eight parties signing the declaration were Albania, Bosnia and Herzegovina, Bulgaria, Kosovo**, the FYR Macedonia, Montenegro, Serbia, and Slovenia. Croatia also agreed to participate, but for formal reasons had to delay its signature. Greece participated as an observer. In the Declaration of Intent it is stated that the institute shall operate with the mission of ‘Science for Peace’ and that the parties have a common vision and encourage the cooperation of their researchers.

Thus, this initiative to establish a ‘SEE institute for sustainable technologies’ has become a regional project. It was also decided to set up a steering committee to guide future decisions.

The success of a similar initiative following the CERN model has been demonstrated recently by the SESAME Project in Jordan, which unifies member states with different political systems and religions in the Middle East, all of which work peacefully together.

Two options are being considered for the initiative:

- i) 4th Generation Synchrotron Light Source for Science and Technology (SEE-LS);
- ii) Facility for Tumour Hadron Therapy and Biomedical Research (SEE-HTR).

These two options have been proposed because of their outstanding promise in achieving the objectives of promoting cooperation in science, technology, and industry, and facilitating the education and training of talented young people and engineers based on the transfer of knowledge and technology from European centres.

*Minister of Science, Montenegro.

†Professor emeritus of the University of Hamburg and former Director-General of CERN.

**This designation is without prejudice to positions on status and is in line with UNSC 1244/1999 and the ICJ opinion on the Kosovo Declaration of Independence.

Two groups of international experts have worked out conceptual designs for the two options. These designs are presented in this document. In some respects the two options offer similar benefits to the SEE region, but they also have different and complementary aspects that justify the presentation of both.

The first objective, which both options have in common, is not only to extend existing research activities but also to create completely new opportunities for cutting-edge research and technological development for the welfare of the region. Secondly, it is hoped that, by struggling and working together towards a common goal, the human relations between scientists and engineers as well as between administrators and politicians from countries with different and sometimes problematic histories will be an essential element in building up mutual trust, as has been successfully demonstrated by the examples of CERN and SESAME.



Fig. 1.1: Representatives at the signing of the Declaration of Intent. From left: Prof. Blazenka Divjak, Minister of Science and Education, Republic of Croatia; Prof. Vladimir Popovic, State Secretary, Republic of Serbia; Dr Tomaz Boh, State Secretary, Republic of Slovenia; Mr Ervin Demo, Vice Minister of Education and Sports, Republic of Albania; Mr Shyqiri Bytyqi, Minister of Education, Science and Technology, Kosovo[‡]; Dr Sanja Damjanović, Minister of Science, Montenegro; Prof. Herwig Schopper, former Director-General of CERN; Prof. Renata Deskoska, Minister of Education and Science, The FYR of Macedonia; Mr Andrija Pejovic, Minister of European Affairs, Montenegro; Dr Adil Osmanovic, Minister of Civil Affairs, Bosnia and Herzegovina; Prof. Kostadin Kostadinov, Advisor to the Minister of Education and Science, Republic of Bulgaria; Prof. Costas Fountas, scientist, Hellenic Republic.

Both options also have in common that training of the younger generation is an essential and integral part of the initiative. Realization of these projects will take several years, which would provide sufficient time not only to train the team that will build and later operate these installations but also to form a user community. In both cases, specialized users in the important fields that will be served by the facilities do not yet exist in the SEE region and have to be created. This will be an essential part of capacity-building. The training will mainly consist of two parts. First, fellowships will be granted to young people so that they can go to European laboratories for one or two years to receive education and training as scientists or engineers in various specialist fields. The management of such a programme would be the responsibility of the projects, which will select promising candidates from the region and find laboratories to host them. The second component of training is the organization of workshops and schools for future users. This would be done by a training programme committee to be set up under the initiative. Contacts have already been established with IAEA at Vienna, and the hope is to obtain financial contributions for such a training programme, as in the case of SESAME.

[‡]This designation is without prejudice to positions on status and is in line with UNSC 1244/1999 and the ICJ opinion on the Kosovo Declaration of Independence.

EXECUTIVE SUMMARY

Transfer of technology and know-how in general are also vital parts of the initiative. In order to make this efficient, for both options it is suggested not to order the basic accelerator complexes as a unit from industry but rather, with the help of existing experts and laboratories in Europe, to create the appropriate team for the facility in question. This is the usual way in which most scientific laboratories have been created in Europe. Only conventional equipment would be bought off-the-shelf from industry; for new developments, prototypes will be ordered, and later production contracts will be awarded to industry. This allows for great flexibility in using the most modern technologies for the projects and, as experience has shown, provides an extremely efficient means of technology transfer to industry. It also reduces the total cost of the projects, as the global risk burden is not placed on the shoulders of industry. To facilitate collaboration with industry, it is envisaged that a kind of ‘training programme for and with industry’ will be established, with the task of explaining to firms not yet in contact with research institutions how to cooperate and how to present proposals for adjudication of contracts.

With the construction of the SEE-LS there will be many opportunities for technology transfer to the SEE countries. First, procurement of the different components for the machine and beam lines (magnets, vacuum system, girders, power supplies, control system, etc.) can be preferentially assigned to local industries. Wherever the capabilities of local industries are lacking, a joint R&D programme for pre-series prototypes could be established, thus promoting these industries. The prototypes should be manufactured in the SEE-LS member countries by giving their industries special education/training from other synchrotron radiation light source (SRL) facilities and from the staff of the SEE-LS. With production of the prototypes, the member countries’ industries should be encouraged to respond to a later call in the tendering process. As for the procurement of components, it will be necessary to educate the local industries in how to bid successfully according to the procurement rules of the most advanced EU countries.

We believe that, like the training programme, the technological know-how transfer programme outlined above would help to create a skilled community of scientists who will be attracted to working at the facility and will no longer seek employment elsewhere in Europe, thus reversing or ameliorating the brain drain suffered by the region.

Finally, it should be mentioned that both projects could give rise to spin-off activities not directly linked to the facilities but which can provide an initial spark for new activities in the region. We mention two examples. Both of the proposed facilities are based on particle accelerators and so need electric power, which would account for a non-negligible part of the operating costs. To reduce the cost of electricity, one could consider installing solar panels. This should not be done for the facility in isolation, since power is needed also when the sun is not shining; on the other hand, solar-generated power can be supplied to the general network when the accelerator is not working. Therefore, such an installation must be integrated into the regional power network. A second spin-off development might be the creation of regional broadband digital networks. Both facilities would serve large user communities, spread across the region and even all of Europe. To transmit data from the central laboratory to users, a network constructed for the facility and its users could become a model for a wider network for the region, much as the World Wide Web originally created for users of CERN has become a global network.

In some respects the two options presented are quite different, however, which justifies their individual consideration and is part of why they are attractive in complementary ways for the region. We discuss a few aspects in which they differ.

The two facilities would serve quite different ‘user communities’. An SRL would be attractive to scientists in universities and in many fields of industry, ranging from the medical and life sciences to chemistry, physics, material science, and environmental sciences, and even extending to studies of cultural heritage. About a thousand scientists would be associated with the SEE-LS facility, designing and constructing special beams, even if many similar facilities exist in Europe. As in most fundamental sciences, it will take some time before any new discoveries can propagate to the market. Also, the creation of new spin-off firms could take time.

A hadron therapy and research (HTR) facility would yield immediate benefits for the health of society as well as long-term results for biological and medical science. Every year many hundreds of foreign medical doctors and scientists will work at the facility, mainly in radiobiology. On the other hand, its target is a rather special community, consisting mainly of researchers and clinicians in oncology, biomedicine, radiobiology, and medical physics. Hence the scope of the HTR facility for general capacity-building would be more restricted than that of an SRL. However, given its proposed combination of therapy and biomedical research, with about 50% of daily time devoted to research, it would be the first such facility in Europe.

As far as financing is concerned, the two options are rather complementary. The SRL facility would be used almost exclusively for research. Therefore the funds for investments and operation would have to come mainly from research programmes, of both the European Commission and the national partners. The HTR facility, on the other hand, would be used to treat patients for about 50% of its operating time; hence its operation would be partially financed from fees paid mainly by national health programmes. The investment contributions from the European Commission would be expected to come from programmes dedicated to infrastructure development.

This report presents the conceptual design for the SEE-LS option. It is not a replacement for the full proposals that will have to be produced by the teams responsible for implementation. Hence, in this report a number of variants are mentioned, leaving room for future choices tailored to the final conditions and needs.

The proposed 4th generation light source, with a circumference of 350 m and 16 straight sections, has for an energy of 2.5 GeV an emittance of 178 pmrad. At a later stage the machine could be upgraded to 3 GeV. The estimated budget is roughly €170 million, and the first X-rays should be emitted in six years. The conceptual design shows that for 2.5–3 GeV, a 4th generation light source can be built with a circumference of 350 m.

The members of the committee were R. Bartaloni, A. Nadji, Ch. Quitmann, T. Rayment, P. F. Tavares, and D. Einfeld (chairman). All members had only limited time in which to work on the project because of duties at their home institutes. To produce a detailed conceptual design report a team of up to 20 people is needed for a period of up to two years.

2 Synchrotron radiation

Ch. Quitmann and T. Rayment

2.1 Synchrotron radiation facilities

Synchrotron radiation facilities are high-brilliance light sources that offer unique possibilities for investigating nature. They provide outstanding tools for both fundamental and applied research and support technology in a wide range of areas. Indeed, synchrotron radiation research has become a major factor in the progress of science and technology in all industrially developed countries. The characteristics of synchrotron radiation are described in detail in Appendix A.

A general overview of the electromagnetic spectrum is presented in Fig. 2.1. Synchrotron radiation light covers the spectrum from infrared and visible through ultraviolet to X-rays.

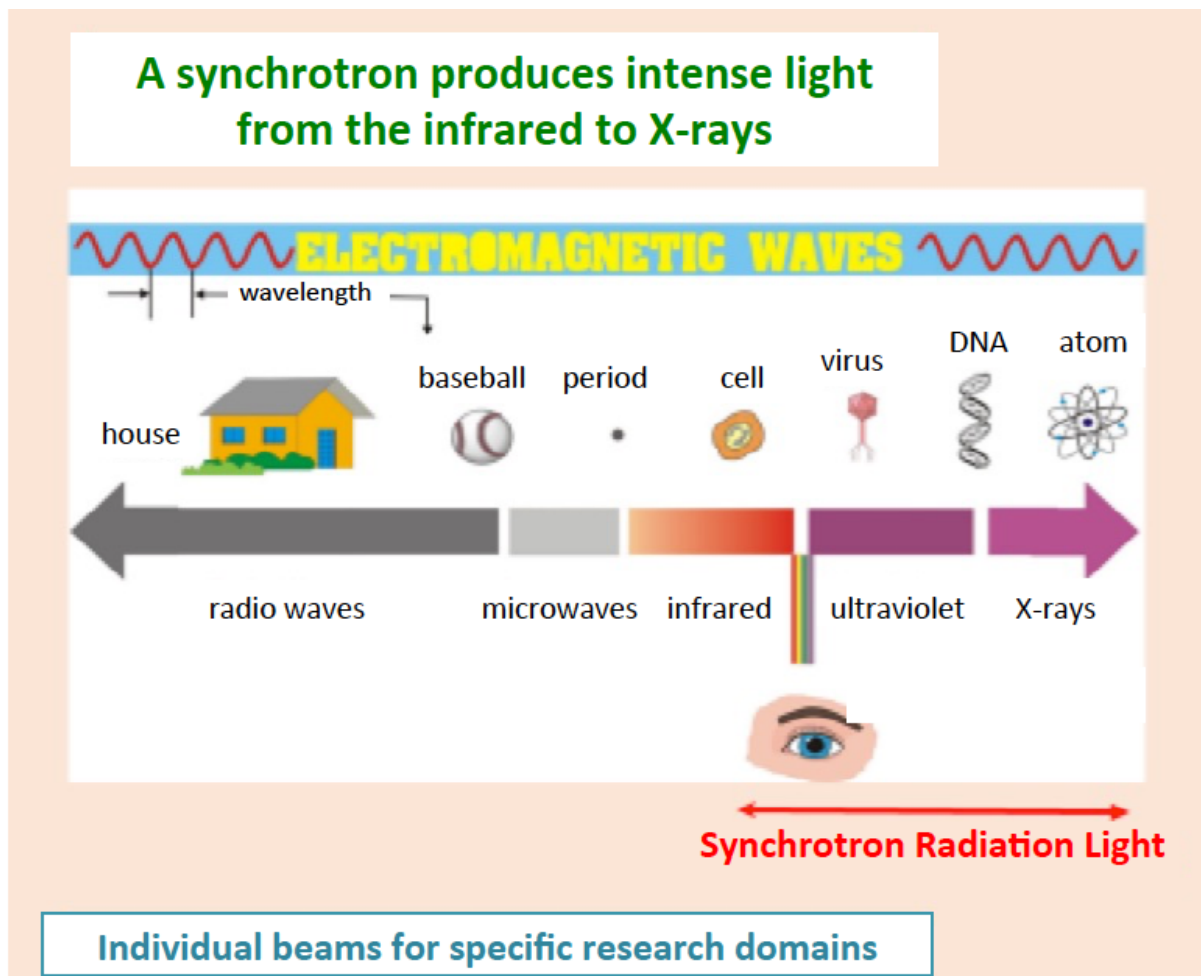


Fig. 2.1: The electromagnetic spectrum from radiation waves to X-rays

More than 60 such light sources exist in the world, with 14 in Europe (Fig. 2.2) [2.1]. While these facilities have much technology in common, each is a unique fit to the needs of its users. Tens of thousands of users in physics, chemistry, materials science, biomedicine, human heritage, technology, and other disciplines utilize these facilities for their research. Experiments with synchrotron light (Fig. 2.3) have produced and continue to produce many landmark results in science and technology. Synchrotron light source facilities offer research capacity for users in almost all universities and research institutes, and increasingly they are playing an essential part in industrial research and development. In Fig. 2.3, just a few examples of research topics that can be investigated with synchrotron radiation are shown. The network of users strongly contributes to a culture of equal opportunities for all researchers, overcoming topical, national, financial, age, and gender barriers.

The facilities themselves have been continually improved over the years by the introduction of new technologies and adaptation to the specific demands of local user communities. The design of the source and the associated equipment are chosen according to the interests of potential users. Special beam lines can be installed for hard X-rays that are of special interest in structural biology and imaging, whereas infrared beam lines at the other extreme of the spectrum can be used for materials research and archaeology. As a result, no two of these many facilities are identical, but each is adapted to the particular needs of a country or region.

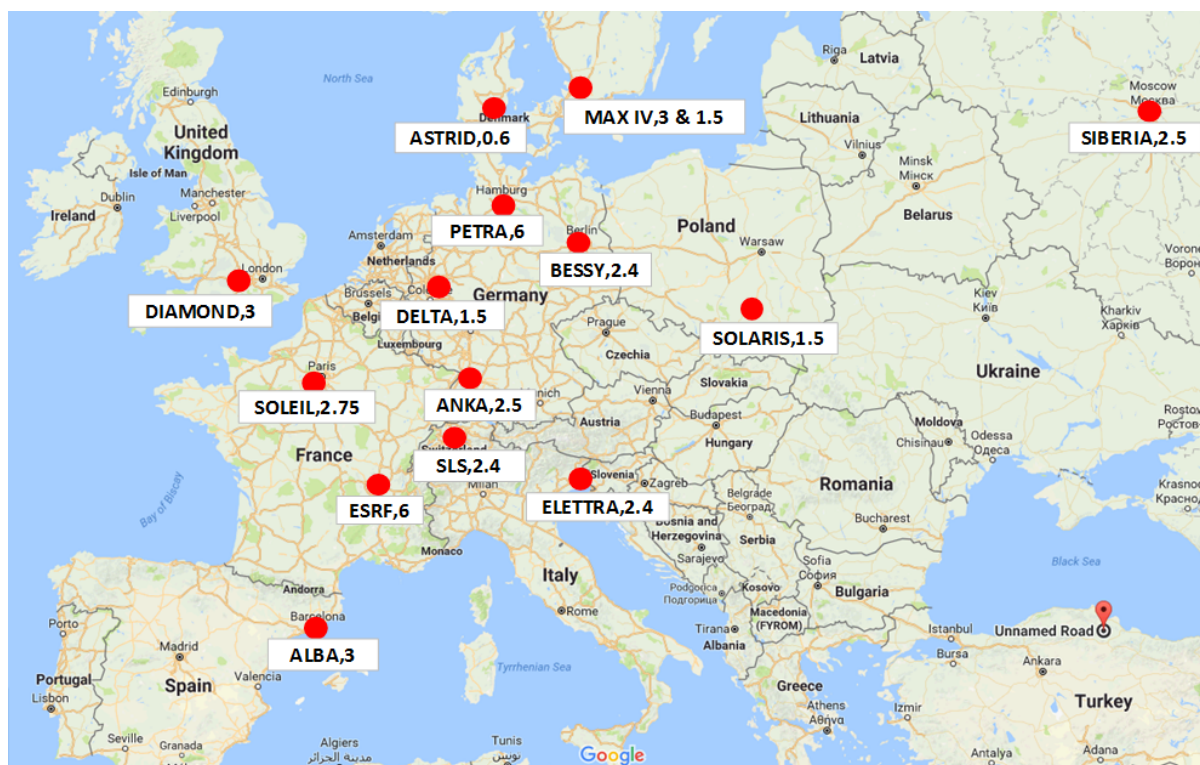


Fig. 2.2: Synchrotron radiation light sources in Europe with energy in GeV

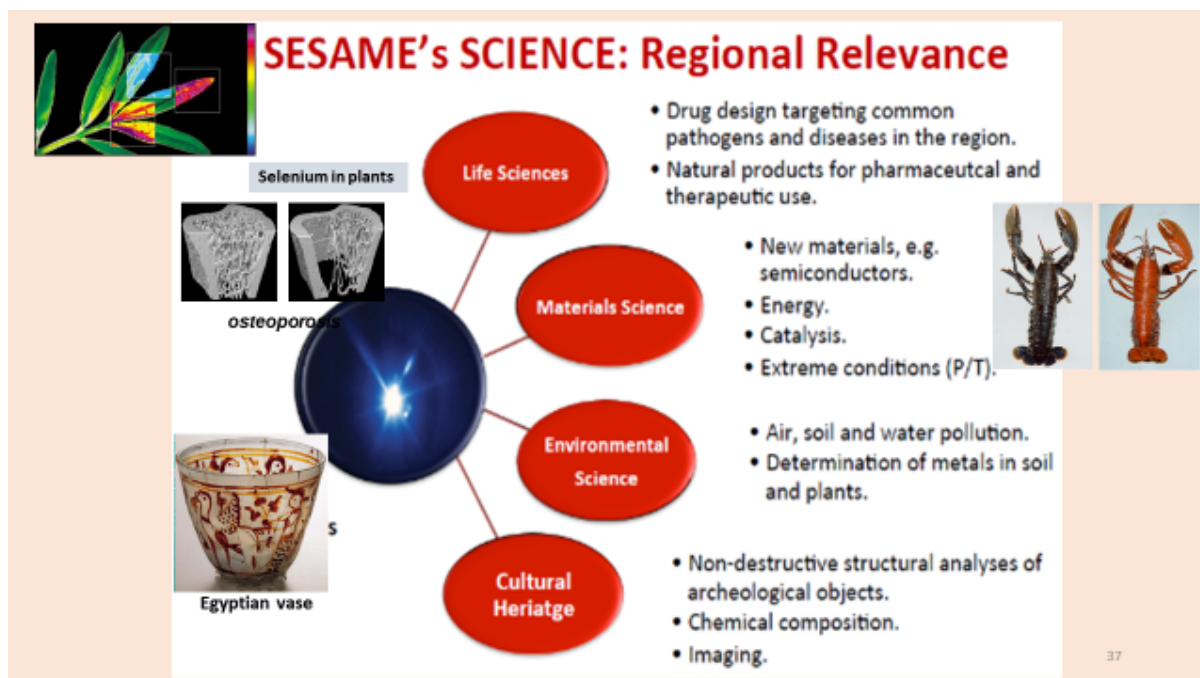


Fig. 2.3: A selection of research areas that can be investigated with synchrotron radiation

Users of synchrotron light sources from universities, research institutes, and industry will spend relatively short periods of time at the facility. They will prepare the objects to be investigated at their home institutions, put the objects into a special beam at the facility, record the data, and finally do their analyses at home. Transfer of the data will require and stimulate the creation of a powerful digital network and thereby contribute to the regional digital economy. Much of the analysis software is open source, and use of it can lead to collaborations with established experts worldwide.

2.2 Description of a synchrotron light source

The principal layout of a synchrotron radiation light source (SRL) is presented in Fig. 2.4. An SRL consists of two parts: the accelerator complex and the experimental hall with the beam lines.

Synchrotron light is emitted when electrons travelling at close to the speed of light are accelerated by a magnetic field. Because it is costly and difficult to make electrons travel this quickly, it makes sense to accelerate them once and then keep them travelling in a circle so that each time they go around the circle ('ring') they give out light. This is the primary role of the accelerator complex. This 'ring' of electrons allows many (typically 10–40) unique, independent, and purpose-designed laboratories (beam lines) to be positioned around the ring within a single experimental hall.

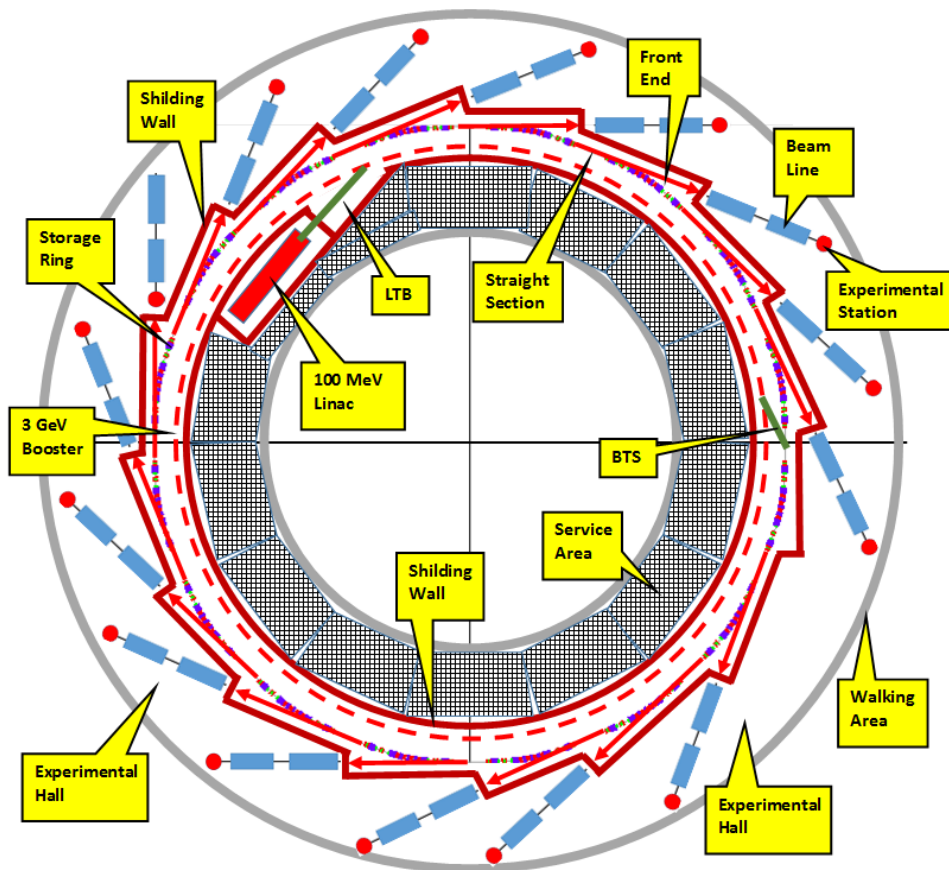


Fig. 2.4: Layout of a synchrotron light source facility

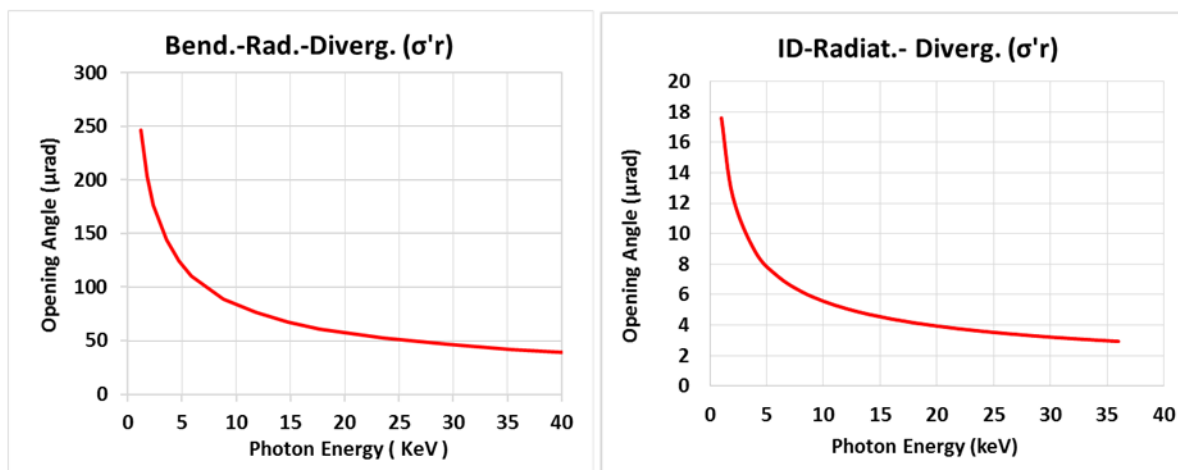


Fig. 2.5: The opening of the synchrotron radiation cone from the bending magnet (left-hand side) and the insertion device radiation (right-hand side).

To achieve the necessary high energies, the electrons must be accelerated in steps. First, they are accelerated in a linear accelerator (linac) up to about 100 MeV; then they are transferred (via a linac-to-booster transfer line, LTB) to a booster synchrotron where they are accelerated to the final storage ring energy; finally they are sent (via a booster-to-storage ring transfer line, BTS) to the storage ring, where huge numbers (typically many billions) of electrons accumulate to give very intense light. Since the electrons constantly lose energy through the emission of storage ring (SR) light, these losses must be compensated continuously by high-frequency electromagnetic fields using accelerating cavities. The electrons always travel in tubes evacuated to ultra-low pressures, the so-called vacuum system. To keep the electrons together, special focusing magnets have to be introduced between the bending magnets. The magnet system together with the high-frequency system and the vacuum system form a rather complicated arrangement with many possibilities of being adapted for cost-to-performance optimization. The storage ring consists of a series of so-called achromats (up to 30 and possibly more). The technical arrangements of the different components are the same within all achromats. Straight sections with a length of several metres connect the achromats. These straight sections accommodate the insertion devices for producing radiation with a special high brilliance which is tailored to each beam line (see Fig. 2.5); the details are described in Appendix A.

Synchrotron radiation is emitted when a relativistic electron beam is deflected in the bending magnets or in insertion devices (see Fig. 2.5). The spectral range of energy of the photon beams originating at these devices is extremely broad: from infrared through ultraviolet up to hard X-rays (Fig. 2.6). This is one of the properties that make SRLs so attractive, besides the enormous intensity they provide. From the insertion devices and bending magnets the light is transported by specially designed front ends and beam lines to the experimental hatch in the experimental hall. These beam lines will have very different properties depending on the scientific questions to be studied. However, in most cases they will include mirrors and a monochromator, which will select the most appropriate wavelength in the broad spectrum and focus it onto the sample. Some beam lines are very simple, whereas the construction of others can be quite demanding technical projects. As one example, the layout of a beam line used for X-ray absorption spectroscopy with an overall length of 35 m is displayed in Fig. 2.7.

SYNCHROTRON RADIATION

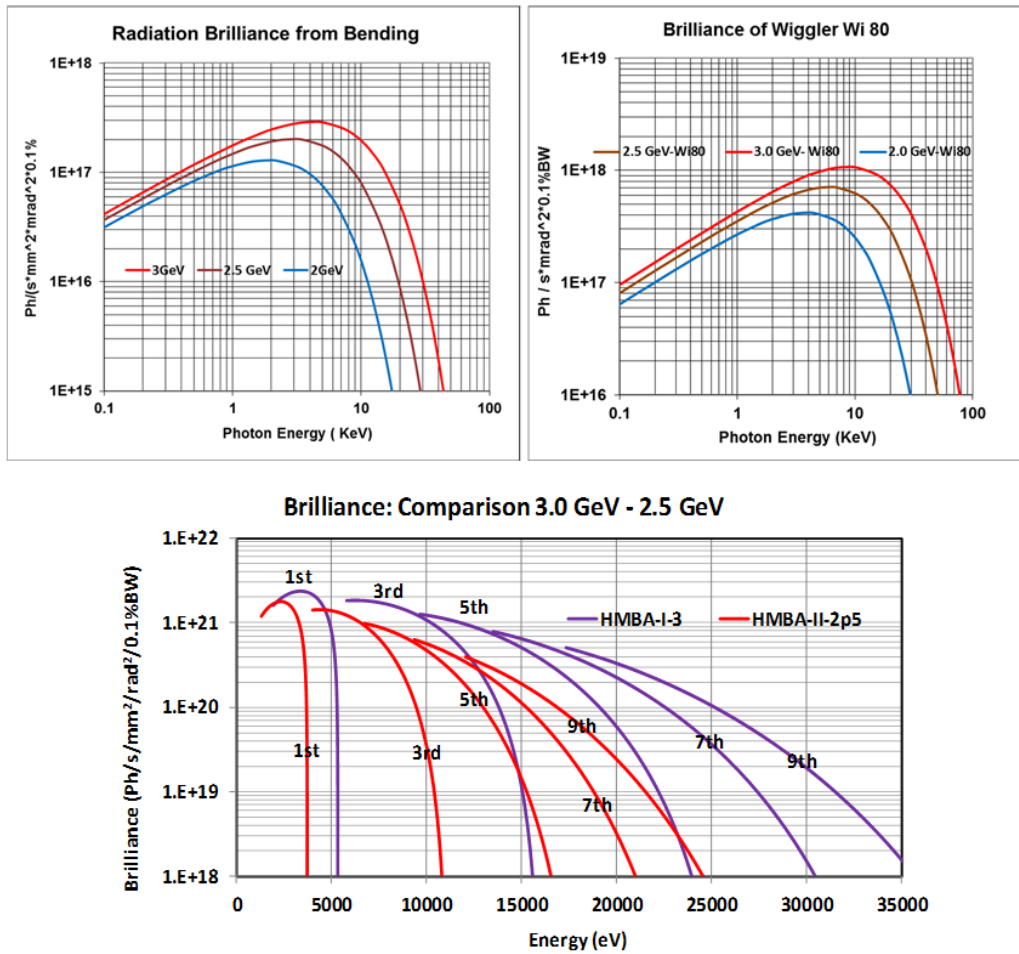


Fig. 2.6: Synchrotron radiation brilliance emitted from a relativistic beam deflected in a bending magnet and wiggler (above) and in an insertion device (below).

Synchrotron light facilities are often used as super-microscopes to explore the structure of matter at scales down to the diameters of atoms or below. In such applications the spatial resolution of the radiation is extremely important; this is the smallest distance that can still be resolved. The spatial resolution is largely determined by the geometrical properties of the circulating electron beam, in particular the cross-section and angular divergence of the beam. The smaller both are, the better the resolution in the experiments will be. To characterize the quality of the electron beam, various parameters are used that essentially boil down to the product of the beam cross-section and the angular divergence; this product is called the *emittance* of the beam and is constant around the ring. The emittance depends on the design of the magnets of the electron accelerator and cannot be changed later.

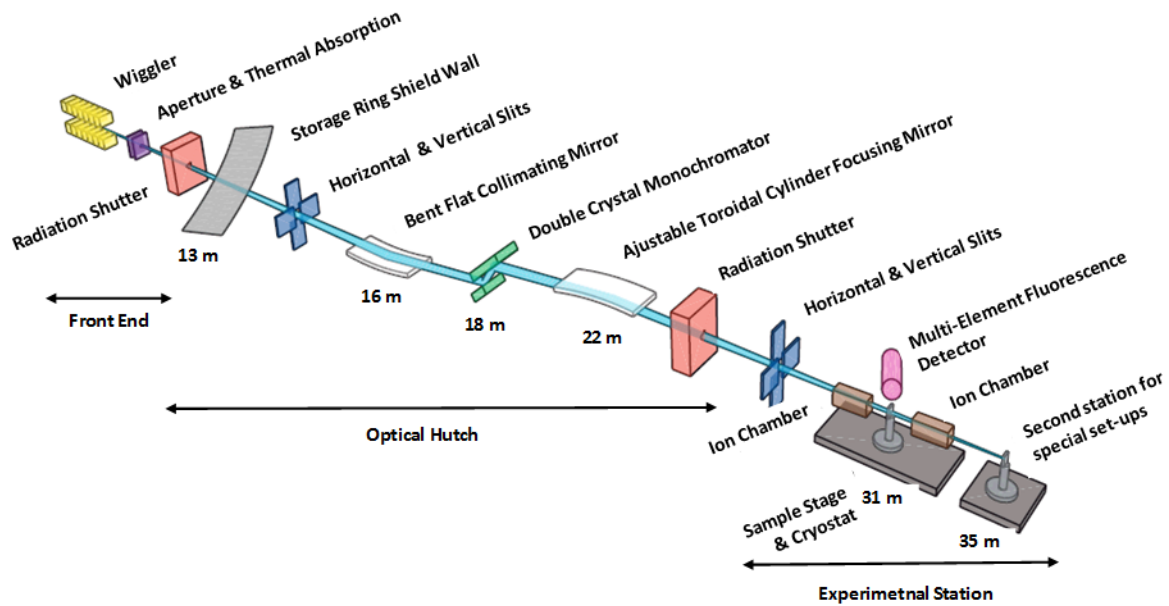


Fig. 2.7: Layout of the X-ray absorption spectroscopy (XAS) beamline at the Australian SRL [2.2]

SRLs offer another possibility, which makes them extremely attractive and versatile as research instruments. If the straight insertions are properly designed, special devices can be installed between the bending magnets. These so-called insertion devices are called *wigglers* or *undulators* and can produce light beams with special characteristics chosen according to the requirements of users. The most recent facilities built (e.g. MAX IV at Lund [2.3]) were designed to give high priority to such beam properties and not so much to higher electron energies. They are called ‘4th generation light sources’.

Thus, a synchrotron radiation facility is characterized by a number of parameters which can be chosen by taking into account the interests of potential users, optimization of construction and operation costs, the know-how of future staff, and other general aspects. Selecting these parameters is the first major task in preparing a final design.

2.3 Scientific case and selection of beam lines

The proposal to build a SEE International Institute for Sustainable Technology (SEIIST) is utterly compelling when one considers the benefit to the people of the region. However, the case for building SEIIST rests ultimately upon the value of the science and technology and the range of areas on which it can have an impact. The value of the project is expected to be realized for the SEE region over an extended period of time.

Worldwide, SRLs provide illuminating and essential insights which extend to virtually all aspects of scientific activity, but for every existing facility a proposal has been made on the basis of the particular needs of the community it serves. No single facility can cover every application. Therefore, a goal of the SEIIST must be to establish itself as a partner in the international network of synchrotrons. One way of achieving this is through participating in the League of European Accelerator-based Photon Sources (LEAPS, <https://www.leaps-initiative.eu/>) [2.4], a consortium of 13 synchrotrons and three free electron lasers across Europe.

Furthermore, because the first part of the project will involve constructing the storage ring and building regional capacity, it is envisaged that from day one there will be a small number of operating beam lines (applications laboratories). Over a longer period of time, perhaps a decade, new beam lines will be built which would allow the facility to grow to full maturity and capacity. A process for choosing beam lines will be established which takes into account the needs of all stakeholders in SEE countries. Before then, three very general technical themes can be identified for which synchrotron light would

offer exciting opportunities [2.5]. These are summarized here and analysed in more detail in the next section.

- **Spectroscopy** [2.6] with X-rays can only be carried out at synchrotron facilities. It has applications spanning physics, chemistry, surface science, nanoscale science, biological science, environmental and earth sciences, and other areas ranging from the fundamental to the industrial. Cultural heritage and conservation science can also benefit from access to this tool. X-ray spectroscopy is a non-destructive, chemically selective tool with a large user community and is a core capacity which is greatly oversubscribed worldwide.
- **Imaging** [2.7]: the first recorded X-ray image was of the hand of Roentgen's wife in 1895; since that time, imaging has become synonymous with X-rays. The past two decades have seen revolutions in X-ray imaging which have made it possible to image nanometre-sized structures in 3D. With synchrotron light it is possible to image in exquisite detail; examples include processes—in real time—of technological importance (e.g. welding, corrosion, 3D printing), biomaterials (e.g. bone, arterioskeletal disease, plants), soil and earth science samples, and cultural heritage objects.
- **Structure** [2.8, 2.9]: X-rays provide the pre-eminent tool for determining the structure of matter at an atomic scale. Synchrotron light allows the structure of large molecules relevant to human health and wellbeing (such as viruses and proteins) to be determined in a matter of minutes, and it has become an integral part of the pharmaceutical industry and life sciences research. Synchrotron light is of equal importance in physics, materials science, and materials chemistry, in which it plays a key role in the development of new battery materials, energy conservation, green industrial processes, and bioengineering.

The vision is of an institute which will train and retain the next generation of scientists and technologists within the SEE region. But it can do much more than this; it can reverse the tide of migration of talent away from the region in recent years. In the early years of the institute most staff will have been trained outside the region and be returning home. SEE-LS will have unique appealing aspects which will, without doubt, attract scientists from across the world and establish the SEE region as a zone of excellence.

2.3.1 *Considerations of likely scientific fields for SEEIIST*

When considering what beam lines should be built, it is possible to analyse the choices in many ways; the most powerful and compelling consideration is the scientific areas that will be enhanced. With a few notable exceptions, beam lines serve a wide community, and every community can benefit from access to a broad portfolio of beam lines. Indeed, one of the most powerful features of synchrotron light sources is that they are science led; often users first come to a facility to use one technique, but then their work flourishes in novel directions from having access to a broad range of different techniques. Knowledge transfer across disciplines, national borders, and generations is an intrinsic feature of synchrotron light sources.

Because support for a synchrotron light source must come primarily from those who will use the source, it is essential to consider what the major groups of users are likely to need. The SEE science community, although unique, must surely have much in common with user communities worldwide, and so it is helpful to consider briefly the needs of five major science and technology groupings which are commonly identified in Europe.

2.3.1.1 *Integrated structural biology and the medical and life sciences*

Ever since the determination of the structure of DNA, structural biology has become increasingly important. Knowledge of the atomic structure of the functional components of cells is now recognized to be a fundamental factor in understanding and curing major diseases. Use of SRLs is an essential way in which pharmaceutical companies develop new drugs. In Europe, structural biologists form the largest single group of SRL users. This group of users has very clear requirements of synchrotron facilities. They demand just-in-time access to facilities which have become highly automated and very sophisticated. The key technique they use is X-ray diffraction for carrying out macromolecular crystallography (MX). There are many such facilities currently available in Europe, and these facilities compete to host the most competitive science projects. For this reason, a careful analysis will be needed of the current strengths and requirements of the SEE structural biology community to discern whether there is already sufficient access to MX facilities elsewhere in Europe or whether construction of a SEE MX beam line is a necessary part of a coherent development plan.

Although knowledge of structure at an atomic level (at Å to nm length scales) is the core requirement of integrated structural biology, it is insufficient for a full understanding of the biological components, and tools are needed for determining how the components function in partnership at larger length scales (nm to µm). Synchrotron facilities provide two classes of tools: small-angle scattering and imaging. Small-angle scattering is used to find out how complexes assemble on the 10–500 nm length scale, and imaging now extends from the millimetre scale down to less than 20 nm. Beam lines that have such capabilities are among the most highly oversubscribed in Europe and would be strong contenders for inclusion within the initial portfolio.

2.3.1.2 *Chemistry and catalysis*

Chemistry plays a major role in all developed economies worldwide, being responsible for as much as 5% of global GDP, and it has been said that about 90% of all chemical processes involve the use of a catalyst. The development of new processes is a key part of ongoing efforts to find novel ways of making the feedstock of current chemicals from sustainable sources and to use feedstocks from renewable sources to make entirely new alternatives to materials that currently necessitate the exploitation of non-renewable resources. The long-term vision is to be able to design catalysts specific to every process. Research in chemistry and catalysis has benefited enormously from the availability of synchrotron facilities. Decades ago, model systems were studied *ex situ* under idealized conditions (e.g. ultra-high vacuum, single crystals), but in recent years it has become normal to study systems under *operando* conditions of high temperature and pressure and complexity of composition and form.

Furthermore, it is now recognized that it is essential to be able to employ a number of different techniques under the same conditions. For example, it is vital to know the chemical state of a catalyst at the atomic level, but also to know how this interacts with the meso- and long-range structure. This can be achieved by using a combination of spectroscopic and diffraction tools (atomic-level structure), small-angle scattering (meso-structure), and imaging (long-range and system-level structure). Finally, these techniques must be developed alongside and with the analytical techniques found in a modern chemical laboratory. It is envisaged that SEE-LS will facilitate collaborations between existing SEE institutions to create a world-competitive centre for chemistry and catalysis which will benefit the whole region.

2.3.1.3 *Engineering and materials science*

The SEE nations have a long history of engineering, but in recent decades the economic fortunes of the engineering sector have suffered because of political turmoil and fierce competition from emerging economies [2.10, 2.11]. It is widely recognized that pre-eminence in the fields of engineering and materials science is a key factor for any nation wishing to sustain (or regain) economic competitiveness and move towards a model of sustainable economic growth. Engineering is both a discipline and a system of processes whereby materials are transformed into objects of practical, social, and economic value. The range of applications of engineering is massive, spanning enormous length

scales, from bridges and aircraft to micro-miniature, even nanoscale, machines. Engineering was once mostly concerned with the processes by which objects are formed (e.g. casting, machining, welding). However, in a world in which sustainability is of increasing importance, it is vital to consider the whole life cycle of manufactured objects, encompassing their birth (e.g. deposition, casting, sintering, fabrication), use (e.g. behaviour under load or in gas conditions), death (e.g. failure, corrosion), and finally recycling (making objects suitable for reuse and preventing environmental pollution). Synchrotrons provide valuable tools for every stage of the engineering life cycle.

Engineered objects are usually complex because they rely on properties of one part interacting with and improving the performance of other parts for the benefit of the whole. In the past it was essential to take an object apart to understand the detailed properties of its constituent parts. However, in modern engineering synchrotrons have made it possible to use X-rays for imaging and diffraction from the nano- to the macro-scale; in particular, the intensity of X-rays is sufficient to penetrate the whole object to be investigated over the full range of length scales needed to understand its detailed properties. It is possible to study materials while they are being formed (i.e. during casting, welding, or additive manufacturing), and subsequently stresses can be measured in working objects (such as a prosthesis).

Development of new materials lies at the foundation of societies' attempts to meet the challenges in rebuilding their manufacturing industries for future low-carbon and sustainable-energy economies. Synchrotron light sources provide facilities of the highest quality and broadest portfolios available for understanding materials. Time matters in a competitive world, and synchrotrons can offer significant and unique advantages in the development cycle of materials, because both measurement and interpretation can be swift and timely. Automation is becoming increasingly important at mature synchrotron facilities; it is the universal hallmark of the working protocols within integrated structural biology, and methods of automation are being transferred to other disciplines such as materials development (for engineering and also chemistry). However, before automation can be implemented, it is necessary for industries and users within the SEE region to determine what measurements are needed most frequently and most urgently within the region. A step-by-step approach to automation, led by the unique blend of needs within the region, is essential. The long-term goal is to provide laboratories in nations distant from a synchrotron facility the same or even better quality of experience as facilities in their home institution.

2.3.1.4 *Condensed matter physics*

There can be no doubt that research into solid state physics has utterly transformed the world we live in, because it is the discoveries in this discipline that have led to the creation of all modern methods of digital communication and made possible the computing revolution—from the first computer which took up a whole room to ubiquitous pocket-sized supercomputers (smart phones). It is a fact that esoteric concepts in condensed matter physics have paved the way for the leaps in technology which have made the lifestyles of today possible.

It remains true that the frontiers of physics are very hard to explain to non-experts and that immense efforts continue to be expended to understand and develop materials with new properties. But there are common threads within this endeavour. The thread which is most common is an understanding that the electronic properties of materials depend on the precise positioning of atoms with specific properties and that the subtle interplay that takes place when individual atoms are brought together produces new collective phenomena in magnetism, electronic structure, and electron dynamics. These collective behaviours are influenced by nanostructure quantum fluctuations, giving hints of new states of matter. This area of fundamental physics offers the prospect of constructing practical quantum computers—the next paradigm shift in computing technology.

Condensed matter physics requires tools for determining where atoms are and their chemical, magnetic, and electronic states. Synchrotrons provide an extensive suite of tools to support condensed matter physics. Some of the tools, such as diffraction and X-ray spectroscopy, are in common with other areas, and condensed matter physicists would share access to the facilities according to need (and

competitive peer review). Other tools may be dedicated to condensed matter physics; these beam lines tend to employ low-energy (20–1000 eV) X-rays or so-called tender X-rays (500–3000 eV) for two reasons. Firstly, the energies of these X-rays are sufficient only to excite and probe the valence (or outermost) electrons of matter, which are predominantly responsible for the physical properties being studied; secondly, X-rays with these energies can penetrate only a short distance into matter. This is important because the behaviour of many advanced materials is determined by the structure of the outermost few layers of atoms. Information provided by such soft X-rays is not obstructed by signals from the bulk. Another technique of beam lines dedicated to the study of condensed matter physics is X-ray photoelectron spectroscopy, which makes it possible to study the structure of the electrons in matter that are responsible for all the key properties of interest in solid state physics, for example high-temperature superconductivity and critical quantum behaviours. Such facilities can help bring together advances in theory and the development of new materials, which when combined will pave the way for breakthroughs that can transform the digital world as we know it.

2.3.1.5 *Environmental and earth sciences and cultural heritage*

The SEE region, in common with the rest of Europe, is facing enormous environmental challenges in the context of finite or diminishing resources coupled with growing and changing economic needs. At the same time, human populations and the demands they make on the environment are causing increasing damage to the atmosphere, water, and soil. A major challenge facing society is to identify and use natural resources in the most sustainable way possible and, in recognition of the harm done in ages past, to engage in environmental remediation wherever possible [2.12].

Spatial and chemical heterogeneity and complexity are universal hallmarks of the minerals, soils, and fluids studied in the environmental and earth sciences. For example, soils are structures made up of various minerals, biomaterials, plants, bacteria, and soil-dwelling animals (e.g. worms). This structural complexity is critical to the proper functioning of soil. Trace elements are an essential part of soil, but regrettably many soil environments have been spoilt as a consequence of past industrial activity. There are many places in the SEE where the soil has been damaged by mining, extraction, and energy generation [2.13]. Synchrotrons provide a uniquely useful suite of tools to assist in knowledge-based remediation (rather than bury-and-forget) policies. X-ray spectroscopy combined with imaging makes it possible to determine not only where and how contaminants are distributed in the soil environment but also, most importantly, the chemical state of each contaminant. This knowledge is absolutely key in helping to decide how best to remove contaminants. It is now possible to measure chemical speciation for concentrations as low as a few ppm in situ.

Nanomaterials are finding increasing use in the modern world because they can offer special advantageous properties compared with bulk materials; however, nanomaterials may cause environmental problems when they are disposed of after use. This is becoming a growing issue of concern in the 21st century as surprisingly large quantities of nanomaterials are being used and yet comparatively little consideration has been given to their effects on the environment. This is a challenge that modern synchrotrons can help with: the latest generation of scanning X-ray microscopes are capable of resolving length scales as small as 10 nm [2.14], which when combined with spectroscopy makes it possible to follow the chemical pathways of nanomaterial pollutants in the environment.

Steady supplies of minerals and other elements remain important to the economic security of a region, and so the search for new and secure supplies and better methods of extraction will continue across the SEE region. The ability of synchrotron-based spectroscopy to determine the chemical states of important elements at low concentrations will be vital in such endeavours. In addition, improvement in extraction methods requires deep understanding of the structure of materials. For a complex material, gaining such understanding is made simpler by the use of diffraction combined with imaging techniques afforded by synchrotrons. Finally, processes of extraction can be modelled under operational conditions by building upon the techniques developed for chemical catalysis described in section 2.3.1.2 above.

The SEE countries have a cultural heritage which matches—and in many places surpasses—that found elsewhere in Europe. Understanding this heritage is of enormous interest to the people of the

region, and synchrotrons provide powerful tools which make it possible to look deep inside fragile and uniquely valuable cultural objects to determine their provenance and aid in their conservation. There are now examples within Europe of how national and regional synchrotron facilities can collaborate with people in charge of the conservation of cultural heritage to build capacity that is uniquely equipped to meet the specific needs of a region. Currently no facility in Europe is designed to meet the needs of the unique SEE region, and so compromises are inevitable. Therefore, the construction of SEE-LS will provide opportunities to bring together conservationists and experts in building synchrotron facilities to create an institution that will promote understanding and facilitate conservation of the cultural heritage of the SEE for the next generation.

2.4 Design parameters of the SEE light source

The more than 60 SRL facilities in the world have energies in the range of 0.5–3 GeV. Most users are particularly interested in X-rays, and the energy spectrum of the X-rays depends on the maximum electron energy of the storage ring. Facilities with electron energies below 2 GeV will emit mainly soft X-rays with a spectrum up to 10 keV. Electrons with energies of around 3 GeV emit radiation in the hard X-ray regime, up to 30 keV.

Many users (mainly those interested in structural molecular research) want to have hard X-rays; therefore most of the latest SRLs are 3 GeV machines that produce hard X-rays. Because the cost of these facilities rises sharply with energy, one might consider a first-stage facility in SEE with an energy of 2.5 GeV. This would save on initial investment while allowing for a later upgrade to 3 GeV by adding additional radio-frequency power.

Also of importance to users is the brilliance of the SRL, which is the number of emitted photons normalized with respect to the radiation opening angle and area (see Fig. 2.5). The brilliance is inversely proportional to the emittance and proportional to the stored electron current. The emittance is in general proportional to the third power of the deflection angle of the bending magnets. Hence, to obtain a small emittance, it is much better to install a greater number of short bending magnets instead of a few long magnets. This is one of the elements of the new concept of MAX IV [2.14]. Furthermore, the highest brilliances are obtained from insertion devices that are located in the straight sections. To take advantage of this fact and to enable many beam lines from insertion devices, the storage ring should be designed with a sufficient number of straight sections. In addition, it is expected that in the future more users will be looking for a higher degree of *radiation coherence* in order to open up new areas of application of synchrotron radiation. The coherence increases with smaller emittance as well. Figure 2.8 shows the coherence of the light from 3rd generation (emittance = 4 nm rad) and 4th generation (emittance = 0.2 nm rad) light sources. Going from a 3rd to 4th generation light source, the coherence increases by more than an order of magnitude. Sources that combine all of these aspects—an emittance smaller than 300 pm rad, a large number of straight sections, and a high degree of coherence—are called 4th generation light sources.

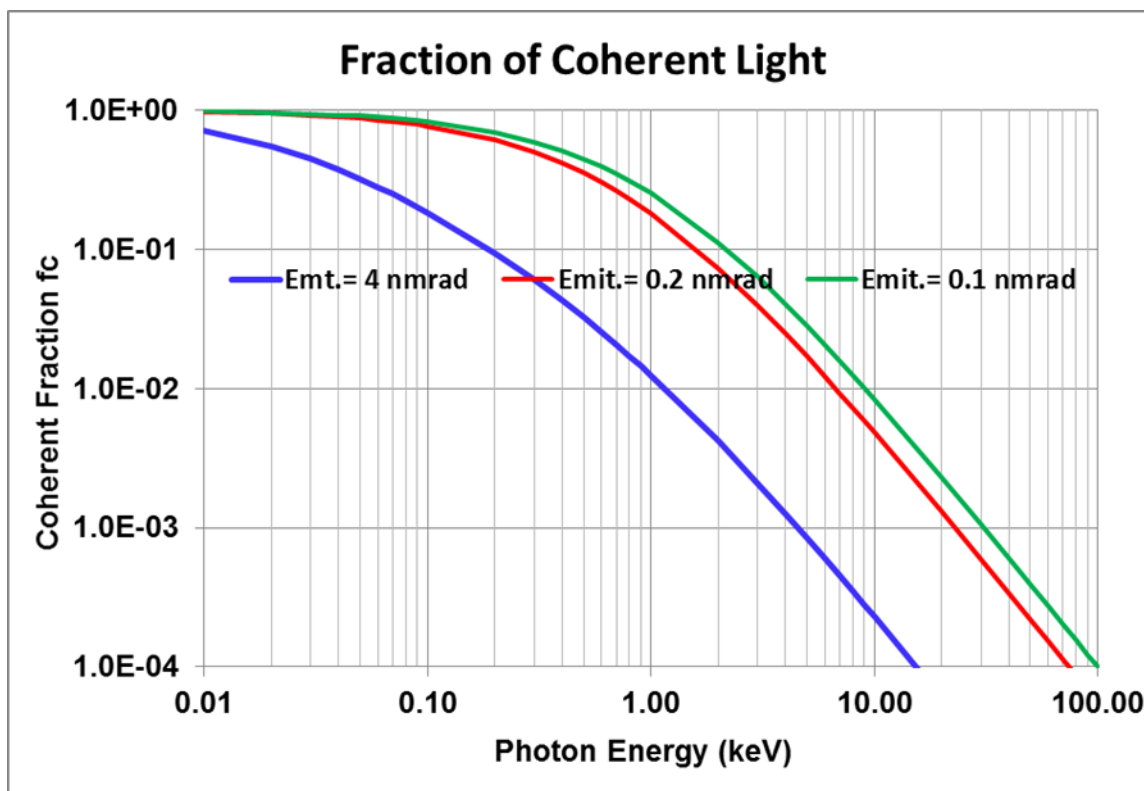


Fig. 2.8: The fraction of coherent light as a function of the photon energy

In order to be fully competitive, the SEE-LS project should be a 4th generation light source. Keeping in mind the aspects mentioned above, preliminary studies have shown that the following parameters would offer an attractive compromise between excellent performance and reasonable cost: energy of 2.5 GeV (with a possibility of upgrading to 3 GeV), emittance of less than 200 pmrad, circumference no larger than 350 m to save on investment costs, a magnet lattice with 16 straight sections for the installation of insertion devices, and a current of 400–500 mA in the machine.

Different types of lattices have been investigated to see which can meet these requirements of a 4th generation light source: a 7 multi-bend achromat (7MBA), as for MAX IV [2.14] and the upgrade of SLS; a double triplet achromat (DTBA), as for the upgrade of Diamond [2.15] and ELETTRA [2.16]; and a hybrid multi-bend achromat (HMBA), as for the ESRF-EBS [2.16] and the upgrade of APS [2.18] and other machines. The result is that a solution based on the HMBA lattice but incorporating some new ideas can satisfy the required criteria for the SEE-LS. For the different components and subsystems, the best proven technology will be used in order to minimize cost and risk. This will produce a state-of-the-art facility that is world-leading in some respects. The overall capacity for beam lines will be up to 14 insertion devices (10 undulators, two wigglers, and two superconducting wigglers). In addition, several bending magnet beam lines (up to 16) can be constructed. The choice of the beam lines to be installed initially would, of course, depend on the interest of users.

The proposed design is unique in the sense that it combines the best techniques of previous facilities, such as the magnets from the European Synchrotron Radiation Facility (ESRF) [2.17] and the vacuum and radio-frequency system from the MAX IV laboratory [2.14].

The injector will use a 100 MeV linac as pre-injector together with a full-energy booster synchrotron. The 100 MeV linac will be a commercial one, while the booster synchrotron will have to be designed and built by SEE-LS. The booster synchrotron will be located in the machine tunnel to save on costs and to obtain a small emittance so as to reduce electron losses during injection, minimize the shielding around the storage ring, and increase the injection efficiency.

The accelerator complex should fulfil the following requirements.

SYNCHROTRON RADIATION

- i) It should have high flux over a wide energy range, from carbon (K-edge = 285 eV) for scanning transmission X-ray microscopy (STXM) to palladium (K-edge = 24.4 keV) for extended X-ray absorption fine structure (EXAFS).
- ii) It should have high brightness over a more limited range, from carbon (K-edge = 285 eV) for STXM to selenium (K-edge = 12.6 keV) for multi-wavelength anomalous diffraction (MAD) in protein crystallography.
- iii) In case higher-energy X-rays (> 25 keV) are needed (e.g. tomography on thick samples, EXAFS on $Z > 46$ elements), it will suffice to later install moderate-flux and low-brightness beam lines based on few-pole wigglers.
- iv) It should have sufficient straight sections for insertion device-based beam lines, which probably means 12- or 16-fold periodicity. The only foreseeable need for bending magnet beam lines is for electron beam diagnostics, and possibly one or two infrared beam lines.
- v) An emittance of 200 pm rad is possible for the most ambitious facilities at present and will thus be the goal of a less ambitious facility to be completed in around 10 years from now.
- vi) Since ultra-fast experiments are not prioritized, the radio-frequency system can be chosen to maximize brightness and reliability while minimizing cost. A 100 MHz system based on commercial frequency-modulation technology seems a reasonable starting point.
- vii) It should have a 300–350 m circumference accommodating 12–16 straight sections with insertion device beam lines only. Bend magnet beam lines should be made available for diagnostic purposes and for one or two infrared beam lines.
- viii) It should have a ring energy of around 2.5–3.0 GeV so that high brightness is achieved over a photon energy range from carbon (K-edge = 285 eV) for STXM to selenium (K-edge = 12.6 keV) for protein crystallography (MAD). High flux should be provided up to palladium (K-edge = 24.4 keV). For energies above 20 keV or so, this might be best achieved using multi-pole wigglers.

References

- [2.1] lightsources.org, <https://web.archive.org/web/20190402180802/https://lightsources.org/>, last accessed April 2nd 2019.
- [2.2] X-ray absorption spectroscopy (factsheet), Australian Synchrotron, <https://web.archive.org/web/20190319131136/https://archive.synchrotron.org.au/images/stories/beamline/factsheets/synchrotron-fact-sheet--xrayas-sept08.pdf>, last accessed March 19th 2019.
- [2.3] P.F. Tavares *et al.*, *J. Synchrotron Rad.* **25** (2018) 1291, <https://doi.org/10.1107/S1600577518008111>
- [2.4] League of European Accelerator-based Photon Sources, <https://web.archive.org/web/20190331214839/https://www.leaps-initiative.eu/>, last accessed March 31st 2019.
- [2.5] J. Als-Nielsen and D. McMorrow, *Elements of Modern X-Ray Physics*, 2nd ed. (Wiley, New York, 2012), <https://doi.org/10.1002/9781119998365>
- [2.6] J.A. van Bokhoven and C. Lamberti, *X-Ray Absorption and X-Ray Emission Spectroscopy: Theory and Applications* (Wiley, New York, 2016), <https://doi.org/10.1002/9781118844243>
- [2.7] Proc. 14th International Conference on X-Ray Microscopy (XRM2018), *Microscopy and Microanalysis* **24** (2018) Supplement S2.
- [2.8] E. Pechkova and C. Riekell (eds.), *Synchrotron Radiation and Structural Proteomics* (CRC Press, Boca Raton, Florida, 2011), <https://doi.org/10.1201/b11434>
- [2.9] T.A. Ezquerro, M.C. Garcia-Gutierrez, A. Nogales, and M. Gomez (eds.), *Applications of Synchrotron Light to Scattering and Diffraction in Materials and Life Sciences* (Lecture Notes in Physics No. 776, Springer, Berlin, 2009), <https://doi.org/10.1007/978-3-540-95968-7>

- [2.10] World Bank Group, The Western Balkans: Revving up the engines of growth and prosperity, Report No. ACS22690, November 2017, <https://openknowledge.worldbank.org/handle/10986/28894>
- [2.11] European Environment Agency, Environmental trends and perspectives in the Western Balkans: Future production and consumption patterns, EEA Report No 1/2010, <https://doi.org/10.2800/39288>
- [2.12] C. Stuhlberger (ed.), *Mining and environment in the Western Balkans* (United Nations Environment Programme, Vienna, 2010), <https://www.unenvironment.org/resources/report/mining-and-environment-western-balkans>
- [2.13] Y.-S. Yu *et al.*, *Nano Letters* **15** (2015) 4282, <https://doi.org/10.1021/acs.nanolett.5b01314>
- [2.14] P.F. Tavares, S.C. Leemann, M. Sjöström, and Å. Andersson, *J. Synchrotron Rad.* **21** (2014) 862, <https://doi.org/10.1107/S1600577514011503>
- [2.15] Diamond Light Source, <https://web.archive.org/web/20190506103232/https://www.diamond.ac.uk/Home.html>, last accessed May 6th 2019.
- [2.16] Elettra and FERMI lightsources, <https://web.archive.org/web/20180703123835/https://www.elettra.trieste.it/lightsources/elettra/elettra-2-0.html?showall=>, last accessed July 3rd 2018.
- [2.17] EBS - Extremely Brilliant Source, <https://web.archive.org/web/20171106091328/http://www.esrf.eu/home/UsersAndScience/Accelerators/ebs---extremely-brilliant-source.html>, last accessed November 6th 2017.
- [2.18] Advanced Photon Source, <https://web.archive.org/web/20171118223907/https://www1.aps.anl.gov/about/welcome>, last accessed November 18th 2017.

3 Layout of a synchrotron light source

D. Einfeld

The main components of a synchrotron light source are (see Fig. 3.1): linac as pre-accelerator, linac-to-booster transfer line, booster synchrotron, booster-to-storage ring transfer line, storage ring, front ends, beam lines, and end stations [3.1,3.2]. The main functions of the components are described in the following.

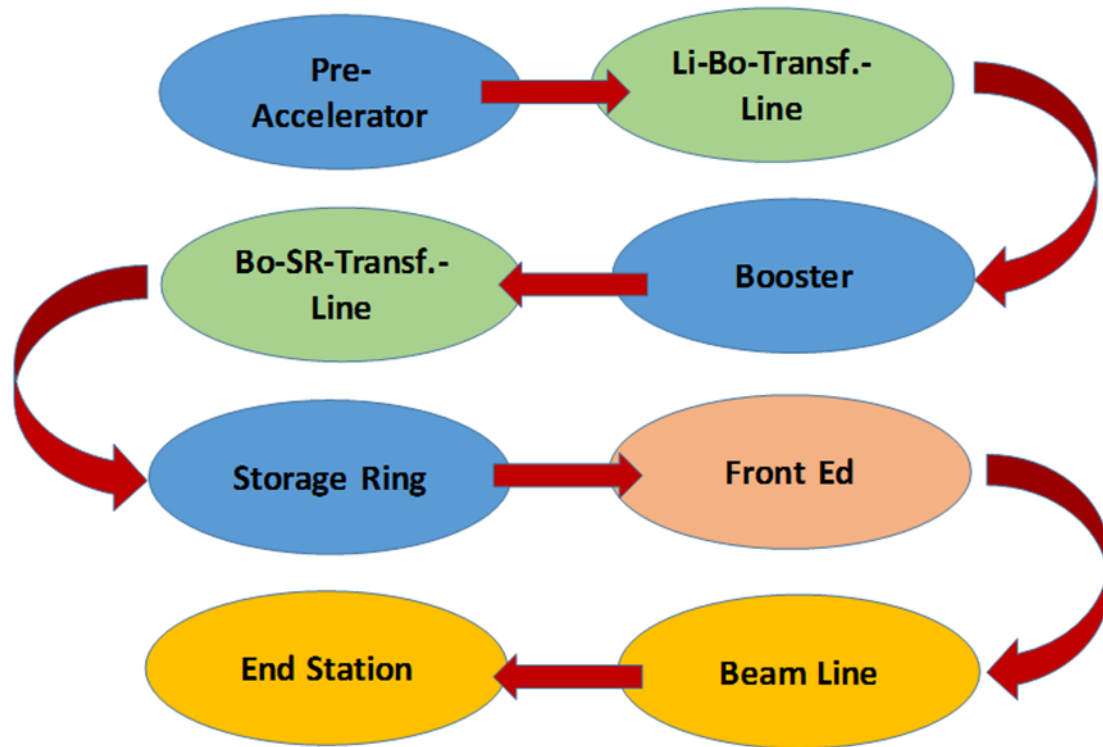


Fig. 3.1: The main sections of a synchrotron light source

- **Pre-accelerator:** In most cases the pre-accelerator is a linac that produces a current of 4–10 mA with an energy of at least 100 MeV. The duration of the electron pulse should be a few μsec , and the duration of the pulse itself should be 1–2 nsec with a frequency of 500 MHz. It is described in more detail in section 14.2.
- **Linac-to-booster transfer line (LTB):** This transfers the beam from the linac to the booster with high efficiency. The final energy of the linac should be in the range of 100–150 MeV (see section 14.3).
- **Booster synchrotron:** This accelerates the beam from the pre-accelerator up to the operation energy of the storage ring (2.5–3 GeV). To reach a high injection efficiency, the emittance of the booster synchrotron should be 10 nmrad or less. The repetition rate of the booster should be in the range of 1–5 Hz (see section 14.1).
- **Booster-to-storage ring transfer line (BTS):** This transfers the beam from the booster to the storage ring with high efficiency (see section 14.4).
- **Storage ring:** This accumulates the beam injected from the synchrotron and stores it at currents up to 400 mA. The stability of the stored beam has to be in the sub-micrometre region. According to the requirements of users, the emittance should be small and the number and length of straight sections should be high. All of these factors are determined by the lattice of the machine. As an example, the lattice for the SRL ALBA [3.2] is presented in Fig. 3.2.

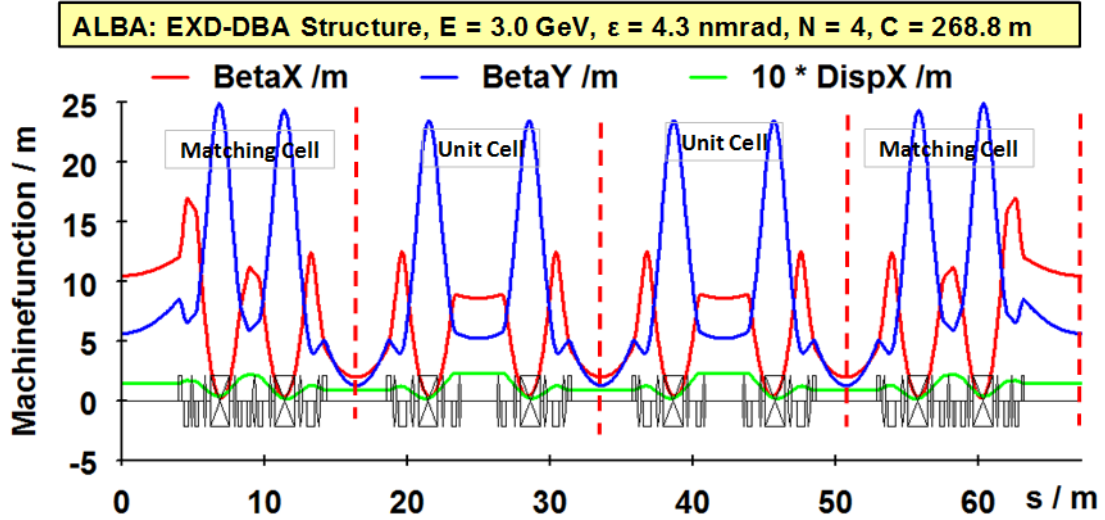


Fig. 3.2: The machine function in an achromat of ALBA

The lattice of the storage ring in ALBA consists of four achromats, leading to 24 straight sections overall. The machine functions $\beta_x(s)$ (in red), $\beta_y(s)$ (in blue), and $\eta_x(s)$ (in green) of an achromat of the ALBA lattice are shown in Fig. 3.2. The values of $\beta_x(s)$ and $\beta_y(s)$ determine the envelopes $E_x(s)$ and $E_y(s)$ according to Eqs. (3.1) and (3.2), as well the divergences $E'_x(s)$ and $E'_y(s)$ of the beam in the machine for the nominal energy E_0 :

$$E_x(s) = \sqrt{A_x \beta_x(s)}, \quad E_y(s) = \sqrt{A_y \beta_y(s)}, \quad (3.1)$$

$$E'_x(s) = \sqrt{A_x / \beta_x(s)}, \quad E'_y(s) = \sqrt{A_y / \beta_y(s)}, \quad (3.2)$$

The values of A_x and A_y define the acceptances of the machine in the horizontal and vertical directions [3.3]. For a stored beam envelopes A_x and A_y are the emittances ε_x and ε_y .

The closed orbit for energy deviations ΔE is given by the dispersion function $\eta_x(s)$ according to

$$D_x(s) = \eta_x(s) \left(\frac{\Delta E}{E} \right) \quad (3.3)$$

- **Front ends:** Over the front ends (see Figs. 3.3 and 3.4), coupled with the vacuum system of the storage ring, the photo beam coming from the bending magnets or insertion devices of the circulating electron beam in the storage ring will be passed to the beam lines in the experimental hall.
- **Beam lines:** Through the beam lines the photon beam will pass to the end station. Each beam line has a special layout, depending on the experiment. The arrangements of the beam lines in the case of ALBA are shown in Figs. 3.7 and 3.8
- **End station:** Within the end station are the samples exposed, and the corresponding detectors measure the stray light from the sample.

The layout of the accelerator complex is presented in Fig. 3.5. The booster synchrotron and the storage ring are mounted in the same machine tunnel. Adjacent to the machine tunnel is the so-called linac bunker. At the centre of the building is the service area for the equipment (radio-frequency system,

LAYOUT OF A SYNCHROTRON LIGHT SOURCE

diagnostics, power supplies, vacuum, etc.) needed for operation of the linac, booster synchrotron, and storage ring. Not all of the space at the centre of the building is needed for the service area, and a free area is available, which is called the courtyard. For the Swiss light source this area is used for offices and laboratories. The arrangement of the booster and storage ring in the same tunnel (for ALBA) is shown in Fig. 3.6 [3.2]. The storage ring is on the left side and the booster is on the right. The space between the two, needed for installation and maintenance, is between 0.8 and 1.5 m wide.

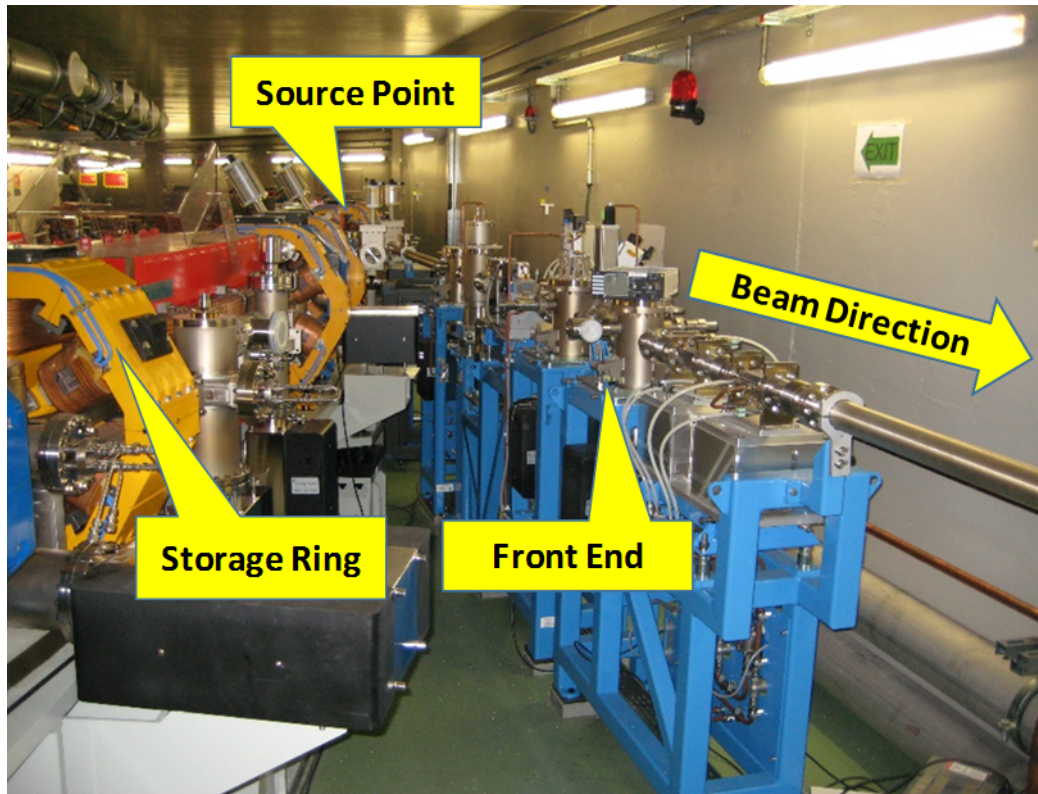


Fig. 3.3: The first part of the front end, which comes from the source point

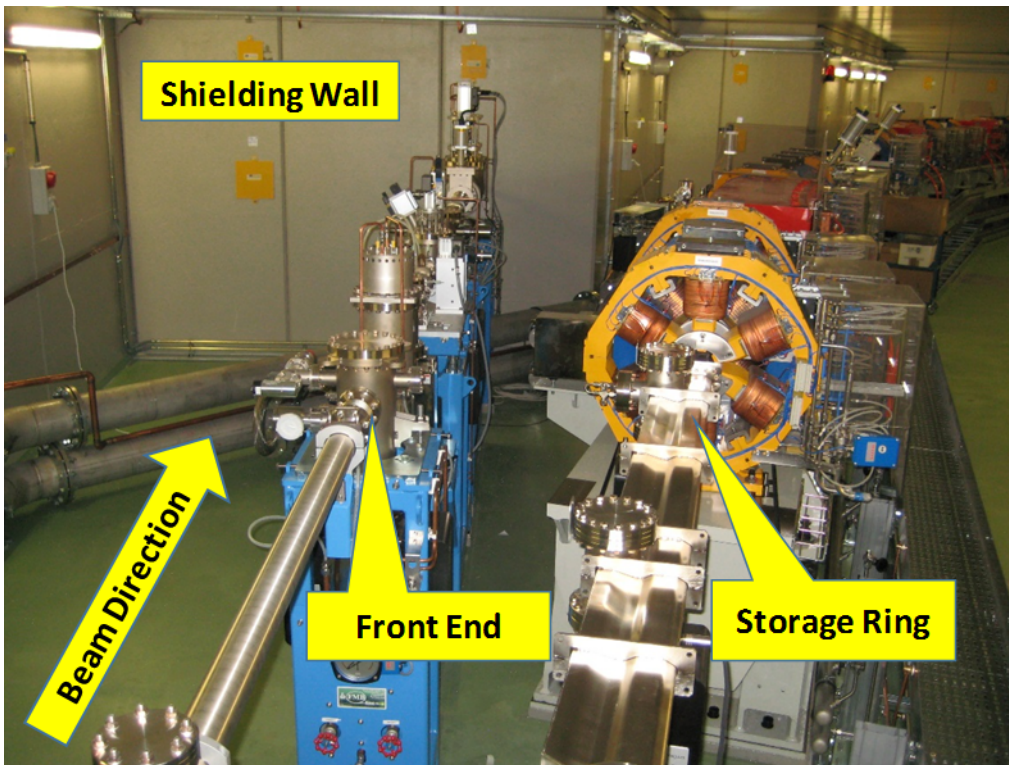


Fig. 3.4: The second part of the front end, which goes to the shielding wall

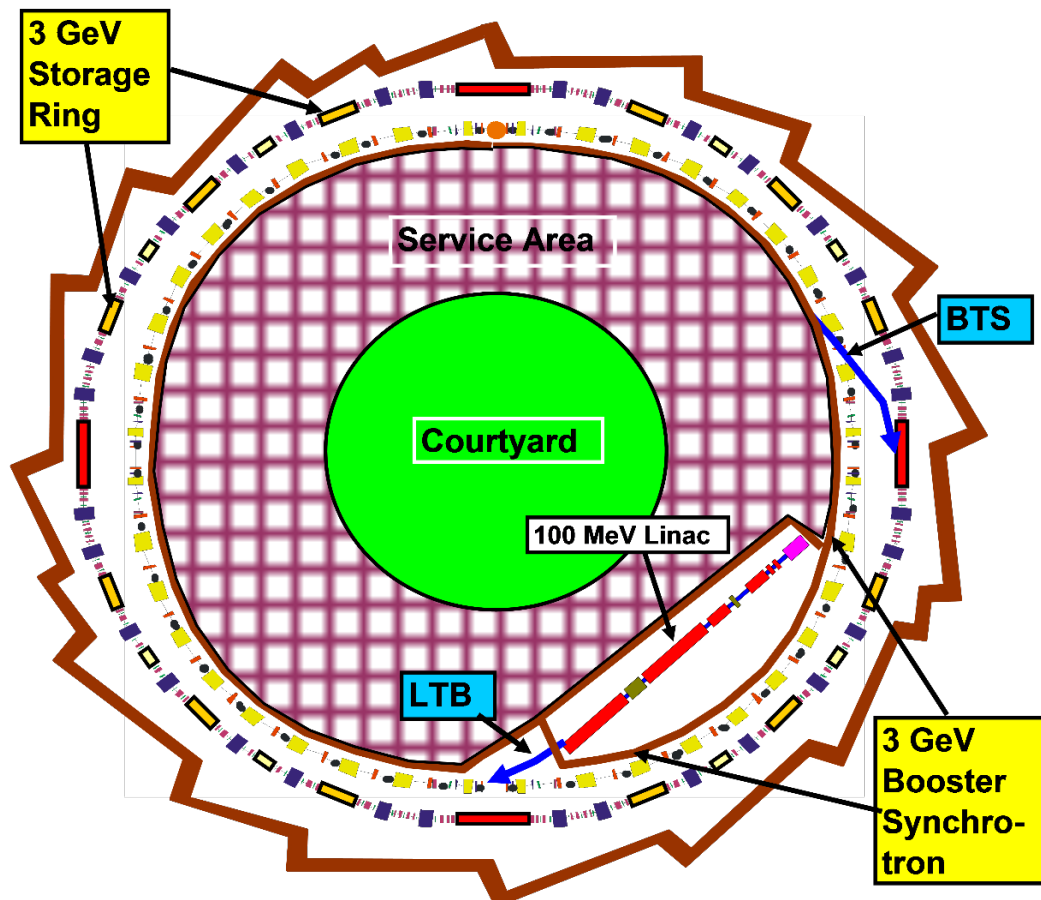


Fig. 3.5: The layout of the accelerator complex

LAYOUT OF A SYNCHROTRON LIGHT SOURCE

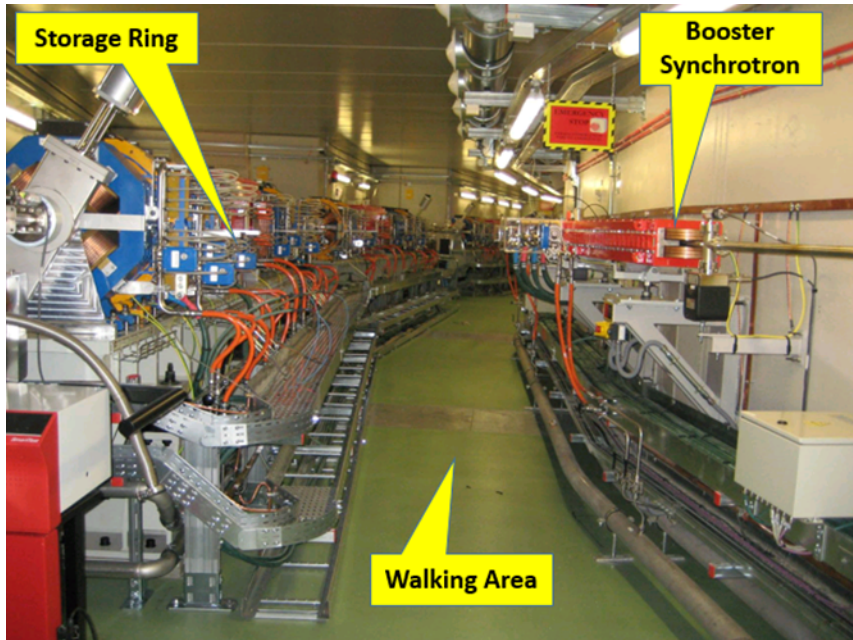


Fig. 3.6: The machine tunnel with the storage ring on the left-hand side and the booster synchrotron on the right-hand side.

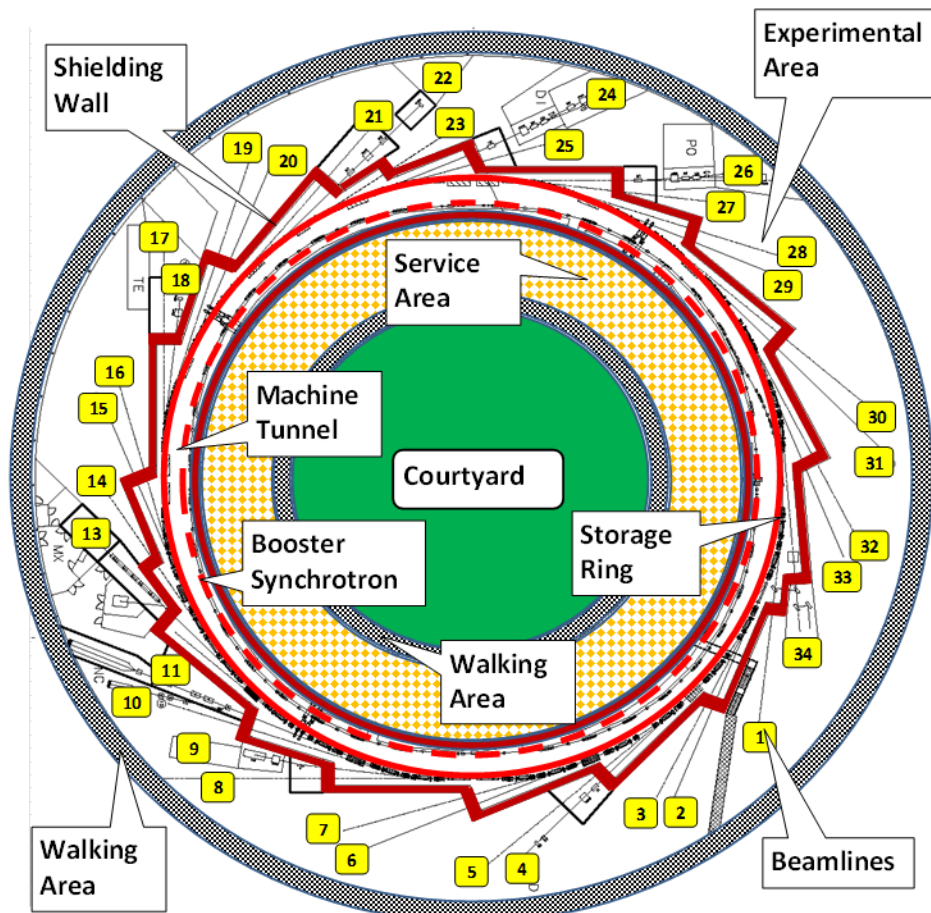


Fig. 3.7: Arrangement of the possible beam lines in the experimental area of ALBA

The arrangement of the beam lines in the experimental hall of ALBA [3.4] is presented in Fig. 3.7, and Fig. 3.8 is a photograph of the ALBA experimental hall. Around the machine tunnel is a 1.5 m-thick shielding wall. The front ends are located between the storage ring and the shielding wall.

Right after the shielding wall are the beam lines with the corresponding safety hatches and the end station (see Fig. 3.8). The experimental hall at ALBA has space for 34 beam lines coming from the insertion devices and from the bending magnets. At present there are seven beam lines at ALBA.



Fig. 3.8: Beam lines in the experimental hall of ALBA

References

- [3.1] lightsources.org, <https://web.archive.org/web/20190402180802/https://lightsources.org/>, last accessed April 2nd 2019.
- [3.2] D. Einfeld, ALBA synchrotron light source commissioning, Proc. IPAC2011, San Sebastián, Spain, 4–9 September 2011, p. 1.
<http://accelconf.web.cern.ch/AccelConf/IPAC2011/papers/moxaa01.pdf>
- [3.3] H. Wiedemann, *Particle Accelerator Physics* (Springer, Berlin, 2015),
<https://doi.org/10.1007/978-3-319-18317-6>
- [3.4] ALBA, <https://web.archive.org/web/20180706033038/https://www.cells.es/en>, last accessed July 6th 2018.

4 Lattice considerations

D. Einfeld

4.1 Introduction

One of the first proposals for the lattice design of a *diffraction-limited light source* was produced in the early 1990s [4.1–4.5]. At that time the new 3rd generation light sources ALS, ESRF, and ELETTRA were commissioned in record time. All three machines reached their target specifications without any significant beam-dynamic problems and have operated reliably ever since. The successful commissioning results built confidence in the ability to operate storage rings with horizontal emittances an order of magnitude lower, in the 0.5 nmrad range. With a coupling of 1%, the vertical emittance would be of the order of 5 pmrad. The original calculations having been performed over 20 years ago, the new MAX IV [4.6] facility will be the first SRL to implement a sub-nmrad variant of this design, and other proposed machines are following the multi-bend achromat (MBA) concept.

One of the most important factors in synchrotron radiation research is photon beam brilliance, which in storage rings is determined by the electron beam emittance and the coupling between the horizontal and vertical planes. Even in the limit of zero beam emittance, however, the phase space of the radiation emission from an undulator is itself finite due to diffraction effects at the source. For single-mode photon emission, the corresponding diffraction-limited ‘emittance’ of the photon beam is given by

$$\varepsilon(\text{phot}) \leq \frac{\lambda}{4\pi} = 0.159\lambda = 98.66 \text{ pmrad} / (E_\gamma / \text{keV}), \quad (4.1)$$

where λ is the X-ray wavelength and E_γ is the photon energy in keV [4.7, 4.8]. For photon energies of 1, 5, and 10 keV, the corresponding beam emittance should be smaller than 100, 20, and 10 pmrad, respectively. Equation (4.1) has been much debated, and there is still no consensus that the factor of 4π in the denominator is numerically correct [4.8]. Nevertheless, a light source is referred to as ‘diffraction-limited’ when the electron beam emittance is less than that of the radiated photon beam at the desired X-ray wavelength.

By way of review, recall that the horizontal emittance of an electron storage ring beam is determined by a balance between two competing processes: 1) quantum excitation of betatron oscillations from photon emission according to Eq. (3.3) and 2) longitudinal re-acceleration within the radio-frequency (RF) cavities to bring the beam to the nominal energy E_0 again. The basic formula for calculating storage ring emittance, assuming isomagnetic bend magnets and no insertion devices, is summarized [4.9] as

$$\varepsilon = C_q \gamma_0^2 \frac{\langle H \rangle_{\text{mag}}}{J_x \rho}, \quad (4.2)$$

where $C_q = 3.841 \times 10^{-13}$ m is a constant, γ_0 is the relativistic Lorentz factor, J_x is the Robinson partition number evaluated for the horizontal plane, ρ is the dipole magnet bending radius, and $\langle H \rangle_{\text{mag}}$ is the average of H evaluated in the bending magnets,

$$\langle H \rangle = \frac{1}{2\pi\rho_0} \int \gamma\eta^2 + 2\alpha\eta\eta' + \beta\eta'^2 ds. \quad (4.3)$$

The definitions of $\alpha(s)$ and $\gamma(s)$ are

$$\alpha(s) = -\frac{1}{2}\beta'(s), \quad \gamma(s) = \frac{1 + \alpha^2(s)}{\beta(s)}. \quad (4.4)$$

In Eqs. (4.3) and (4.4), α , β , and γ are the standard position-dependent Twiss parameters in the horizontal plane, and η and η' are the horizontal dispersion function and its first derivative, respectively. As a general rule, for low emittance one has to minimize the integral quantity $\langle H \rangle_{\text{mag}}$ to maintain sufficient straight-section free space for insertion devices and operate at sufficiently high beam energy to meet the spectral requirements of the user community.

4.2 Low-emittance lattice design

Referring again to Eq. (4.2), the horizontal beam emittance is seen to scale with the square of the beam energy, scale linearly with $\langle H \rangle_{\text{mag}}$, and be inversely proportional to the partition number J_x . For bending magnets with a pure dipole field, $J_x = 1$. Since the H -function is determined by the Twiss parameters and the dispersion in bending magnets, low emittance can be achieved if the beam sigma matrix and $\eta(s)$ have specifically controlled values within the bending magnets. For example the horizontal emittance can be analytically evaluated for two well-known cases: the first bend magnet of a flat-field *double-bend achromat* (DBA) lattice [4.10]; and the centre bend magnet of a flat-field *triple-bend achromat* (TBA) structure [4.11] (see Fig. 4.1).

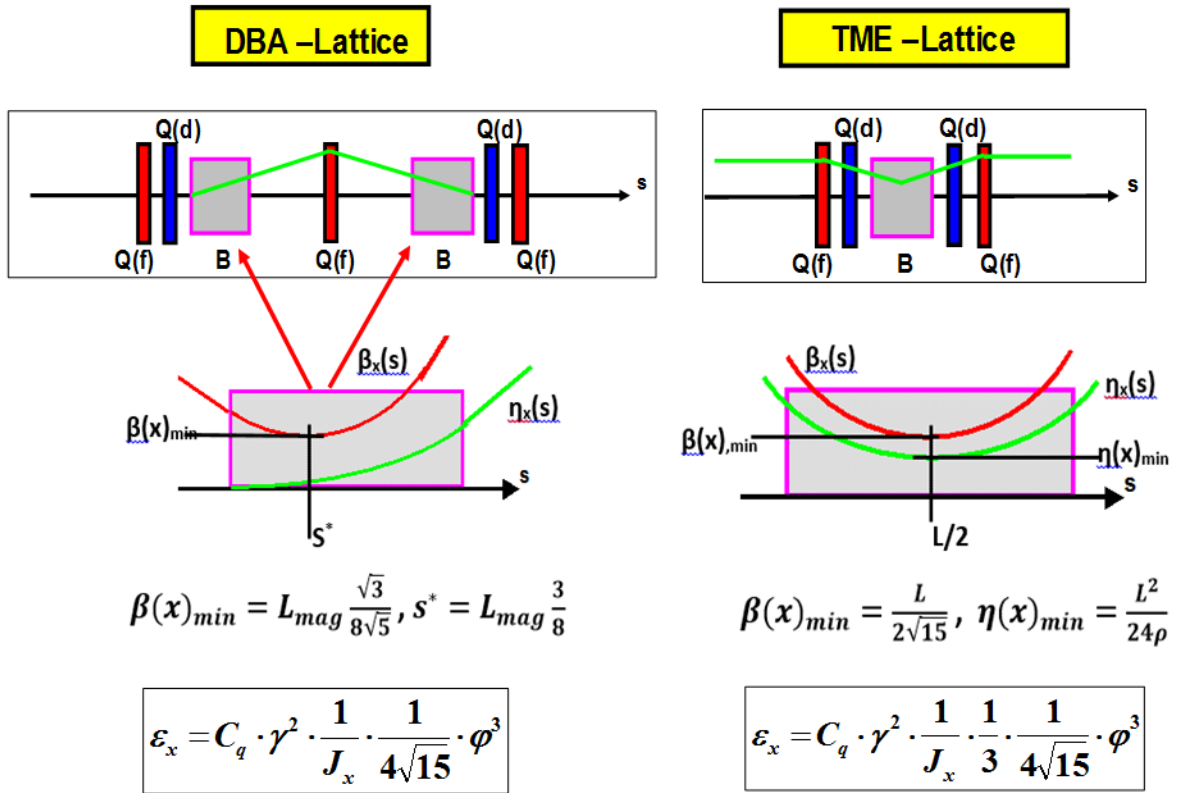


Fig. 4.1: The DBA lattice and TME structure to attain a minimum emittance

The *theoretical minimum emittance* (TME) of a storage ring beam can be attained only when both the horizontal beta function and the horizontal dispersion reach a minimum at the centre of the bending magnets. These conditions are met when $\beta_{\min} = L / 2\sqrt{15}$ and $\eta_{\min} = L^2 / (24\rho)$ [4.12, 4.13], yielding

$$\varepsilon(\text{TME}) = C_q \gamma_0^2 \frac{1}{J_x} \times \frac{1}{3} \times \frac{1}{4\sqrt{15}} \phi^3 = \frac{31.65 \text{ nmrad}}{J_x} \left(\frac{E}{\text{GeV}} \right)^2 \left(\frac{\phi}{\text{rad}} \right)^3. \quad (4.5)$$

LATTICE CONSIDERATIONS

According to Eq. (4.5), the TME is proportional to the third power of the dipole magnet deflection angle ϕ and the square of the electron energy. In practice, most conventional light sources operate with a horizontal emittance of two to five times the TME value.

The optimum emittance of a DBA lattice is a factor of 3 above TME (see Fig. 4.1). The horizontal partition number J_x is given by

$$J_x = 1 - D, \quad D = \frac{1}{2\pi\rho^2} \int \eta[1 - 2k\rho^2] ds, \quad (4.6)$$

where $k(s)$ is the normalized quadrupole gradient in the bending magnets. For bending magnets with a pure dipole field, $J_x = 1$. Vertical focusing in the bending magnets increases J_x to a maximum of 2, yielding a reduction in emittance of up to a factor of 2; however, the energy spread goes up and could have negative effects.

The introduction of damping wigglers serves to increase the radiated energy loss per turn, U_0 , by an amount U_{wi} [4.12, 4.13, 4.14], and to first approximation this decreases the emittance as follows:

$$\varepsilon_{wi} = \varepsilon_0 \frac{U_0}{U_0 + U_{wi}}, \quad (4.7)$$

$$U_0 = 88.46 \text{ keV} \times \frac{\left(\frac{E}{\text{GeV}}\right)^4}{\left(\frac{\rho}{\text{m}}\right)}, \quad (4.8)$$

$$U_{wi} = 0.633 \text{ keV} \times \left(\frac{L}{\text{m}}\right) \left(\frac{E}{\text{GeV}}\right) (B_m)^2. \quad (4.9)$$

In Eqs. (4.7)–(4.9), U_0 is the energy loss per turn in the bending magnets and U_{wi} is that in the insertion devices.

To achieve low emittance in the storage ring, the following points should be considered.

- (i) The number of magnets has to be large, which means using *multi-bend achromat* (MBA) cells with five or more bending magnets.
- (ii) The outer bending magnets must be shorter by roughly a factor of 2.
- (iii) The bending magnets should be of combined-function construction with vertical focusing to increase and maximize J_x . Combined-function bending magnets also have the advantage of yielding a compact machine design, and they can often increase separation of the beta functions at sextupole locations.
- (iv) Damping wigglers can be installed to increase radiative energy loss per turn and therefore decrease emittance.
- (v) Longitudinal-gradient bending magnets have the potential to further decrease emittance [4.14].

4.3 The synchrotron radiation brilliance

The brilliance is calculated according to

$$B = \frac{\dot{N}}{2\pi^2 \Sigma_x \Sigma_y \Sigma_{x'} \Sigma_{y'}}, \quad (4.10)$$

where \dot{N} is the photon flux in the central cone, which depends only on the number of periods, the beam current, and a function independent of the machine parameters. Hence, for a given insertion device, the flux for each harmonic is the same, and the energy at which each harmonic is located depends on the energy of the machine, as shown in Eqs. (4.11) and (4.12); K is the so-called deflection parameter:

$$E_r(n) = \frac{0.949 \text{ keV} \times \left(\frac{E}{\text{GeV}}\right)^2 \times n}{\left(\frac{\lambda_u}{\text{cm}}\right) \left(1 + \frac{K^2}{2}\right)}, \quad (4.11)$$

$$K = 0.934 \times \left(\frac{B_0}{T}\right) \left(\frac{\lambda_u}{\text{cm}}\right). \quad (4.12)$$

Therefore, the differences between the brilliances of different lattices will come from the factor

$$\frac{1}{\Sigma_x \Sigma_y \Sigma_{x'} \Sigma_{y'}}. \quad (4.13)$$

The denominator in (4.13) corresponds to the multiplication of convoluted sizes of electron and photon beams, i.e.,

$$\Sigma_x = \sqrt{\sigma_x^2 + \sigma_r^2}, \quad \Sigma_y = \sqrt{\sigma_y^2 + \sigma_r^2}, \quad \Sigma_{x'} = \sqrt{\sigma_{x'}^2 + \sigma_{r'}^2}, \quad \Sigma_{y'} = \sqrt{\sigma_{y'}^2 + \sigma_{r'}^2}. \quad (4.14)$$

The beam sizes and divergences $\sigma_x, \sigma_y, \sigma_{x'}$ and $\sigma_{y'}$ depend on machine parameters, the emittance ε , and the beta functions β_x and β_y . If the dispersion function at the position of the undulator is zero, $\sigma_x, \sigma_y, \sigma_{x'}$ and $\sigma_{y'}$ are given by

$$\sigma_x = \sqrt{\varepsilon_x \beta_x}, \quad \sigma_y = \sqrt{\varepsilon_y \beta_y}, \quad \sigma_{x'} = \sqrt{\varepsilon_x / \beta_x}, \quad \sigma_{y'} = \sqrt{\varepsilon_y / \beta_y}. \quad (4.15)$$

The photon size and dispersion σ_r and $\sigma_{r'}$ for each harmonic depend on the length of the undulator L and the characteristic undulator wavelength λ [4.8]:

$$\sigma_r = \frac{1}{\sqrt{2\pi}} \sqrt{\lambda L}, \quad \sigma_{r'} = \frac{1}{\sqrt{2}} \sqrt{\frac{\lambda}{L}}, \quad \lambda = \frac{l_u}{2\pi\gamma^2} \left(1 + \frac{K^2}{2}\right). \quad (4.16)$$

Here K is the deflection parameter, L is the length of the undulator, l_u is the undulator period, and n is the harmonic number. According to the investigations by Kim [4.15], the dimension of the photon source size differs by a factor of $1/2$. The machine energy is given by the factor $1/\gamma^2$, so higher machine energy means lower wavelength (or higher photon energy). Therefore photon size decreases with machine energy, and hence brilliance, which depends on the photon size, increases with machine energy.

The cross-section and divergence of the undulator radiation are presented in Figs. 4.2 and 4.3. The radiation cross-section $\sigma(r)$ goes from $2 \mu\text{m}$ at 4 keV to $0.6 \mu\text{m}$ at 36 keV . The horizontal cross-section $\sigma(x)$ for the different lattices goes from 40 to $70 \mu\text{m}$; hence the radiation cross-section has only a marginal influence on the brilliance. What is important is the horizontal beam cross-section σ_x , given by the emittance and the beta function. According to the data given for the vertical direction, the radiation cross-section has a non-negligible effect on the brilliance.

It is completely different for the influence of the radiation divergence $\sigma_{r'}$ on the brilliance. In the horizontal direction the two contributions are approximately equal, but in the vertical direction the divergence $\sigma_{r'}$ of the undulator radiation determines the brilliance. Hence the beta function in the vertical direction, β_y , does not have a big influence on the brilliance of the undulator radiation.

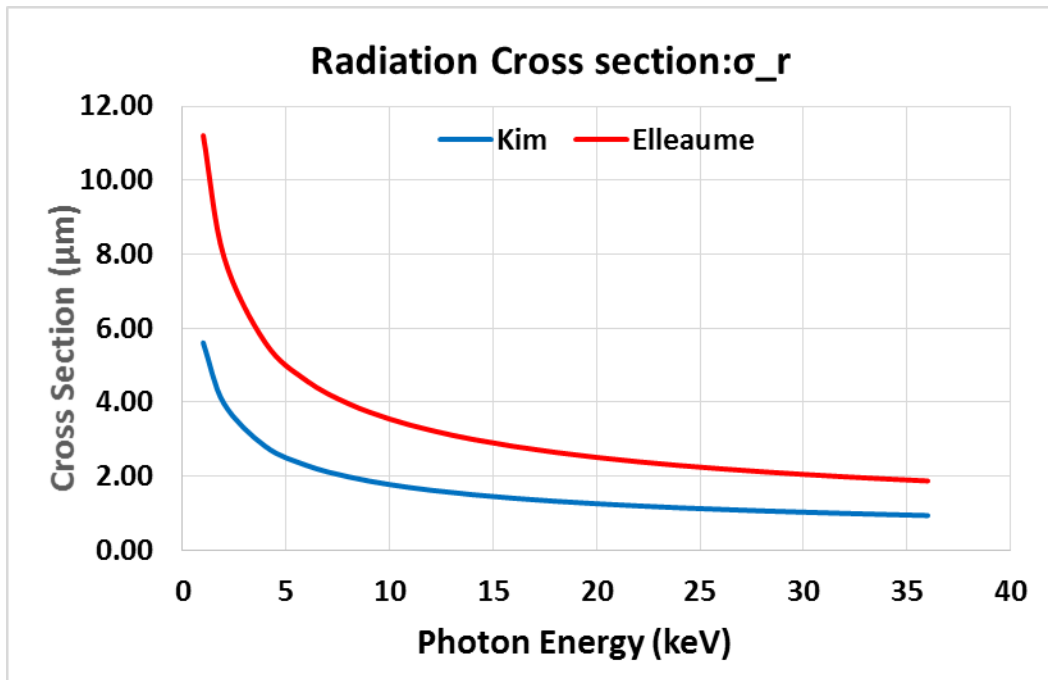


Fig. 4.2: Dependence of the radiation cross-section on the undulator photon energy (according to [4.8] and [4.15]).

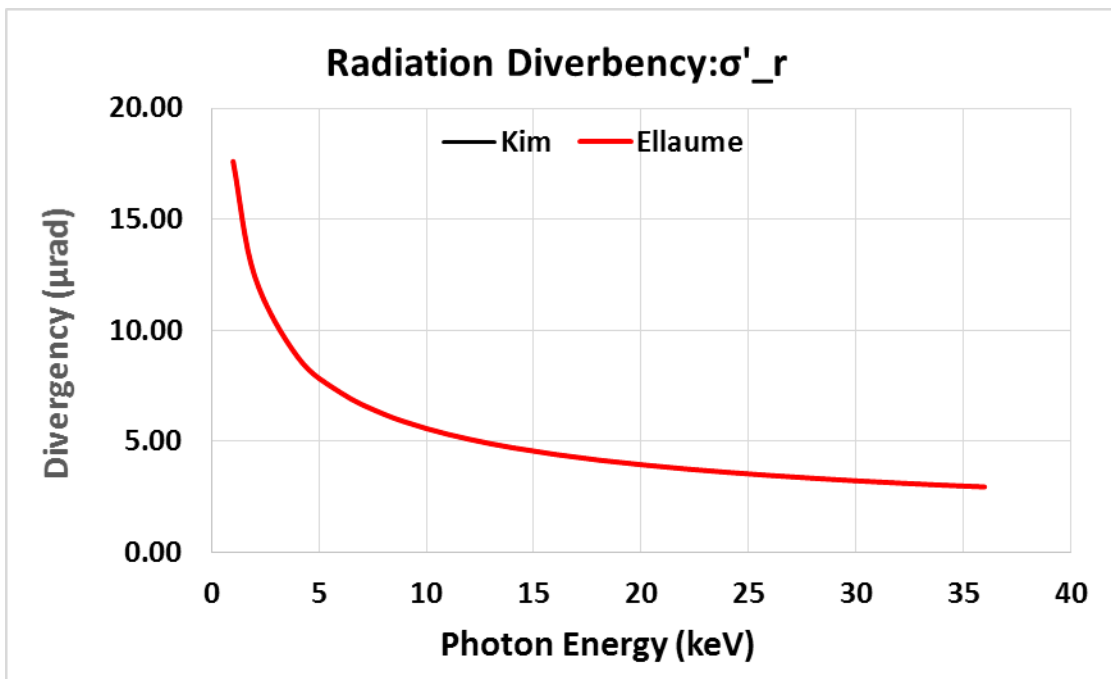


Fig. 4.3: Dependence of the radiation divergence on the undulator photon energy

The emittance ε_r of synchrotron radiation from the insertion devices is $\sigma_r \sigma'_r$, and the corresponding plot is displayed in Fig. 4.4.

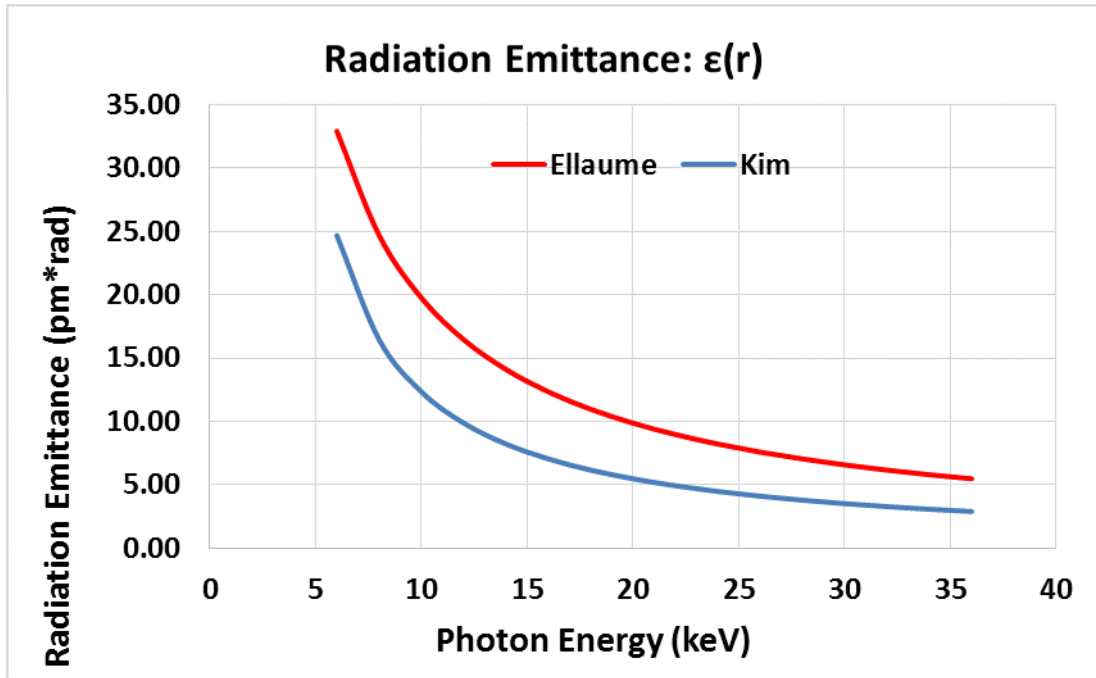


Fig. 4.4: Dependence of the synchrotron radiation emittance on the photon energy

The photon energy E_r of the undulator is proportional to the square of the beam energy and the harmonic number n ; see Eqs. (4.11) and (4.12). It is inversely proportional to the undulator period λ_u and a function of the undulator parameter K . Hence, by increasing beam energy from 2.5 to 3 GeV, the photon energy will be increased by a factor of 1.44.

This investigation shows that the emittance of the photon beam in the whole energy range is smaller than 30 pmrad. The emittance of the SEE-LS should be around 250 pmrad; hence, for the brilliance calculations the photon emittance does not have any influence. To achieve a high brilliance the cross-section of the stored electron beam has to be minimized, and this has to be done by decreasing the emittance as well the beta functions.

4.4 Lattice for the SEE-LS

Well-known lattices for the 4th generation light sources are: a) the 7MBA lattice used for MAX IV [4.16]; b) the 5 multi-bend achromat (5MBA) used for SIRIUS [4.17]; c) the HMBA lattice used for the upgrade of ESRF and other light sources [4.18, 4.19]; d) the double double-bend achromat (DDBA) and double triple-bend achromat (DTBA) lattices used for a possible upgrade of Diamond [4.20, 4.21]; e) the S6BA (also a DTBA) used for the upgrade of ELETTRA [4.22]; and f) the 7MBA lattice with anti-bends and longitudinal gradients in the magnets [4.23] proposed for the upgrade of SLS. Recently, a possible lattice for the upgrade of SOLEIL was presented [4.24]. The lattice file of SOLEIL is not available at present, and the lattice file used was extracted from the plots of the beta functions. The specifications of all these lattices are summarized in Table 4.1.

The DDBA, DTBA, and S6BA lattices have the advantage of containing an additional straight section in the middle of the achromat. These straight sections can be used to install small insertion devices and all the instrumentation needed for operation of the machine; hence, more space is available for users. This is reflected in the percentage of the circumference devoted to straight sections. The HMBA lattice has the requirement that the phase advance between the dispersion regions must be π (vertical) or 3π (horizontal). This limits the settings for the smallest emittance but reduces the number of sextupoles needed. The specifications, according to a matching for a circumference of roughly 350 m, are given in Table 4.2.

LATTICE CONSIDERATIONS

Table 4.1: Parameters of the 4th generation light source lattices proposed for the upgrade of the facilities

Lattice	MAX IV	HMBA	SIRIUS	DDBA	DTBA	S6BA	SLS-2	SOLEIL-2
Circumference (m)	528	506.28	518.4	561	561	259.2	290.4	354.7
Period	20	22	20	24	24	12	12	20
Achromat-length (m)	26.4	23.013	25.92	23.37	23.37	21.6	24.2	17.73
Energy (GeV)	3	3	3	3	3	2	2.4	2.75
Emittance (pmrad)	328	141	250	272	101	255	102	72
Tune Q_x	44.06	53.6	48.1	51.21	57.45	33.1	37.2	55.2
Tune Q_y	17.76	15.43	13.17	17.31	20.36	9.2	15.3	18.2
Chromaticity ξ_x	-51.47	-87.86	-124.4	-129	-78.15	-75	-95	-134
Chromaticity ξ_y	-51.37	-70.78	-79.9	-93.51	-109.7	-51	-35.2	-125

From the relation that the emittance is proportional to the square of the energy and inversely proportional to the cube of the number of magnets, it is possible to estimate the emittance for this lattice with a circumference of roughly 350 m. Accordingly, lattice files for the matched achromats have been evaluated. The corresponding lattices are presented in Figs. 4.5–4.14

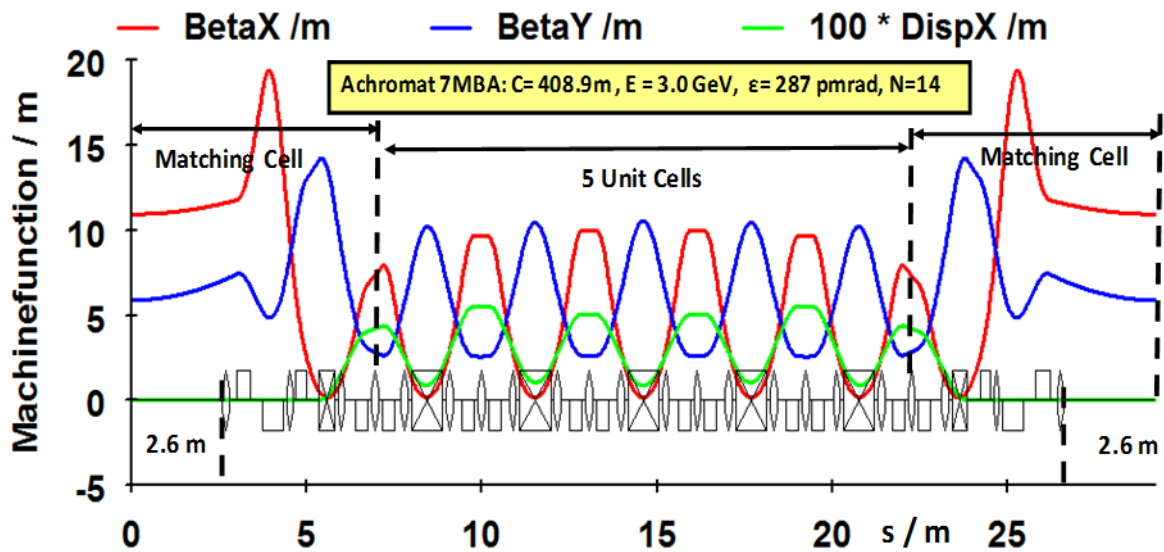
Given the requirements for the circumference, emittance, and number of straight sections, only the HMBA, DTBA, S6BA, and SLS-2 lattices can be taken as candidates for the SEE-LS. Consideration of nonlinear beam-dynamic issues eventually favoured the HMBA and the S6BA. Finally, owing to the reduced numbers of sextupoles and the larger dynamic aperture, the HMBA lattice was chosen as the candidate lattice for the SEE-LS. However, the S6BA lattice is also promising. In making a final decision, and considering the further calculations which have to be done, another lattice solution such as the proposed SOLEIL upgrade cannot be excluded in this case.

4.4.1 The 7MBA lattice

The 7MBA lattice (Fig. 4.5) is built with five unit cells, as shown in Fig. 4.6, and two matching sections. The lattice functions within each unit cell are like a TME structure and those in the matching cell are like a DBA structure (see Fig. 4.1). With a period of $N = 14$ the circumference is roughly 409 m, leading to an emittance of 288 pmrad. In order to reach a circumference of roughly 350 m, the number of achromats has to be reduced to 12, which leads to an emittance of roughly 460 pmrad. In addition, the horizontal chromaticity is quite high, which should reduce the dynamic aperture. Because of this, using large numbers of 7MBA lattices is not an attractive solution for the SEE-LS.

Table 4.2: Parameters of the 4th generation light source lattices that are candidates for the SEE-LS with a circumference of roughly 350 m.

Lattice	7MBA	HMBA I	HMBA II	SIRIUS	DTBA	S6BA	SLS-2	SOLEIL-2
Energy (GeV)	3	3	2.5	3	3	2.5	3	2.75
Circumference (m)	408.9	345.4	329.2	362	361.8	347.2	332.4	354.7
Emittance (pmrad)	288	255	218	806	365	166	131	72
Period	14	16	16	14	16	16	14	20
Tune Q_x	45.23	41.38	37.2	31.39	39.24	44.18	43.29	64.4
Tune Q_y	12.41	12.26	12.22	10.39	13.22	12.39	10.92	22.3
Chromaticity ξ_x	-128.9	-104.73	-79.27	-97.4	-59.1	-109	-79.87	-157
Chromaticity ξ_y	-46.74	-70.58	-60.26	-37.97	-73	-82.4	-38.36	-127
U_o (keV)	609	484	280	494	510	310	1131	340
J_x	1.34	1.71	1.86	1.43	1.46	1.45	1.7	1.71
$\sigma_x(0)$ (μm)	56.1	70.9	55.8	131.4	45.7	44	19.4	8.5
$\sigma_y(0)$ (μm)	5.4	2.8	3.4	6	3.9	3.2	6.3	2.2
$\sigma'_x(0)$ (μrad)	5.1	3.6	3.9	6.13	8	3.8	6.8	8.5
$\sigma'_y(0)$ (μrad)	0.92	1.76	1.48	0.83	1.29	1.53	0.8	2.24
Area (μm^2)	302.94	198.52	189.72	788.4	178.23	140.8	122.22	18.7
Percentage	17.9	26.1	27.4	27.1	37.5	31.7	22.3	25

**Fig. 4.5:** The machine functions of a 3 GeV-7MBA lattice (like MAX IV)

4.4.2 The 3 GeV HMBA I lattice

Completely different from the 7MBA lattice is the HMBA lattice (see Fig. 4.7) as proposed for the upgrade of the ESRF [4.18, 4.19]. The lattice consists of two DBA structures for the matching to the straight sections and a matching section in the middle of the arc (see Fig. 4.7). To reduce the number of sextupoles, the phase advance between the two DBA structures has to be $\Delta\phi(x) = 3\pi$ and $\Delta\phi(y) = \pi$; this places some limitations on the selection of the working points (tunes). With a period of $N = 16$ and an energy of 3 GeV, the circumference is 345.4 m, leading to an emittance of 255 pmrad. The horizontal chromaticity is also quite high, but a first dynamic aperture calculation has shown that an acceptable value can be reached, which could be a solution. For the installation of the injection, the RF system,

and machine components, up to four straight sections are needed; hence, for the installation of insertion devices there should be 12 straight sections, whereas for the 7MBA only 10 straight sections are available to the user. This is a big advantage of the HMBA over the 7MBA lattice.

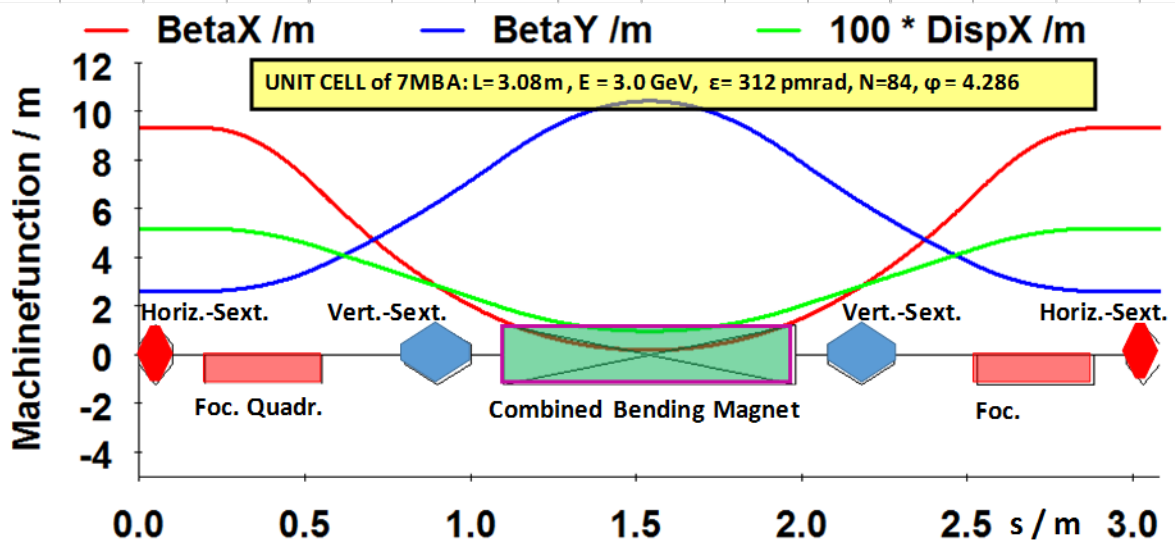


Fig. 4.6: The arrangements of magnets and the machine functions of a 3 GeV unit cell of the 7MBA lattice

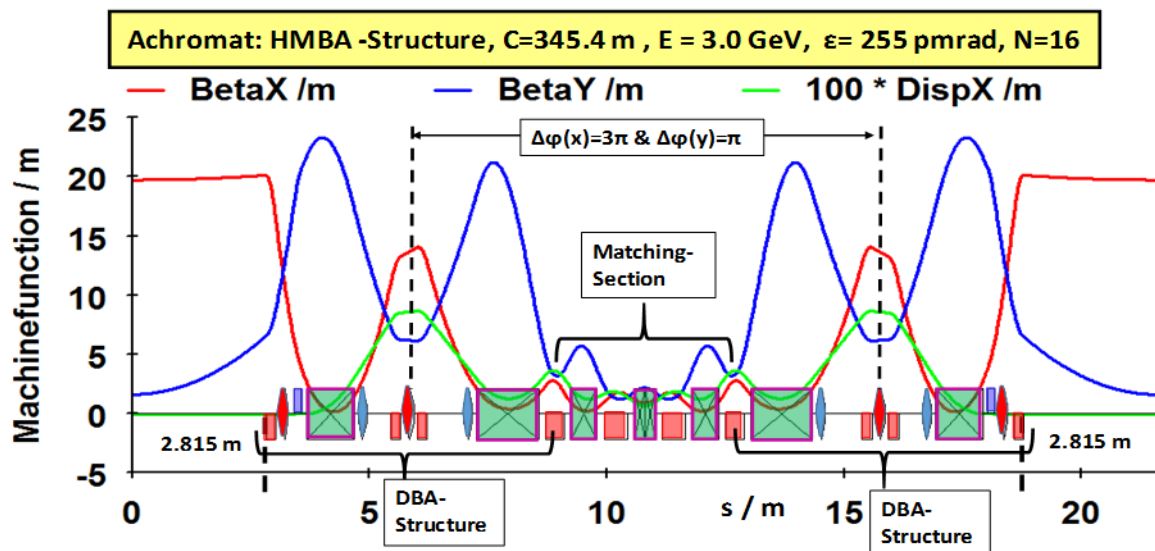


Fig. 4.7: The machine functions of a 3 GeV HMBA I lattice (like ESRF-EBS)

4.4.3 The 2.5 GeV HMBA II lattice

In order to see the difference in the energy, the 3 GeV version was also matched to an energy of 2.5 GeV (see Fig. 4.8). Accordingly, the emittance reduces to 218 pmrad and the circumference goes down to 329.2 m. According to the scaling of the emittance with the energy, the emittance of the HMBA I lattice should go down to 177 pmrad for 2.5 GeV. Hence there is still some room for optimization. The length of the straight section is 5.63 m. This lattice could be a solution for the design of the SEE-LS. A further advantage of the 2.5 GeV version is that the radiated energy per turn decreases by a factor of around 2 (from 484 to 280 keV—see U_0 in Table 4.2); this reduces the cost of the RF system.

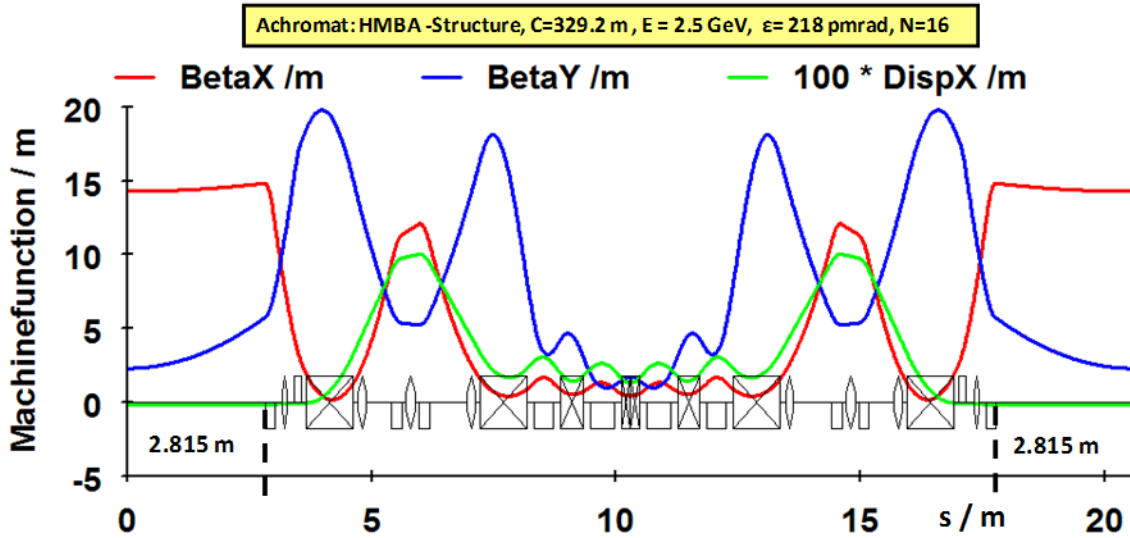


Fig. 4.8: The machine functions of a 2.5 GeV HMBA II lattice (like ESRF-EBS)

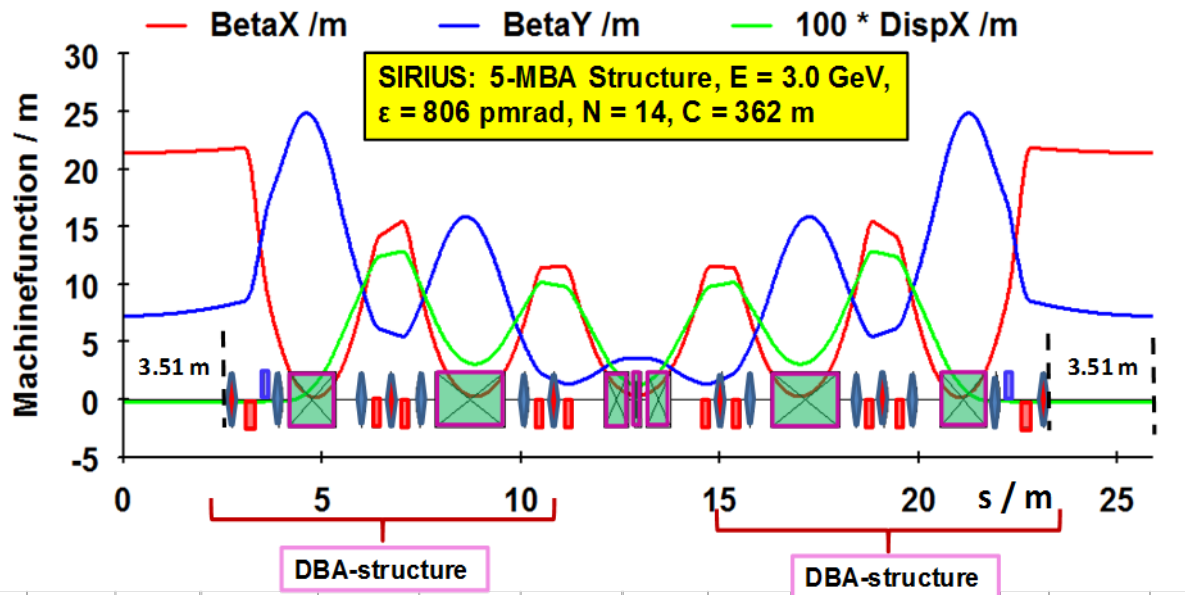


Fig. 4.9: The machine functions of a 3 GeV 5MBA lattice (like SIRIUS II)

4.4.4 The 3 GeV 5MBA lattice

The 5MBA lattice of SIRIUS, matched to a circumference of roughly 350 m, is presented in Fig. 4.9. The structure of the 5MBA is roughly the same as that of the HMBA (see above), except that the matching of the two matching cells will be done by only one bending magnet. With a circumference of 362 m and a period of $N = 14$, an emittance of 806 pmrad could be reached. The scaling of the original SIRIUS lattice with an emittance of 250 pmrad and $N = 20$ would result in an emittance of roughly 730 pmrad, so there is still some room for optimization. Nevertheless, because of the high emittance and the relative low number of straight sections available to the user, this lattice is not a good candidate for the SEE-LS.

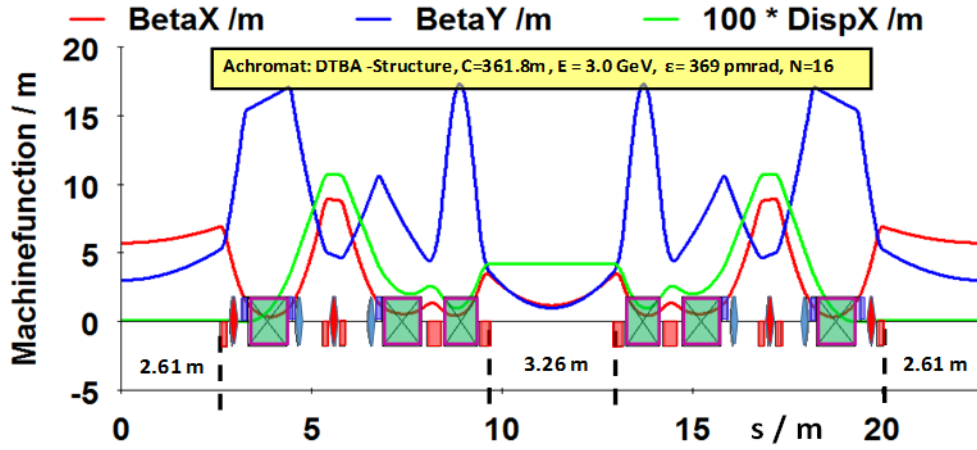


Fig. 4.10: The machine functions of a 3 GeV DTBA lattice (like the upgrade of Diamond)

4.4.5 The 3 GeV DTBA lattice

This lattice (see Fig. 4.10) yields a relatively large emittance of 365 pmrad with a circumference of 361.8 m. As for the other lattices, the period is $N = 16$. Also, the phase advance between the two DBA structures has to be $\Delta\phi(x) = 3\pi$ and $\Delta\phi(y) = \pi$. The advantage of this lattice is the additional straight section in the middle of the arc. This straight section can be used for the installation of the RF system as well as other machine components. Because of the relatively large emittance and circumference, this is not considered a candidate lattice for the SEE-LS.

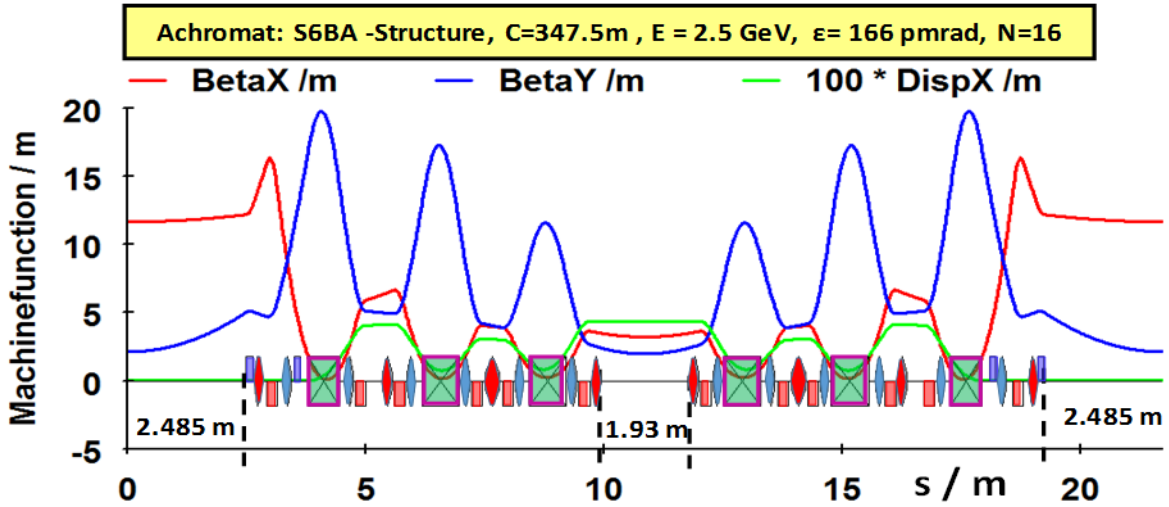


Fig. 4.11: The machine functions of a 2.5 GeV S6BA lattice (like the upgrade of ELETTRA)

4.4.6 The 2.5 GeV S6BA lattice

This lattice (see Fig. 4.11) leads to a circumference of 347.2 m and an emittance of 166 pmrad for an energy of 2.5 GeV, which in comparison with the other lattices is fairly low [4.25]. As for the other lattices, the period is $N = 16$. Like the DTBA lattice, the S6BA has the advantage of having an additional straight section in the middle of the arc. The chromaticities are rather high, but initial calculations have shown that a sufficient dynamic aperture should be attainable. This is so far a very good solution, if an energy of 3 GeV is not needed. Because there is no condition on the phase advance, the number of sextupoles is relatively high, but the flexibility in choosing the tune values is high as well.

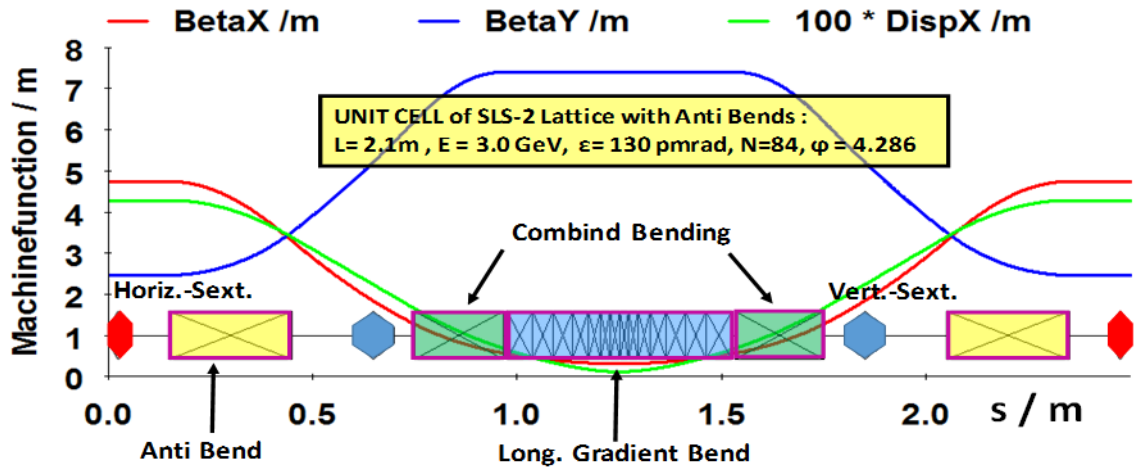


Fig. 4.12: The machine functions within the unit cell of the 3 GeV lattice proposed for the upgrade of SLS

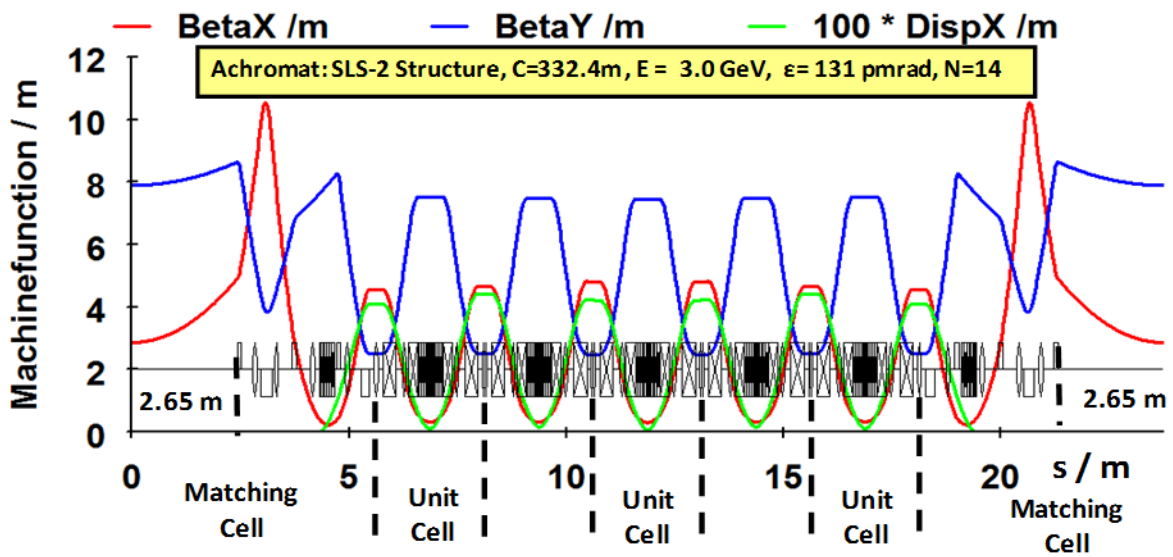


Fig. 4.13: The machine functions of the 3 GeV lattice proposed for the upgrade of SLS

4.4.7 The 3 GeV SLS-2 lattice

For the upgrade of the SLS, a 7MBA lattice will also be used. There is, however, a big difference between the lattice of its unit cell and that of MAX IV (compare Figs. 4.12 and 4.6): instead of using a quadrupole at the beginning of the unit cell, a so-called ‘anti-bend’ will be used. An anti-bend [4.23] is a shifted quadrupole and reflects the beam to the outer side of the ring; hence the anti-bend has a focusing as well as a deflection effect. The consequences for the machine function can be seen by comparing Figs. 4.6 and 4.12. In Fig. 4.6 the dispersion function has values of around 2 cm, whereas in Fig. 4.12 it has a value of more or less 0 cm. Also, the horizontal beta function has smaller values with the anti-bends in the middle of the bend, with 768,ing. Both effects decrease the emittance by a lot.

In addition to using the anti-bend, the emittance is reduced by means of a longitudinal gradient bending magnet, in which the magnetic field goes up to 2.5 T. The introduction of the longitudinal gradient and the anti-bend greatly reduces the emittance; the emittance of the unit cell decreases from 349 to 144 pmrad. The anti-bend and the longitudinal gradient both change the emittance by a factor of 1.5; for an energy of 2.5 GeV the emittance would go down to roughly 90 pmrad. However, the magnets are very complicated to build, and first dynamic aperture calculations have yielded a relatively small value. With a period of $N = 14$, the available straight sections are a bit smaller than in other lattices. Because of its complexity, small dynamic aperture, and reduced number of straight sections, the SLS-2 lattice will not be considered as a candidate for the SEE-LS.

4.4.8 The 2.75 GeV SOLEIL-2 lattice

For the upgrade of SOLEIL, the proposed lattice is shown in Fig. 4.14. The lattice file is not officially available, so the editor generated the file from different plots [4.24, 4.26] presented at various workshops and conferences. It is more or less an HMBA lattice as for the upgrade of the ESRF. A new element is the incorporation of anti-bends to reduce the emittance further. With the length of the achromat being roughly 17.5 m, it is a very compact design; therefore it is possible to obtain a period of $N = 20$ with a circumference of 353.1 m. Because the final design is not finished, this lattice will not be considered as a solution for the SEE-LS.

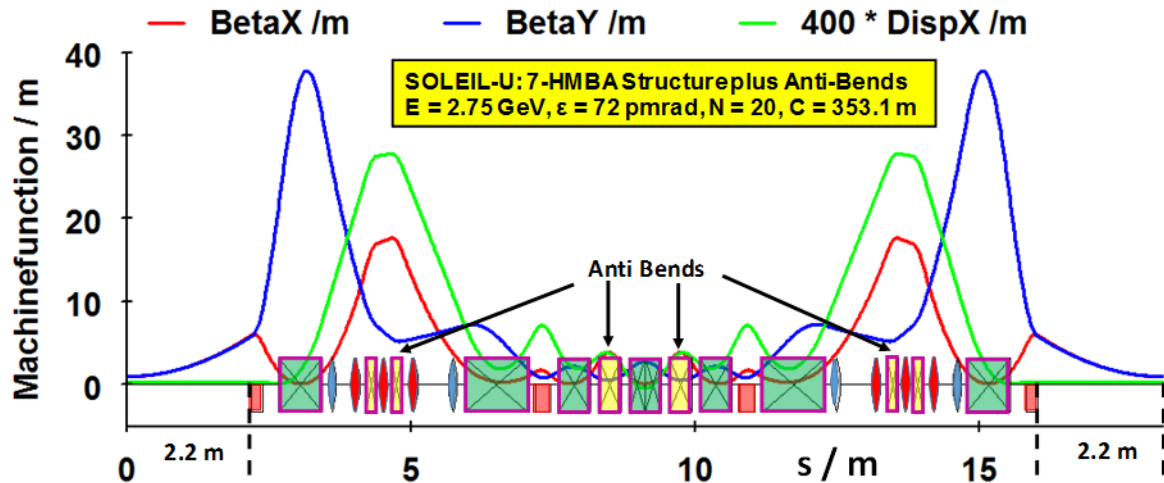


Fig. 4.14: The machine functions of the 2.75 GeV lattice proposed for the upgrade of SOLEIL

4.4.9 Number of magnets

One factor for the budget is the number of components and, in this case, the number of magnets. The different lattices discussed here require the following numbers of magnets.

- **7MBA**: 98 bending magnets, 252 quadrupoles, and 308 sextupoles; a total of 658 magnets
- **HMBA**: 112 bending magnets, 160 quadrupoles, and 128 sextupoles; a total of 400 magnets
- **SIRIUS**: 70 bending magnets, 168 quadrupoles, and 196 sextupoles; a total of 434 magnets
- **DTBA**: 96 bending magnets, 256 quadrupoles, and 128 sextupoles; a total of 480 magnets
- **S6BA**: 96 bending magnets, 256 quadrupoles, and 288 sextupoles; a total of 640 magnets
- **SLS-2**: 272 bending magnets, 160 quadrupoles, and 336 sextupoles; a total of 768 magnets
- **SOLEIL-2**: 140 bending magnets, 200 quadrupoles, and 200 sextupoles; a total of 540 magnets.

The SLS-2 lattice has the largest number (768) and the HMBA the smallest number (400) of magnets.

4.5 Brilliance calculations

Brilliance calculations have been done for a *cryogenic permanent magnet undulator* (CPMU) with a period length of 16 mm and a beam current of 500 mA. The detailed parameters of the insertion device are given in Table 4.3, in which ε_n denotes the photon energy of the n th harmonic.

Table 4.3: Data for the CPMU 16 used for the brilliance calculations

Parameter	Value	Value	Unit
Energy	3	2.5	GeV
Gap value	4.2	4.2	mm
B_0	1.26	1.26	T
Total length	2	2	m
Period length (λ_0)	16	16	mm
Number of periods	125	125	
K value	1.88	1.88	
λ_1	0.00	0.00	μm
σ_r	5.71	6.85	μm
σ'_r	12.68	15.22	μrad
$\varepsilon_{1^{\text{st}}}$	1.93	1.34	keV
$\varepsilon_{3^{\text{rd}}}$	5.78	4.02	keV
$\varepsilon_{5^{\text{th}}}$	9.64	6.69	keV
$\varepsilon_{7^{\text{th}}}$	13.49	9.37	keV
$\varepsilon_{9^{\text{th}}}$	17.35	12.05	keV
$\varepsilon_{11^{\text{th}}}$	21.20	14.72	keV

The brilliances for the 3 GeV HMBA, 2.5 GeV HMBA, 2.5 GeV S6BA, and 3 GeV MAX IV lattices are presented in Fig. 4.15 for harmonic numbers up to $n = 9$. The maximum brilliance is in the range of 3×10^{21} photons/s/mm²/rad²/0.1%BW for the soft-X-ray region and goes up to 1×10^{18} photons/s/mm²/rad²/0.1%BW for the hard X-ray region (35 keV photon energy). In order to exhibit the differences between a 3 GeV and a 2.5 GeV electron beam, the corresponding brilliances are plotted in Fig. 4.16. Going from 2.5 GeV to 3 GeV, the brilliance will increase by photon energies of roughly 10 keV.

The brilliances of the different lattices for different photon energies are summarized in Table 4.4. In general there are not great differences between the different lattices. This was already explained in chapter 1 and is due to the large contribution of the undulator radiation. Owing to the small emittance of SLS-2, this lattice provides the highest brilliance, greater by around a factor of 2 than the others.

For a beam energy of 2.5 GeV, the brilliances of up to 10 keV are roughly the same as for 3 GeV. For photon energies of roughly 15 keV, the brilliance is smaller by approximately a factor of 2, and for 20 keV it is smaller by a factor of 10 for a beam energy of 2.5 GeV. For photon energies as high as 20 keV, the brilliance at 2.5 GeV is more than one order of magnitude smaller in comparison to a 3 GeV machine (see Fig. 4.16).

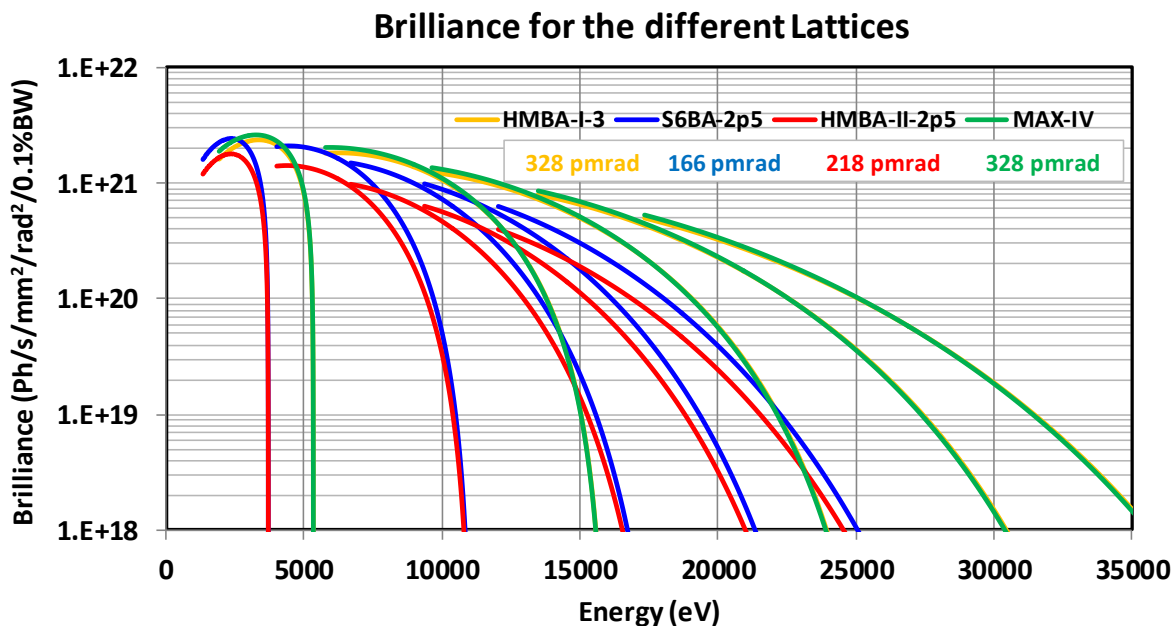


Fig. 4.15: Brilliances of the insertion device CPMU 16 for the 3 GeV HMBA, 2.5 GeV HMBA, 2.5 GeV S6BA, and 3 GeV MAX IV lattices.

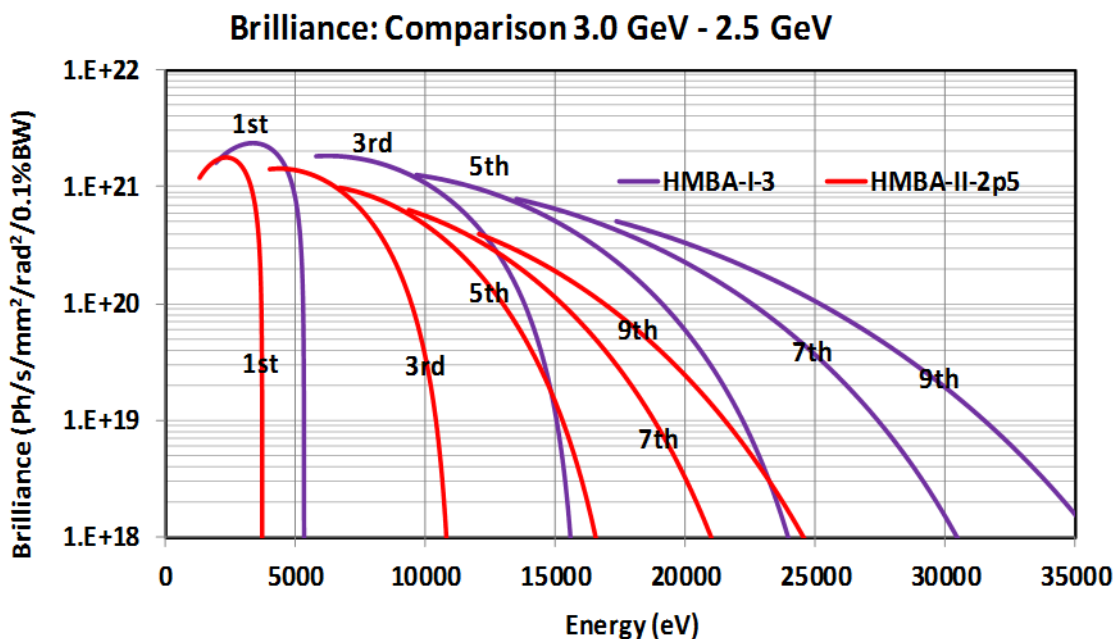


Fig. 4.16: Brilliances of the insertion device CPMU 16 for the 3 GeV HMBA and 2.5 GeV HMBA lattices

Table 4.4: Brilliances in photons/(s mm² mrad² 0.1BW) of the various lattices for different photon energies in keV.

Lattice	Energy	5 keV	10 keV	15 keV	20 keV	25 keV	30 keV
MAX IV	3 GeV	3.70E+21	2.60E+21	1.45E+21	6.50E+20	2.00E+20	3.00E+19
7MBA	3 GeV	2.50E+21	1.70E+21	9.50E+20	4.50E+20	1.40E+20	2.10E+19
HMBA	3 GeV	3.40E+21	2.60E+21	1.50E+21	7.30E+20	2.20E+20	3.60E+19
DTBA	3 GeV	3.20E+21	2.00E+21	1.10E+21	4.60E+20	1.30E+20	1.90E+19
SLS-2	3 GeV	5.20E+21	3.90E+21	2.05E+21	9.90E+20	3.00E+20	5.00E+19
HMBA	2.5 GeV	2.70E+21	1.40E+21	4.40E+20	5.40E+19		
S6BA	2.5 GeV	3.90E+21	2.10E+21	7.00E+20	8.50E+19		

As mentioned in section 4.4, the brilliance is a function of the beam cross-section, given by the beta function. The dependence of the brilliance on the beta functions is presented in Table 4.5. At lower photon energies, the brilliance increases by roughly a factor of 2 for smaller beta functions, but at higher photon energies the brilliance goes through a maximum around beta function values of 5–10 m/rad. This is more clearly seen in Table 4.6, in which the brilliances are normalized so that the values corresponding to the largest beta function become 1.

Table 4.5: Brilliances of the 3 GeV HMBA lattice for different beta functions and photon energies in keV

Beta value	5 keV	10 keV	15 keV	20 keV	25 keV	30 keV
19.73	3.40E+21	2.60E+21	1.50E+21	7.30E+20	2.20E+20	3.60E+19
15	4.00E+21	3.20E+21	1.90E+21	8.50E+20	2.70E+20	4.20E+19
10	4.60E+21	3.60E+21	2.05E+21	9.50E+20	2.90E+20	4.60E+19
5	6.00E+21	4.40E+21	2.40E+21	1.05E+21	3.00E+20	4.70E+19
2.5	7.20E+21	4.80E+21	2.50E+21	1.00E+21	2.60E+20	3.70E+19
1.61	7.50E+21	4.30E+21	2.20E+21	8.50E+20	2.00E+20	2.90E+19

Table 4.6: Normalized brilliances of the 3 GeV HMBA lattice for different beta functions

Beta value	5 keV	10 keV	15 keV	20 keV	25 keV	30 keV
19.73	1.00	1.00	1.00	1.00	1.00	1.00
15	1.18	1.23	1.27	1.16	1.23	1.10
10	1.35	1.38	1.37	1.30	1.32	1.28
5	1.76	1.69	1.60	1.44	1.36	1.31
2.5	2.12	1.85	1.67	1.37	1.18	1.03
1.61	2.21	1.65	1.47	1.16	0.91	0.81

4.6 Summary

Based on the given emittance of 131 pmrad, the SLS-2 lattice seems the most favourable one, but the machine is complex, the dynamic aperture is small, and the costs will be higher than for the other lattices. This lattice also has a large number of magnets and is perhaps not the best solution for the SEE-LS.

Next comes the 6SBA lattice, with a relatively small emittance of 166 pmrad at 2.5 GeV and an additional straight section in the middle of the arc. Initial calculations for the dynamic aperture show promising results. This lattice could be suitable for the SEE-LS, but it still has to be optimized.

The 3 GeV HMBA I and 2.5 GeV HMBA II lattices are possible solutions too.

The DTBA lattice can achieve a fairly large emittance, but its main advantage is the additional straight section in the middle of the arc.

The 7MBA lattice is not attractive because of the larger emittance, larger circumference, and reduced period.

The emittance and the brilliance are not the only relevant factors in choosing the lattice type. One also has to look at the overall cost of the project. A main part of the cost comes from the RF system and is determined by the radiation loss per turn, U_0 . For the 2.5 GeV machines (see Table 1) U_0 is at least a factor of 2 smaller than for the 3 GeV machines. Hence one could start with a 2.5 GeV version and later upgrade to 3 GeV.

The 3 GeV HMBA I lattice scaled to an energy of 2.5 GeV results in an emittance of 177 pmrad. The difference in length between the two solutions at 3 GeV and 2.5 GeV is only 16.2 m, which is insignificant. Hence, for the first proposal of a lattice for the SEE-LS, the 3 GeV HMBA I lattice operating at an energy of 2.5 GeV should be used.

At present the SOLEIL-2 lattice cannot be used as a proposal for the SEE-LS because the details of the lattice are not known. At the 6th Diffraction Limited Storage Ring (DLSR) Workshop held at the Lawrence Berkeley National Laboratory, some more lattices were presented with much better results.

Using an HMBA lattice for the first proposal has the further advantage that many components from the ESRF-EBS upgrade can be used.

References

- [4.1] D. Einfeld and M. Plesko, Design of a diffraction limited light source, Proc. SPIE Electron-Beam Sources of High-Brightness Radiation, San Diego, California, USA, 29 November 1993. <https://doi.org/10.1117/12.164802>
- [4.2] D. Einfeld and M. Plesko, *Nucl. Instrum. Methods Phys. Res. A* **335** (1993), 402, [https://doi.org/10.1016/0168-9002\(93\)91224-B](https://doi.org/10.1016/0168-9002(93)91224-B)
- [4.3] D. Einfeld, J. Schaper, and M. Plesko, Design of a diffraction limited light source (DIFL), Proc. 10th ICFA Beam Dynamics Panel Workshop: 4th Generation Light Sources, Grenoble, France, 22–25 January 1996. <http://doi.org/10.5281/zenodo.2671721>
- [4.4] D. Einfeld, J. Schaper, and M. Plesko, Design of a diffraction limited light source (DIFL), Proc. Particle Accelerator Conference, Dallas, Texas, USA, 1–5 May 1995, p. 177. <https://doi.org/10.1109/PAC.1995.504602>
- [4.5] D. Einfeld, J. Schaper, and M. Plesko, *J. Synchrotron Rad.* **21** (2014) 856, <https://doi.org/10.1107/S160057751401193X>
- [4.6] P.F. Tavares *et al.*, *J. Synchrotron Rad.* **25** (2018) 1291, <https://doi.org/10.1107/S1600577518008111>
- [4.7] R. Coisson, *Opt. Eng.* **27** (1988) 273250, <https://doi.org/10.1117/12.7977923>
- [4.8] H. Onuki and P. Elleaume (eds.), *Undulators, Wigglers and Their Applications* (Taylor & Francis, New York, 2003), <https://doi.org/10.4324/9780203218235>
- [4.9] A. Roper, Lattices and emittances, CAS-CERN Accelerator School: Synchrotron Radiation and Free Electron Lasers, Grenoble, France, 22–27 April 1996, CERN-1998-004 (CERN, Geneva, 1998), p. 91. <http://dx.doi.org/10.5170/CERN-1998-004.91>
- [4.10] R. Chasman, K. Green, and E.M. Rowe, *IEEE Trans. Nucl. Sci.* **22** (1975) 1765, <https://doi.org/10.1109/TNS.1975.4327987>
- [4.11] D. Einfeld and G. Muelhaupt, *Nucl. Instrum. Methods* **172** (1980) 55, [https://doi.org/10.1016/0029-554X\(80\)90607-2](https://doi.org/10.1016/0029-554X(80)90607-2)
- [4.12] M. Sommer, Optimization of the emittance of electron storage rings, Report LAL/RT/83-15 (Laboratoire de l'Accélérateur Linéaire, Orsay, 1983), <http://inspirehep.net/record/195918>
- [4.13] G. Wüstefeld, The minimization of the natural emittance in the triple bend achromat, Report BESSY TB 108/87 (March 1987).
- [4.14] R. Nagaoka and A.F. Wrulich, Emittance minimisation with longitudinal dipole field variation, *Nucl. Instrum. Methods Phys. Res. A* **575** (2007) 292, <https://doi.org/10.1016/j.nima.2007.02.086>
- [4.15] K.-J. Kim, Characteristics of synchrotron radiation, AIP Conf. Proc. **184** (1989) 565, <https://doi.org/10.1063/1.38046>
- [4.16] S.C. Leemann, Recent improvements to the lattices for the MAX IV storage rings, Proc. IPAC2011, San Sebastián, Spain, 4–9 September 2011, p. 3029. <http://accelconf.web.cern.ch/AccelConf/IPAC2011/papers/thpc059.pdf>
- [4.17] L. Liu *et al.*, A new 5BA low emittance lattice for Sirius, Proc. IPAC2013, Shanghai, China, 12–17 May 2013, p. 1874. <https://inspirehep.net/record/1338708>
- [4.18] J.L. Revol *et al.*, ESRF upgrade phase II, Proc. IPAC2013, Shanghai, China, 12–17 May 2013, p. 1140. <https://inspirehep.net/record/1337024>
- [4.19] S. Liuzzo *et al.*, Hybrid multi bend achromat at 3 GeV for future 4th generation light sources, Proc. IPAC2016, Busan, Korea, 8–13 May 2016, p. 2822. <https://doi.org/10.18429/JACoW-IPAC2016-WEPOW006>
- [4.20] R. Bartolini *et al.*, Novel lattice upgrade studies for Diamond light source, Proc. IPAC2013, Shanghai, China, 12–17 May 2013, p. 240. <https://inspirehep.net/record/1336784>

- [4.21] R. Bartolini, Design and optimisation of nonlinear dynamics in diffraction-limited synchrotron light sources, Proc. IPAC2016, Busan, Korea, 8–13 May, 2016, p. 33. [https://doi.org/ 10.18429/JACoW-IPAC2016-MOZA02](https://doi.org/10.18429/JACoW-IPAC2016-MOZA02)
- [4.22] E. Karantzoulis *et al.*, Status of Elettra and future upgrade, Proc. IPAC2018, Vancouver, Canada, 29 April – 4 May 2018, p. 4054. <https://doi.org/10.18429/JACoW-IPAC2018-THPMF010>
- [4.23] A. Streun, *Nucl. Instrum. Methods Phys. Res. A* **737** (2014) 148, <https://doi.org/10.1016/j.nima.2013.11.064>
- [4.24] A. Loulerge *et al.*, Baseline lattice for the upgrade of Soleil, Proc. IPAC2018, Vancouver, Canada, 29 April – 4 May 2018, p. 4726. <https://doi.org/10.18429/JACoW-IPAC2018-THPML034>
- [4.25] E. Karantzoulis, Overview of the ELETTRA 2.0 project, 6th DLSR Workshop, Lawrence Berkeley National Laboratory, 29–31 October 2018. <https://web.archive.org/web/20190515084118/https://drive.google.com/file/d/1rQNFApCusRtNNV40qaDVhwJgMt1ul8YQ/view>
- [4.26] L. Nadolski, Progress report of the lattice studies for the SOLEIL upgrade, 6th DLSR Workshop, Lawrence Berkeley National Laboratory, 29–31 October 2018. https://web.archive.org/web/20190515084525/https://drive.google.com/file/d/1Dnq9h9-yMTaEVpvJH_iaZsjTCnSpGxGe/view

5 Beam dynamics and layout of the SEE-LS

D. Einfeld and H. Ghasem

5.1 Introduction

The highest priority of a synchrotron light source is that the stored electron beam in the storage ring has to deliver a photon beam with high brilliance and stability. According to the latest technology used for the construction of synchrotron light sources and the required photon spectrum, the following points should be followed for the layout of the SEE-LS.

- The energy should be in the range of 2.5–3 GeV in order to reach, with an ‘in-vacuum’ undulator, photon energies of 20–30 keV.
- The natural emittance has to be smaller than 250 pmrad; it should be a 4th generation light source.
- The lattice should be optimized for a high photon flux density, which means introducing in a straight section so-called ‘mini beta sections’.
- The lifetime should be large enough (greater than 8 hours) to reduce the radiation level in the experimental hall, and there should be only two injections per day.
- The energy acceptance has to be at least 3% (lifetime requirement).
- The design current should be 400 mA.
- A ‘topping up’ injection mode must be possible so as to have a constant head load on the optical components of the beam lines.
- Feedback systems have to be introduced to achieve sub-micron stability of the stored electron beam.
- According to the available budget, the circumference has to be around 350 m.
- The option to use a single bunch at a later stage should be kept open.
- The pre-accelerator should be a linac with an energy of at least 100 MeV.
- The booster synchrotron should be in the same tunnel as the storage ring. For a high injection efficiency, the emittance of the booster should be smaller than 10 nmrad.
- The booster synchrotron and the storage ring should be in the same tunnel.

5.2 Beam dynamics of the proposed SEE-LS

As discussed in chapter 4, the 3 GeV HMBA lattice will be selected as a solution for the layout of the SEE-LS in order to meet the above-mentioned requirements. To save on investment costs, the machine will first operate with an energy of 2.5 GeV and later be upgraded to 3 GeV. Accordingly, in this section the data of the machine will be presented for the 2.5 GeV case.

The machine functions within one achromat of this solution are presented in Fig. 5.1, and the corresponding magnet structure is shown in Fig. 5.2. The requirements for the circumference C , the emittance ε , and the period N are, with $C = 354$ m, satisfied with $N = 16$ and $\varepsilon = 178$ pmrad. The machine functions (twist parameters) within one achromat are shown in Fig. 5.1 and the magnetic structure in Fig. 5.2. To minimize the number of sextupoles, the phase advance between the middle of the DBA structures should be approximately $\Delta\phi(\text{horizontal}) = 3\pi$ and $\Delta\phi(\text{vertical}) = \pi$. In most of the HMBA structures, the bending magnets in the DBA structure have a longitudinal gradient; in this proposal a horizontal gradient will be used in order to decrease the emittance more because of the higher partition number J_x .

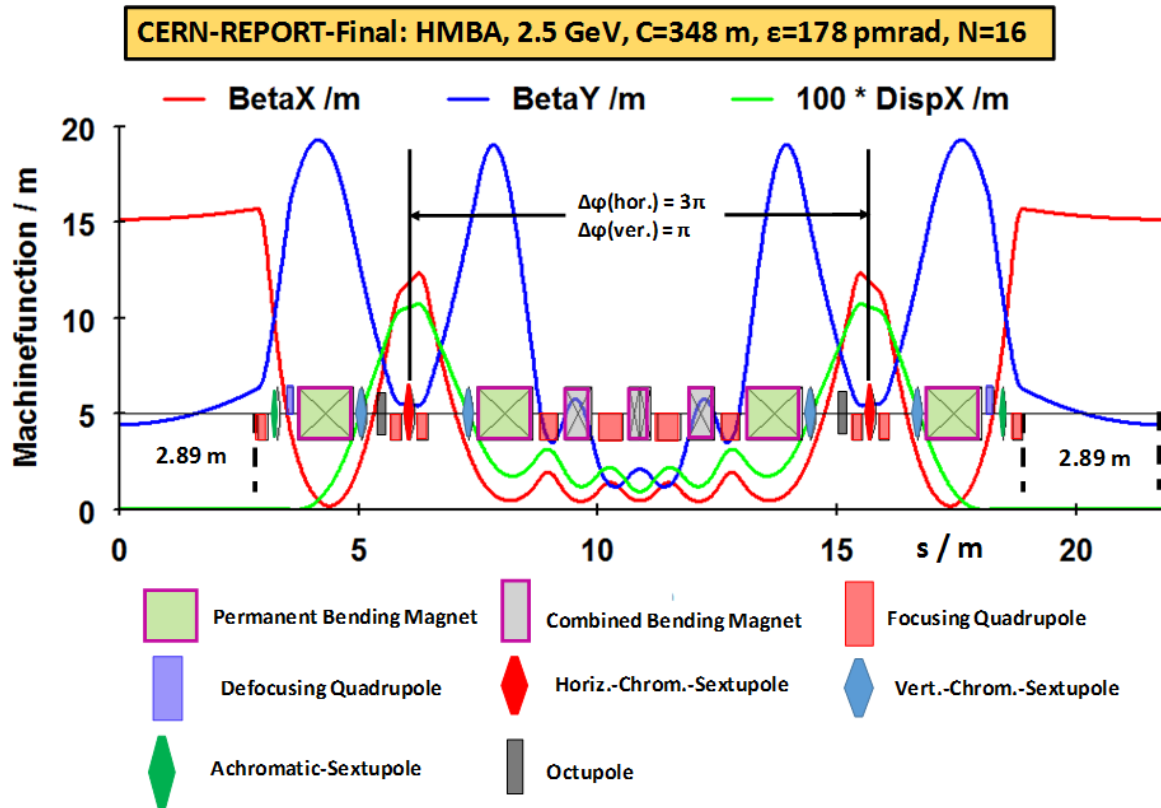


Fig. 5.1: Machine functions within one achromat of the proposed lattice for the SEE-LS

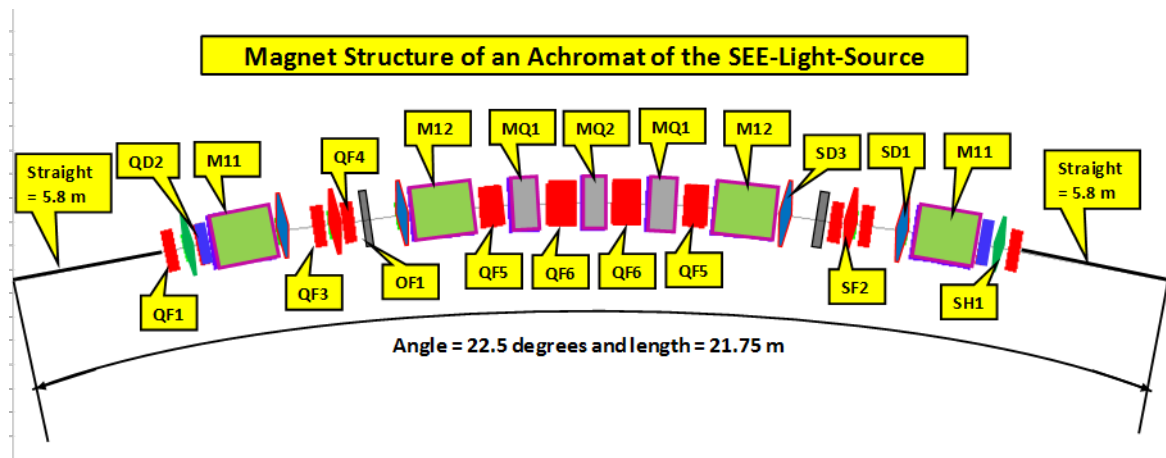


Fig. 5.2: The magnet structure within one achromat of the proposed lattice for the SEE-LS

The functions for the beginning and end of the achromat and DBA structure are displayed in more detail in Fig. 5.3, and those for the matching between the two DBA structures are shown in Fig. 5.4. The cross-sections of the beam in the middle of the straight sections are $\sigma(x) = 51.2 \mu\text{m}$ and $\sigma(y) = 4.7 \mu\text{m}$ for a coupling of 3%, leading to a vertical emittance of 5 pmrad, which is the lowest emittance that has been reached so far. The resonance diagram with the working point and the movement of the tunes with energy are given in Figs. 5.5 and 5.6, respectively.

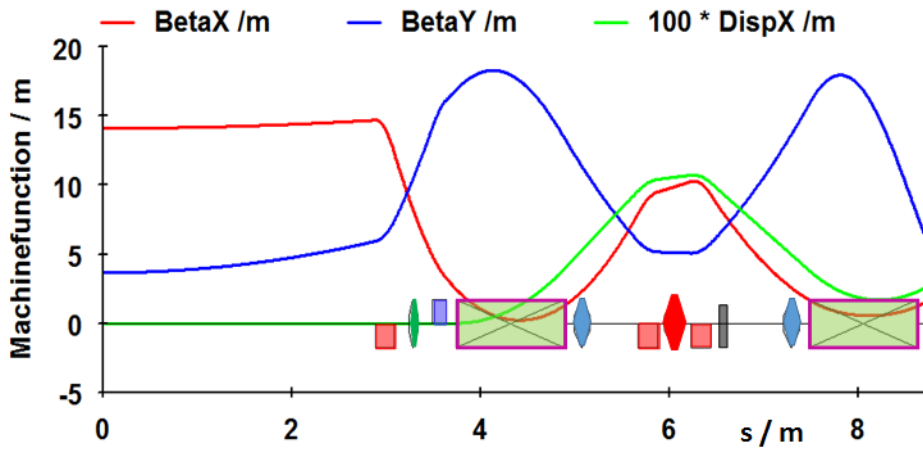


Fig. 5.3: The machine functions within the matching section of the SEE-LS

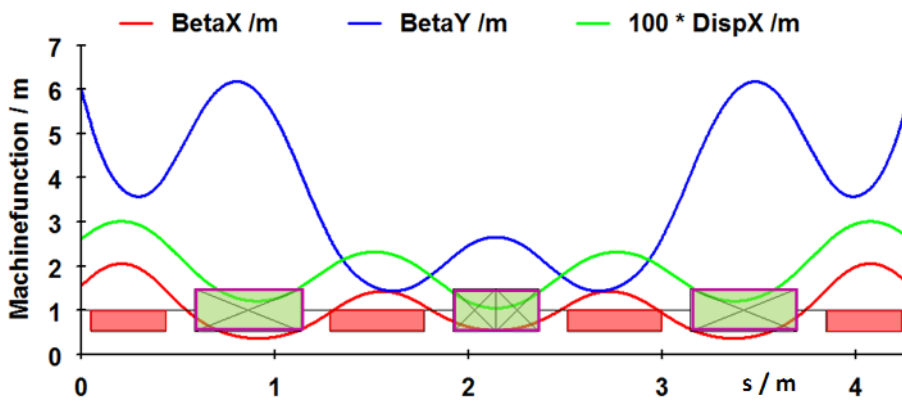


Fig. 5.4: The machine functions in more detail for the middle part of the achromat

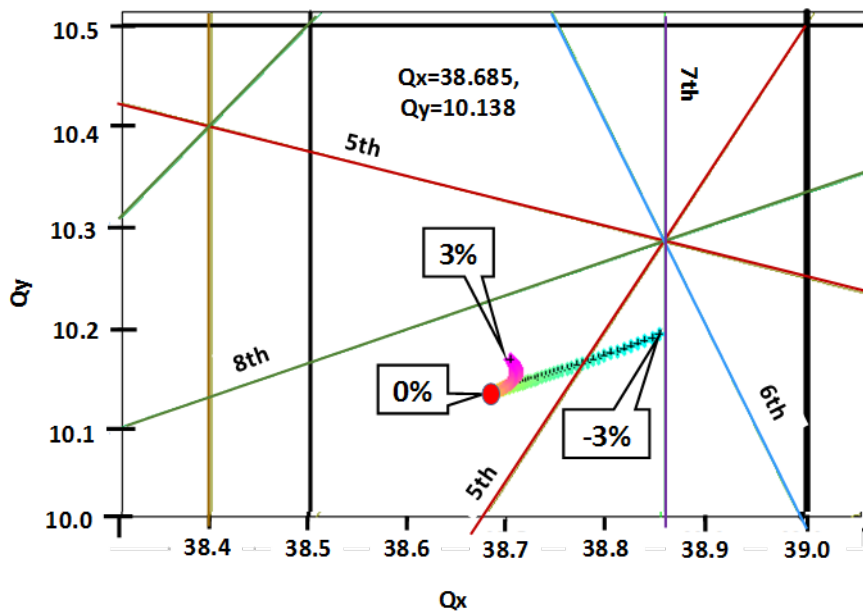


Fig. 5.5: The working point with the tunes as a function of energy deviation

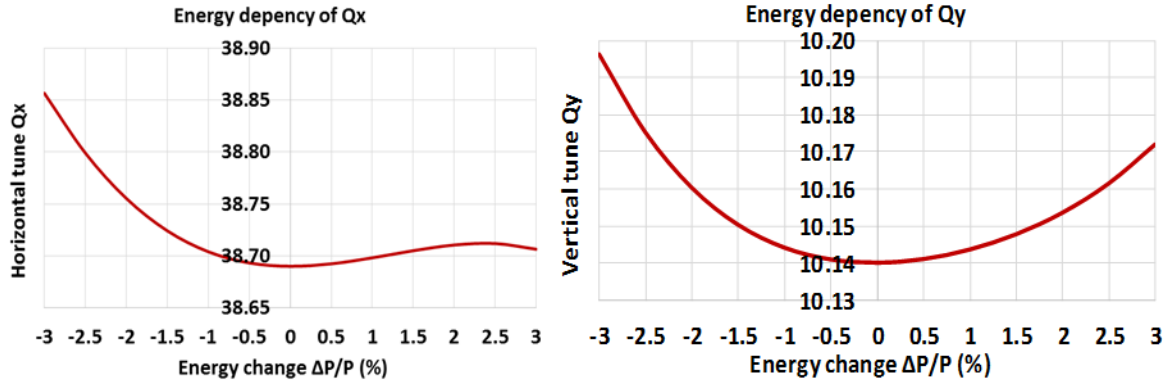


Fig. 5.6: The energy dependence of the tune shift in the horizontal (left-hand side) and vertical (right-hand side) directions.

The dynamic apertures for energy deviations ($\Delta E/E$) of up to $\pm 3\%$ are presented in Fig. 5.7 for the bare lattice without any misalignments and errors of the magnets. Values of $\pm 7-8$ mm should be sufficient for a high-efficiency injection.

The cross-sections of the beam, $\sigma(x)$ and $\sigma(y)$, within one achromat are displayed in Fig. 5.8 (where $\sigma(y)$ is magnified by a factor of 10). The cross-sections of the beam in the middle of the straight sections are $\sigma(x) = 51.2 \mu\text{m}$ and $\sigma(y) = 4.7 \mu\text{m}$. Within the DBA sections the cross-sections have a maximum, and in the middle of the achromat they have a minimum.

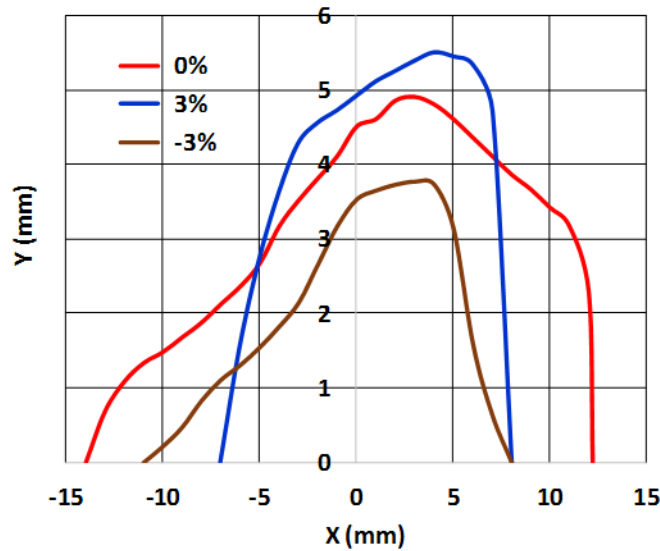


Fig. 5.7: Dynamic aperture of the HMBA lattice for energy deviations up to $\pm 3\%$

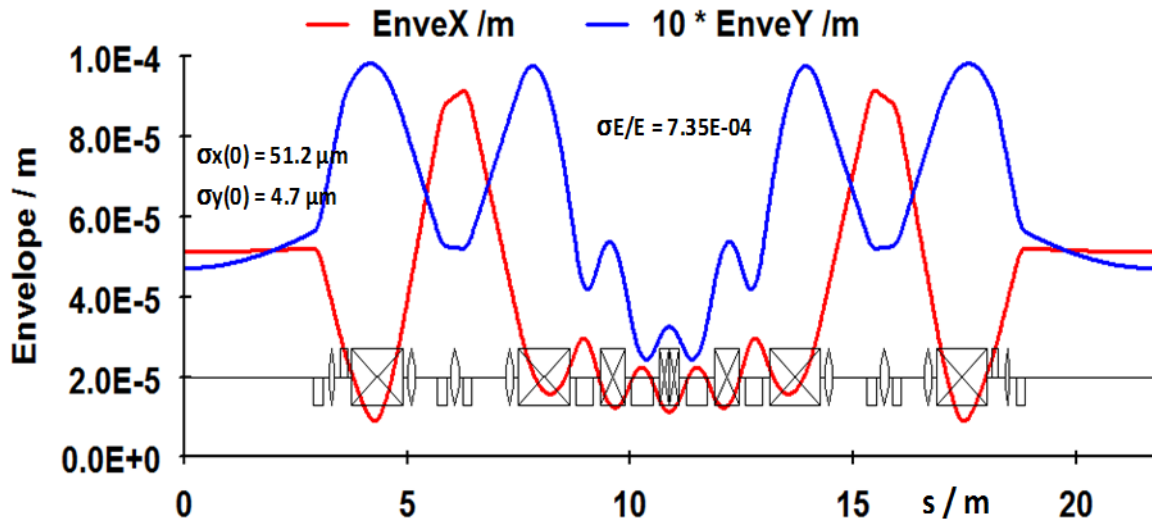


Fig. 5.8: The horizontal and vertical cross-sections of the beam within an achromat (the vertical one is enlarged by a factor of 10).

To check if there is still some room for optimization of the lattice, the contributions of the bending magnets to the emittance are calculated. The corresponding numbers are M11 = 17.1%, M12 = 14.9%, MQ1 = 12.6%, and MQ2 = 10.8% (see Fig. 5.9). This shows that the deflection angle of the bending magnets still needs to be optimized. Calculations show that an emittance in the vicinity of 150 pmrad can be reached but with the disadvantage that the chromaticity increases with a reduction in the dynamic aperture. Nevertheless, this optimization has to be done during the final design of the lattice.

SEEIIST: 7 HMBA, N=16, Jx=1.785									
	Angle=	3.70	3.65	2.60	2.60	2.60	3.65	3.70	degrees
	1.) = $ H/\rho^3 $ =	16.40	13.90	12.50	13.30	12.50	13.90	16.40	$*10^{-08}$
	2.) = $ 1/\rho^2 $ =	3.63	3.53	3.74	4.68	3.74	3.53	3.63	$*10^{-03}$
	1.) / 2.) =	4.52	3.94	3.34	2.84	3.34	3.94	4.52	$*10^{-05}$
	SUM = [1.] / 2.) / Jx =				14.81				$*10^{-05}$
	Magn. Contribut.:	17.09	14.90	12.64	10.82	12.64	14.90	17.09	%
					Sum =				100.1 %

Fig. 5.9: The contributions of the different magnets to the emittance

A comparison of the SEE-LS lattice design with other light sources can be done via a plot [5.1] of the emittance divided by the normalized energy as a function of the circumference. Such a plot is presented in Fig. 5.10, including the machines of the 3rd and 4th generations. SEE-LS is represented by a white circle. Because of the reduced number of achromats given by the circumference, SEE-LS is well situated within the range of 4th generation light sources. This means that SEE-LS will indeed be a 4th generation light source.

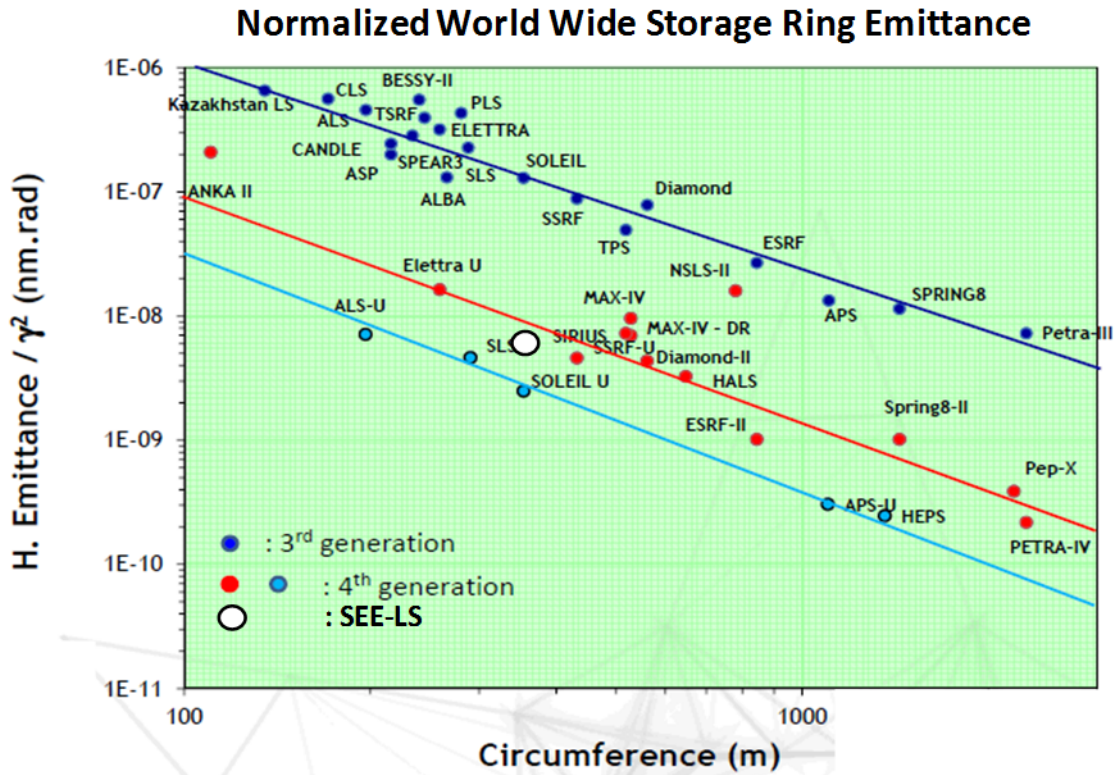


Fig. 5.10: Normalized worldwide storage ring emittances

Brilliance of SEE-LS - Light Source

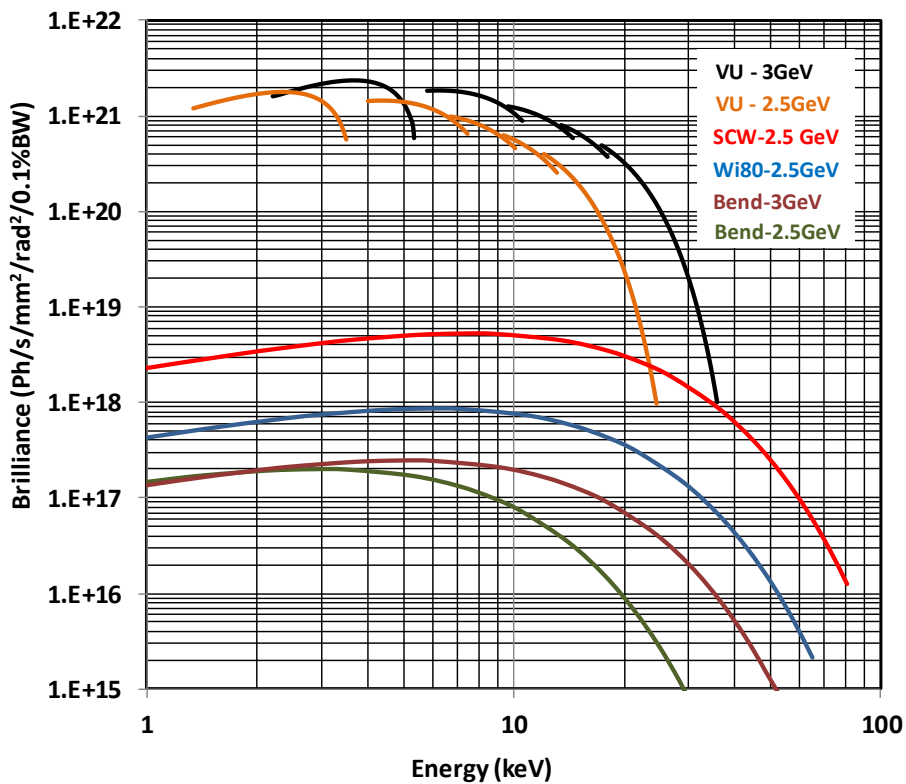


Fig. 5.11: The brilliance of SEE-LS for different energies and insertion devices

BEAM DYNAMICS AND LAYOUT OF THE SEE-LS

The brilliance and fraction of coherent light of the photon beam are plotted in Figs. 5.11 and 5.12, respectively. The brilliance has been calculated for different insertion devices (vacuum undulators, superconducting wigglers, and classical wigglers) as well as for different energies. The coherence increases considerably upon decreasing the emittance from 4 to 0.2 nmrad; but further decreasing the emittance to 0.1 nmrad has only a small effect on the fraction of coherent light.

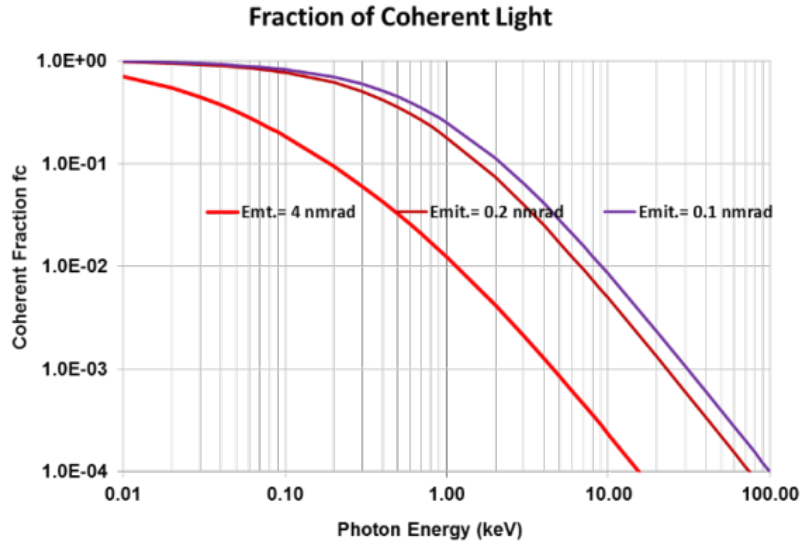


Fig. 5.12: The coherence of SEE-LS for different energies and insertion devices

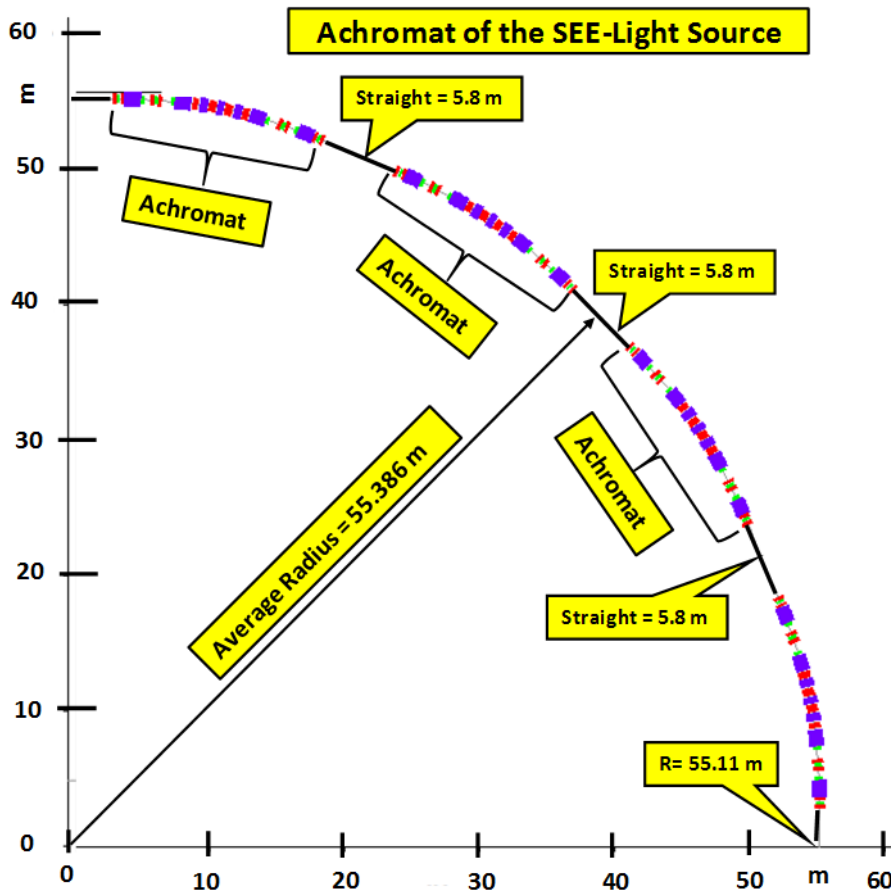


Fig. 5.13: The layout of one achromat of the storage ring

5.3 Layout of the proposed SEE-LS

The layout of one quadrant of the SEE-LS with four achromats and four straight sections is presented in Fig. 5.13. The average radius is 55.4 m and the length of the straight sections is 5.8 m. The layout of the whole machine, along with the main accelerator parameters, is presented in Fig. 5.14.

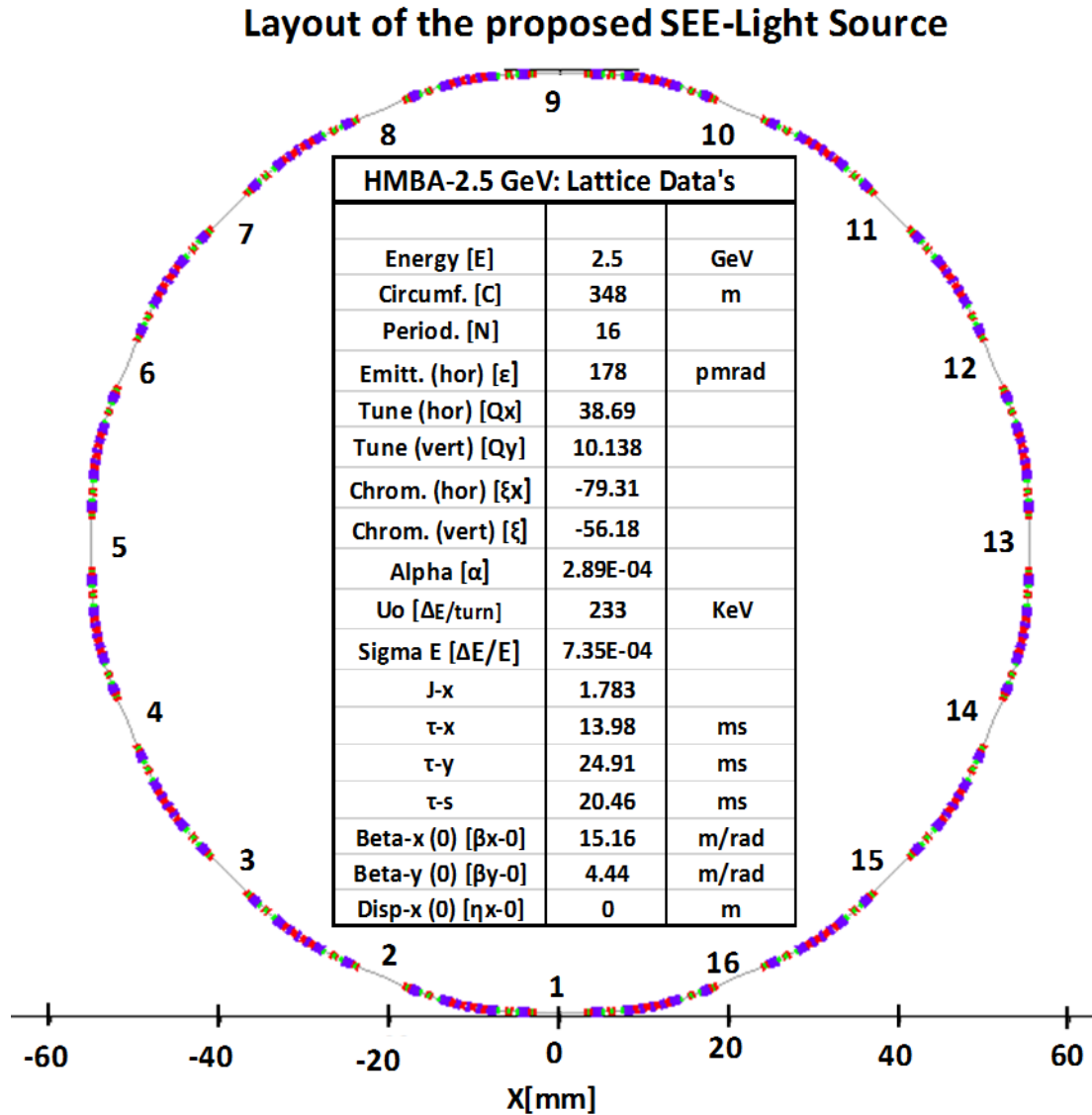


Fig. 5.14: The layout of the storage ring together with the main parameters of the proposed lattice for the SEE-LS.

5.4 Specification of the magnets and RF system

The magnet structure within an achromat of the proposed lattice for the SEE-LS is presented in Fig. 5.15 and the specifications of the magnets are given in Table 5.1.

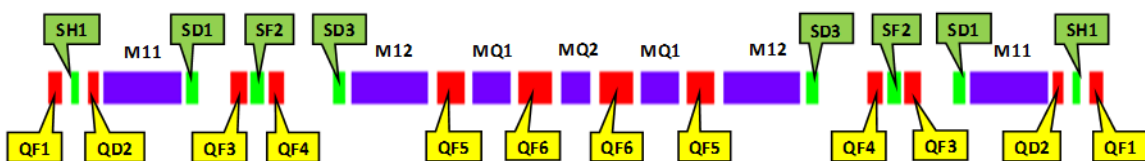


Fig. 5.15: The magnet structure within an achromat of the proposed lattice for the SEE-LS

Table 5.1: Parameters of the magnets

Element	Length (m)	Defl.-angle (degrees)	Radius (m)	Gradient (T/m)	B'' (T/m ²)	$B(\text{pole})$ (T)
M11	1.15	3.7	17.8081	4.3196	-91.462	0.468
M12	1.15	3.65	18.0521	9.14788	126.436	0.462
MQ1	0.55	2.6	12.1203	29.2115	-1805.9	
MQ2	0.44	2.6	9.69621	32.1468	1448.82	
		<i>k</i> -value	(mm)			
QF1	0.2	4.4228	16.4	36.882		0.605
QD2	0.15	-2.7487	16.4	-24.921		-0.376
QF3	0.212	2.949	16.4	24.592		0.403
QF4	0.212	3.1092	16.4	25.928		0.425
QF5	0.388	6.6183	12.7	55.190		0.701
QF6	0.484	5.8611	12.7	48.876		0.621
		<i>M</i> -value	(mm)			
SH1	0.1	43.448	19.2		724.631	0.1308
SD1	0.166	4.299	19.2		71.6993	0.01294
SF2	0.2	77.398	19.2		1290.85	0.233
SD3	0.166	-150.01	19.2		-2501.9	-0.4516

5.4.1 Specification of the magnet system

The bending magnets are running at a field of 0.47 T, with a gradient of up to 10 T/m; the sextupole component with roughly 2000 T/m² is new, and experts of the ESRF [5.2] are sure that this should be possible with permanent magnets. MQ1 and MQ2 are special magnets with a higher field, gradient, and sextupole component. The quadrupoles QF1 to QF6 have a modest gradient and no sextupole component. The sextupoles have a modest sextupole component too.

For the design of the magnets the space required in the vertical direction has to be evaluated. Space in the vertical direction is needed to capture the off-energy particles. The corresponding plot is presented in Fig. 5.16, showing the dispersion function magnified by a factor of 100. The required space in the vertical direction is given by $\eta(\Delta E/E)$. For Fig. 5.16, a safety factor of $F = 1.5$ has been introduced as well. The result is that at the beginning and end of the achromat a good field region of up to ± 12 mm is needed, and in the middle a region of ± 6 mm is needed.

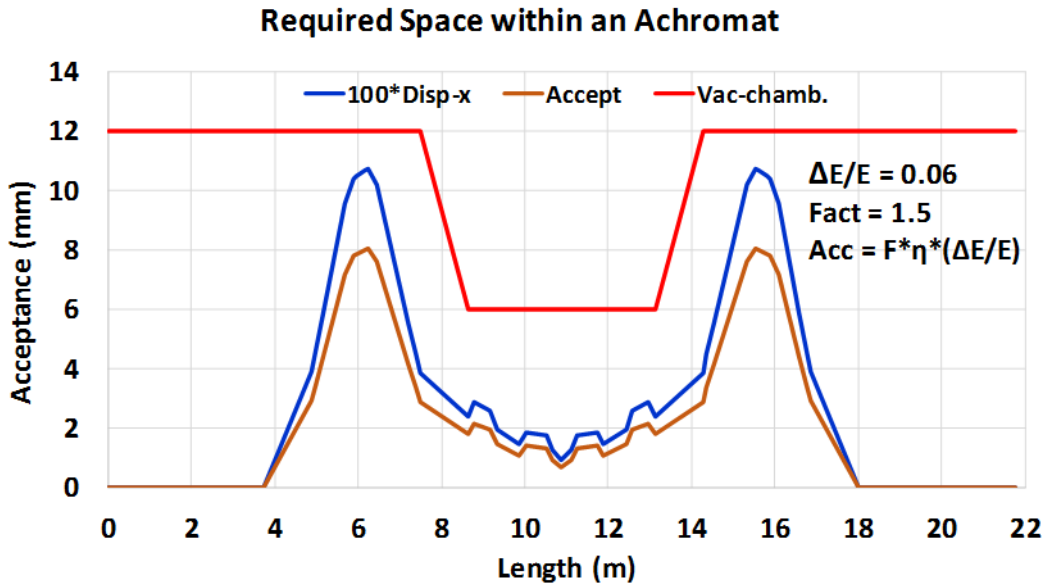


Fig. 5.16: The required space within the magnets of the SEE-LS

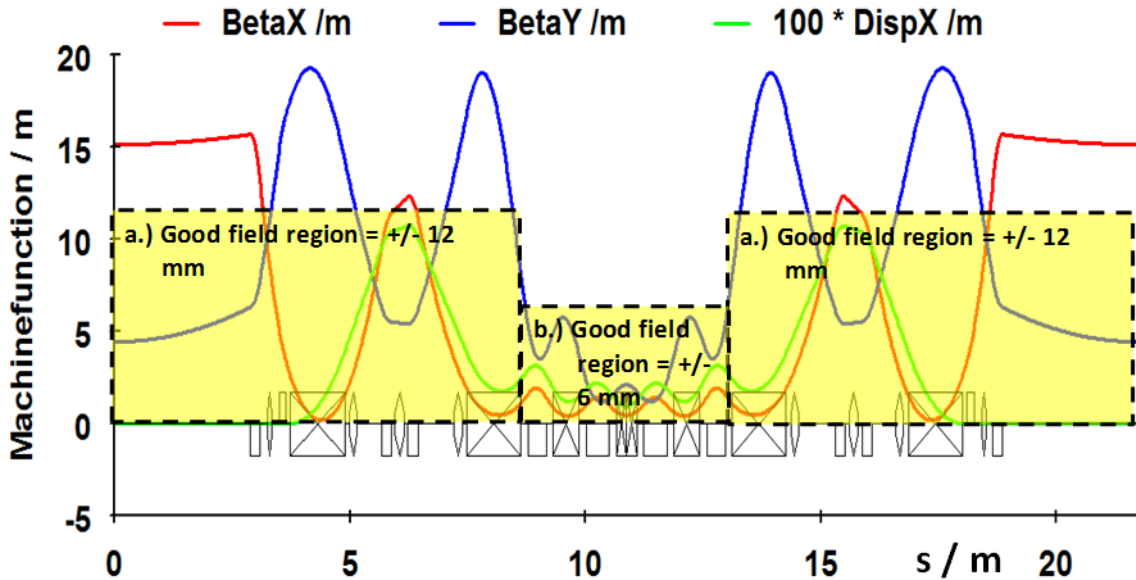


Fig. 5.17: Required space for the two regions: a) at the beginning and the end of the lattice; b) in the middle part

The middle part includes the quadrupoles QF5 and QF6 as well the bending magnets MQ1 and MQ2 (see Figs. 5.15 and 5.17).

5.4.2 Specification of the RF system

The frequency of the RF system should be 100 MHz in order to increase the bunch length and correspondingly the lifetime. The intention is to use a copy of the 100 MHz MAX IV RF system. A further advantage is that the required amplifiers are commercially available. The main parameters for the RF system are given in Table 5.2.

Table 5.2: Parameters for the design of the RF system (r.m.s. is the root mean square value)

Parameter		Value	Unit
Energy	E	2.50	GeV
Current	I_o	400.00	mA
Circumference	C	348.00	m
Momentum compaction	α	2.880E-04	
Energy loss per turn	U_o	0.233	MeV
RF frequency	F_{rf}	100.00	MHz
RF harmonic number	h	116	
Peak effective RF voltage	V_{rf}	1.40	MV
Overvoltage factor	q	6.00	
Bucket size	ε_{max}/E	0.090	
Synchrotron phase angle	Φ_s	9.60	degree
Synchrotron frequency	Ω_s	9.28	kHz
Natural r.m.s. energy spread	$\sigma E/E$	7.14E-04	
Bunch current in multi-bunch mode	I_b	3.45	mA
R.m.s. bunch length at zero current	σ_{so}	6.65	mm
R.m.s. bunch length at zero current	σ_{so}	22.17	psec
Peak current in multi-bunch mode		72.04	A
Vacuum chamber half-height	b	8.00	mm
Vacuum chamber half-width	h	11.00	mm
Vacuum chamber cut-off frequency	$\omega c = c/b$	37.47	GHz

5.5 Lifetime of the stored beam

5.5.1 Introduction

The requirements of users are good stability, a small cross-section, and a long lifetime of the beam. The desire for a small cross-section and the desire for a long lifetime of the beam are contradictory, because the Touschek lifetime goes with the cross-section of the beam. The lifetime of the stored beam is determined by the cross-section of the different processes of interaction of the stored beam with the atoms and molecules within the vacuum chamber. These processes are: 1) elastic scattering of the beam at the nucleus (Coulomb scattering); 2) inelastic scattering at the nucleus (bremsstrahlung); 3) elastic scattering at the bounded electrons of the atoms and molecules; 4) inelastic scattering at the bounded electrons of the atoms and molecules; and 5) Touschek lifetime [5.3–5.7].

The lifetime τ according to an exchange process is given by

$$\tau = \frac{1}{\sigma \cdot n \cdot c}, \quad (5.1)$$

where:

σ is the cross-section of the exchange process;

n is the particle density within the vacuum chamber;

c is the speed of light ($2.9989 \times 10^8 \text{ ms}^{-1}$).

The pressure in the vacuum chamber gives the density n :

$$n = 3.22 \times 10^{22} \text{ m}^{-3} \cdot (p / \text{Torr}) n_z, \quad (5.2)$$

where n_z is the number of atoms per molecule.

Substituting c and n into Eq. (5.1) gives the lifetime

$$\tau = \frac{1.04 \times 10^{-18} \text{ s cm}^2}{\sigma (p / \text{Torr}) n_z} = \frac{2.88 \times 10^{-22} \text{ hours}}{(\sigma / \text{cm}^2) (p / \text{Torr}) n_z}. \quad (5.3)$$

The calculation of the cross-sections of the different exchange processes will be performed below.

5.5.2 Elastic scattering at the nucleus (Coulomb scattering)

The cross-section for this exchange process is

$$\sigma_{\text{Coul}} = \frac{2}{\gamma^2} \pi r_e^2 Z^2 \left\{ \frac{\langle \beta_x \rangle \beta_{x,0}}{A_x^2} + \frac{\langle \beta_y \rangle \beta_{y,0}}{A_y^2} \right\}, \quad (5.4)$$

where:

r_e is the classical electron radius (2.82×10^{-13} cm);

Z is the charge of the nucleus;

γ is the normalized or reduced energy ($1957(E/\text{GeV})$);

A is the aperture;

$\beta_{i,0}$ is the beta function, where the aperture has a minimum;

β_i is the average beta function.

Upon substituting the values of π and the classical electron radius into Eq. (5.4), the cross-section is given by

$$\sigma_{\text{Coul}} = 2.50 \times 10^{-25} \text{ cm}^2 \cdot \frac{2Z^2}{\gamma^2} \left\{ \frac{\langle \beta_x \rangle \beta_{x,0}}{A_x^2} + \frac{\langle \beta_y \rangle \beta_{y,0}}{A_y^2} \right\}. \quad (5.5)$$

From Eqs. (5.3) and (5.5), the lifetime for Coulomb scattering is

$$\tau_{\text{Coul}} = 2.21 \times 10^9 \text{ hours} \cdot \frac{(E / \text{GeV})^2}{Z^2 (p / \text{nTorr}) n_z} \left\{ \frac{\langle \beta_x \rangle \beta_{x,0}}{A_x^2} + \frac{\langle \beta_y \rangle \beta_{y,0}}{A_y^2} \right\}^{-1}. \quad (5.6)$$

With the data $\langle \beta_x \rangle = 7.0$ m/rad, $\beta_{x,0} = 15.2$ m/rad, $\langle \beta_y \rangle = 8.79$ m/rad, $\beta_{y,0} = 19.44$ m/rad, $A_x = 10$ mm, $A_y = 10$ mm, $Z = 7$, $n_z = 2$, and $p = 2$ nTorr, the lifetime is
 $\tau_{\text{Coul}} = 23.3$ hours .

The Coulomb scattering lifetime is proportional to the square of the energy. Changing the energy from 2.5 to 3.0 GeV would increase the lifetime by a factor of 1.44 to 33.6 hours.

In order to reach an SEE-LS lifetime of more than 40 hours, the pressure should be less than 1 nTorr.

5.5.3 Inelastic scattering at the nucleus (bremsstrahlung)

The cross-section for the inelastic scattering at the nucleus is:

$$\sigma_{\text{Brems}} = \frac{16}{411\pi} \cdot \pi r_c^2 Z^2 \ln\left(\frac{183}{Z^{1/3}}\right) \cdot \left\{ \ln\left(\frac{1}{(\delta E / E)_{\text{rf}}}\right) - \frac{5}{8} \right\}. \quad (5.7)$$

After substituting values for all the constants in Eq. (5.7), the cross-section becomes

$$\sigma_{\text{Brems}} = 3.10 \times 10^{-27} \text{ cm}^2 \cdot Z^2 \ln\left(\frac{183}{Z^{1/3}}\right) \cdot \left\{ \ln\left(\frac{1}{(\delta E / E)_{\text{rf}}}\right) - \frac{5}{8} \right\}. \quad (5.8)$$

Thus the lifetime for the bremsstrahlung is

$$\tau_{\text{Brems}} = \frac{9.29 \times 10^4 \text{ hours}}{(p / \text{nTorr}) n_z Z^2 \ln\left(\frac{183}{Z^{1/3}}\right)} \cdot \left\{ \ln\left(\frac{1}{(\delta E / E)_{\text{rf}}}\right) - \frac{5}{8} \right\}^{-1}. \quad (5.9)$$

With $Z = 7$ the lifetime will be

$$\tau_{\text{Brems}} = \frac{415.6 \text{ hours}}{(p / \text{nTorr}) n_z} \cdot \left\{ \ln\left(\frac{1}{(\delta E / E)_{\text{rf}}}\right) - \frac{5}{8} \right\}^{-1}. \quad (5.10)$$

With an energy acceptance of 4.0% for the RF system, $n_z = 2$, and a pressure of 2 nTorr, the lifetime for the bremsstrahlung is

$$\tau_{\text{Brems}} = 40.1 \text{ hours}.$$

To strongly influence the lifetime of the bremsstrahlung, it is only possible to decrease the pressure. With a pressure of 1 nTorr the lifetime would be doubled to 80.2 hours.

5.5.4 Elastic scattering at the shelf electrons

The electrons of the stored beam can be scattered at the bounded electrons of the atoms and molecules. During this process energy from the stored electrons is transferred to the shelf electrons. If this energy is larger than the energy acceptance of the RF system, the scattered electrons will be lost. The cross-section for the elastic scattering at the shelf electrons of the atoms and molecules is given by

$$\sigma_{\text{Coul}}(e) = \frac{2}{\gamma} \cdot \pi r_c^2 Z \cdot \frac{1}{(\delta E / E)_{\text{rf}}} = 3.181 \times 10^{-25} \text{ cm}^2 \frac{Z}{\gamma} \cdot \frac{1}{(\delta E / E)_{\text{rf}}}. \quad (5.11)$$

Substituting Eq. (5.11) into Eq. (5.3) gives the corresponding lifetime:

$$\tau_{\text{Coul}}(e) = 1.128 \times 10^4 \text{ hours} \frac{(E / \text{GeV})(\varepsilon_{\text{rf}} / \%) }{Z(p / \text{Torr}) n_z}. \quad (5.12)$$

For an energy of 2.5 GeV, a pressure of 2 nTorr, $Z = 7$, $n_z = 2$, and an energy acceptance of 4%, the lifetime will be

$$\tau_{\text{Coul}}(e) = 40.3 \text{ hours}. \quad (5.13)$$

On decreasing the pressure the lifetime would go up.

5.5.5 Inelastic scattering at the shelf electrons

This is the same process as described in section 5.5.3, but the stored electrons will be scattered at the shelf electrons of the atoms or molecules. The corresponding cross-section is

$$\sigma_{\text{Brems}}(e) = \frac{16}{411\pi} \cdot \pi r_c^2 Z \cdot \left\{ \ln\left(\frac{2.5\gamma}{(\delta E / E)_{\text{rf}}}\right) - 1.4 \right\} \cdot \left\{ \ln\left(\frac{1}{(\delta e / E)_{\text{rf}}}\right) - \frac{5}{8} \right\}. \quad (5.14)$$

Upon substituting values for the constants the cross-section becomes

$$\sigma_{\text{Brems}}(e) = 3.10 \times 10^{-27} \text{ cm}^2 Z \cdot \left\{ \ln \left(\frac{2.5\gamma}{(\delta E / E)_{\text{rf}}} \right) - 1.4 \right\} \cdot \left\{ \ln \left(\frac{1}{(\delta e / E)_{\text{rf}}} \right) - \frac{5}{8} \right\}. \quad (5.15)$$

The corresponding lifetime is

$$\tau_{\text{Brems}}(e) = \frac{9.30 \times 10^4 \text{ hours}}{Z(p / \text{nTorr})n_z} \cdot \left\{ \ln \left(\frac{2.5\gamma}{(\delta E / E)_{\text{rf}}} \right) - 1.4 \right\}^{-1} \cdot \left\{ \ln \left(\frac{1}{(\delta e / E)_{\text{rf}}} \right) - \frac{5}{8} \right\}^{-1}. \quad (5.16)$$

For an energy of 2.5 GeV, a pressure of 2 nTorr, $Z = 7$, $n_z = 2$, and an energy acceptance of 4%, the lifetime will be

$$\tau_{\text{Brems}}(e) = \frac{9.30 \times 10^4 \text{ hours}}{7 \times 2 \times 2} \cdot \{12.63 - 1.4\}^{-1} \cdot \{3.22 - 0.625\}^{-1}, \quad (5.17)$$

that is,

$$\tau_{\text{Brems}} = 114 \text{ hours}. \quad (5.18)$$

5.5.6 Touschek lifetime

Within the bunches the electrons perform movements, and this leads to scattering between the stored electrons within one bunch. This scattering process has to be treated as Coulomb scattering. The lifetime of this so-called Touschek effect is given by

$$\tau_{\text{Tou}} = \frac{8\pi\gamma^2 \sigma_x \sigma_y \sigma_l \varepsilon_{\text{acc}}^3}{r_e^2 c N_e} \cdot \frac{1}{D(\xi)}. \quad (5.19)$$

In terms of the bunch volume $V_B = (4\pi)^{3/2} \sigma_x \sigma_y \sigma_l$ the Touschek lifetime is

$$\tau_{\text{Tou}} = \frac{8\pi\gamma^2 V_B \varepsilon_{\text{acc}}^3}{(4\pi)^{3/2} r_e^2 c N_e} \cdot \frac{1}{D(\xi)}. \quad (5.20)$$

Upon substituting values for the constants, Eq. (5.20) becomes

$$\tau_{\text{Tou}} = 6.57 \times 10^7 \text{ hours} \frac{(V_B / \text{mm}^3) \gamma^2 \varepsilon_{\text{acc}}^3}{N_e} \cdot \frac{1}{D(\xi)}. \quad (5.21)$$

where:

σ_x is the average cross-section in the horizontal direction;

σ_y is the average cross-section in the vertical direction;

σ_l is the average cross-section in the longitudinal direction;

V_B is the bunch volume;

ε_{acc} is the energy acceptance of the accelerator, which is normally the energy acceptance of the RF system;

ξ is the normalized function $(\varepsilon_{\text{acc}} / \gamma \sigma'_x)^2$, with $\sigma'_x = \varepsilon_x \gamma_x + \eta'^2 (\sigma_E / E)^2$ being the maximum slope of the stored electrons;

$D(\xi)$ is a normalized function.

The function $D(\xi)$ is plotted in Fig. 5.18. Upon inserting the values of the constants into Eq. (5.21), the Touschek lifetime will be

$$\tau_{\text{Tou}} = 0.538 \text{ hours} \frac{hf(E / \text{GeV})(\sigma_x / \text{mm})(\sigma_y / \text{mm})(\sigma_l / \text{mm})(\varepsilon_{\text{acc}}^3 / \%)^3}{(I / \text{A})(C / \text{m})D(\xi)}. \quad (5.22)$$

where f is the filling factor and C is the circumference in metres.

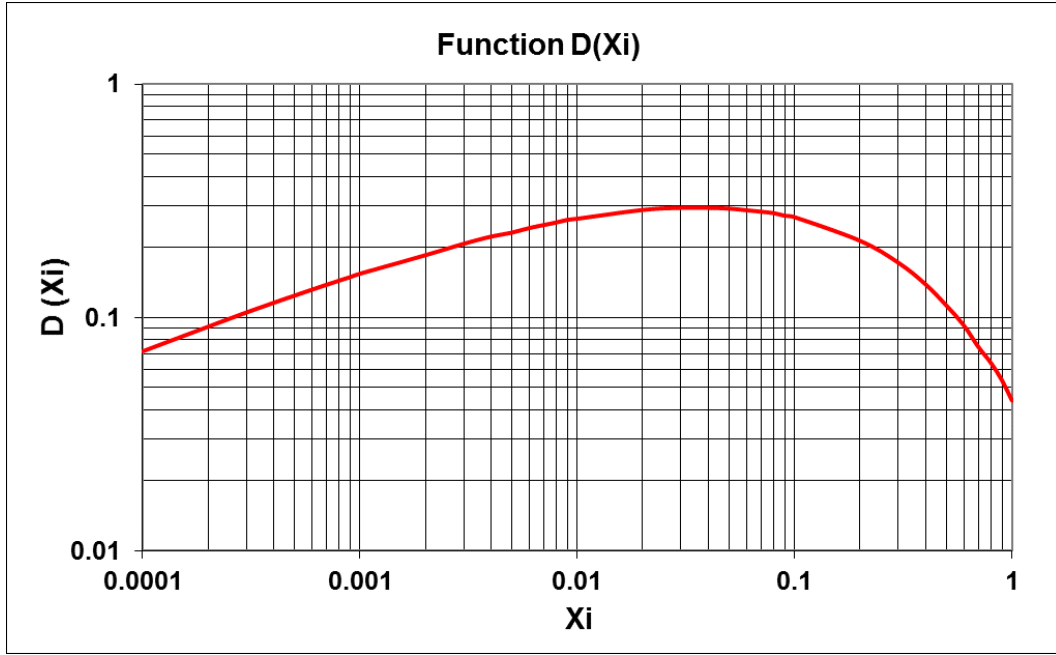


Fig. 5.18: The function $D(\xi)$ for the calculation of the Touschek lifetime

For SEE-LS we have the following data: $E/\text{GeV} = 2.5$, $h = 116$, $C/\text{m} = 348$, $I/A = 0.4$, $f = 0.8$, $\langle\sigma_x / \text{mm}\rangle = 0.465$, $\langle\sigma_y / \text{mm}\rangle = 0.040$, $\sigma_l / \text{mm} = 9$, $\varepsilon_x/\text{pmrad} = 178$, $\langle\gamma_x\rangle = 1.5$, $(\eta')_{\text{max}} = -0.4$, $\sigma_E/E = 0.00074$, $\langle\sigma'_x\rangle = 0.00003 \text{ rad}$, $\langle\xi\rangle = 0.0027$, $\varepsilon_{\text{acc}} = 4.0\%$, $D(\xi) = 0.2$.

With these values, the Touschek lifetime will be

$$\tau_{\text{Tou}} = 1.6 \text{ hours} . \quad (5.23)$$

If a third harmonic cavity is used, the bunch length would increase to 42 mm with a Touschek lifetime of 7.2 hours. Because users require a long beam lifetime, it is expected that third-harmonic cavities will have to be used.

5.5.7 Conclusions regarding beam lifetime

The total lifetime of the stored beam is given by

$$\frac{1}{\tau_{\text{Total}}} = \frac{1}{\tau_{\text{Coul}}(N)} + \frac{1}{\tau_{\text{Brems}}(N)} + \frac{1}{\tau_{\text{Coul}}(e)} + \frac{1}{\tau_{\text{Brems}}(e)} + \frac{1}{\tau_{\text{Tou}}} . \quad (5.24)$$

The values of the total lifetime are summarized in Table 5.3 for pressures of 2 and 1 nTorr.

Table 5.3: Lifetimes for the different interaction processes

	$\tau_{\text{Coul}}(N)$	$\tau_{\text{Brems}}(N)$	$\tau_{\text{Coul}}(e)$	$\tau_{\text{Brems}}(e)$	τ_{Tou}	τ_{Total}
$P = 2 \text{ nTorr}$	23.3 h	40.1 h	40.3 h	114 h	7.2 h	4.2 h
$P = 1 \text{ nTorr}$	46.6 h	80.1 h	80.6 h	227 h	7.2 h	5.2 h

According to Table 5.3, the overall lifetime is determined by the Touschek effect. To achieve a lifetime in the range of 10 hours the pressure should be smaller than 1 nTorr.

References

- [5.1] R. Bartolini, Design and optimisation of nonlinear dynamics in diffraction-limited synchrotron light sources, Proc. IPAC2016, Busan, Korea, 8–13 May, p. 33. <https://doi.org/10.18429/JACoW-IPAC2016-MOZA02>
- [5.2] J. Chavane, ESRF, private communication.
- [5.3] A. Ropert, Lattices and emittances, CAS-CERN Accelerator School: Synchrotron Radiation and Free Electron Lasers, Grenoble, France, 22–27 April 1996, CERN-1998-004 (CERN, Geneva, 1998), p. 91. <http://dx.doi.org/10.5170/CERN-1998-004.91>
- [5.4] R.P. Walker, Synchrotron radiation, CAS-CERN Accelerator School: 5th General Accelerator Physics Course, Jyväskylä, Finland, 7–18 September 1992, CERN-1994-001 (CERN, Geneva, 1994), p. 437. <http://dx.doi.org/10.5170/CERN-1994-001.437>
- [5.5] P.J. Bryant and K. Johnsen, *The Principles of Circular Accelerators and Storage Rings* (Cambridge University Press, Cambridge, 1993). <https://doi.org/10.1017/CBO9780511563959>
- [5.6] C. Bocchetta, Lifetime and beam quality, CAS-CERN Accelerator School: Synchrotron Radiation and Free Electron Lasers, Grenoble, France, 22–27 April 1996, CERN-1998-004 (CERN, Geneva, 1998), p. 221, <http://dx.doi.org/10.5170/CERN-1998-004.221>
- [5.7] R. Walker, Insertion devices: undulators and wigglers, CAS-CERN Accelerator School: Synchrotron Radiation and Free Electron Lasers, Grenoble, France, 22–27 April 1996, CERN-1998-004 (CERN, Geneva, 1998), p. 129. <http://dx.doi.org/10.5170/CERN-1998-004.129>

6 Components of the SEE-LS

Ch. Benabderrahmane, G. Le Bec, J. Chavanne and D. Einfeld

The different components needed for building a light source are shown in Fig. 6.1. The colour of each box represents the division responsible for the component: green for the Accelerator Division, blue for the Engineering Division, and pink for the Computer Division.

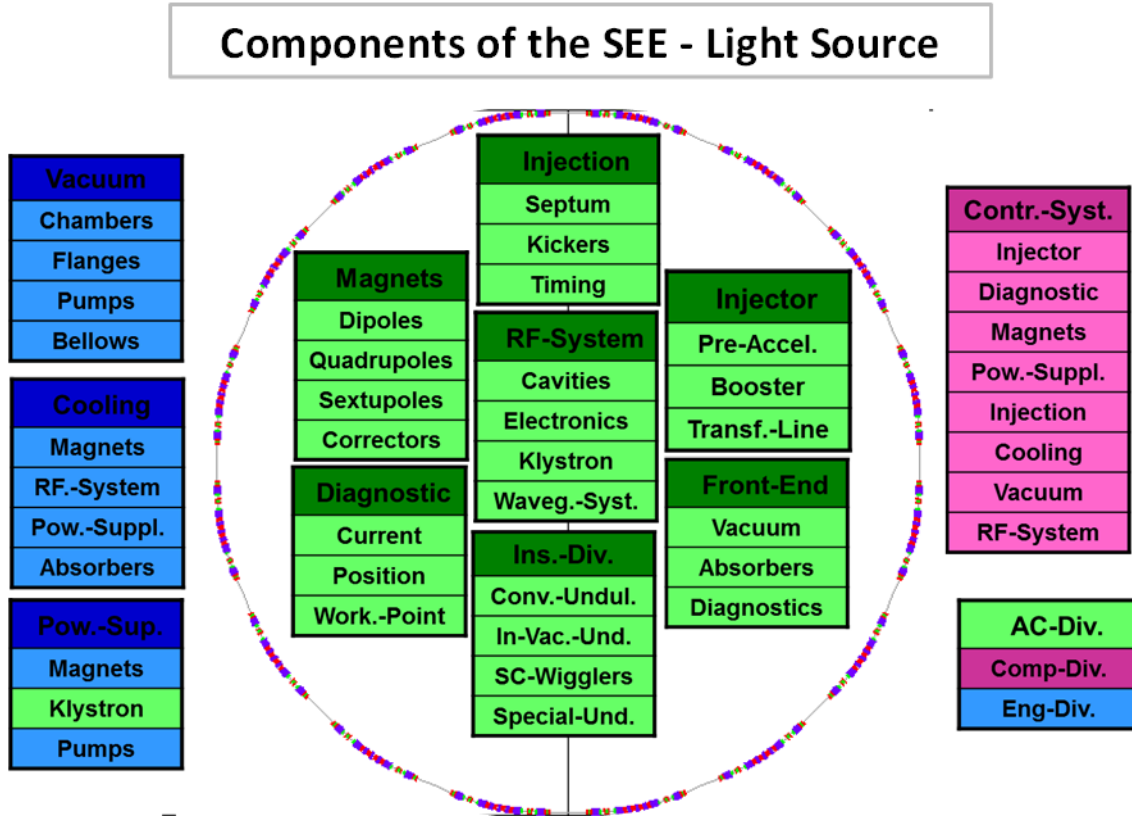


Fig. 6.1: Overview of the different components needed for an accelerator (synchrotron light source)

The magnets include the dipoles, quadrupoles, sextupoles, and correctors needed for the storage ring and booster synchrotron. No sextupoles are needed for the transfer lines. The dipoles perform the deflection and focusing, while the quadrupoles perform the focusing and defocusing; the sextupoles compensate partly for the energy dependency of the focusing of the quadrupoles, and the correctors compensate for some deflection errors due to the dipoles and quadrupoles. The details of the design of the magnets are described in chapter 7. The magnets have to be fixed on a rigid and very stable girder system, which is described in chapter 8.

The power supplies are needed to power the different magnets with high accuracy, the amplifier of the RF system, and the vacuum pumps. The power supplies for the magnets are described in detail in chapter 11.

The injection elements consist of the kicker, septum, and timing system. The kickers are fast magnets with a low magnetic field for kicking the beam out of or into the accelerator. The septa are the first or last elements of the transfer line that move the beam out of or into the transfer line. Sometimes the septum is also a fast magnet, but it is generally much slower than the kickers. The kicker and septa need a very accurate timing system to power the magnets at the right time with an accuracy of the order of nanoseconds.

The RF system has to compensate, by the electrical field in the cavities, the losses from emitting the synchrotron radiation. It consists of amplifiers (klystrons, inductive output tube, and solid-state

amplifier), which connect via the waveguide system to the cavities. The low-level electronics are needed to control the whole RF system, which is described in more detail in chapter 10.

To make various measurements of the stored beam (current, position, tunes, chromaticity, emittance, etc.) in the transfer lines, booster synchrotron, storage ring, and front end, a diagnostic system is required. To measure each characteristic of the beam a special device is needed. The diagnostic system for a synchrotron light source is described in detail in chapter 12.

The vacuum system, comprising the chambers, pumps, bellows, flanges, etc., has to deliver an ultra-high vacuum in all the chambers of the accelerator chain in order to achieve a long lifetime in the storage ring and minimize the electron losses for a low dose rate. To avoid instabilities, the chamber in the storage ring must have a small impedance. The vacuum system is described in more detail in chapter 9.

The heart of the accelerator is the control system; it is connected more or less to every component of the accelerator complex for the controls, settings, measurements, etc. The control system is described in more detail in chapter 15.

7 Magnets of the storage ring

Ch. Benabderrahmane, G. Le Bec, J. Chavanne and D. Einfeld

The specifications of the magnets according to the lattice (chapter 5) are presented in Table 7.1. The lattice of the SEE-LS is similar to that of the ESRF-EBS [7.1], so for the first step it is proposed to use the same layout for the magnets. Therefore the parameters have to be updated accordingly.

Table 7.1: Specifications of the magnets for the proposed storage ring of the SEE-LS

Element	Length (m)	Defl. angle (degrees)	Radius (m)	Field (T)	Gradient (T/m)	B'' (T/m ²)	$B(\text{pole})$ (T)
M11	1.15	3.7	17.8082	0.46827	4.3196	-90.562	0.468
M12	1.15	3.65	18.0521	0.46194	9.14788	126.419	0.462
MQ1	0.55	2.6	12.1203	0.68802	29.2085	-1805.9	0.75
MQ2	0.44	2.6	9.69621	0.86003	32.1468	1448.82	0.75
QF1	0.2				36.7686		0.603
QD2	0.15				-24.551		0.403
QF3	0.212				24.7695		0.406
QF4	0.212				25.8483		0.423
QF5	0.388				54.8623		0.697
QF6	0.484				48.7261		0.619
SH1	0.1					724.626	0.135
SD1	0.166					71.6921	0.013
SF2	0.2					1396.5	0.26
SD3	0.166					-2659.3	0.495

7.1 Bending magnets

The bending magnets M11 and M12 should be built in the same way as for ESRF-EBS [7.1], the upgrade of the ESRF. These are permanent magnets. In addition to the properties of the ESRF magnets, the proposed magnets will have a gradient too. According to Table 7.1, the magnets also have a sextupole component. In an upgrade of the lattice it should be possible to include separate sextupoles to eliminate this sextupole component. The layout of the dipole bending magnet is shown in Figs. 7.1–7.5.

The length of the ESRF-EBS magnet is roughly 1.8 m, while that of the SEE-LS magnet will be 1.15 m. Given the reduced length, the magnet will be composed of three modules. The bending magnet consists of three main components (see Fig. 7.2): the yoke, the permanent magnets, and the iron poles. For excitation of the magnetic field one needs six permanent magnets: four side magnets, one top magnet, and one bottom magnet. The dimensions of the magnet are given in Fig. 7.3 and the pole profile is displayed in Fig. 7.4 according to the required gradient of up to 10 T/m. The gradient is quite high, but an expert at the ESRF [7.2] does not see it as a show-stopper in terms of the design.

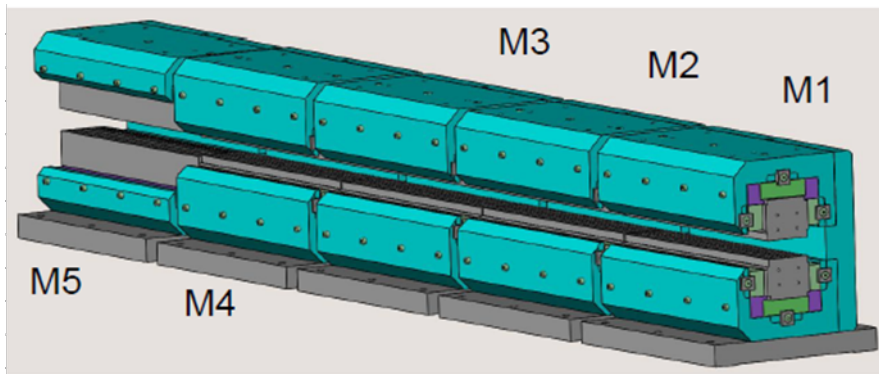


Fig. 7.1: The layout of the permanent bending magnets M11 and M12, according to that of the ESRF-EBS project. The SEE-LS magnets will be composed of three modules.

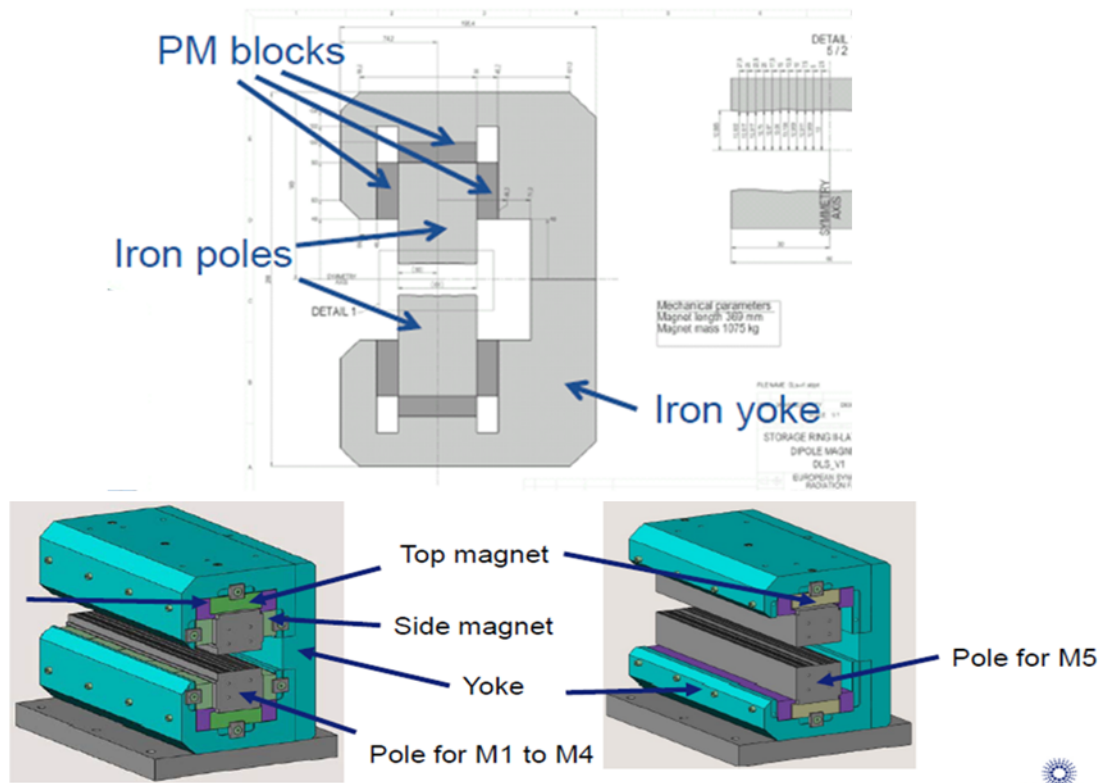


Fig.7.2: The different components used for the modules M1 to M4 and M5

M1-M4: Dimensions

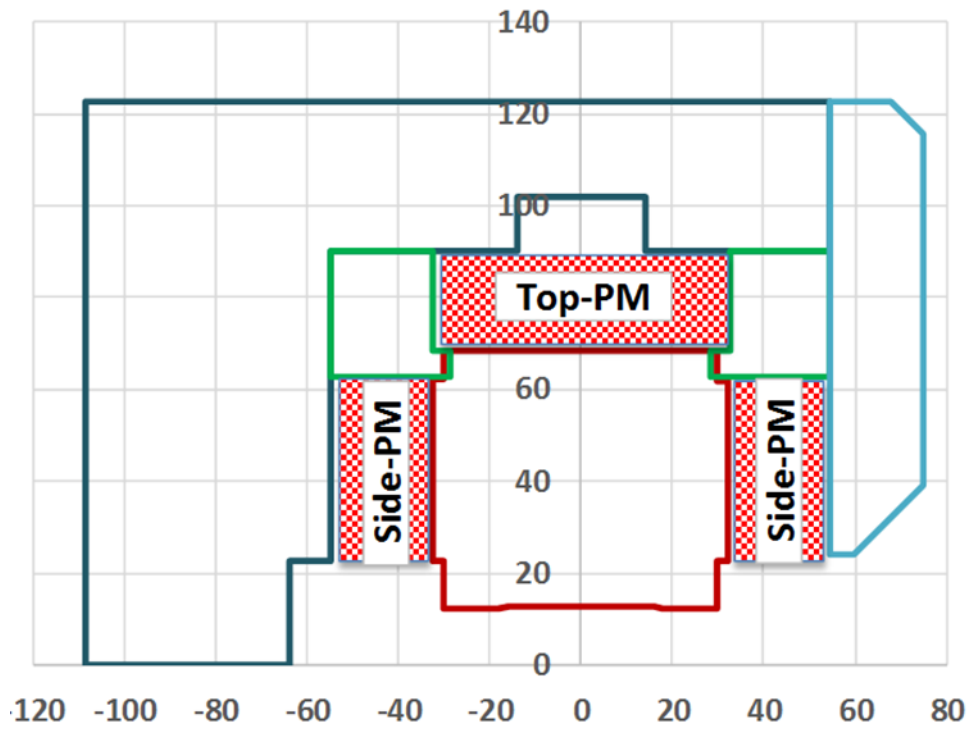


Fig. 7.3: Dimensions of the modules M1–M3 with the locations of the top and side permanent magnets. The contour of the pole is represented by a brown line.

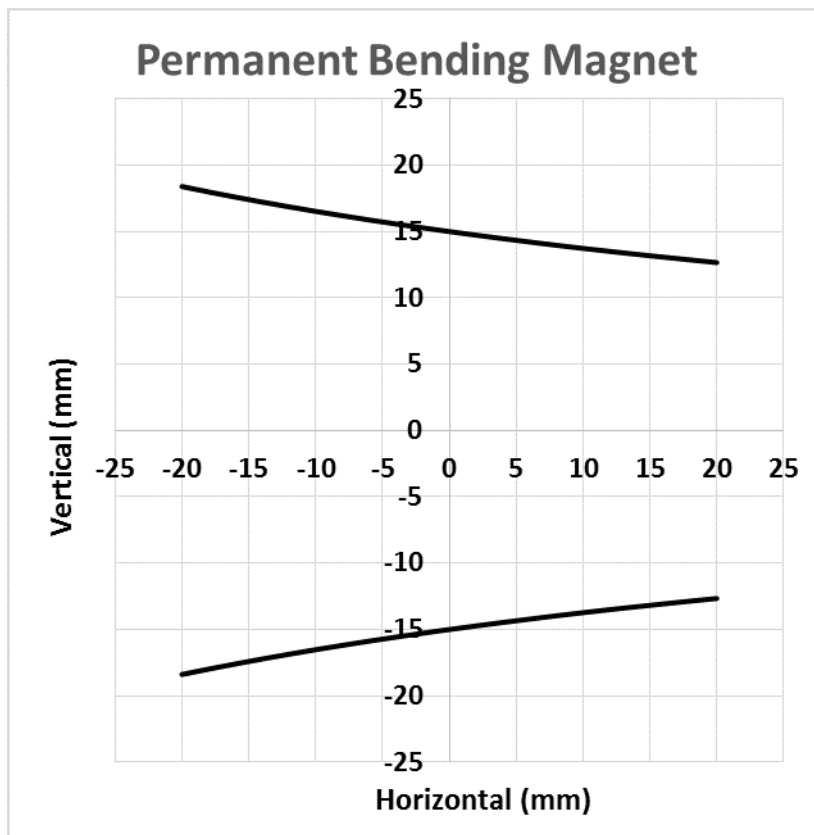


Fig. 7.4: The pole profile of the bending magnet according to the required gradient of 32 T/m

To fix the magnets on the girders a special support is needed; this support is shown in Fig. 7.5 along with the magnet. The modules are fixed on a so-called top plate, which is mounted on the base support. For the alignment procedure, the base support can be moved in the horizontal as well as the vertical direction.

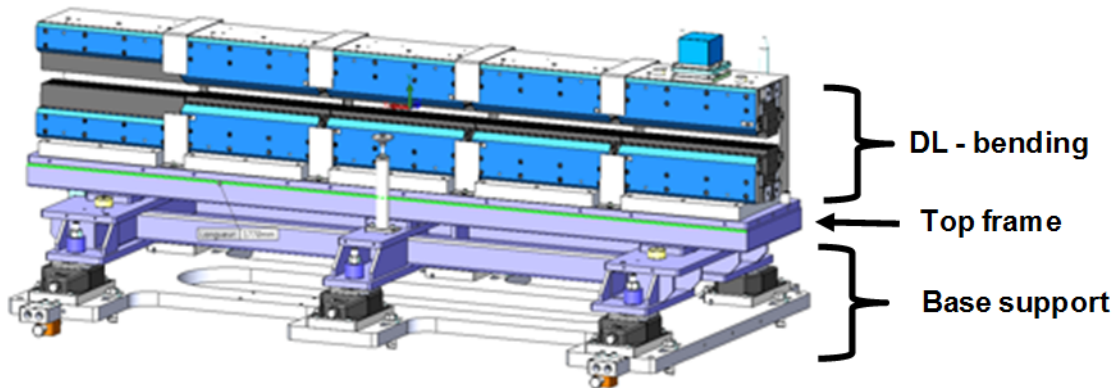


Fig. 7.5: The bending magnet M11 with the top plate and support

7.2 Combined bending magnets

The combined bending magnets MQ1 and MQ2 operate with a field of 0.7–0.9 T and a gradient of up to 32 T/m. These are special magnets, and the basis for the design is that used for the ESRF-EBS (see Fig. 7.6)

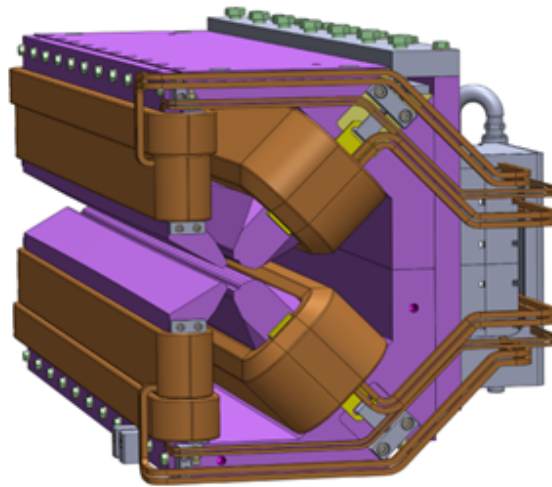


Fig. 7.6: Layout of the combined bending magnets MQ1 and MQ2

Because of the high gradient, there is a special arrangement of the poles, as shown in Fig. 7.7, and a special profile of the poles (see Fig. 7.8). To reach the required field homogeneity, a special setting of correction coils is needed (see Fig. 7.7). The parameters of the magnets are given in Table 7.2.

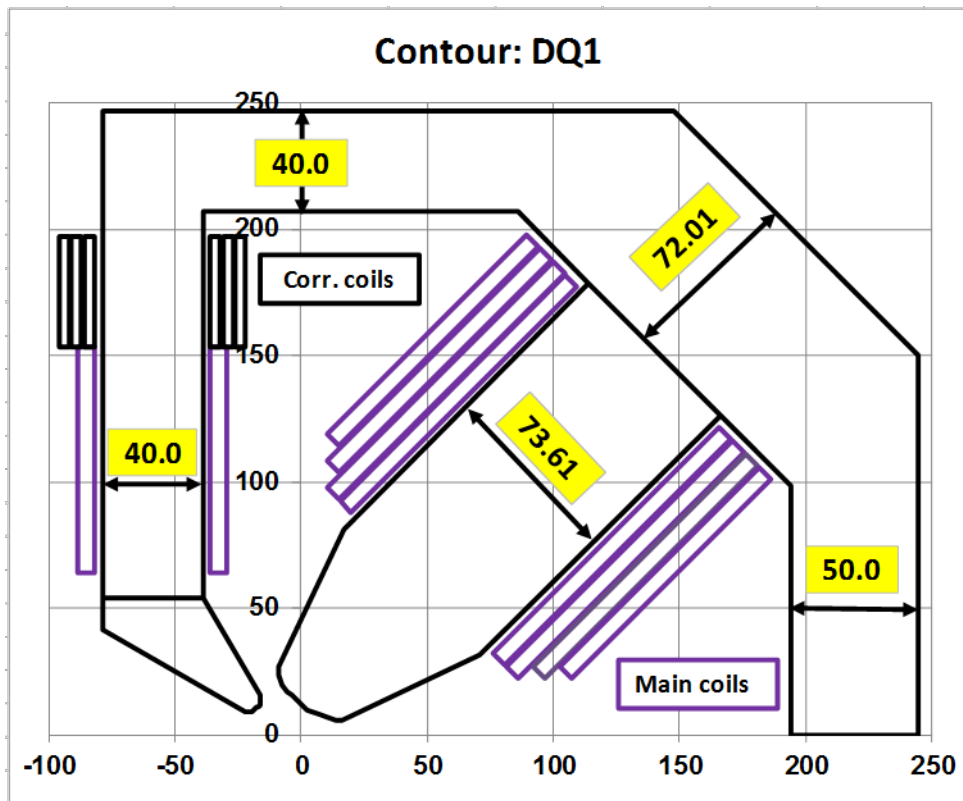


Fig. 7.7: Profile of the combined bending magnet MQ1 with the main and the correction coils

This magnet will be similar to bending magnet DQ1 of the ESRF-EBS.

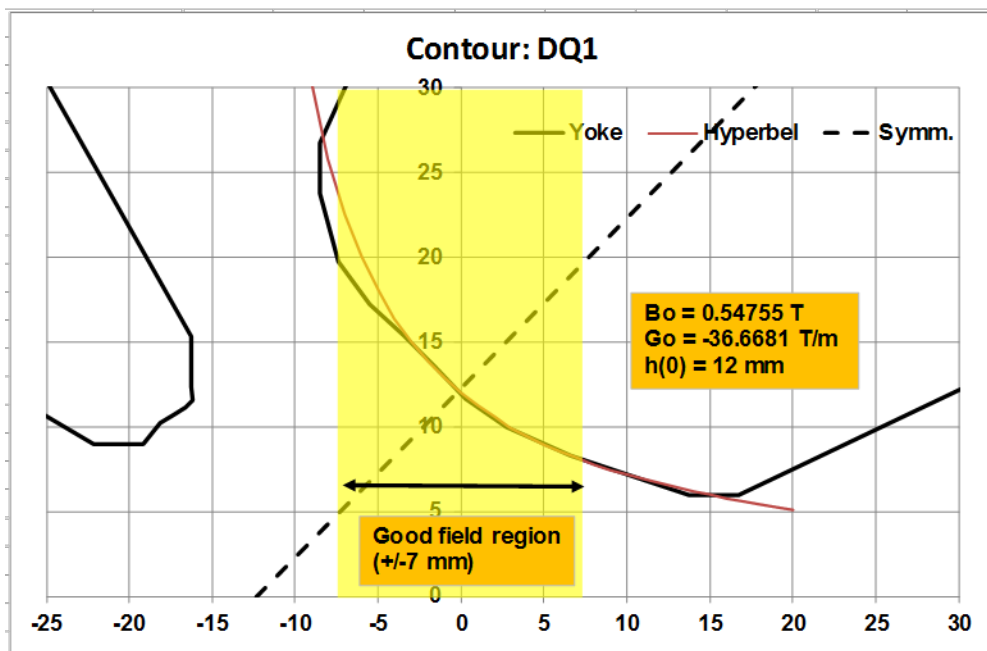


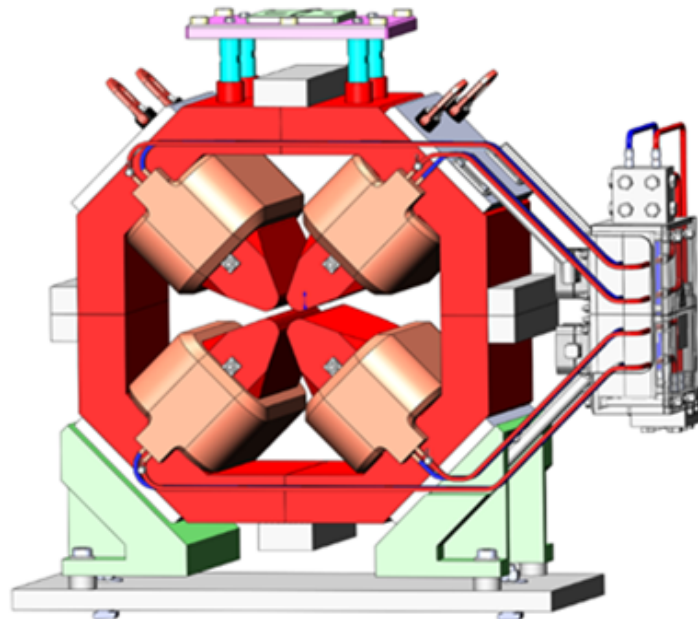
Fig. 7.8: Detailed contour of the MQ1 and MQ2 poles. For comparison, the hyperbolic contour also given. The good field region is $\pm 7 \text{ mm}$.

Table 7.2: Parameters of the combined bending magnet MQ1

Parameter	Value	Unit
Field	0.86	T
Gradient	32	T/m
Current	87	A
Turns (main)	65	
Turns (aux.)	12	
Amp turns	6.7	kA turns
Coil dimensions	6.5×6.5	mm \times mm
Pipe diameter	4	mm
Conductor area	28.67	mm ²
Resistance	221	m Ω
Voltage	19.2	V
Power (kW)	1.67	kW
Current density	3.04	A/mm ²
Cooling circuits	2	
Pressure drop	7.2	bar
Water flow	0.63	l/min
Water velocity	0.84	m/s
Temperature rise	19	K
Reynolds number	3350	

7.3 Medium-gradient quadrupoles

QF1, QD2, QF3, and QF4 are so-called medium-gradient quadrupoles, requiring a gradient of up to 30 T/m. The specifications are given for the QF4 quadrupole with the highest gradient, 25.9 T/m. The general layout of the quadrupole is given in Fig. 7.9.

**Fig. 7.9:** Layout of medium-gradient quadrupole

MAGNETS OF THE STORAGE RING

The cross-section of a quarter of the quadrupole and the pole profile are displayed in Fig. 7.10. The parameters of the quadrupole are summarized in Table 7.3.

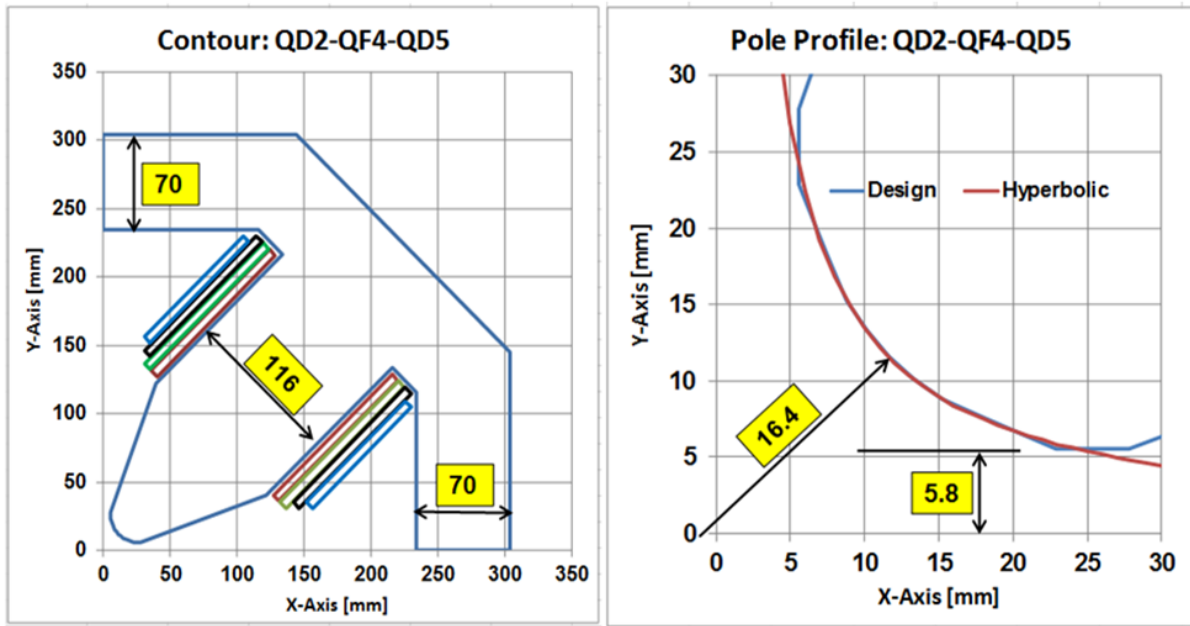


Fig. 7.10: Lamination and pole profile for the medium-gradient quadrupoles

Table 7.3: Parameters of the medium-gradient quadrupole QF4

Parameter	Value	Unit
Gradient	26	T/m
Bore radius R_0	16.4	mm
$B(\text{pole})$	0.426	T
Current	45	A
Turns	68	
Amp turns	3.00	kA turns
Coil dimensions	6×6	mm \times mm
Pipe diameter	3	mm
Conductor area	28.07	mm ²
Resistance	143	m Ω
Voltage	6.32	V
Power (kW)	0.278	kW
Current density	1.57	A/mm ²
Magnet inductance	129	mH
Time constant	0.9	s
Cooling circuits	2	
Pressure drop	7.0	bar
Water flow	0.37	l/min
Water velocity	0.872	m/s
Temperature rise	5.4	K
Reynolds number	2620	

Because of the low power and low temperature rise, the number of turns can be decreased and will have to be optimized.

7.4 High-gradient quadrupoles

QF5 and QF6 are so-called high gradient quadrupoles, requiring a gradient of up to 55 T/m. The specifications are given for the QF5 quadrupole with the highest gradient, 55 T/m. The general layout of the quadrupole is given in Fig. 7.11.

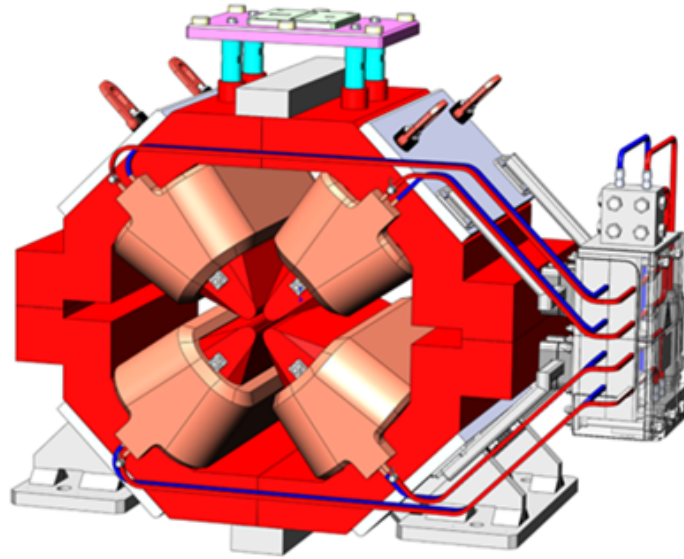


Fig. 7.11: Layout of high-gradient quadrupole

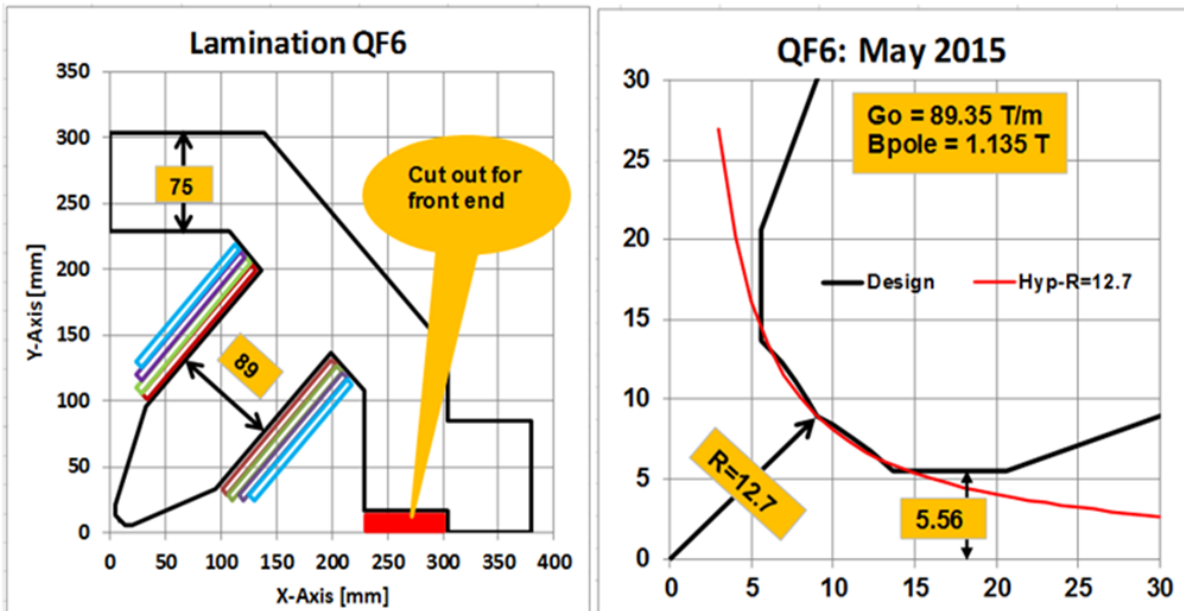


Fig. 7.12: Lamination and pole profile for the high-gradient quadrupoles

The cross-section of a quarter of the quadrupole and the pole profile are shown in Fig. 7.12. The parameters of the quadrupole are summarized in Table 7.4.

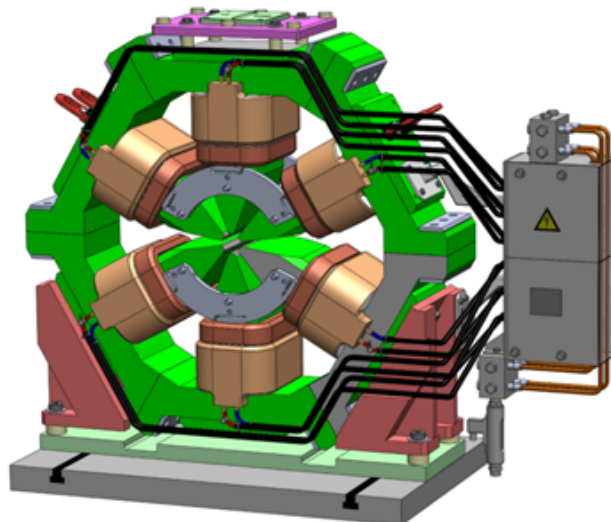
Table 7.4: Parameters of the high-gradient quadrupole QF5

Parameter	Value	Unit
Gradient	55	T/m
Bore radius R_0	12.7	mm
$B(\text{pole})$	0.625	T
Current	54.7	A
Turns	77	
Amp turns	3.53	kA turns
Coil dimensions	6×6	mm \times mm
Pipe diameter	3	mm
Conductor area	28.07	mm ²
Resistance	204.2	m Ω
Voltage	11.17	V
Power (kW)	0.611	kW
Current density	1.95	A/mm ²
Magnet inductance	272	mH
Time constant	1.33	s
Cooling circuits	2	
Pressure drop	7.05	bar
Water flow	0.303	l/min
Water velocity	0.714	m/s
Temperature rise	12	K
Reynolds number	2140	

Because of the low power and low temperature rise, the number of turns can be decreased and will have to be optimized. Furthermore, it is possible to decrease the length of the quadrupole.

7.5 Sextupoles

The largest sextupole component B is around 2700 T/m², this value can be reached with the design used for the ESRF-EBS. The layout of the sextupole is presented in Fig. 7.13, and the lamination and pole profile are given in Fig. 7.14. The pole profile perhaps still needs to be optimized.

**Fig. 7.13:** Layout of the sextupole

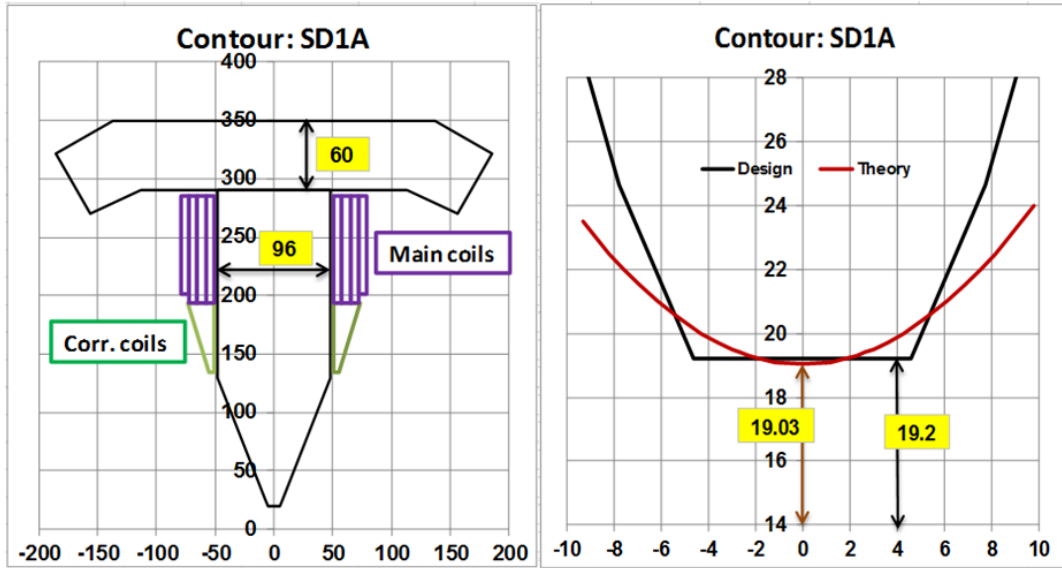


Fig. 7.14: Lamination and pole profile of the sextupole

Table 7.5: Parameters of the sextupole SD3

Parameter	Value	Unit
Diff.-Gradient	2700	T/m ²
Bore radius R_0	19	mm
$B(\text{pole})$	0.49	T
Current	48.2	A
Turns	51	
Amp turns	2.46	kA turns
Coil dimensions	6×6	mm \times mm
Pipe diameter	3	mm
Conductor area	28.07	mm ²
Resistance	122.1	m Ω
Voltage	5.88	V
Power (kW)	0.283	kW
Current density	1.716	A/mm ²
Magnet inductance	79.3	mH
Time constant	0.65	s
Cooling circuits	2	
Pressure drop	7.0	bar
Water flow	0.41	l/min
Water velocity	0.98	m/s
Temperature rise	4.9	K
Reynolds number	1477	

The sextupole has correction coils so that there is the possibility of making a beam correction in the horizontal as well as the vertical direction. The parameters of the sextupoles are summarized in Table 7.5. The number of turns can still be reduced in order to increase the temperature rise.

7.6 Correctors

The correctors have to make a kick in both directions of roughly 0.5 mrad. The layout of the corrector is given in Figs. 7.15–7.17, and the corresponding parameters are presented in Table 7.6.

MAGNETS OF THE STORAGE RING

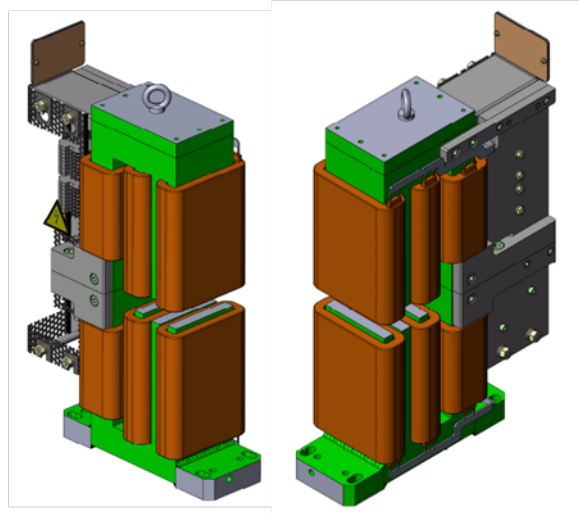


Fig. 7.15: Layout of the correctors

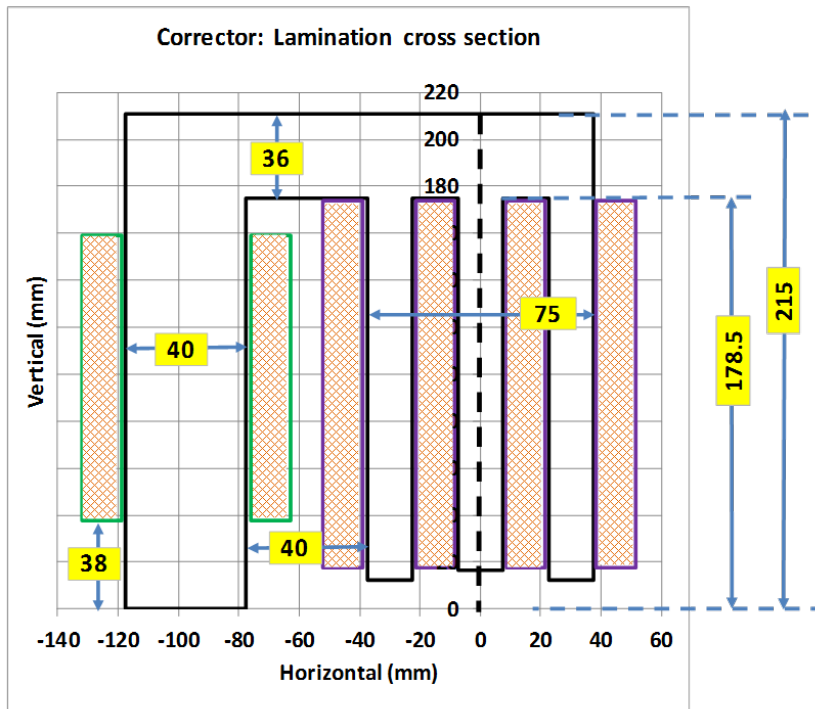


Fig. 7.16: Lamination and pole arrangement of each corrector

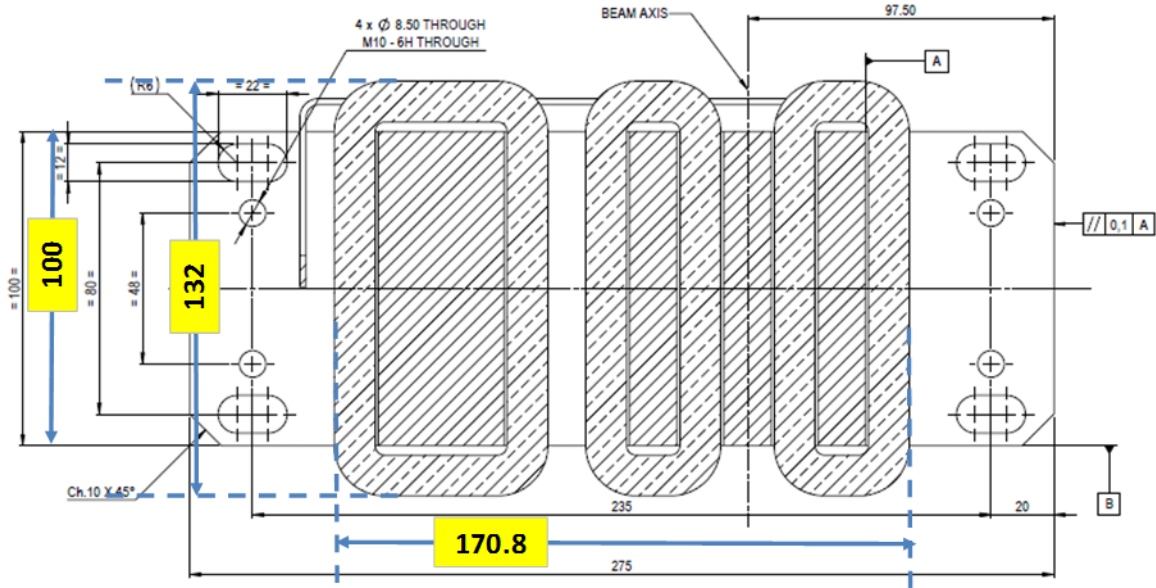


Fig. 7.17: Dimensions of each corrector

Table 7.6: Parameters of the correctors

Parameter	Value	Unit
Vertical integrated dipole	10	T mm
Horizontal integrated dipole	10	T mm
Skew integrated quadrupole	0.12	T
Mechanical length	100	mm
Gap	25	mm
Overall width	450	mm
Overall height	523.2	mm
Overall length	150	mm
Nominal current	2	A
Electrical resistance coil1	2,5	W
Voltage coil1	5	V
Inductance coil1	0.98	H
Electrical resistance coil2	2	W
Voltage coil2	4	V
Inductance coil2	0.94	H
Power loss per coil1	10	W
Power loss per coil2	8	W
Copper conductor size	2x0.9	mm ²
Corner radius	2	mm
Number of turns for coil1	900	turns
Number of turns per coil2	620	turns
Number of pre-series magnets	2	
Number of series magnets	96	

7.7 Octupoles

The layout of the octupoles, the size of the lamination, and the pole profile are presented in Figs. 7.18–7.20. The parameters are given in Table 7.6.

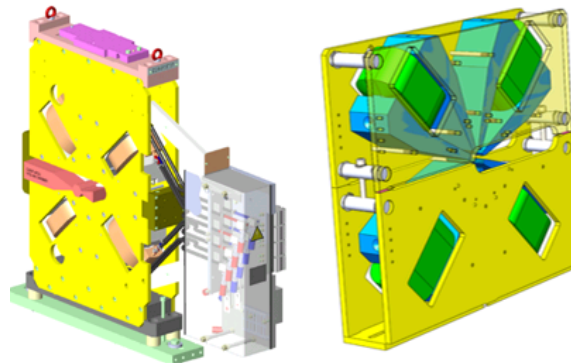


Fig. 7.18: Layout of the octupoles

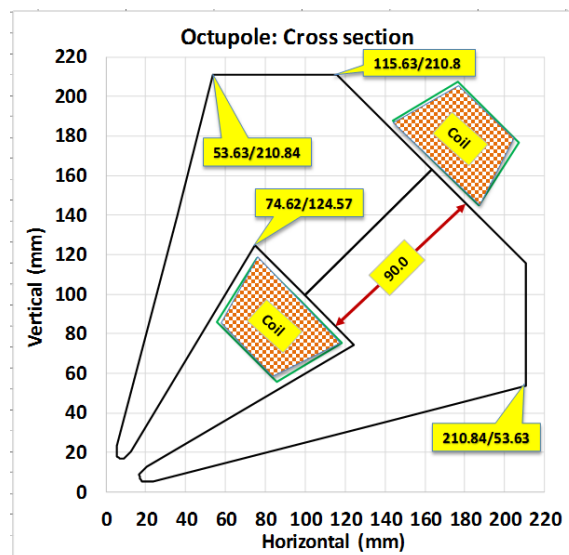


Fig. 7.19: Dimensions of the octupoles with the arrangements of the coils

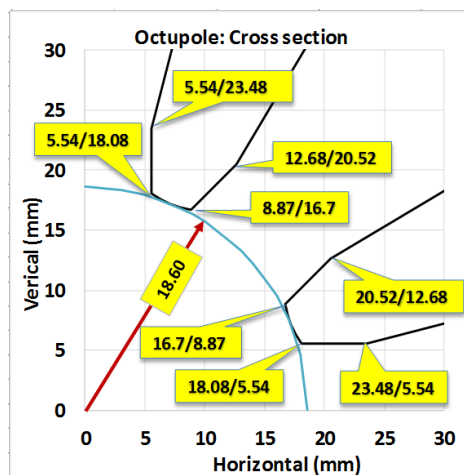


Fig. 7.20: Dimensions of the octupole pole profile

Table 7.7: Parameters of the octupoles

Parameter	Max. curr.	Nom. curr.
Bore radius [mm]	18.6	18.6
Yoke length [mm]	90	90
Total length [mm]	114	114
Current [A]	104	53.4
Integrated B'' [T/m ²]	7013.5	3598
Centre field gradient B'' [T/m ³]	71795	36868
Magnetic length [mm]	97.69	97.59
Gap between poles [mm]	11.08	11.08
Number of A-turns/coil	3744	1922.4
Number of turns/coil	36	36
Conductor length/coil [m]	12.8	12.8
Total electrical resistance [m Ω]	31.04	31.04
Total inductance [mH]	21.61	11.11
Input voltage [V]	3.23	1.66
Power [W]	335.73	88.51
Current density in copper [A/mm ²]	3.70	1.90
Conductor width [mm]	6	6
Conductor height [mm]	6	6
Hole diameter [mm]	3	3
Corner radius [mm]	1	1
Copper cross-section [mm ²]	28.07	28.07
Pressure drop [bar]	7.2	7.2
Number of coils in series	4	4
Water speed [m/s]	1.57	1.57
Water flow per circuit [l/min]	0.7	0.7
Water flow per magnet [l/min]	0.7	0.7
Temperature elevation per circuit [K]	7.4	1.9

References

- [7.1] ESRF-EBS project, EBS storage ring technical report (ESRF, Grenoble, 2018), https://web.archive.org/web/20190506105503/https://www.esrf.eu/files/live/sites/www/files/about/upgrade/documentation/Design_Report-reduced-jan19.pdf
- [7.2] J. Chavanne, ESRF, private communication.

8 Girder system

J.-C. Biasci and D. Einfeld

8.1 Introduction

The cross-sections of the beam in the straight sections are $\sigma(x) = 51.2 \mu\text{m}$ and $\sigma(y) = 4.7 \mu\text{m}$. The user requirement for beam stability is one-tenth of the beam size; hence the stability has to be in the sub-micrometre range. The beam stability is determined by the stability of the magnets as provided by the girder system supporting the magnets. For a 4th generation light source, a very stable girder system with ‘eigen-frequencies’ greater than 50 Hz is required. Furthermore, some movements of the girders should be adjusted in real time. A new type of girder system has been introduced at the Swiss light source [8.1] that involves: 1) fixing up to six magnets on the very well machined top plate of the girder system; and 2) installing a so-called mover system for real-time adjustment of the girder. Roughly the same system with some modifications and improvements has been used for the most recently built synchrotron light sources. The girder system should have the following properties:

- easy to install (in terms of handling, pre-alignment, and magnet disassembly for service);
- fast, accurate, and easy to align (not only with three-point support; minimization of clamping effect);
- Y and Z independent adjustments;
- high stiffness and rigidity;
- the design goal of having the first frequency greater than 50 Hz requires multiple support points (more than three).

All the requirements can be met with the girder system designed for the upgrade of the ESRF, and so it is proposed to make a copy of this system.

The supports of the storage ring magnets and vacuum chambers rely on 85 girders (84 plus one for the injection straight section), including four girders for each of the 16 storage ring cells. Each girder has to support seven to nine magnets, with a layout that can cope with the space constraints and the necessity of having flanges and bellows between the vacuum chambers supported by adjacent girders. The girders are all identical with a length of about 5.1 m.

The girder alignment requirements are 50 μm in both the vertical and the transverse directions; to respect the inter-girder alignment tolerances, a realignment of the girders in the vertical direction will be necessary every six months because of the medium-term displacements of the storage ring floor. For this purpose, each girder should be equipped with a ± 5 mm motorized vertical adjustment and a ± 5 mm manual transverse adjustment with 5 μm resolution.

Initial efforts have been made to develop a motorized girder system with optimum stability for the new girder systems.

8.2 General design

The girder that meets all the above requirements is based on the concept of the orthogonal heptagon, derived from the orthogonal hexapod. A body in space has six degrees of freedom, so by putting it on six supports, for each of them blocking movement of a point in only one direction and ensuring no rotations, an easily adjustable isostatic system is obtained.

This is the concept used in commercial hexapods on six articulated jacks and in the cam system of Diamond, SLS, Petra III, etc. Unfortunately, this system is not sufficiently stiff to meet our stability requirement. So it was decided to modify it by introducing a supplementary leg in the vertical direction, losing the perfect isostaticity but greatly increasing the stiffness. Four motorized supports in the vertical direction, instead of three, permit the adjustment of height, pitch, and roll.

The two jacks in the transverse direction allow translation in Y , and the yaw and one jack are used for longitudinal adjustment. The hyper-stativity of the system must be managed by adjusting carefully the four vertical legs to ensure that each of them carries its load correctly. The girder itself is made of normal carbon steel. Special attention is given to the welding, which should be continuous and of nearly full penetration type. The layout of the girder system is presented in Fig. 8.1.

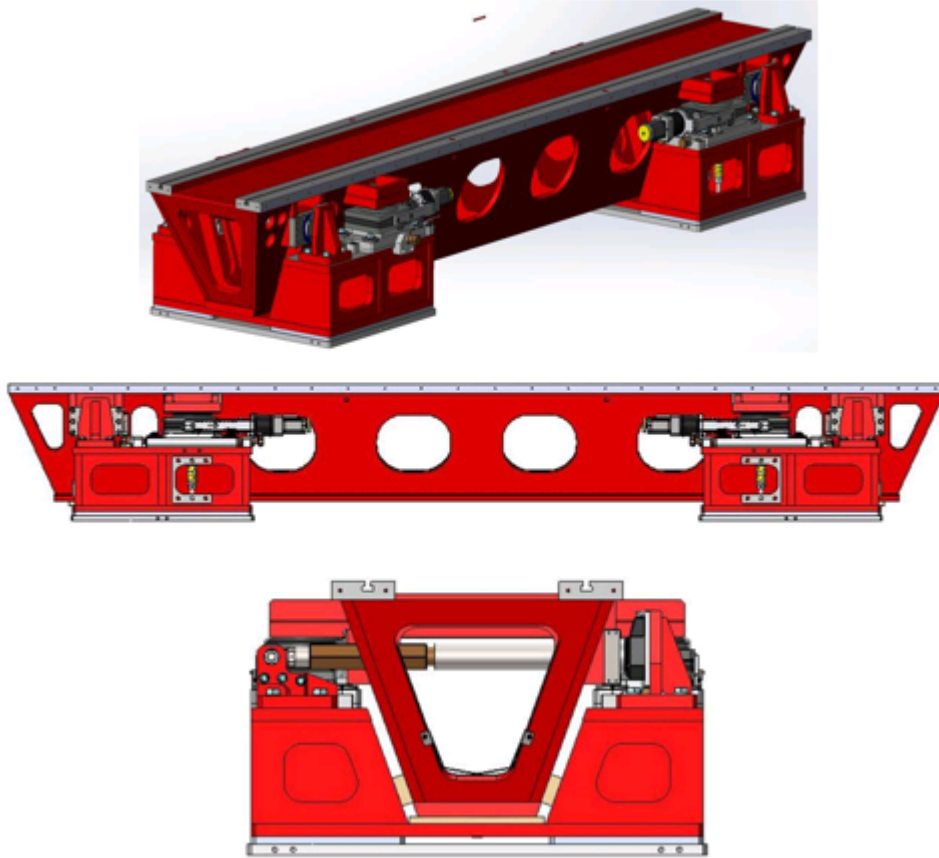


Fig. 8.1: Layout of the ESRF-EBS girder, which would be used for the SEE-LS too

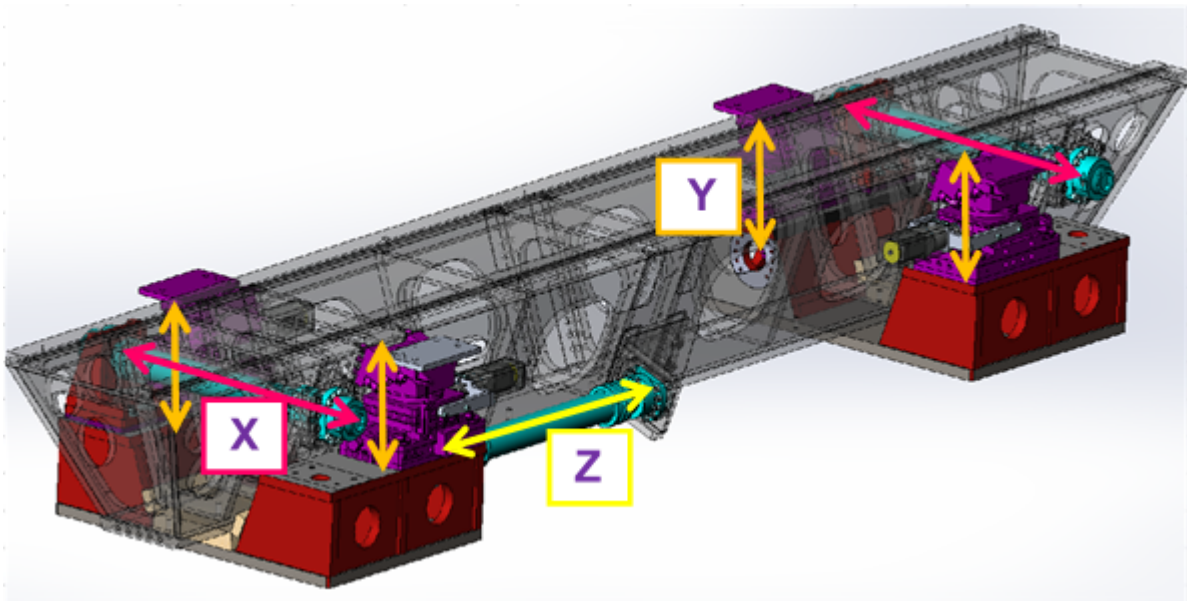


Fig. 8.2: The movement system for adjustments in the three directions

GIRDER SYSTEM

Figure 8.2 shows how the positions in the three directions can be changed with a total of six moving systems. For movement in the vertical system a motorized system is used. More details are presented in Figs. 8.3 and 8.4.

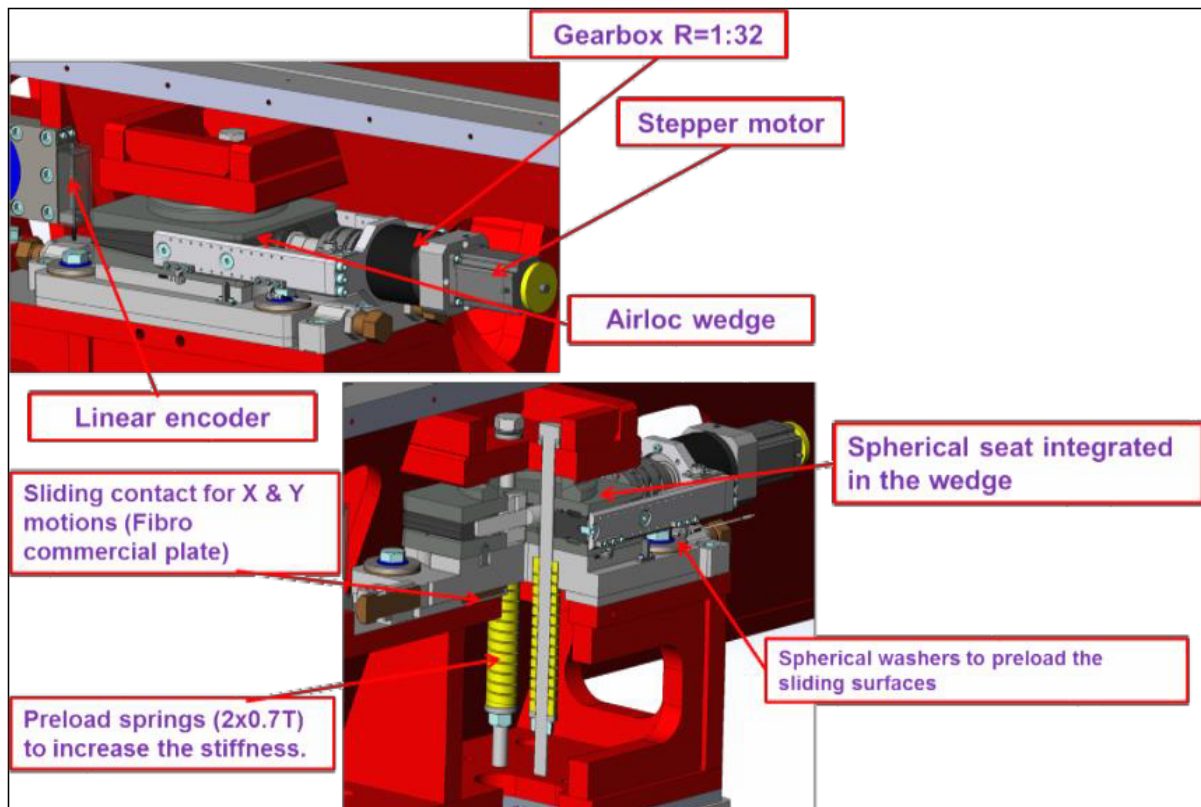


Fig. 8.3: Vertical foot design

Three functions:

- 1) horizontal adjustment (+/- 3.5mm continuous, +/-15mm global)
- 2) guiding the vertical movement (ensuring no lateral displ. during the vertical adjustment)
- 3) improving the stiffness of the girder

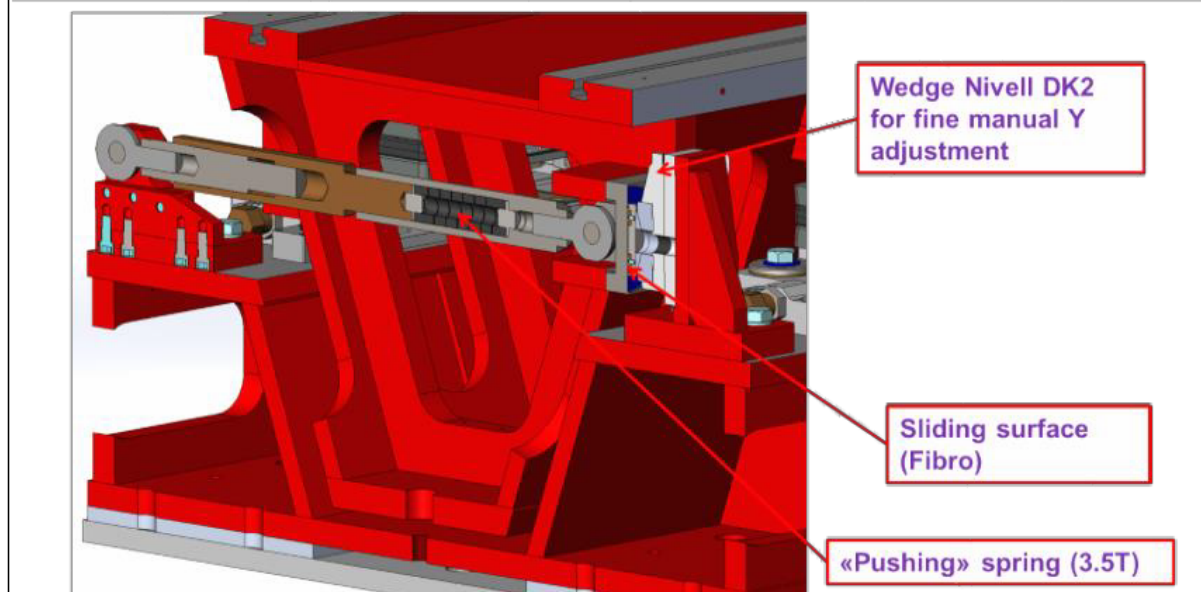


Fig. 8.4: Horizontal foot design

8.3 Girder performance

Vibration measurements and analysis were undertaken on a prototype girder installation (see Fig. 8.5). The initial test was performed on four feet without magnets. Since the results obtained were satisfactory, as the first horizontal mode was above 80 Hz, the tests carried on with measurements on the girder with dummy magnets. In this configuration, the first magnet mode was found at 42 Hz, while the more global first girder mode dropped to 51 Hz. The amplification with respect to the floor vibration level is weak and does not exceed 1 μm peak to peak. Therefore, the prototype girder's behaviour complies with the vibration specifications.

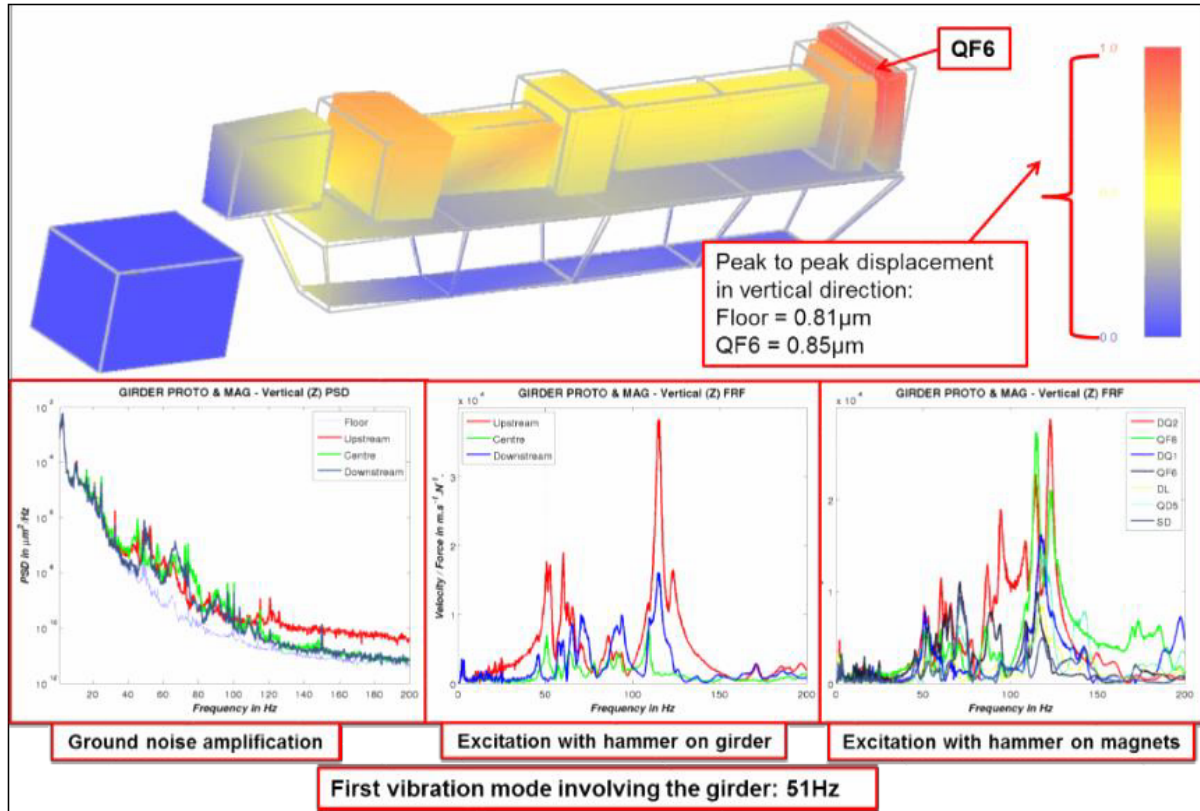


Fig. 8.5: Prototype girder vibration analysis results

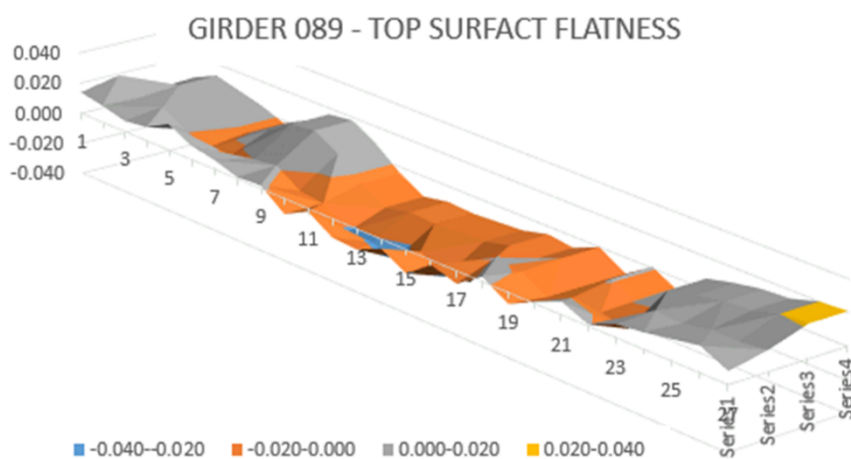


Fig. 8.6: Flatness of the upper plate of the girders

8.4 Locations of magnets on the girders

The locations of the different magnets on the girders are presented in Figs. 8.7–8.10.

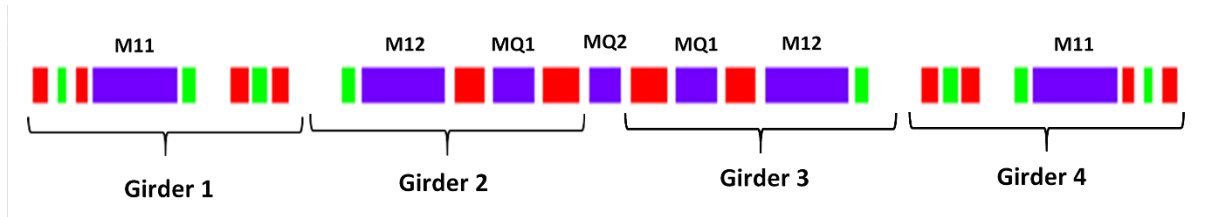


Fig. 8.7: Placement of the magnets of an achromat on the four girders

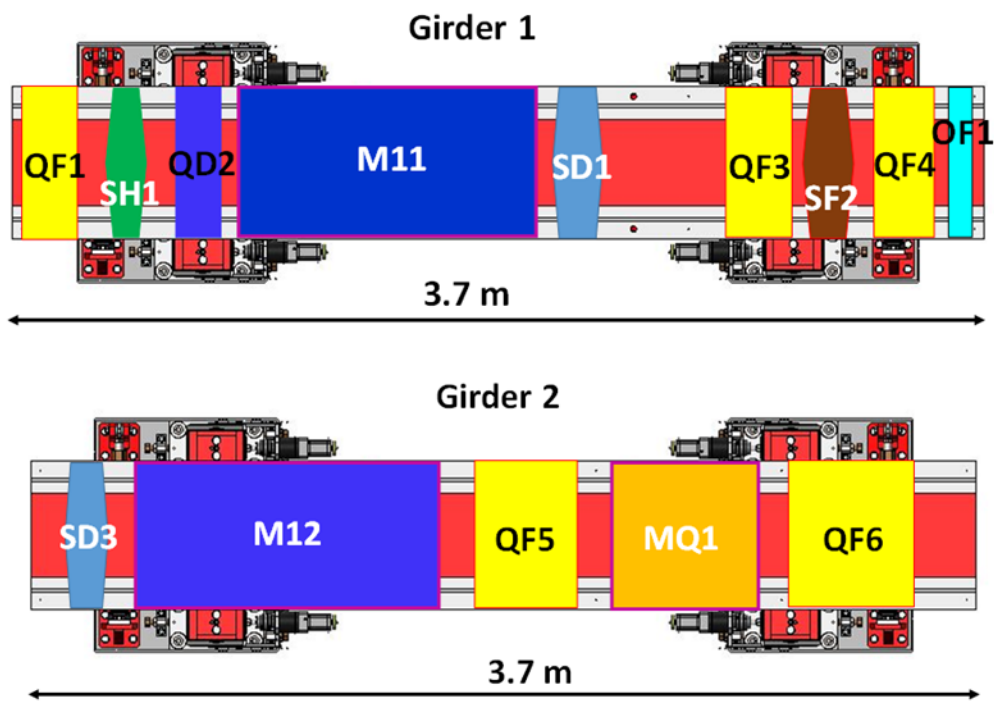


Fig. 8.8: Arrangement of the magnets on girders 1 and 2

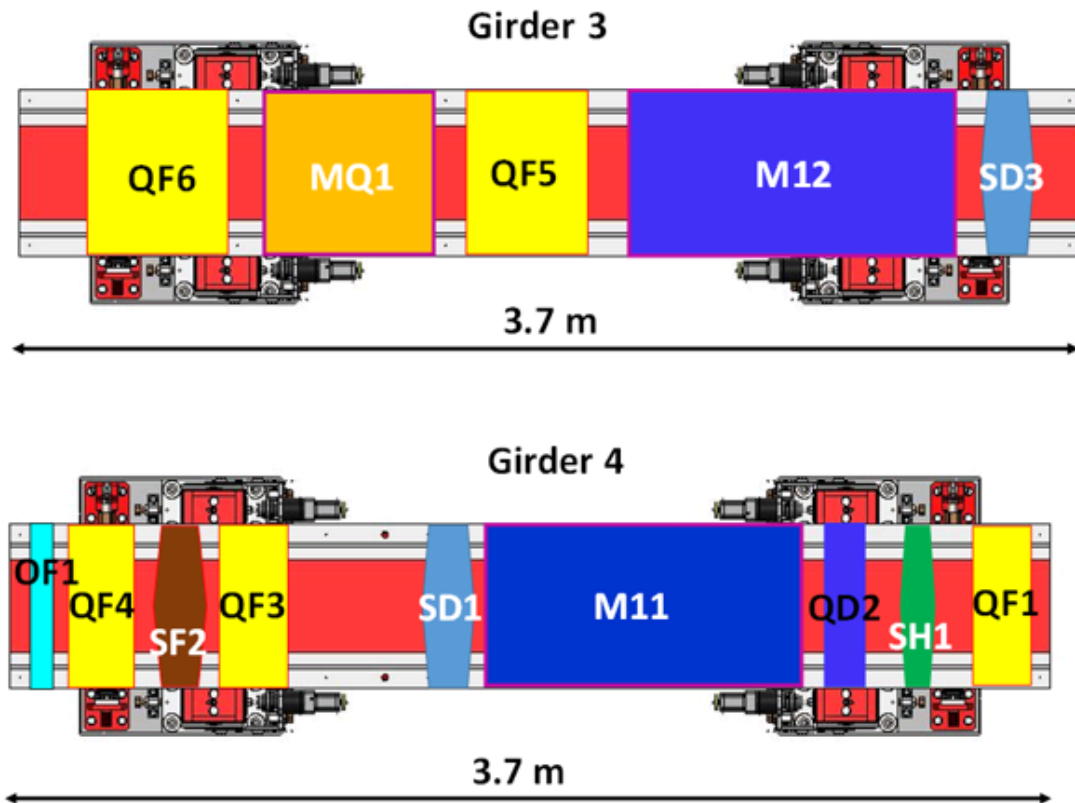


Fig. 8.9: Arrangement of the magnets on girders 3 and 4

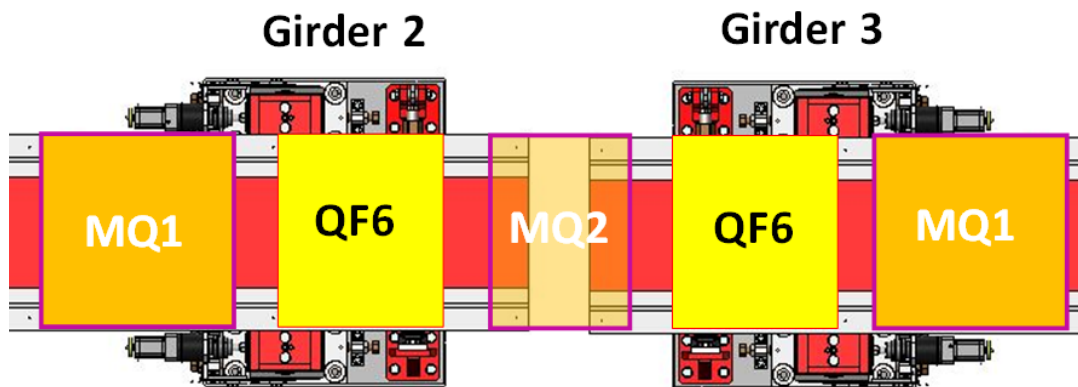


Fig. 8.10: Arrangement of the magnet MQ2 on girders 2 and 3

References

- [8.1] S. Zelenika *et al.*, *Nucl. Instrum. Methods Phys. Res., A* **467** (2002) 99, [https://doi.org/10.1016/S0168-9002\(01\)00246-7](https://doi.org/10.1016/S0168-9002(01)00246-7)
- [8.2] ESRF-EBS project, EBS storage ring technical report (ESRF, Grenoble, 2018), <https://web.archive.org/web/20190506105503/https://www.esrf.eu/files/live/sites/www/files/about/upgrade/documentation/Design Report-reduced-jan19.pdf>

9 Vacuum system

E. Al-Dmour

The vacuum system design of SEE-LS will employ state-of-the-art techniques used by the newly built synchrotron radiation facilities. The magnet openings are small, and accordingly the vacuum chambers will have small apertures; therefore they will be conductance-limited vacuum chambers. Consequently, lumped pumps are not an efficient approach to achieving the necessary target vacuum pressure levels. To overcome this issue, a non-evaporable getter (NEG) coating will be used, which will allow a high pumping speed for active gases along with reduced photon-induced desorption; as a result, a few ion pumps will be used, mainly to remove noble gases at the areas of high outgassing.

9.1 The vacuum layout

The storage ring of the SEE-LS is divided into 16 achromats, and the vacuum system layout will follow this sectioning; ultra-high vacuum (UHV) valves with RF fingers will be placed on each side of the achromat, allowing a space of 5.4 m for the insertion devices (IDs). Figures 9.1 and 9.2 show the layout of one vacuum section.

The vacuum chamber will be made of oxygen-free silver bearing copper. The chamber profile on the extremities of the achromats will be circular with an inside diameter of 24 mm, while in the middle of the achromat the chamber will be elliptical (with internal dimensions of 18 mm × 22 mm). The chamber will have a thickness of 1 mm, and distributed cooling will be included along its length to remove the power from the synchrotron radiation striking the chamber wall. A cross-section of the vacuum chambers, together with the magnet profiles, is shown in Fig. 9.3; the clearance to the magnets is 0.5 mm. The cross-section is slightly larger than that of the MAX IV storage ring (22 mm inside diameter); thus, one can have even smaller apertures and use the additional clearance to the magnets for heaters and insulation, which allows in situ bake-out for the vacuum chambers.

The photon extraction occurs after the first dipole of the achromats, and the chamber at this location must have an antechamber through which the photon beam will pass to the front ends. The chamber will pass through the sextupole after the first dipole, and then a crotch absorber is placed where the photon beam and the electron beam become separated. A similar layout for the MAX IV storage ring is shown in Fig. 9.4. Figure 9.5 shows the area of extraction of the photon beam and Fig. 9.6 a cross-section of the chamber at the exit of the sextupole.

Bellows with RF fingers will be welded onto each side of the vacuum chamber body; this will allow the chamber to expand due to thermal expansion when the beam hits the walls. In case an in situ bake-out is implemented, bellows with a larger stroke should be considered. Beam position monitors (BPMs) will be connected on each side of the chambers; standalone BPMs will be used, similar to the design at MAX IV (see Fig. 9.7). The BPMs will be supported by the magnet structure with a mechanical design which aims to minimize the mechanical motion of the BPM bodies as a result of heating of the vacuum chambers by the incident synchrotron radiation.

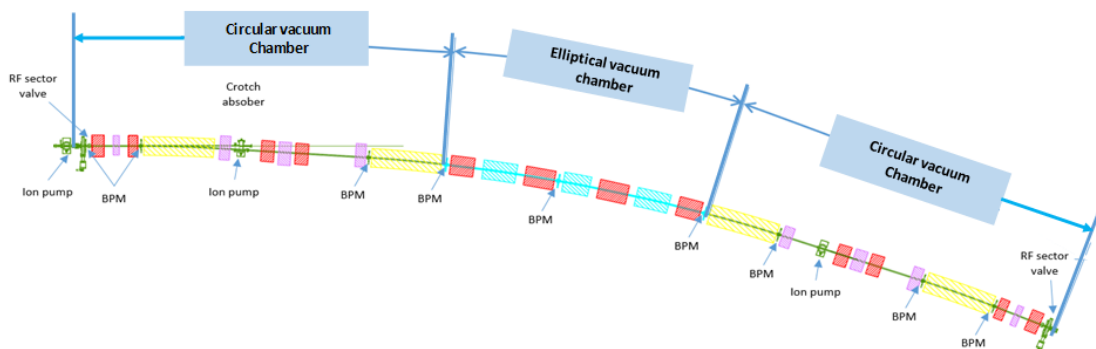


Fig. 9.1: The layout of the vacuum system of one achromat

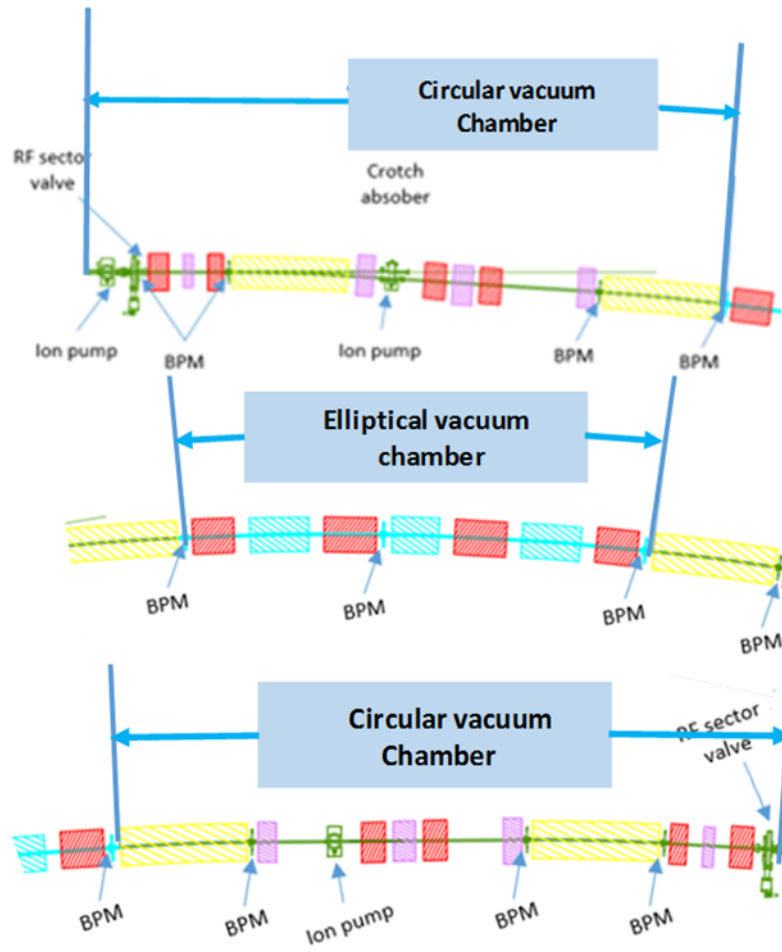


Fig. 9.2: The layout of the vacuum system at the beginning, middle, and end of one achromat

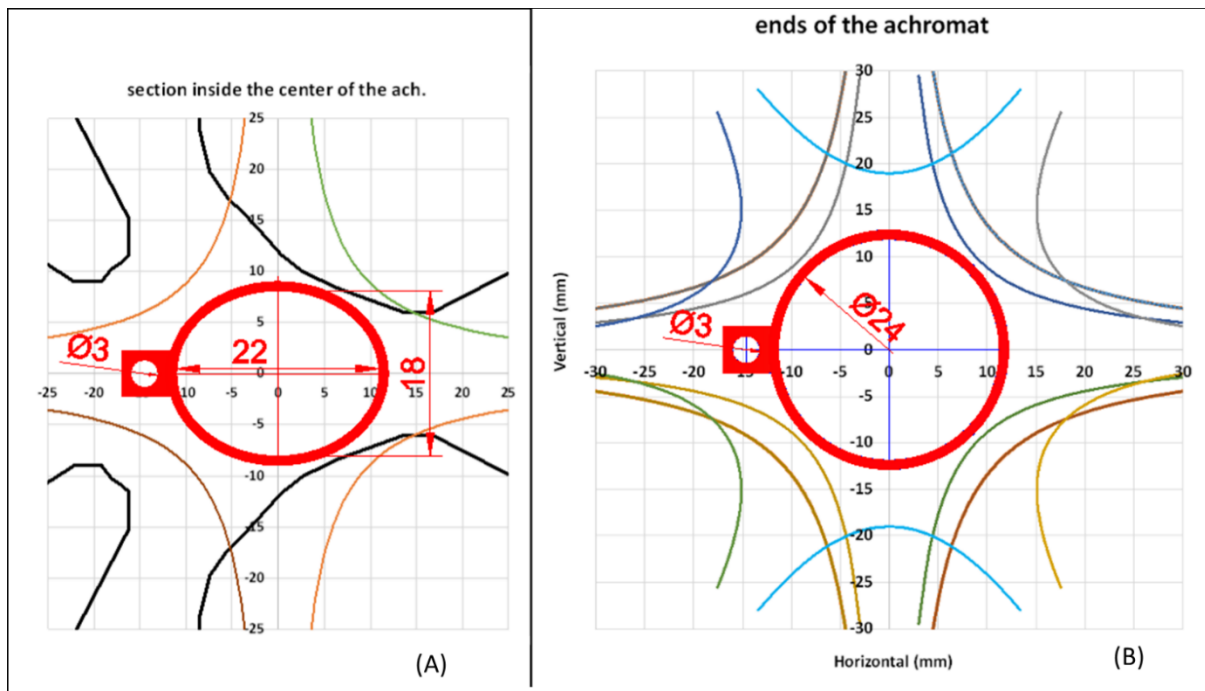


Fig. 9.3: The cross-section of the vacuum chambers inside the magnets: (A) at the centre of the achromat; (B) on the edges of the achromat.

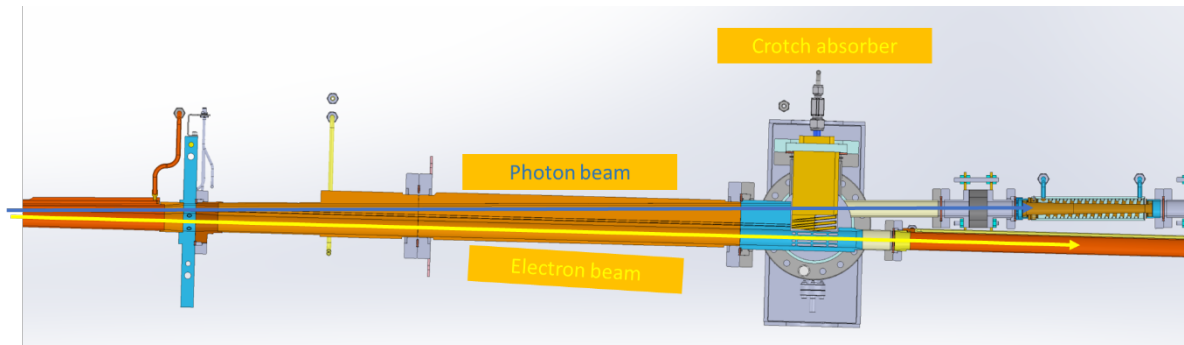


Fig. 9.4: The area of the photon beam extraction of MAX IV

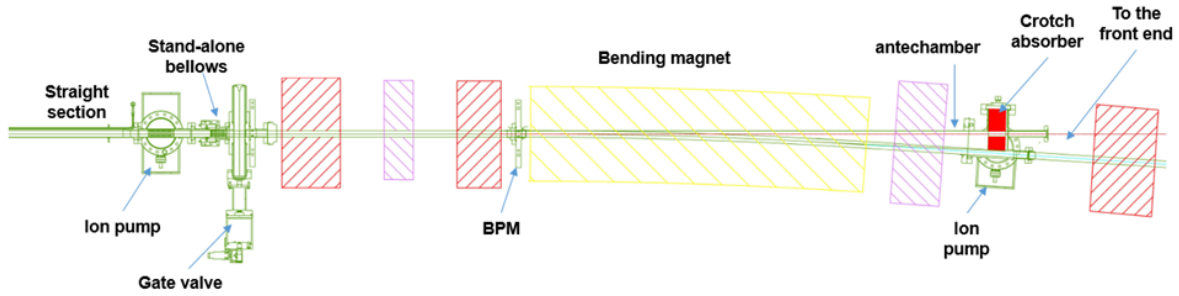


Fig. 9.5: The area of the photon beam extraction for SEE-LS

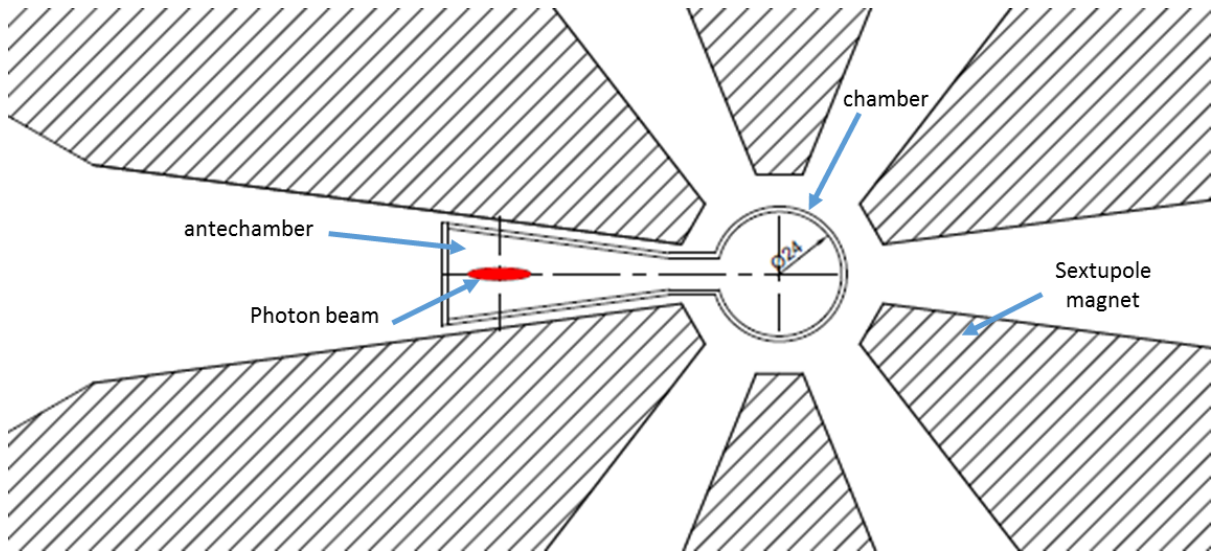


Fig. 9.6: Section inside the sextupole before the crotch absorber, the chamber with an antechamber

The overall mechanical design of the vacuum chambers needs to carefully take into account the beam coupling impedance, in terms of both the limitations it could impose on the maximum attainable beam current and the potential chamber heating due to beam-induced fields. In general, a chamber that is as smooth as possible is desired from an impedance point of view, and the choice of copper as the chamber material also minimizes resistive wall impedance effects.

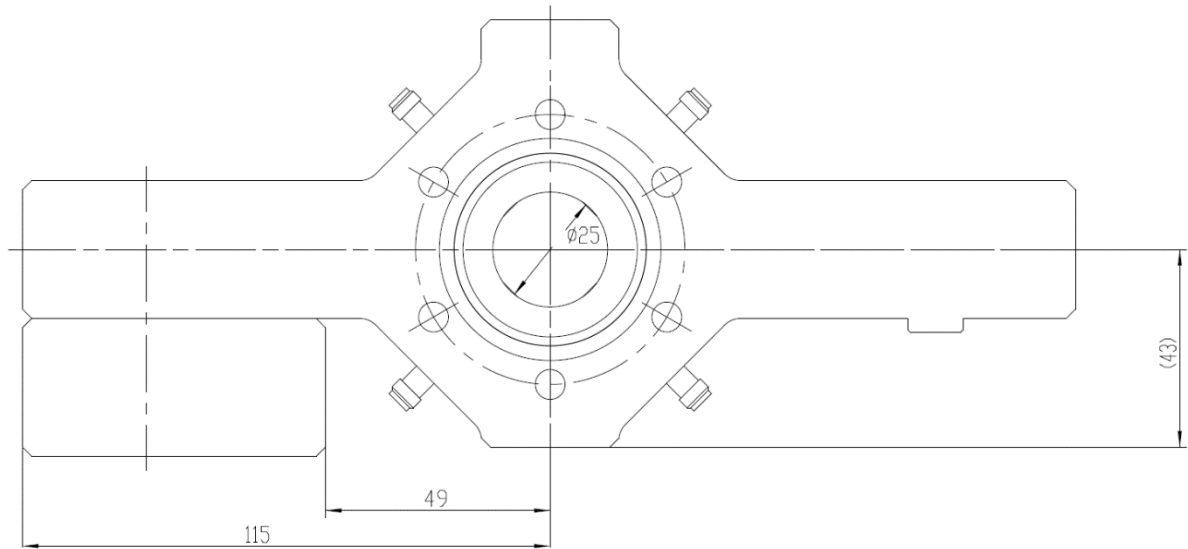


Fig. 9.7: The standalone BPM of MAX IV

The conceptual design of the chambers follows that used at the MAX IV 3 GeV storage ring, and technologies developed at MAX IV will be adapted to the small apertures that the SEE-LS storage ring will have. Figure 9.8 shows a cross-section of the unit cell vacuum chamber of MAX IV, including the distributed cooling in the side of the chamber and the welded bellows on the extremities. Figure 9.9 shows a 3D view of the unit cell of the MAX IV chamber, and Fig. 9.10 shows some parts and the chambers of the MAX IV storage ring [9.1].

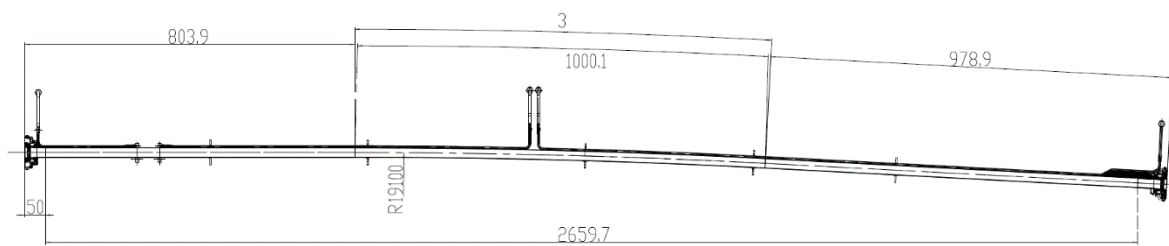


Fig. 9.8: A cross-section of the unit cells of the MAX IV vacuum chamber

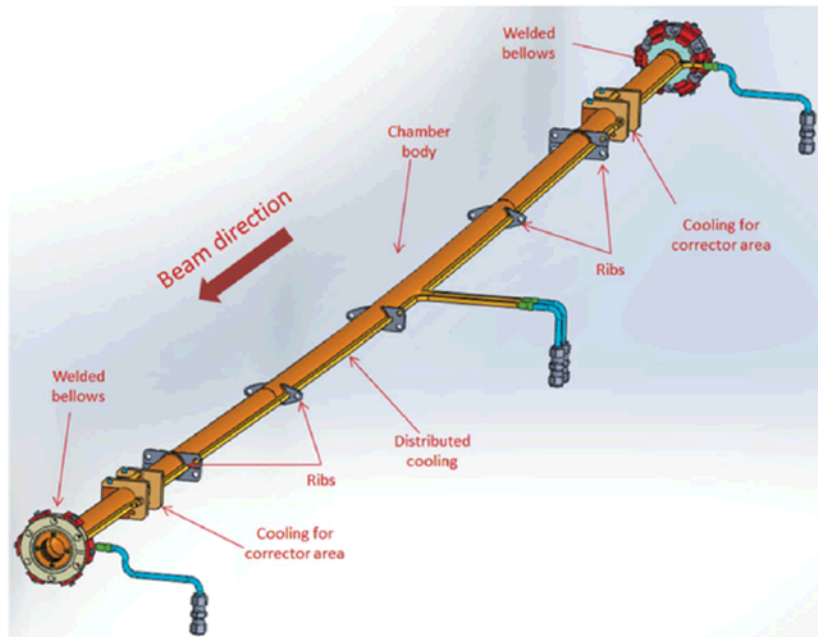


Fig. 9.9: Three-dimensional view of the unit cells of the MAX IV vacuum chamber

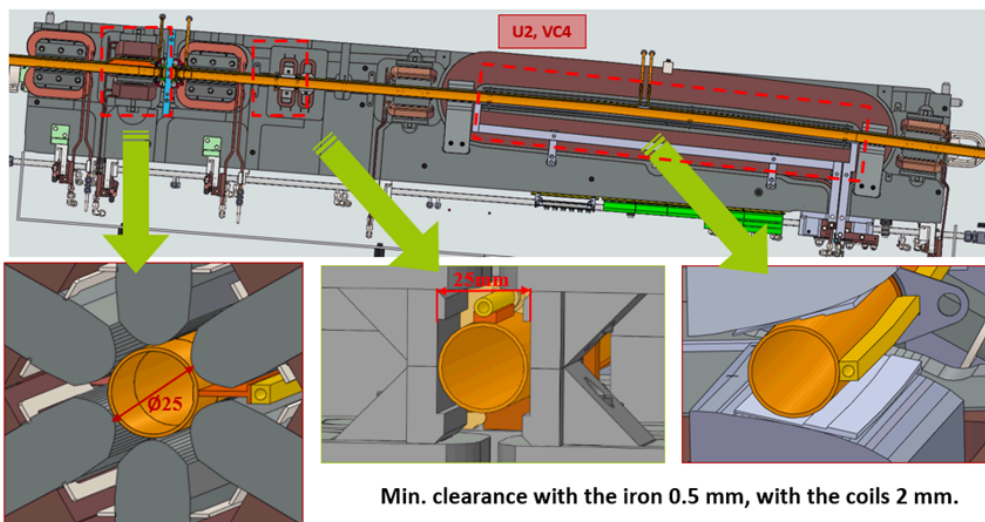


Fig. 9.10: MAX IV vacuum chamber layout, showing the cross-section of the beam pipe with the cooling tubes in the different magnets.

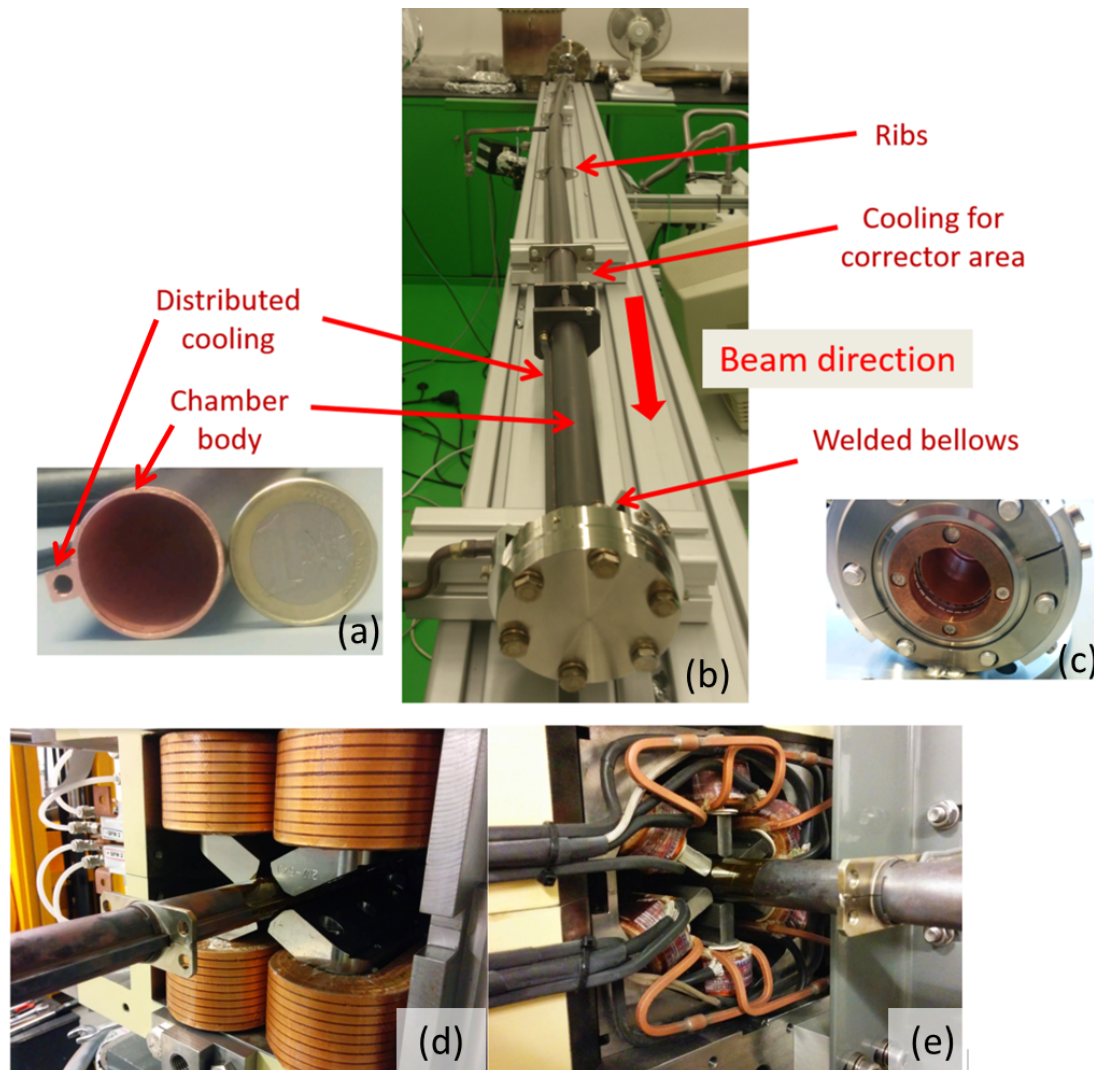


Fig. 9.11: MAX IV vacuum chamber layout: (a) cross-section of the vacuum tube with cooling pipe; (b) one assembly of MAX IV vacuum chamber; (c) welded bellows; (d) the chamber inside the quadrupole magnet; (e) the chamber inside the sextupole magnet.

9.2 The synchrotron radiation power from bending magnets

The total power from the bending magnets is around 93 kW, which must be absorbed by the walls of the vacuum chambers; the crotch absorber will receive around 600 W of power from the M11 bending magnet. The synchrotron radiation from the bending magnet has a small vertical opening of 0.2 mrad. Each type of dipole will contribute differently to the total power budget and has a different power density; Table 9.1 shows a summary of the angular and linear power densities, as well as the total power from each type of dipole of the achromats.

9.3 The pumping speed needed

The simulations for estimating the pumping speed needed for vacuum systems or the pressure profile for systems having NEG coating are not straightforward, mainly because the sticking coefficients of the various gases could vary depending on the NEG saturation.

The following paragraph gives a rough estimation of the pumping speed needed; more detailed calculations (considering the different gases, beam doses, etc.) must be performed.

Table 9.1: Power densities from the dipole magnets on the vacuum chamber walls

Element	Field	Angular power density	Linear power density on the chamber wall	Power density on the chamber wall	Total power per achromat
	(T)	(W/mrad)	(W/mm)	(W/mm ²)	(kW)
M11	0.47	12.36	0.73	5.68	1.60
M12	0.46	12.20	0.69	5.38	1.55
MQ1	0.69	18.16	1.50	13.60	1.65
MQ2	0.86	22.70	2.05	20.62	1.03
Total power per achromat (kW) =					5.83
Overall ring power (kW) =					93.27

The main source of gas inside the vacuum chambers during operation is photon-stimulated desorption (PSD); the outgassing due to PSD is estimated to be 3.3×10^{-5} mbar l/s. In order to achieve the target pressure of 10^{-9} mbar (which would allow a good beam lifetime, in excess of 10 hours), the total pumping speed should be at least 33 000 l/s for mass 28. The main source of pumping down will be from the NEG coating. CERN has reported that the pumping speed from activated NEG coating for hydrogen is around 0.5 l/(s cm²), and that for CO or N₂ is around 5 l/(s cm²) [9.2]. Assuming that the NEG coating is almost saturated all along the ring circumference and that its pumping capacity for mass 28 is reduced to 0.2 l/(s cm²), we would have a pumping speed of around 43 000 l/s from the NEG coating. In addition, each achromat will have four small ion pumps, which are needed for pumping noble gases that are not pumped by the NEG coating and are also needed in areas of high outgassing to limit the NEG saturation in those areas. The total pumping speed from all the ion pumps in the ring will be around 3000 l/s. The overall estimated pumping speed installed will be around 47 000 l/s, which is higher than what is needed; however, this would allow a better pressure to be achieved sooner. A summary of the calculations for the total pumping speed is shown in Table 9.2.

Table 9.2: Estimation of the total pumping speed needed for the storage ring

Parameter	Value	Unit
Target dynamic pressure	1.00E-09	mbar
PSD yield after conditioning	1.00E-06	Molecules/ph
Total photon flux	8.08E+20	photons/s
PSD outgassing	3.26E-05	mbar.l/s
Total pumping speed needed	32643.20	l/s
Pumping speed for nitrogen from NEG coating (assuming semi-saturated coating): 0.2 l/(s cm ²)	43730.97	l/s
Pumping speed for nitrogen from ion pumps (effective pumping speed around 50 l/s, four ion pumps per achromat)	3200	l/s
Total pumping speed installed	46930.97	l/s

A fully NEG-coated vacuum system will provide faster conditioning than that of traditional vacuum systems, which are based on the use of lumped pumps. Figure 9.10 shows the MAX IV normalized average pressure rise versus the accumulated beam dose [9.3]. The conditioning slope is 0.82, a value slightly higher than that reported during the commissioning of other facilities [9.4, 9.5].

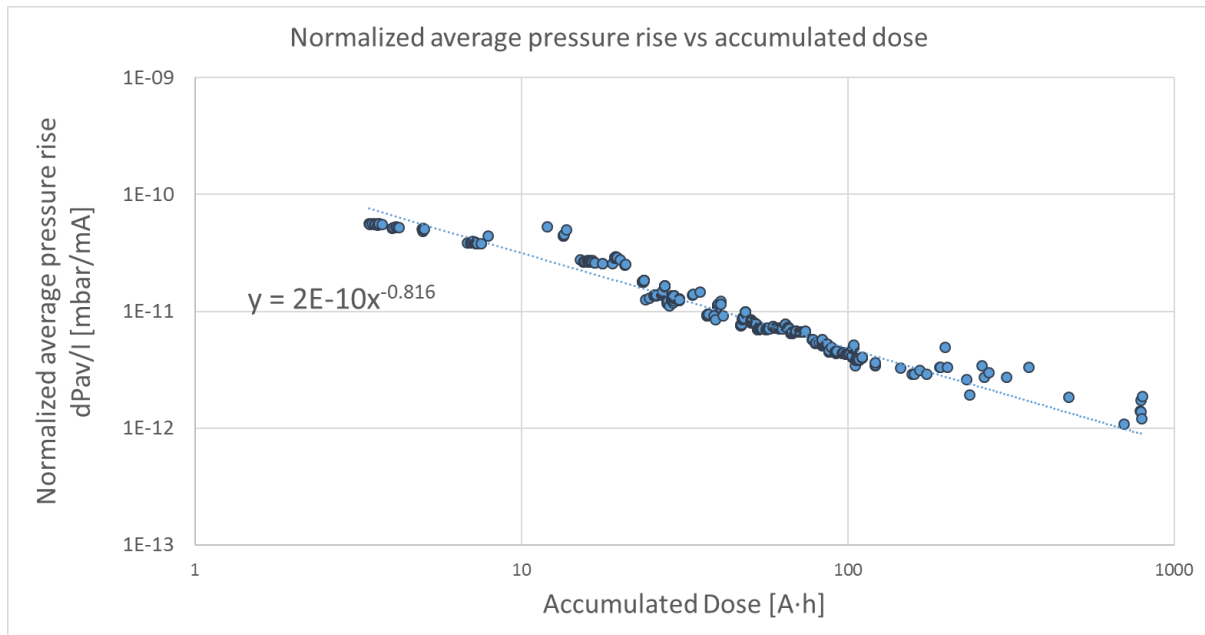


Fig. 9.12: The normalized average pressure rise (mbar/mA) versus the accumulated beam dose (A h) for the MAX IV 3 GeV storage ring.

With a value of 10^{-12} mbar/mA, according to Fig. 9.12 a pressure of 1.9 nTorr could be reached with a current of 250 mA. This meets the requirements of the SEE-LS.

The general layout of the vacuum system for accelerators is described in Ref. [9.6].

References

- [9.1] E. Al-Dmour *et al.*, *J. Synchrotron Rad.* **21** (2014) 878, <https://doi.org/10.1107/S1600577514010480>
- [9.2] P. Chiggiato, Beyond Ti-Zr-V: present development on thin film coating for beam pipes, CERN-TS-NOTE-2008-006 (CERN, Geneva, 2008), <https://cds.cern.ch/record/1119298>
- [9.3] P.F. Tavares *et al.*, *J. Synchrotron Rad.* **25** (2018) 1291, <https://doi.org/10.1107/S1600577518008111>
- [9.4] M.P. Cox *et al.*, *J Phys. Conf. Ser.* **100** (2008) 092011, <https://doi.org/10.1088/1742-6596/100/9/092011>
- [9.5] C. Herbeaux *et al.*, Vacuum conditioning of the Soleil storage ring with extensive use of NEG coating, Proc. EPAC2008, Genoa, Italy, 23–27 June 2008, p. 3696. <https://inspirehep.net/record/795489>
- [9.6] CAS-CERN Accelerator School: Vacuum for Particle Accelerators, Glumslöv, Sweden, 6–16 June 2017, <https://cas.web.cern.ch/schools/glumslöv-2017>

10 Radio-frequency (RF) system

A. Andersson, D. Einfeld, F. Perez, and A. Salom

10.1 Introduction

In an electron storage ring the electrons lose energy from emitting synchrotron radiation when they are deflected in a magnetic field of the bending magnet or of the insertion devices. One of the functions of the RF system is to restore this lost energy. Therefore, an RF system with enough power to achieve this purpose must be provided. In addition, the RF system plays the role of providing stability to the beam and a large energy acceptance in order to achieve a long lifetime. As the length of the electron bunch depends on the characteristics of the RF voltage, one finds that the pulse length and the repetition rate of the emitted synchrotron radiation also depend on the RF frequency.

The transfer of power to the electrons is done by a high-frequency electromagnetic field inside the cavities. At the SEE-LS, powers between 200 and 400 kW have to be transferred to the cavities. The high-frequency electromagnetic field is generated in the amplifiers and transferred to the cavities through the waveguide system. A picture of the RF system of the synchrotron light source ANKA, where one klystron feeds two cavities, is shown in Fig. 10.1. A schematic overview of the whole RF system is given in Fig. 10.2.

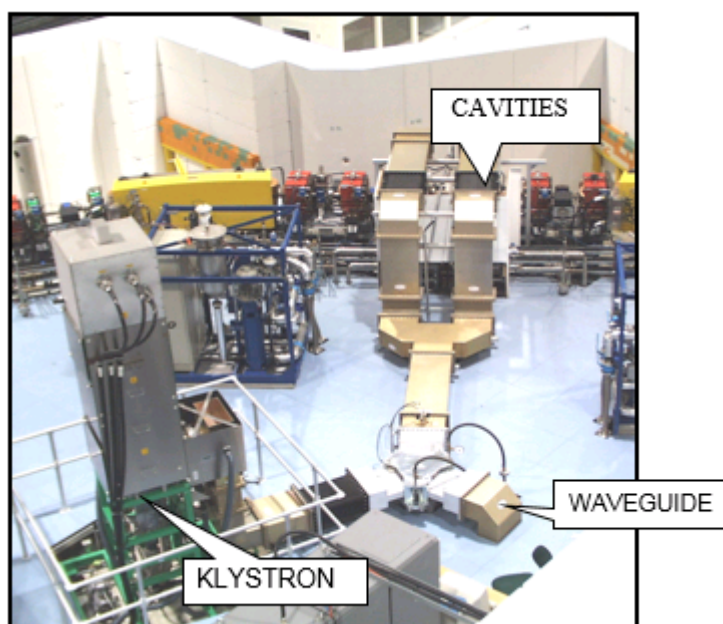


Fig. 10.1: RF system of the ANKA storage ring. A 250 kW microwave power is produced in the klystron. The power passes a circulator, which protects the klystron from the reflected power, is split into two arms by a Magic T, and is then transferred into two cavities.

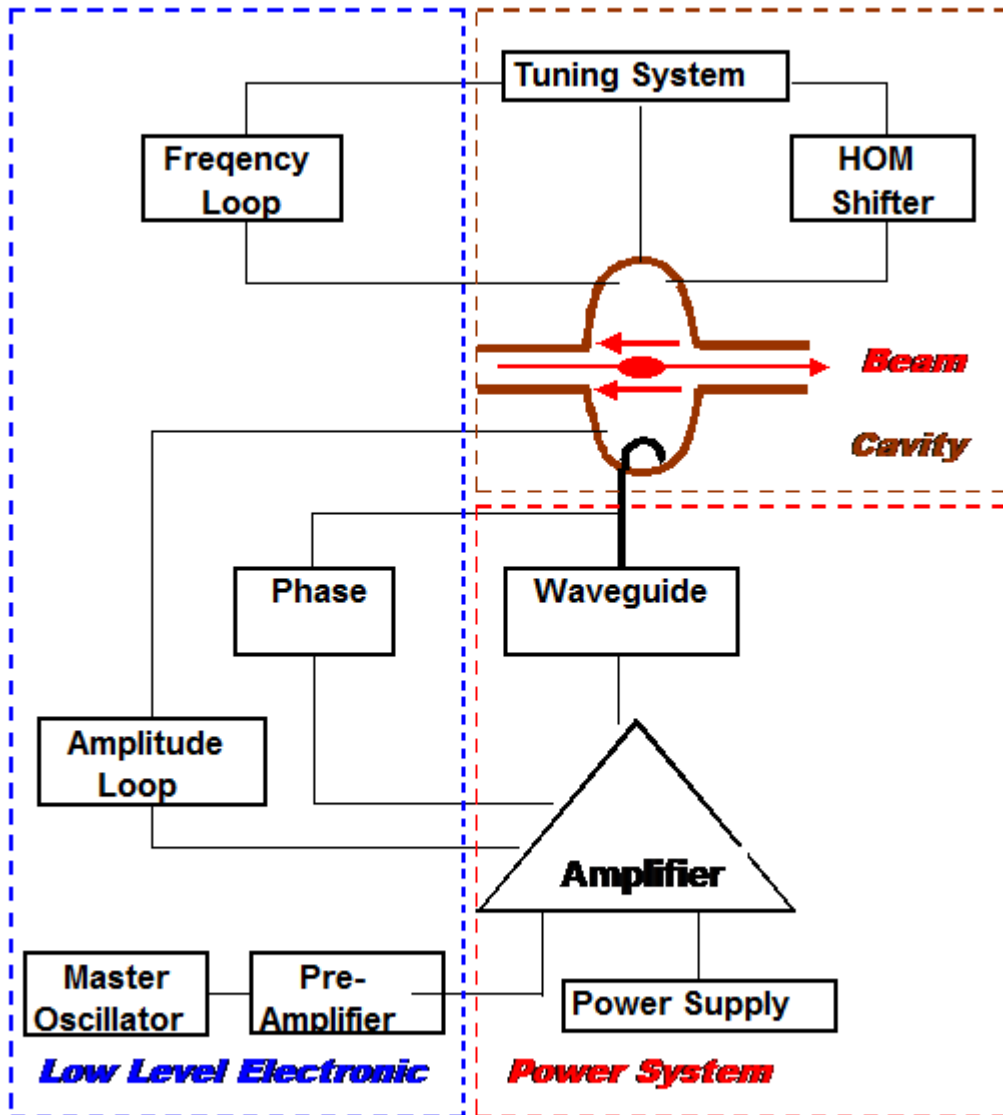


Fig. 10.2: Schematic layout of the RF system for a synchrotron light source; the main groups in the system are the cavities, the power system, and the low-level electronics.

10.2 Components of the RF system

10.2.1 Cavities

A cavity is a resonant structure, a metallic empty volume. Inside it, an electromagnetic field resonates at certain frequencies that are determined by the geometry of the structure. Cavities have a cylindrical geometry, are made of high-conductivity copper, and have some holes to allow the electrons to enter and exit the cavities on their way around the accelerator, the RF power to be fed into the cavity, and pick-up coils for diagnostics and a vacuum pump to be installed.

One of the cavities of MAX IV is shown in Fig. 10.3.

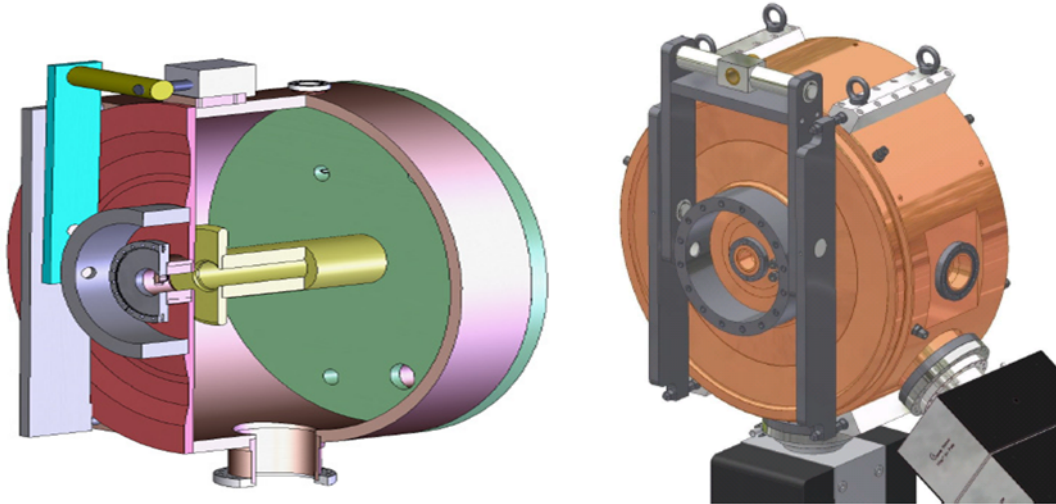


Fig. 10.3: A 3D view of the 100 MHz MAX IV cavity; the length of the cavity is 376 mm and the diameter is 920 mm.

The fundamental mode of the cavity has a frequency of 99.931 MHz, to reach a wavelength of exactly 3.0 metres. The characteristics of the cavity are given by the shunt impedance R_s and the quality factor Q (see Table 10.1). The acceleration of the beam occurs with the fundamental mode.

Furthermore, the cavities have higher-order modes that also react with the beam and lead to so-called multi-bunch instabilities. A well-established method for dealing with multi-bunch instabilities is fine-tuning of the high-order modes of the cavities by accurate mechanical movement of the endplate.

Table 10.1: Fundamental mode parameters

Parameter	Unit	Value
Frequency	MHz	99931
Quality factor, Q		19200
Shunt impedance, R_s	$M\Omega$	0.8
Max. cavity voltage	kV	300
Max. cavity power	kW	56
Max. coupler power	kW	112

10.2.2 Amplifier

A klystron is a high-power RF amplifier with an amplification factor of about 10 000 (a gain of 40 dB). It is driven by a 25 W solid state amplifier that in turn has to be driven by a signal generator, which creates the 500 MHz primary signal.

10.2.3 Waveguide system

The waveguide system connects the amplifier to the cavities and is the path for the RF power. The power out of the amplifier passes a circulator, which is a three-port waveguide system that isolates the amplifier from the cavities. Any reflected power from the cavities is dumped into a water load installed in one of the ports. The power is then split into two by a Magic T (evenly in amplitude and in phase) and transferred to the two cavities.

Bi-directional couplers are used to monitor forward and reflected power in the line. There are four: one after the amplifier, one after the circulator, and two before the two cavities. A phase shifter in one arm going to one cavity adjusts the phase between the two cavities.

Two water loads, one in the third arm of the circulator and the other in the fourth arm of the Magic T, dissipate any reflected power. Transitions, bends, and straight sections complete the line. All the components will be able to cope with the full power, 250 kW.

10.2.4 Low-level electronics

Each of the RF units has to be controlled by a complete low-level system with which to adjust the frequency, amplitude, and phase of the RF signal in the cavity. This is achieved with the so-called tuning, amplitude, and phase loops (see Fig. 10.2).

With the frequency loop, the cavity is maintained in resonance with respect to the master oscillator frequency. In practice it is set slightly out of resonance to obtain greater stability. An amplitude loop for each RF plant is used to maintain the voltage in the cavities at the required value. The phase loop is used to keep the phase between the plants constant.

10.2.5 Principle of operation

The cavity is connected over the waveguide system with the RF amplifier, which feeds the high-frequency power P_{gen} from the amplifier into the cavity (see Fig. 10.4). This RF power builds up an electric field, which accelerates the beam. The electron bunch within the cavity has a fixed relationship to the electric field, given by the synchronous phase $\Phi(0)$. At the phase $\Phi(0)$ the electron is on average getting back the energy losses according to the emission of synchrotron light.

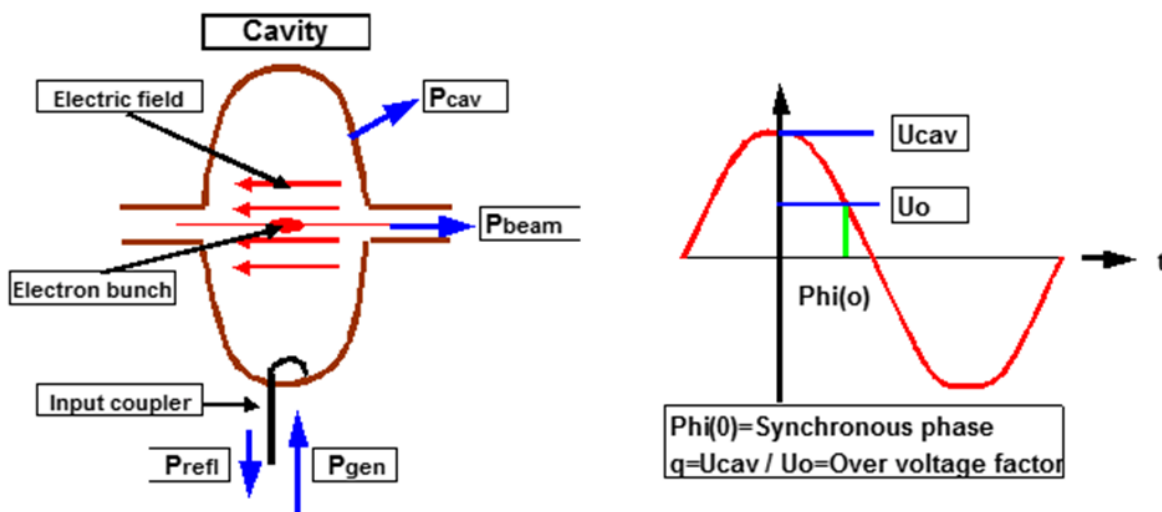


Fig. 10.4: Schematic illustrations of the expressions used in the RF system

The phase $\Phi(0)$ has to be at the falling slope of the electromagnetic field, as shown in Fig. 10.4. The circumference of the accelerator must be an integer multiple of the wavelength of the RF system. For the SEE-LS the intention is to use a 100 MHz system with a wavelength of exactly 3.0 m. The integer is called the harmonic number.

According to the conservation of power, the power of the generator is the sum of the beam, cavity, and reflected power:

$$P_{\text{gen}} = P_{\text{cav}} + P_{\text{beam}} + P_{\text{refl}} , \quad (10.1)$$

$$P_{\text{cav}} = U_{\text{cav}}^2 / (2R_S) , \quad (10.2)$$

$$P_{\text{beam}} = I \cdot U_0 . \quad (10.3)$$

RADIO-FREQUENCY (RF) SYSTEM

Here R_s is the shunt impedance of the cavity, I is the current of the stored electrons in the accelerator, and U_o represents the energy losses to synchrotron radiation by travelling through the bending magnets, wigglers, and undulators or other insertion devices. These losses are given in Eqs. (10.4) and (10.5):

$$U_{0,\text{bend}} = 88.5 \text{ keV} \cdot (E[\text{GeV}])^4 / \rho[\text{m}] , \quad (10.4)$$

$$U_{0,\text{wigg}} = 0.633 \text{ keV} \cdot L[\text{m}] \cdot (E[\text{GeV}])^2 \cdot (B_m[\text{T}])^2 . \quad (10.5)$$

where:

E is the energy of the electrons;

ρ is the deflection radius in the bending magnets;

B_m is the peak field;

L is the length of insertion device.

The reflected power is zero if the coupling factor of the input coupler has a value of

$$\beta_{\text{opt}} = 1 + (P_{\text{beam}} / P_{\text{cav}}) . \quad (10.6)$$

Due to the fact that more than one cavity will be installed in such a machine, it is necessary to adjust the phase of the microwave inside each cavity so that all of them act coherently to accelerate the beam. The phase between the cavities is determined by the path length of the electron orbit between them, taking into account the fact that the velocity of the electrons is the velocity of light.

10.3 RF system parameters

The parameters of the stored beam—such as bunch length, synchrotron frequency, and energy acceptance—are functions of the main parameters of the storage ring, which are summarized in Table 10.2.

The parameters of the RF system are determined by the power loss according to the synchrotron radiation and the required lifetime of the beam. With an average pressure of 2 nTorr and an energy acceptance of 4%, the so-called gas lifetime and Touschek lifetime are within the same order of magnitude, 6–8 hours. The Touschek lifetime is affected by the energy acceptance of the machine, which is determined by the energy acceptance ε_{HF} and the bunch length σ_1 of the stored electron beam. For example, by increasing the energy acceptance from 3% to 6%, the lifetime would increase by a factor of 2; this means that the overvoltage factor must be as high as possible. Both factors, as well as the synchrotron frequency and the longitudinal tune value, are determined by the overvoltage factor q . The dependence relations are given in Eqs. (10.7)–(10.13) and in Figs. 10.5 and 10.6:

$$U_o = V_{\text{cav}} \sin(\Phi_s) = \frac{1}{q} V_{\text{cav}} , \quad (10.7)$$

$$\varepsilon_{\text{rf}} = \sqrt{k_1 \cdot F(q)} , \quad (10.8)$$

$$k_1 = \frac{U_o}{\pi \alpha h E_o} , \quad (10.9)$$

$$F(q) = 2 \left[\sqrt{q^2 - 1} - \arccos(1/q) \right] , \quad (10.10)$$

$$k_2 = \frac{\alpha h}{\sqrt{2}} \cdot \sqrt{k_1} , \quad (10.11)$$

$$v_s = k_2 \sqrt{q \cos(\Phi_s)} , \quad (10.12)$$

$$\sigma_l = \frac{\alpha \sigma_E C}{2\pi} \cdot \frac{1}{v_s} . \quad (10.13)$$

where:

U_0 is the energy loss per turn;

Φ_s is the synchronous phase;

q is the overvoltage factor;

α is the momentum compaction factor;

h is the harmonic number;

σ_E is the relative energy spread of the beam;

v_s is the longitudinal tune value;

C is the circumference of the machine.

Table 10.2: RF main parameters for the SEE-SL (r.m.s. is the root mean square value)

Parameter	Symbol	Value	Unit
Energy	E	2.50	GeV
Current	I_0	400.00	mA
Circumference	C	348.00	m
Momentum compaction	α	2.880E-04	
Energy loss per turn	U_0	0.233	MeV
RF frequency	F_{rf}	100.00	MHz
RF harmonic number	h	116	
Peak effective RF voltage	V_{rf}	1.40	MV
Overvoltage factor	q	6.00	
Bucket size	ϵ_{max}/E	0.090	
Synchrotron phase angle	Φ_s	9.60	degree
Synchrotron frequency	Ω_s	9.28	kHz
Natural r.m.s. energy spread	σ_E/E	7.14E-04	
Bunch current in multi-bunch mode	I_b	3.45	mA
R.m.s. bunch length at zero current	σ_{s0}	6.65	mm
R.m.s. bunch length at zero current	σ_{s0}	22.17	psec
Peak current in multi-bunch mode		72.04	A
Vacuum chamber half-height	b	8.00	mm
Vacuum chamber half-width	h	11.00	mm
Vacuum chamber cut-off frequency	$\omega c = c/b$	37.47	GHz

10.4 RF system for the SEE-LS

The new generation of synchrotron light sources, of which MAX IV was the first to be realized, is based on a new type of lattice, the so-called multi-bend achromats, where the dispersion function is not allowed to grow to large values. From this principle it follows that the light sources can limit the

horizontal emittance to values lower than a tenth of the conventional ones. However, it follows also that the linear lattice momentum acceptance (determined by the chamber aperture and dispersion function) can be two to three times larger than before and reach values above 5%. Thus, the RF momentum acceptance, or bucket height, should be adapted to this new situation. An RF system of low frequency has an advantage in this respect. Even for a relatively low overvoltage, the ratio of total cavity voltage over energy loss per turn, one can easily reach a bucket height exceeding 5%. An overvoltage of less than 2 will be sufficient for this, and the RF system costs can be kept relatively low. A low-frequency RF system also brings the advantage of a beam spectrum that is limited to relatively low frequencies, because of the longer bunches. This property both limits the RF heating of vacuum chamber components and makes it easier to combat several kinds of high charge instability, in particular coupled-bunch instabilities driven by higher-order modes in the cavities and transverse coupled-bunch instabilities driven by the resistive walls of the compact vacuum chambers. A third advantage is that one may look at the possible bunch lengthening with higher harmonic cavities (HHCs). For example, a bunch lengthening of a factor of 5 is well within reach for a 100 MHz system, whereas for a 500 MHz system this would require so-called overstretching of the bunches. The bunch lengthening by the HHC is crucial for keeping the dilution of the transverse emittances from intra-beam scattering to reasonable levels.

10.5 RF system configuration

The local lattice momentum acceptance for the proposed ring lattice will end at around 6%, even in parts where the dispersion is at a maximum. It is therefore reasonable to aim for 6% RF momentum acceptance. The radiation losses per turn for the bare lattice are 233 keV/turn, and a reasonable assumption is that they could increase to 800 keV/turn for a ring with 15 insertion devices.

For a 100 MHz system with a total RF voltage of 1500 kV, i.e. an overvoltage of 1.875, the bucket height would end at 6%. By choosing the cavity solutions from MAX IV [10.1], one would end up with an RF configuration as in Table 10.3. There we have used the actual measured Q -values for the MAX IV cavities, which deviate slightly from the (conservatively) estimated ones in Ref. [10.1]. A plausible configuration at the commissioning stage is also presented. The same bucket height is reached but at considerably lower RF voltage. A lower RF voltage per cavity is recommended during commissioning, while the vacuum conditions are worse and the field intensity at which sparking becomes an issue (the Kilpatrick limit) is lower.

It is interesting to see that for the final phase, five RF cavities would do the job, and a transmitter size of 100 kW for each cavity would suffice. This would give a good safety margin compared to the MAX IV case, especially regarding the maximum power rating for power couplers and for circulators. The RF configurations for phase 1 and phase 2 are presented in Table 10.3. Phase 1 is for the commissioning and first operation of the system, with four insertion devices and an overall energy loss of 80 keV; phase 2 is the final phase, with the installation of 12 insertion devices and an overall loss of 240 keV.

The flange-to-flange distance for the main cavities is 0.50 m, while it is slightly longer for the Landau cavities. In the present lattice there are two short straight sections of 0.77 m placed symmetrically in the achromat. The second of these short straight sections could possibly house one cavity (the first straight section cannot be used for cavities since the ID light would have to pass here). In this way, no long straight section needs to be sacrificed for RF, but all 15 can be used for IDs. An example of such an installation is shown in Fig. 10.6. The main and Landau cavity (LC) inner profiles are shown in Figs. 10.5 and 10.7, respectively.

Table 10.3: RF configuration for the 2.5 GeV ring

Parameter	Phase 1	Phase 2
Energy loss	310 keV	500 keV
Current	200 mA	400 mA
Total SR power	62 kW	200 kW

Main RF configuration for 6% bucket height		
Total RF voltage	0.9 MV	1.5 MV
Number of cavities	3	5
Cavity voltage	300 kV	300 kV
Cavity $R_{sh}(= V^2/(2P))$	0.8 M Ω	0.8 M Ω
Cu losses per cavity	56 kW	56 kW
Optim. coupl. (beta)	1.3	1.7
No. of RF stations	3	5
Minimum RF station power (with LC losses)	77 kW	96 kW
Landau cavity configuration		
Total LC voltage	257 kV	412 kV
Number of LCs	2	2
LC $R_{sh}(= V^2/P)$	5.3 M Ω	5.3 M Ω
Total LC Cu losses	6.2 kW	16 kW

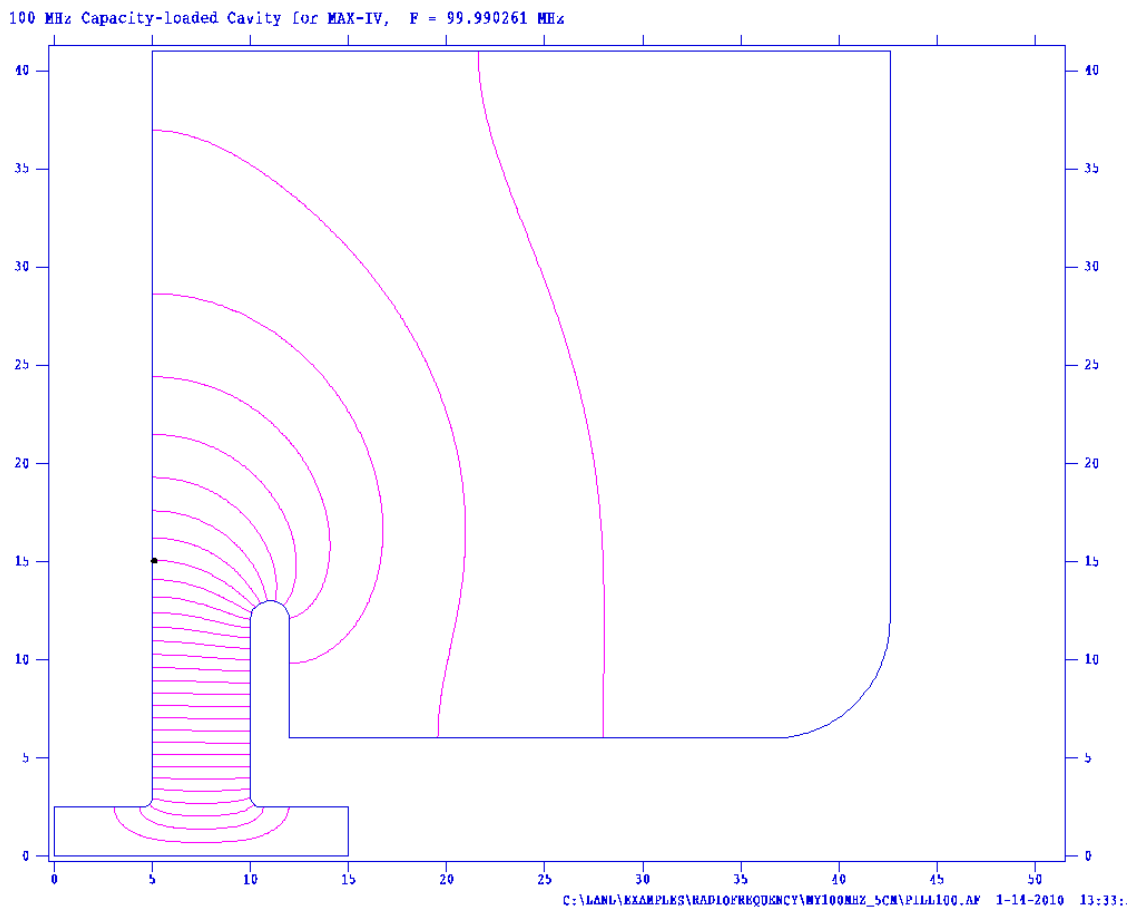


Fig. 10.5: Main cavity inner profile, where the horizontal axis is the beam axis and the vertical axis represents any radial direction; units are centimetres. The length of the cavity is 376 mm and the diameter is 920 mm.

RADIO-FREQUENCY (RF) SYSTEM



Fig. 10.6: A main cavity and the Landau cavity as installed in the MAX IV 3 GeV ring

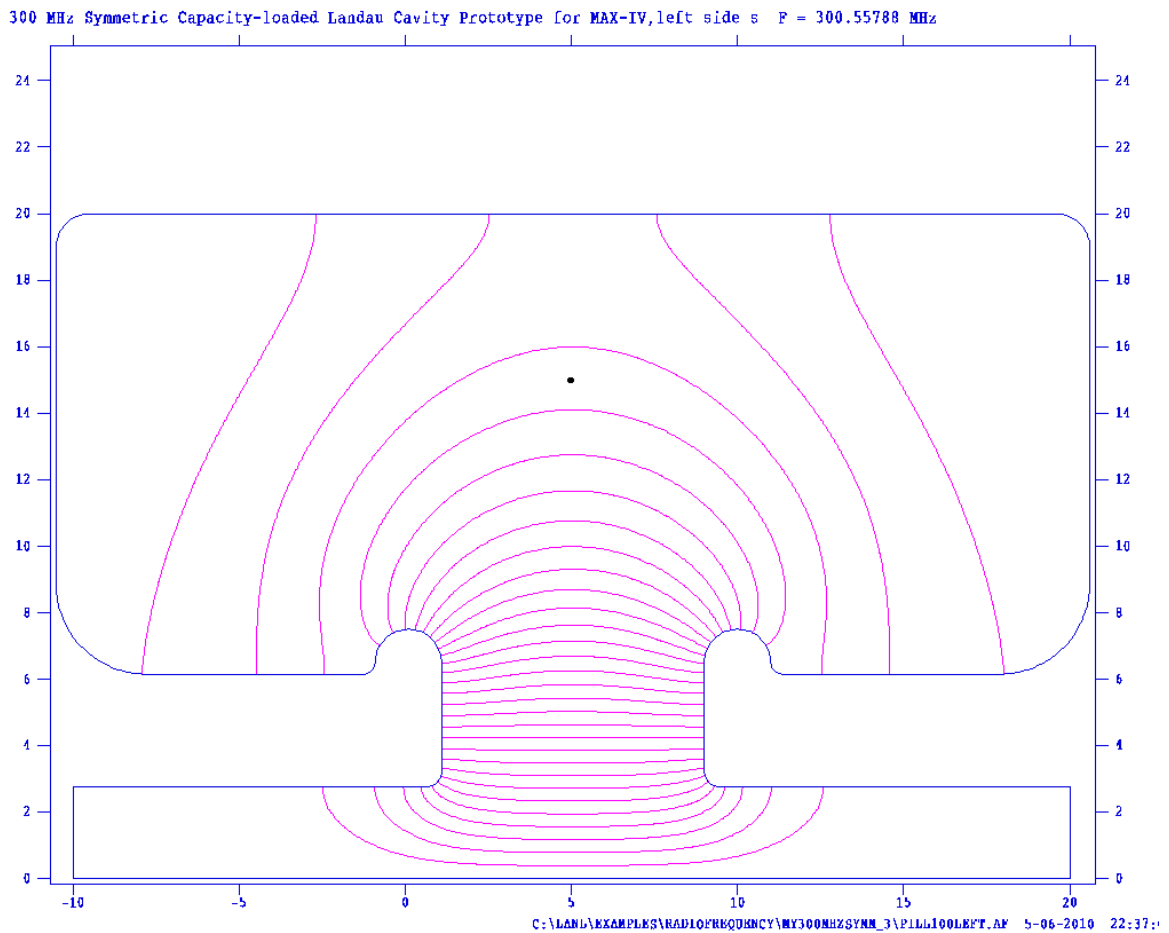


Fig. 10.7: Landau cavity inner profile, where the horizontal axis is the beam axis and the vertical axis represents any radial direction; units are centimetres.

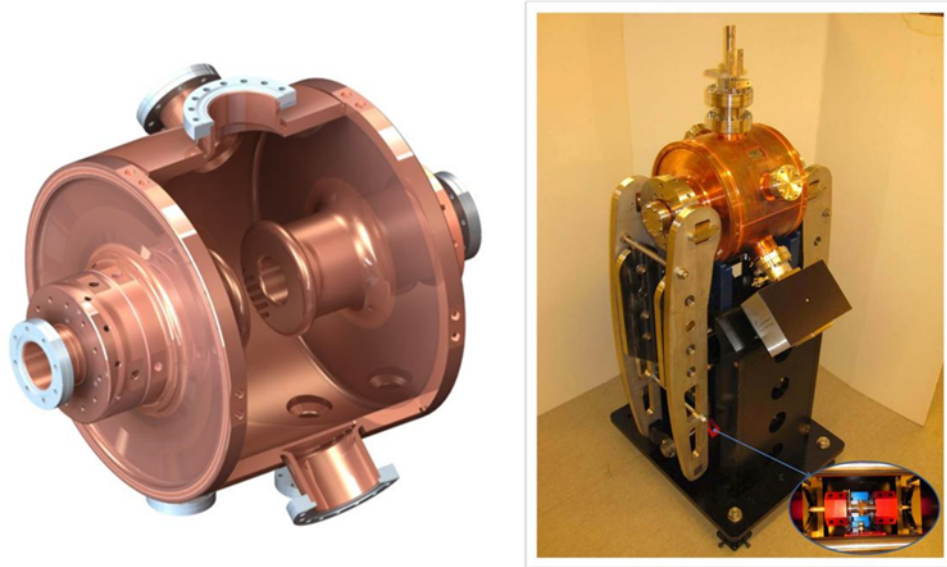


Fig. 10.8: A 3D view of the Landau cavity (left-hand side) and the support of the Landau cavity (right-hand side) as used for the installation in the ring.

Table 10.4: Beam RF parameters for 2.5 GeV ring (r.m.s. is the root mean square value)

Parameter	Phase 1	Phase 2
Synchrotron frequency without LC	1.107 kHz	1.416 kHz
Synchrotron phase without LC	163°	148°
Main cavity detuning ($Q = 19700$)	-6 kHz	-9.5 kHz
LC detuning ($Q = 20800$)	56 kHz	71 kHz
Bunch r.m.s. length without LC (at $\sigma_E = 0.07143\%$)	9 mm	7 mm
Bunch r.m.s. length without LC (at $\sigma_E = 0.07143\%$)	50 mm	42 mm
Peak current	3.9 A	11.5 A

From Table 10.4 we can see that with a fully ID-equipped ring, at the final phase bunch lengthening by a factor of six can be expected, which would bring the peak bunch current down from 69 A to 11.5 A. In reality the bunch shape will deviate from the quartic flat-potential shape, and a slight further elongation, of up to 44 mm, can be achieved by detuning one Landau cavity away from $3 \times \text{RF}$ while tuning the other towards the $3 \times \text{RF}$ line. However, the total power dissipated in the Landau cavities will increase, so the benefit will probably be quite limited. This kind of choice is the same as has been argued in Ref. [10.2], where it is shown that installing a higher Landau cavity shunt impedance than necessary for the exact flat-potential case may be beneficial in combating the Robinson instability. Figure 10.9 shows the bunch shape at the commissioning phase and Fig. 10.10 the shape at the final phase. The lower curve in each figure should be disregarded. Figure 10.11 shows the ideal quartic shape that results from a perfect matching of the product current \times total Landau cavity shunt impedance.

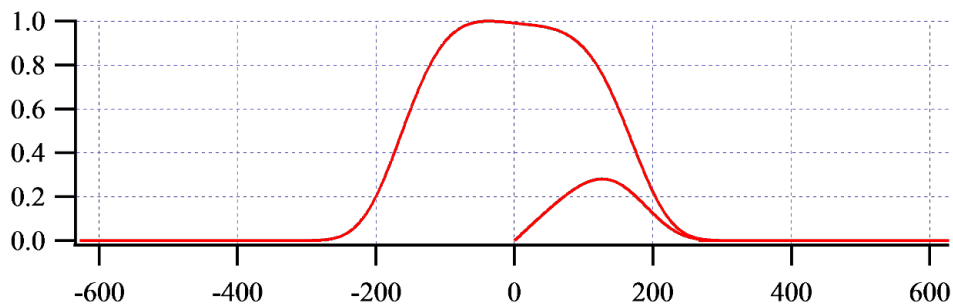


Fig. 10.9: Bunch shape at the anticipated ‘commissioning phase’; horizontal axis is in mrad RF phase

RADIO-FREQUENCY (RF) SYSTEM

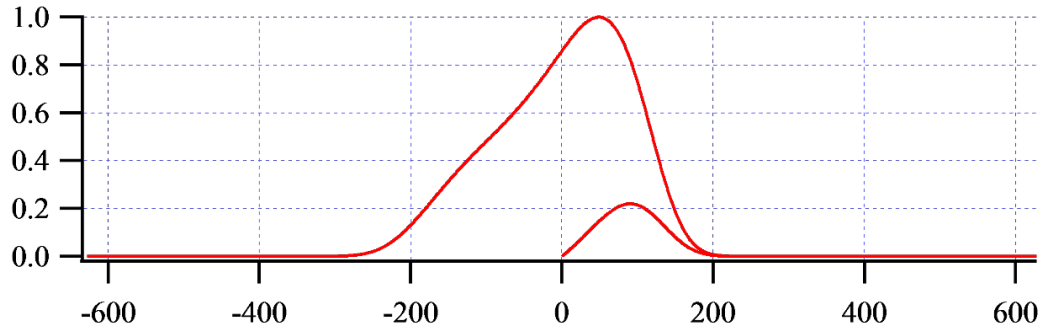


Fig. 10.10: Bunch shape at the anticipated 'final phase'; horizontal axis is in mrad RF phase

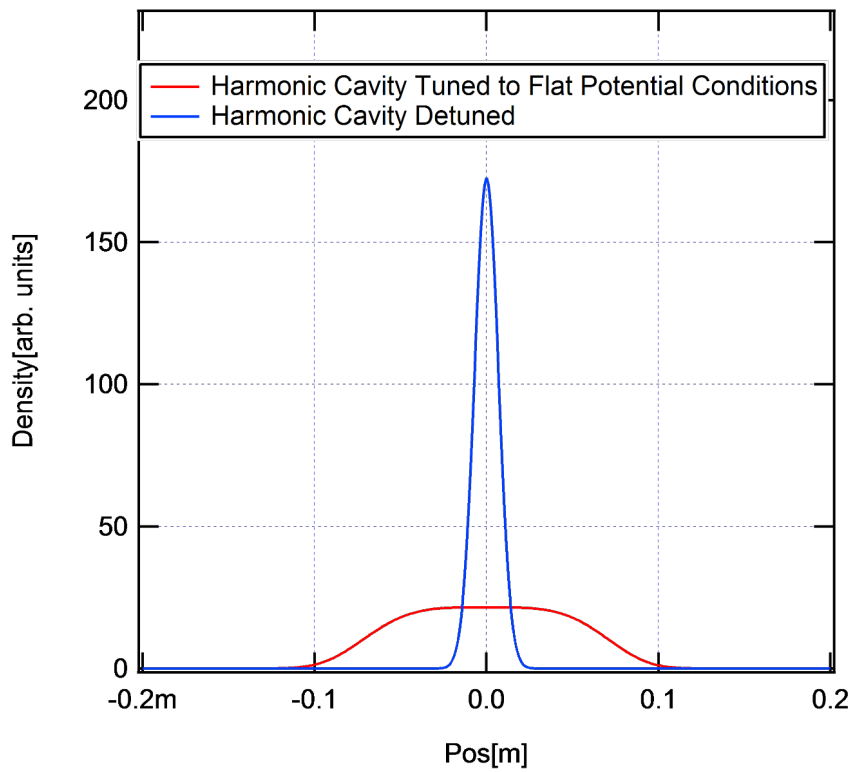


Fig. 10.11: Bunch shape without harmonic cavities (blue) and with harmonic cavities tuned to the 'flat-potential' for the fully ID-equipped ring parameters (red).

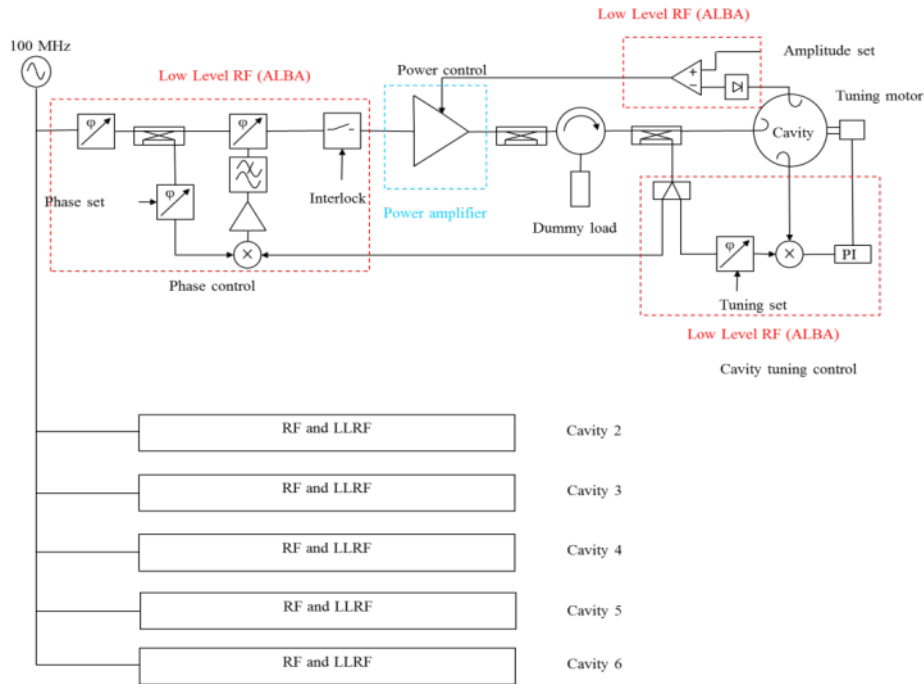


Fig. 10.12: Block diagram of the 2.5 GeV RF system

10.6 Digital low-level RF system

10.6.1 Introduction

The proposed digital low-level RF (LLRF) system should be capable of controlling the amplitude and phase of the RF voltage of the cavities at 100 MHz. It is based on the digital LLRF system of ALBA [10.3, 10.4], implemented with the RF frequency of MAX IV [10.5] and using commercial uTCA digital boards [10.6, 10.7].

10.6.2 Hardware components

The LLRF hardware will be composed of two main subsystems:

- uTCA chassis + Linux PC + FPGA motherboard;
- front ends.

10.6.2.1 uTCA subsystem

The uTCA subsystem will consist of a uTCA chassis with a minimum of four slots, a uTCA Linux PC, and two uTCA FPGA motherboards plus four FMC boards (see Fig. 10.13).

The main digital processor of this LLRF system will be a Virtex-6 FPGA embedded in a uTCA FPGA motherboard, Perseus, provided by Nutaq. Two FMC boards will be plugged into the first motherboard: one with fast ADCs (MI125) and the other with fast DACs (MO1000). A second uTCA FPGA motherboard and FMC board with fast ADCs (MI125) will be added for extra diagnostics and fast interlock ability. The capabilities of this subsystem are:

- 32 digital inputs;
- 32 digital outputs;
- $2 \times$ FMC MI125 with 16 ADCs—14 bits, 125 MHz, AC coupled, 50Ω , 10 dBm maximum input;
- FMC MO1000 with 8 DACs—16 bits, 1 GHz, AC coupled, 50Ω , 10 dBm maximum output;

RADIO-FREQUENCY (RF) SYSTEM

- 2×4 slow ADCs—12 bits, 250 kHz;
- external and internal clocks;
- 2×1 GB RAM for post-mortem analysis.

10.6.2.2 Front end

The front end will be used to distribute the RF signals to the digital boards of the LLRF, and it will up-convert the control signals provided by the digital boards from intermediate frequency (IF) to RF. It will also contain pin diode switches to cut the LLRF drives in case an interlock is detected.

In addition, the front end would provide access to the BNC test point to connect the RF signals being analysed to scopes for diagnostic purposes.

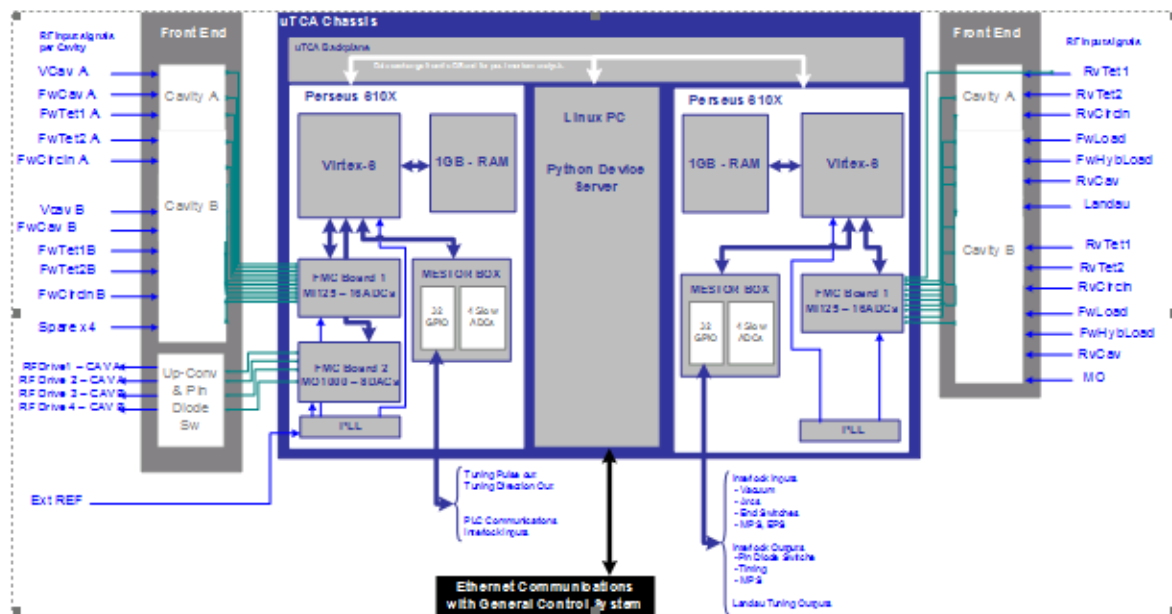


Fig. 10.13: LLRF hardware scheme and signal distribution [10.1]

Figure 10.13 shows the distribution of the signals between the front ends and the digital subsystem, together with the main components of the uTCA system.

A digital patch panel will also be included to adapt the level/logic of digital signals between the LLRF and other systems of the RF plants (motor controllers, programmable logic controllers, machine-protection-system (MPS), etc.).

10.6.3 LLRF firmware description

The main digital signal processing implemented in the FPGA would have the following functionalities:

- monitoring status of RF signals
- controlling amplitude and phase via IQ loops of the cavity field;
- cavity tuning;
- automatic start-up of the system;
- automatic conditioning of the cavity;
- recording of main digital processing signals for post-mortem analysis;
- fast interlock handling.

Figure 10.14 shows a schematic of the main digital signal processing to be applied to the RF signals of each plant.

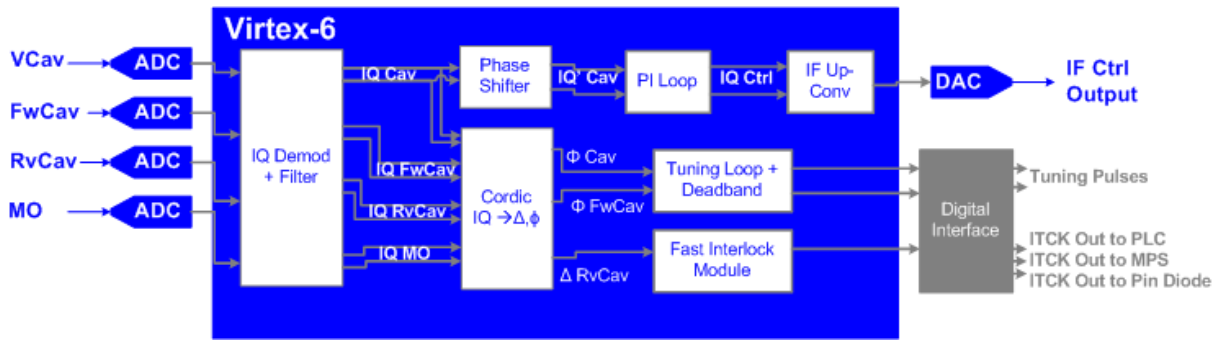


Fig. 10.14: Firmware scheme per RF plant

10.6.3.1 IQ digital demodulation

The RF input signals of the LLRF will be digitalized and IQ demodulated, acquiring 0.75 samples per RF period, as shown in Fig. 10.15. A software counter controlled by the phase of the master oscillator will be used to calculate the relative phase of each signal respect to the MO.

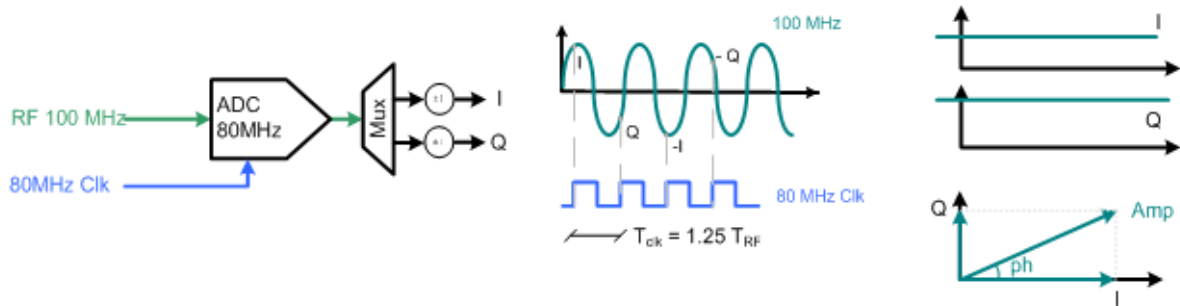


Fig. 10.15: Digital IQ demodulation

10.6.3.2 Control loop specifications

The specifications for the control loops are summarized in Table 10.5.

Table 10.5: Control loop specifications

Loop	Resolution (r.m.s.)	Bandwidth	Dynamic range
Amplitude loop	< 0.5%	≥ 10 kHz	30 dB
Phase loop	< 0.5°	≥ 10 kHz	360°
Tuning	< $\pm 1^\circ$	—	< $\pm 75^\circ$

10.6.3.3 Amplitude and phase loops

When the IQ loops are enabled, the amplitude and phase of the cavity voltage are regulated by controlling the I and Q components of that signal through standard PI loops, as shown in Fig. 10.16. The reference point and parameters of the loop can be adjusted through the graphical user interface (GUI) to make the response of the loop faster or slower (via the constant of proportionality K_p and the integral constant K_i).

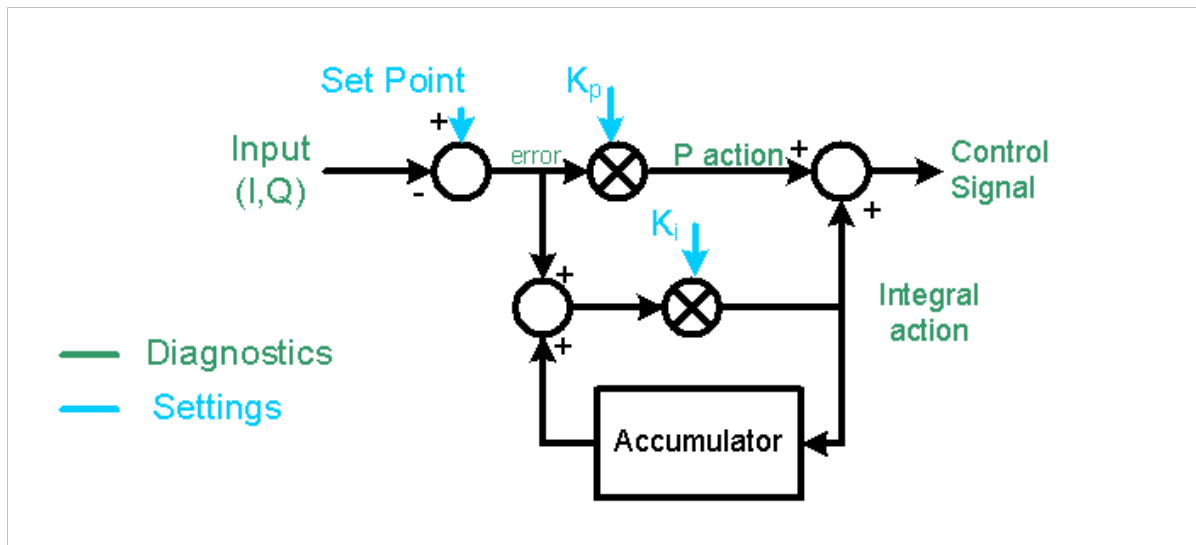


Fig. 10.16: PI loop

When the polar loop mode is enabled, the user can directly control the amplitude independently of the phase. It is also possible to control either the amplitude of one signal (e.g. the cavity voltage) or the phase of another signal (e.g. the forward power of the cavity). This would allow the user to set different bandwidths for the loops.

The amplitude loop bandwidth can work between sub-Hz to a few kHz, while the phase loop can work with a minimum bandwidth of 1–50 kHz.

10.6.3.4 Tuning loop

The tuning loop of the cavities measures the phase difference between the cavity voltage and the forward cavity voltage. If this phase difference is out by a certain margin, which is adjustable by the user, the board sends a train of pulses to move a stepper motor in order to change the shape of the cavity and adjust its resonance frequency.

The cardiac algorithm will be used to translate IQ coordinates to polar coordinates and to compute the tuning diphas. The digital interface will adapt the FPGA digital outputs to the levels required by the motor controller of the cavities plunger. An external parameter will also allow the user to select the frequency of the pulses (from a few Hz to kHz).

10.6.4 LLRF extra utilities

A series of extra utilities will be implemented in the digital LLRF to improve the operability of the RF system. Some examples are listed.

- **Ramping:** A special operation mode could be implemented to ramp the RF power, whereby the voltage of the cavity would be increased following a ramp after a trigger is received. The parameters will be adjustable by the user.
- **Fast interlock:** The reverse power of the cavity will be monitored by the LLRF, and in case its amplitude exceeds a certain value defined by the user, a digital output will be sent from the FPGA board to the digital board interface. The digital interface will then pass this signal on to a fan out so the fast interlock can be transferred to the relevant subsystems to stop the RF plant redundantly.
- **Automatic start-up:** The automatic start-up procedure would allow the user to set a plant in operation after an interlock or a shutdown by following a series of steps, and it will inform the user when the system is ready to operate with beam. This utility has been developed for better usability and fast recovery of the system.

- **Automatic cavity conditioning:** In order to make the conditioning of the cavities easier, a special mode will be implemented in the LLRF whereby the RF drive output will be pulse modulated. The user would be able to set the voltage to be achieved by the cavity, and the system will automatically increase the power to the cavity upon checking the vacuum information.
- **Fast data logger for post-mortem analysis:** The 1 GB RAM would be used to store different diagnostic signals involved in the main digital signal processing of the board, which could be retrieved after interlock detection for post-mortem analysis or upon request by the user. Up to 420 ms of operation data from the two RF plants could be stored simultaneously in the 1 GB RAM of the Perseus system.

References

- [10.1] Å. Andersson *et al.*, The 100 MHz RF system for the MAX IV storage rings, Proc. IPAC2011, San Sebastián, Spain, 4–9 September 2011, p. 193.
<https://inspirehep.net/record/1183697>
- [10.2] P.F. Tavares *et al.*, *Phys. Rev. Spec. Top. Accel. Beams* **17** (2014) 1,
<https://doi.org/10.1103/PhysRevSTAB.17.064401>
- [10.3] A. Salom and F. Pérez, Digital LLRF for ALBA storage ring, Proc. EPAC2008, Genoa, Italy, 23–27 June 2008, p. 1419. <https://inspirehep.net/record/794824>
- [10.4] A. Salom, B. Bravo, J. Marcos, and F. Perez, ALBA LLRF upgrades to improve beam availability, Proc. IPAC2015, Richmond, Virginia, USA, 3–8 May 2015, p. 1022.
<https://doi.org/10.18429/JACoW-IPAC2015-MOPTY042>
- [10.5] A. Salom, F. Perez, Å. Andersson, R. Lindvall, L. Malmgren, A.M. Milan, and A.M. Mitrovic, Digital LLRF for MAX IV, Proc. IPAC2017, Copenhagen, Denmark, 14–19 May 2017, p. 4037, <https://doi.org/10.18429/JACoW-IPAC2017-THPAB135>
- [10.6] A. Salom, E. Morales, and F. Perez, Development of a DLLRF using vommercial uTCA platform, Proc. IPAC2017, Copenhagen, Denmark, 14–19 May 2017, p. 3631.
<https://doi.org/10.18429/JACoW-IPAC2017-THOAA1>
- [10.7] Nutaq, <https://web.archive.org/web/20181204123128/https://www.nutaq.com/>, last accessed December 4th 2018.

11 Power supplies

J.-F. Bouteille and D. Einfeld

11.1 Requirements of the power supplies

The requirements and specifications of the different power supplies for the magnets described in chapter 5 are given in Table 11.1. For the magnets it is proposed to use, as a first step, the same specifications as for the ESRF-EBS upgrade; accordingly this is also proposed for the power supplies [11.1].

In order to power all magnets in a cell individually, 27 power supplies are needed for one cell; with 16 cells this makes a total of 432 current-regulated channels. Adding some spares and the supplies needed for hot-swapping, the number of channels per cell is 36, bringing the total to 576 channels overall. The maximum current for all power supplies is 110 A; the nominal values are 10–20% lower. The accuracy requested varies from 10 to 50 ppm peak to peak, according to beam-dynamic group calculations.

The total quantity of different currents, including correctors to control, is of the order of 800, which is 7 to 8 times greater than for the present machine.

To keep the mean time between failures (MTBF) the same as for the ESRF storage ring, this translates to a requirement of 1500 h of MTBF for the power supply group equipment. Transferred to single power converter, this represents more than 2 million hours of MTBF on average!

Table 11.1: Specifications of the power supplies for the magnets in one cell

me	No. per cell	Coil temp. elevation	Electrical design			Power supply design						
			Ohmic coils	Voltage	Current	Over-voltage factor	Cycling current	Cycling voltage	No. power cables included	Cycling power	No. power cables per cell	
												[mΩ]
1	2	19.3	145	13.0	86.2	1.28	110.0	16.9	1145	1864	2289	
2	2	16	117	11.1	92.3	1.19	110.0	13.6	1057	1501	2114	
3	2	10	100	8.4	82.0	1.34	110.0	11.6	710	1278	1420	
4	4	12.7	117	9.8	82.0	1.34	110.0	13.6	829	1493	3318	
5	2	17.1	117	11.5	95.3	1.15	110.0	13.6	1127	1501	2253	
6	2	12.1	188	18.4	95.4	1.15	110.0	21.5	1776	2362	3553	
8	2	14.7	224	21.2	91.8	1.20	110.0	25.6	1963	2819	3926	
	16										18873	
21	2	15	200	17.6	85.5	1.29	110.0	23.0	1523	2531	3046	
22	1	9.1	140	12.8	90.0	1.22	110.0	16.0	1174	1757	1174	
	3										4220	
3	4	7.22	125	7.9	62.0	1.77	110.0	14.5	501	1599	2004	
	2	8.55	135	8.5	62.0	1.77	110.0	15.6	541	1719	1081	
	6										3086	
1-2	2	827.0	7.6	3.4	107.3	1.03	110.0	3.7	398	407	796	
	2										796	
	27		Total power supply power for one cell for main electromagnets									27.0
											kW	

11.2 Power distribution

For the power architecture it has been decided to use DC/DC converters, fed by an AC/DC rectifier (see Fig. 11.1). In general, up to four cells will be powered by one AC/DC rectifier. For the cells 1 and 16, smaller AC/DC rectifiers will be reused. All the DC/DC converters for one cell will be housed in one cubicle, as shown in Fig. 11.2. The power distribution between the AC/DC rectifier and the DC/DC

converters for each cell is presented in Fig. 11.3. The power connections between the DC/DC converters and the magnets are given in Fig. 11.4.

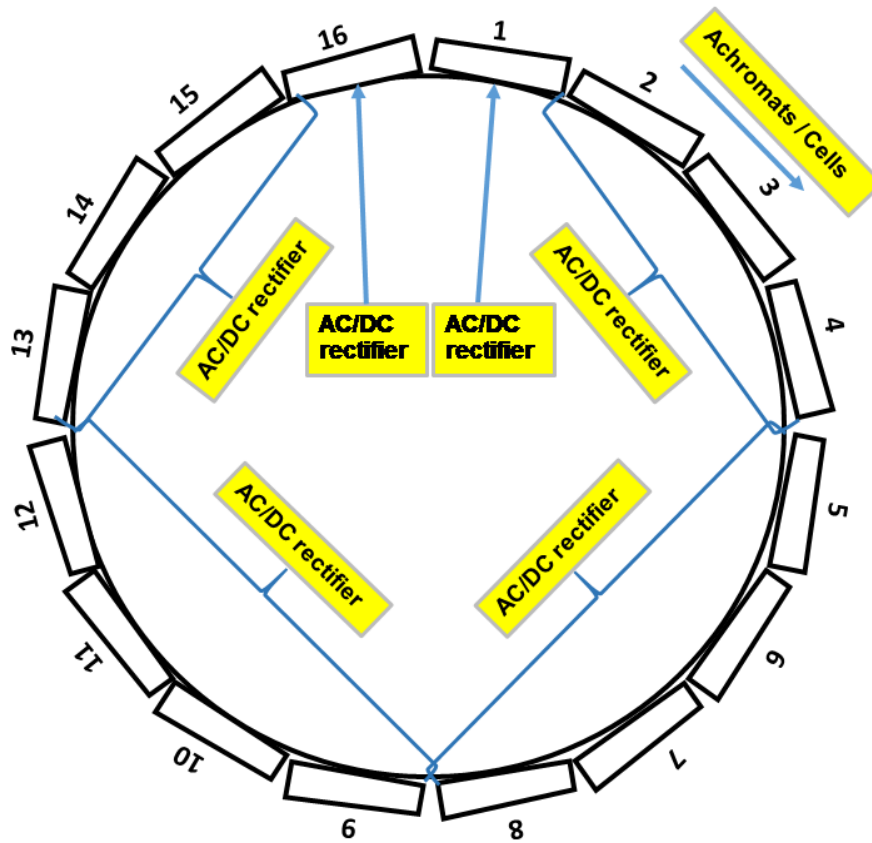


Fig. 11.1: The AC/DC power distribution for the SEE-LS

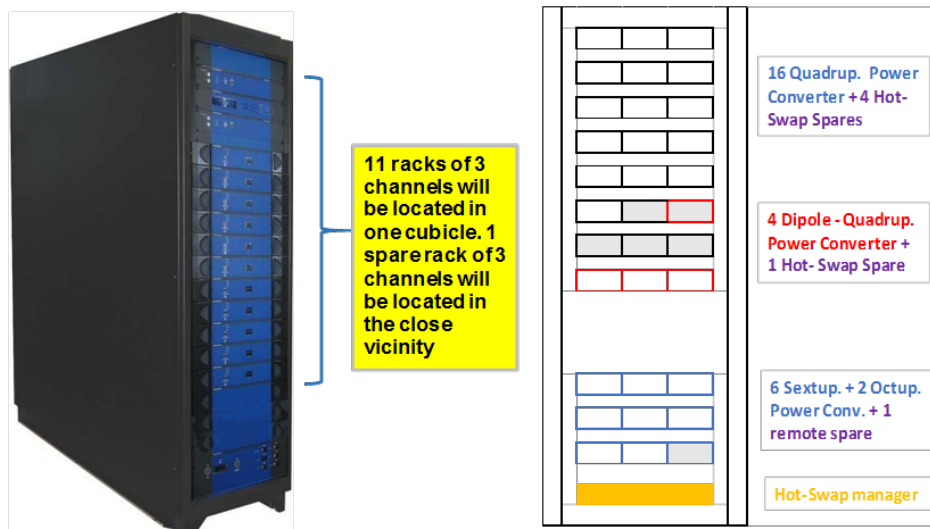


Fig. 11.2: The layout of one cubicle with 11 DC/DC power supplies

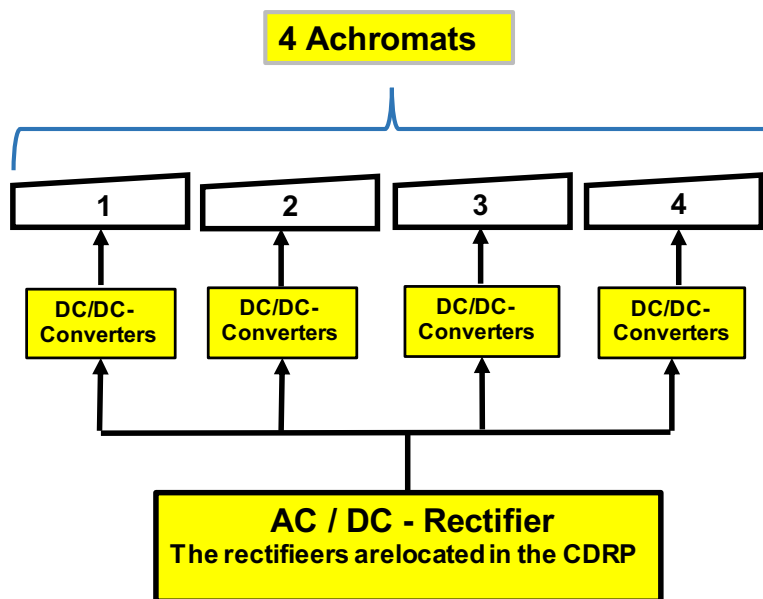


Fig. 11.3: The power distribution between the AC/DC rectifier and the 27 DC/DC converters for each cell/achromat.

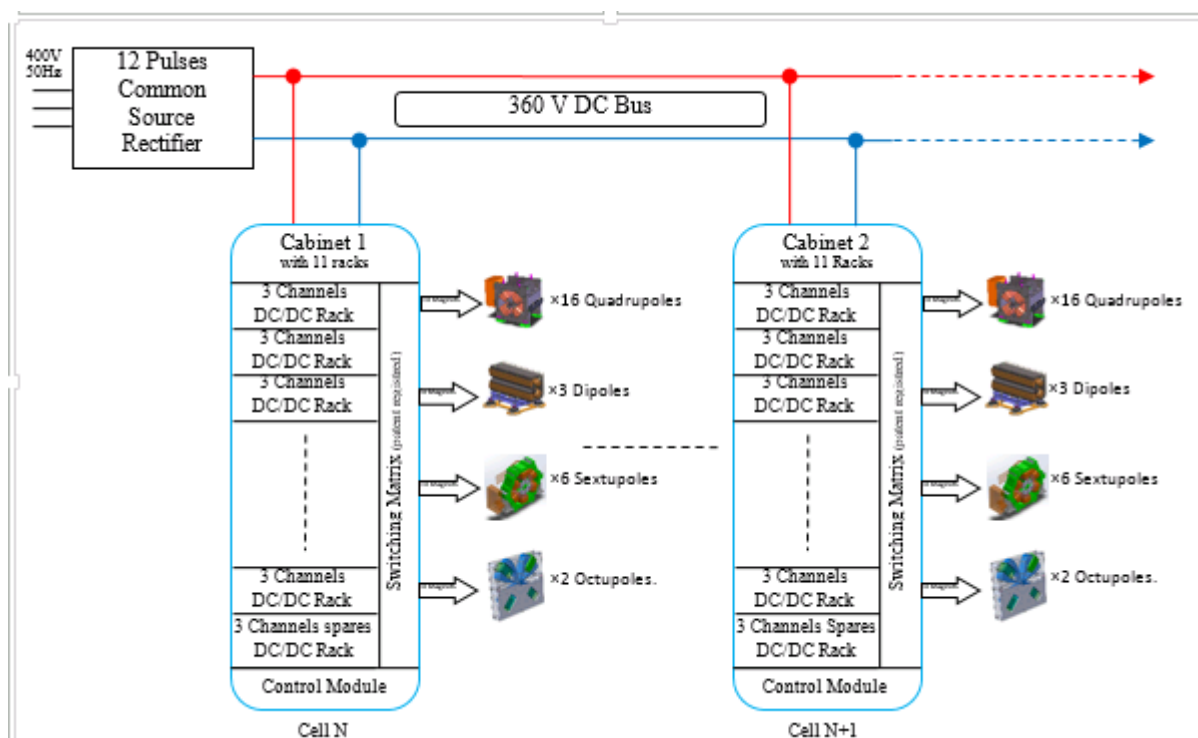


Fig. 11.4: The connections of the DC/DC converters to the different magnets in two cells

11.3 AC/DC rectifier

The purpose of these rectifiers is to ensure a stable voltage at the input of the DC/DC converters. The output DC voltage level is the result of a multi-criteria analysis, which includes evaluation of the prototypes, assessment of availability of the common source park, and optimization of the losses of the DC bus transport infrastructure, among other important tasks. The first analysis proposed in the prototype DC/DC inquiry was from 50 V to 200 V and was based on the APS design. The second analysis indicates that, in order to better reuse the present park of power converters, the voltage 360 VDC optimizes reuse of the family power converter in operation for the present machine and the reuse

of the matrix connection board, which lowers the memory type range register (MTRR) in case of a fault in one common source.

The number of these common sources will be 8 (6 large, 2 smaller, and 1 spare), from most of the six family quadrupole power supplies and the three large sextupole family power supplies. This includes the matrix connection, which will be refurbished with the interface renewed and with possible reuse of dipole and superspare units.

11.4 DC/DC converter

The purpose of these power converters is to regulate the output current from a DC voltage bus delivered from the set of centralized AC/DC rectifiers. The minimum number of DC/DC power converters is 27 per cell, and these will be fitted in a standard cubicle of 42 U hosting all electrical input and output links together with the control network, magnet interlock, and cooling water hoses.

To attain an affordable mean time before failure of 3000 h for the complete power supply equipment, study of similar large instruments such as APS and the result of the WP12 validate the idea of procuring a system in which a faulty converter can be replaced while keeping the beam within the vacuum chamber.

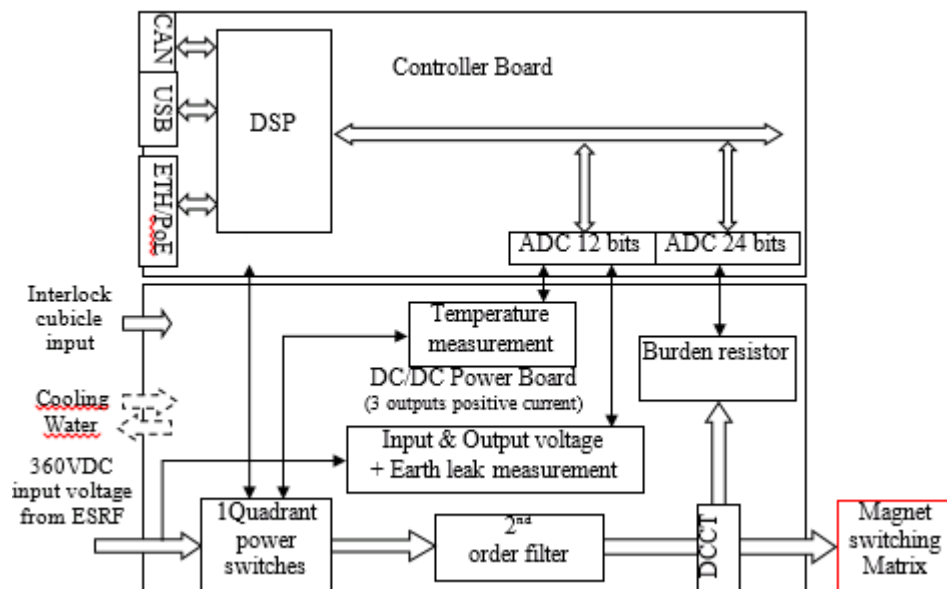


Fig. 11.5: Block diagram of the digital control of the power converter

The 33 DC/DC converters are grouped per cell and located in a single cubicle. A hot-swap matrix will connect 27 outputs from the 33 converters, and the hot-swap manager will survey the output current of the quadrupole and dipole quads; this will enable a fast swap-out of the current source before the beam is lost. This design has been patented by the ESRF under the name ‘hot-swap system’. The sextupole and octupole will be remotely swappable by operator decision to restore one failing channel which is not critical.

The technology chosen is full digital control of each channel adapted to the hot-swap capacity. The use of a standard DC current monitor (DCCT) will be controlled externally by another current sensor to trigger the time to exchange the faulty channel.

For the injection cell equipped with two recovered QD6HG from cell 16, they will come with their existing power supplies. In order to take advantage of the present architecture, we will refurbish and adapt the switching matrix serving the family power supplies. This will enable main DC distribution (360 V) to be ready in less than half an hour in case of breakdown of one of the eight AC/DC rectifiers.

11.5 Spare power supplies

The goal here is to optimize the number of redundant spares and how they are connected in order to operate with the highest global expected MTBF. The initial approach is to verify how many of the 14 channels need a spare channel. The sextupole and octupole magnets are not necessarily involved with the computer-assisted hot-swapping solution. This is of major importance for the six sextupole main coils because of the coupling factor that exists with the corrector channels attached on the iron poles of the magnets. The theory indicates, as a first estimation to be confirmed, that a loss of one sextupole magnet does not kill the beam; only the chromaticity is changed and could be partially compensated for. As a consequence, a solution with a maximum of nine channels per cell equipped with the hot-swapping solution is the first case under evaluation.

The second issue is the number of spare channels to implement, which is governed by the reliability study and also by the minimum availability of standalone channels. This depends on the final electrical, mechanical, and connectivity implementation. The target is to have an independent Ethernet rack driving the redundant channels; the mechanical connectivity has to be identical to that for the ‘normal channel’—two, three, or four channels per rack on the same external DC bus. For example, if the power converter rack has four channels built in, we would need four racks to power 13 channels, and one four-channel rack could serve as a set of redundant units for the nine critical ones. If a rack has three channels built in, we would need four racks to power 13 channels per cell, plus one or two additional racks housing two or three channels that could serve as redundant channels for the nine critical ones.

11.5.1 Minimum implementation

The solution having eight quadrupole magnet power converters backed up by four spares produces a very high MTBF and allows the standby team to exchange the first faulty channel the next morning, rather than waiting for the next mean down time (MDT) maintenance period one week later. This is true only if the channels are grouped by twos at most in one enclosure. The case with three channels per enclosure pushes us to have two racks as spares in order to be able to wait until the next MDT to exchange the faulty channel.

The non-computer-assisted faulty channel replacement will be implemented in the form of one spare for the three DQs and one spare for the six sextupole and two octupole DC/DC converters. Remote exchange of one channel could possibly be launched from the control room with a procedure yet to be worked out. With this minimum implementation, the number of channels to order per cell will be 33 ($16 + 4$, $3 + 1$, and $8 + 1$), for a total of 1056 converters in operation; the spare units will be added to this number according to the philosophy adopted at the contract placement.

11.6 The AC and DC corrector power supplies driven by the fast-orbit feedback

For the AC steerers, the plan is to fully reuse the Bilt power supplies connected to the fast-orbit feedback and the Libera units in operation (see Fig. 11.5) below the running power supplies. Only the location of the cubicles will be subject to discussion with the aim of optimizing the technical gallery space and the control cabling.

These power supplies are currently the ones in operation linked with the Libera units and the computer preparing the set points at 10 kHz for the 288 channels. We foresee no changes to this system, and the latest (Bilt) power supplies will be connected to the special steerers designed for this purpose.

The electrical compatibility in terms of AC coupling and bandwidth is yet to be verified, but this cannot be performed before the first magnet prototype has been delivered.

11.7 The DC corrector power supplies feeding the sextupole auxiliary coils

Some magnets are equipped with auxiliary coils, such as the sextupole magnets and the dipole–quadrupole magnets, and will be powered separately.

The six coils wound around the six sextupole magnet poles per cell will perform vertical, horizontal, and skew adjustments and will therefore need a total of 768 channels (4 circuits per sextupole \times 6 sextupoles per cell \times 32 cells). The present electrical ratings are 2 A and 11 V per channel, leading to 22 W, and we have chosen not to reuse the actual 250 W corrector power supplies (180 units) because of poor reliability, the interface not being supported any more at the control room, and an insufficient number for the new lattice. A survey is needed to evaluate whether an industry-standard commercial product is affordable or if some neighbouring institute would be willing to sell an appropriate design and realization.

This same DC distribution scheme will also be used for the corrector DC distribution (45 V). The switching matrix will be split with more buses to accommodate such a strategy

A DC bus distribution at 45 V will be refurbished from three of the five flexibility power supplies used for high-focusing optic configurations. This will be the input power for 24 channels (4 \times 6 sextupoles per cell) times 32 cells, i.e. 768 DC/DC corrector channels.

11.8 Earth magnetic field compensation power supplies

The present lattice is equipped with two types of field compensation. The first type compensates for the algebraic sum of the family current passing through the straight section. One big loop is fed by the Flex 1 on request during all runs except for the 16-bunch mode. The second type of compensation is performed under a chosen set of straight sections at the request of the WP8 and is fed by individual power supplies connected to a four-wire cable laid just under the insertion devices, with return outside the tunnel. According to the WP8, the new lattice requires that all straight sections be equipped with compensating loops, and furthermore the two planes need to be adjusted for earth field. The maximum total quantity is therefore 54 (2 \times (32 - 5)) in operation, with some spares in case of failure.

The present solution using low-grade power supplies could be extended by reusing the 12 units in operation today. A request for quotation (RFQ) will therefore be necessary when the power size is known. We are also looking to power the units with the DC corrector (2 A 26 W) solutions, adding the 54 requested to the 768 described in section 11.7.

We will soon obtain the magnetic earth field correction current request. This should complete the array of power supplies to procure.

The general layout of power converters for accelerators is presented in Ref. [11.2].

References

- [11.1] ESRF-EBS project, EBS storage ring technical report (ESRF, Grenoble, 2018), https://web.archive.org/web/20190506105503/https://www.esrf.eu/files/live/sites/www/files/about/upgrade/documentation/Design_Report-reduced-jan19.pdf
- [11.2] CAS-CERN Accelerator School: Power Converters, Baden, Switzerland, 7–14 May 2014, CERN-2015-003 (CERN, Geneva, 2015). <https://doi.org/10.5170/CERN-2015-003>

12 Diagnostic system

F. Perez

12.1 Introduction

The diagnostic system will monitor the accelerator performance and beam conditions in different scenarios:

- the initial commissioning;
- periodic start-ups; and
- normal operations for the scientific programme.

For this reason, the diagnostic system [12.1, 12.2] has to be complete and flexible enough to cope with the different situations. In addition, due to the foreseen top-up operation, particular attention should be given to systems that monitor component stability and beam quality in the injector. The goal is to guarantee a steady beam within the nominal specifications. In the main ring, constant beam current and beam stability at the sub-micron level are essential. To this end, a series of electron and photon beam position monitors (BPMs) are distributed around the storage ring.

In summary, the diagnostic system will monitor beam production in the pre-injector (linac), transmission through the beam transport lines, injection efficiency into the booster, injection into the main ring, and, in particular, stored beam quality. This chapter outlines the proposed diagnostic systems for each portion of the accelerator complex.

12.2 Pre-injector diagnostics

In this section diagnostics are specified for a standard linac-based pre-injector system. There will be two main modes of beam production: single- and multi-bunch pulse trains. Also, for top-up, a low-current mode is necessary. In order to maintain high beam quality during extended top-up periods, it is important that the beam energy, bunch charge, and bunch timing remain stable for up to several weeks at a time.

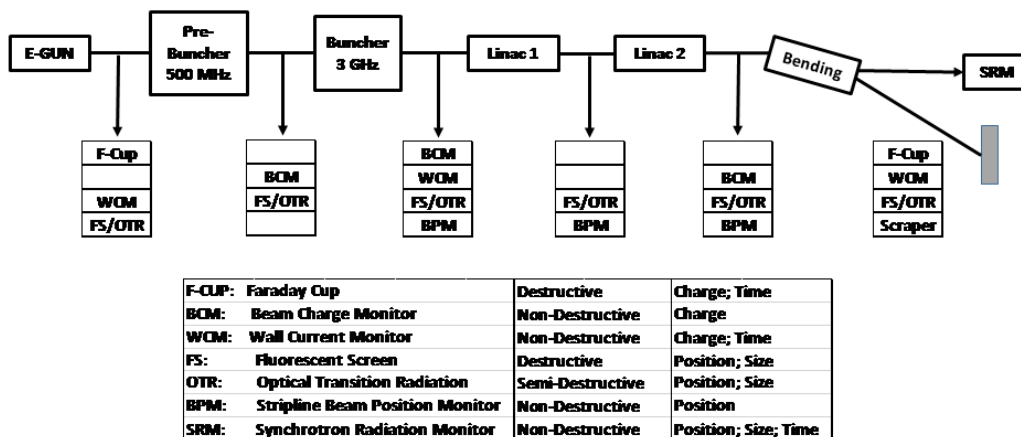


Fig. 12.1: Schematic diagram of pre-injector diagnostic systems (linac)

A schematic diagram indicating the location of the linac diagnostics is shown in Fig. 12.1. Specifically, Faraday cups and wall current monitors measure charge before and after the linac, integrating current transformers (ICTs) measure beam transmission efficiency, and BPMs measure beam position. Fluorescent screens and optical transition radiation monitors (OTRs) are used for beam steering, qualitative beam size measurements, and lattice diagnostics. A synchrotron light monitor viewing radiation from the first LTB dipole magnet measures beam size and time structure of the 100 MeV beam [12.3]. A diagnostic beam line at the end of the pre-injector contains a fluorescent screen, scraper, and Faraday cup to monitor 100 MeV beam properties, including energy spread.

12.2.1 Faraday cup (F-cup)

A retractable Faraday cup is located at the exit of the e-gun to measure macropulse length and total charge prior to entering the linac. The data are used to optimize the single- and multi-bunch pulse modes from the gun. The measurement bandwidth is suitable for transient measurements (total number of S-band buckets). A second Faraday cup is located in the diagnostic beam line following the linac as part of the energy spread measurement.

12.2.2 Beam charge monitor (BCM)

BCMs are located after the pre-buncher, 3 GHz buncher, and linac. The charge monitors provide non-destructive measurement of transport efficiency and are used to optimize linac operation. A likely candidate is the Bergoz BCM with the integrated hold–reset option.

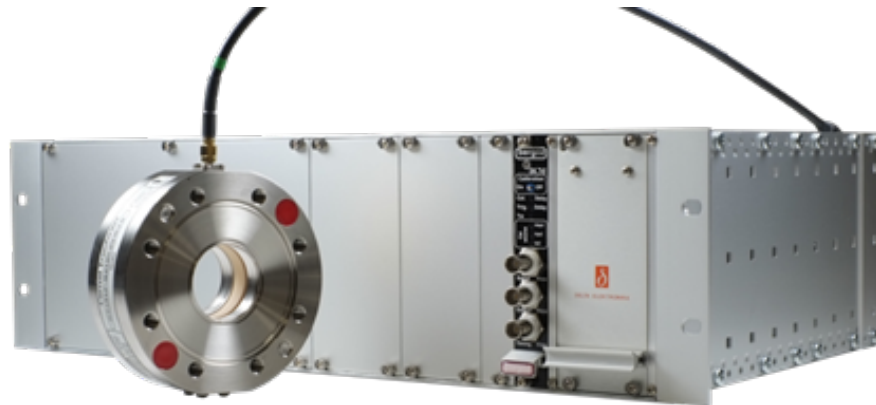


Fig. 12.2: Beam charge monitor from Bergoz [12.16]

12.2.3 Beam position monitor (BPM)

Stripline BPMs measure beam position after the 3 GHz buncher and after each accelerating section. BPMs provide non-destructive measurements for manual beam steering and automatic steering feedback. Where possible, stripline BPM receivers will utilize the same technology as the main ring [12.4].

12.2.4 Fluorescent screen (FS)

Fluorescent screens are relatively simple to construct and provide beam position information at low current. Referring to Fig. 12.1, six such screens are installed in the pre-injector for beam alignment. The YAG:Ce crystals are remotely inserted into the beam path on command, and charge-coupled device (CCD) cameras broadcast the signal back to the control room for visual inspection and digital analysis [12.12].

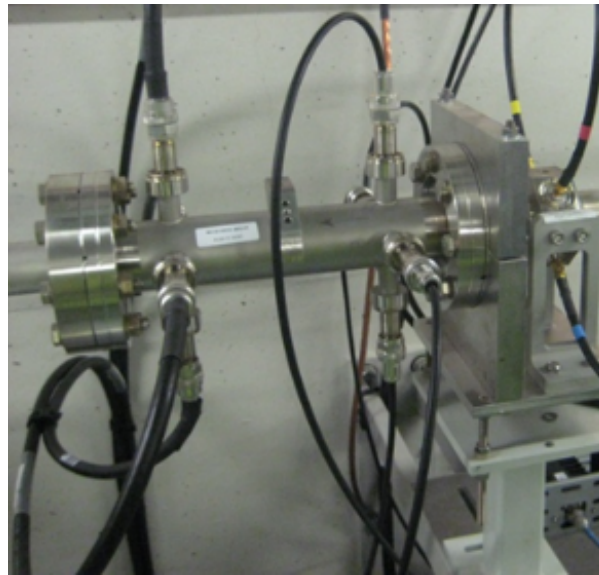


Fig. 12.3: Stripline monitor installed at ALBA [12.5]

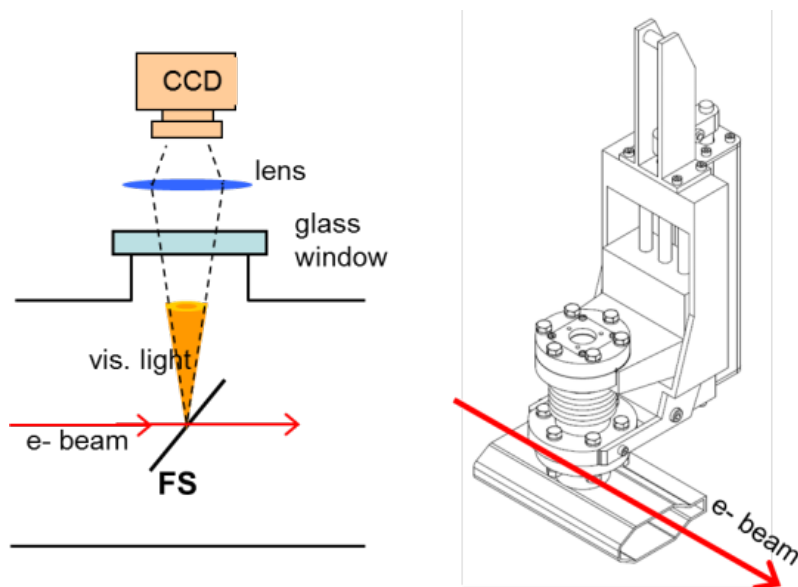


Fig. 12.4: Schematics and drawing of the ALBA fluorescent screen [12.5]

12.2.5 Scraper

The LTB diagnostic beam line contains a horizontal scraper to measure energy spread (the first LTB dipole acts as a spectrometer). The resulting variation in intensity with scraper position is monitored at the second Faraday cup. Since the electron beam must be diverted into the diagnostic beam line, the scraper/Faraday cup system is used only during commissioning, in machine development periods, or as a diagnostic in the event of pre-injector mis-tuning.

12.2.6 RF signal distribution system

Although not a direct beam measurement, RF signal diagnostics are essential to the tuning of the electron gun, bunching systems, and linac. The RF signal distribution system will monitor, among other signals, forward and reflected power waveforms at the gun and each linac section.

12.3 Transfer line diagnostics

Transfer lines direct the electron beam from the linac to the booster (LTB) and from the booster to the storage ring (BTS). The LTB steers the beam at 100 MeV while the BTS steers the beam at full energy (2.5 GeV). For both transfer lines, it is important that beam quality and transport efficiency are maintained for long periods of time, particularly in the top-up mode. Transfer line diagnostic systems will be similar to those of the linac systems where possible.

12.3.1 Fast current transformer (FCT)

Each transfer line will be equipped with two fast current transformers (one at the beginning and one at the end) to measure charge transfer efficiency. By normalizing capture rates in the booster and the main ring to current in the respective upstream transfer lines, injection efficiency can be monitored. Fast current transformers can be used to monitor single-pulse injection efficiency into the main ring.



Fig. 12.5: Fast current transformers (Bergoz) [12.16]

12.3.2 Fluorescent screen (FS)

The LTB and BTS will be equipped with YAG:Ce fluorescent screens at the beginning, middle, and end of the transfer lines, depending on the length of the line. In each case, the third (downstream) screen will be located after the injection septum. CCD cameras will monitor the beam image, with display in the control room and analysis carried out on the digital image [12.14].

12.3.3 Beam position monitor (BPM)

Single-pass BPMs will be installed along the transfer lines to monitor electron beam position. The BPM receivers will be purchased from a commercial vendor or through collaboration. Where possible, the BPM receivers should be the same as the booster/storage ring units to unify systems within the accelerator complex. Readouts will be viewed on the GUI by the operators and stored in the database for diagnostic and analysis purposes.

12.4 Booster diagnostics

The main parameters of the booster synchrotron are not yet fixed, but its function will be to increase the energy of the beam from the 100 MeV of the linac to the 2.5 GeV of the storage ring. The diagnostics listed here are essentially the same for any kind of booster, with the exception of the number of BPMs, which will depend on the circumference, number of cells, and tune of the booster.

12.4.1 Fast current transformer (FCT)

A fast current transformer measures beam current in the booster under a variety of operating conditions. It is important to know the total current and bucket distribution prior to injection into the main storage

ring. For top-up mode, total bunch charge and single-bunch purity must be carefully monitored and controlled.

12.4.2 DC current monitor (DCCT)

The DCCT provides an absolute measure of the average beam current and is used to determine injection rates, loss rates, and beam lifetime. DCCTs are commercially available both as ‘off-the-shelf’ models and as units custom-designed to meet special requirements (www.bergoz.com).

Typical performance features include: 1) DC-to-100 kHz bandwidth, 2) dynamic range of up to 10^7 , and 3) absolute error less than 5×10^{-4} . High-quality, shielded cables will connect the sensor to the front-end electronics and link the front-end electronics to the output chassis.

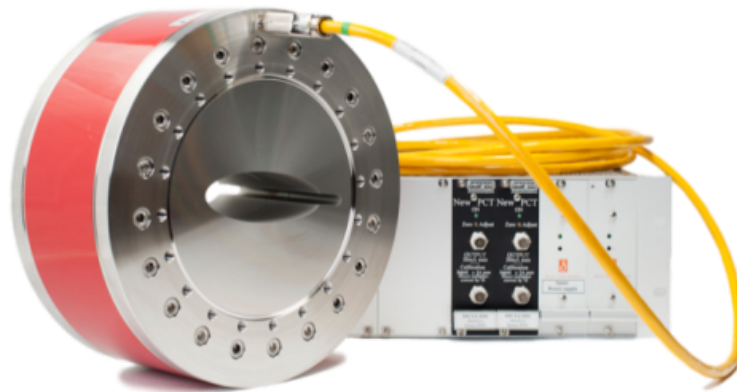


Fig. 12.6: DC current transformers (Bergoz) [12.16]

12.4.3 Fluorescent screen (FS)

A retractable fluorescent screen is located just after the injection septum to monitor location and intensity of the incoming 100 MeV beam. A second screen at the downstream end of the extraction septum serves two functions: 1) half insertion mode—view extracted full-energy beam; and 2) full insertion mode—view first half-turn of the 100 MeV beam. In addition, fluorescent screens can be distributed along the booster, each quarter or half of the ring, in order to check injection parameters, mainly during commissioning and start-ups.

12.4.4 Beam position monitor (BPM)

A certain number of BPMs with single-turn measurement capability will measure beam position in the booster. The exact number will depend on the number of cells and the tune of the machine. It is recommended to have a minimum of four BPMs for each betatron oscillation.

The booster BPM receivers can be interchangeable with the main ring so that after booster commissioning is complete, some receivers can be moved to the main storage ring or used as spares. The BPM receivers will be purchased from a commercial vendor or through some kind of collaboration.

12.4.5 Synchrotron radiation monitor (SRM)

Synchrotron radiation from the booster can be transferred inside the tunnel by simply opening a port in one or two of the bending magnets and installing an optical system to send the beam image to a camera located in a vertical position, outside the plane of radiation [12.6]. Since the emittance of the booster beam is non-critical to within 10% approximately, the transverse beam profile only requires qualitative inspection.

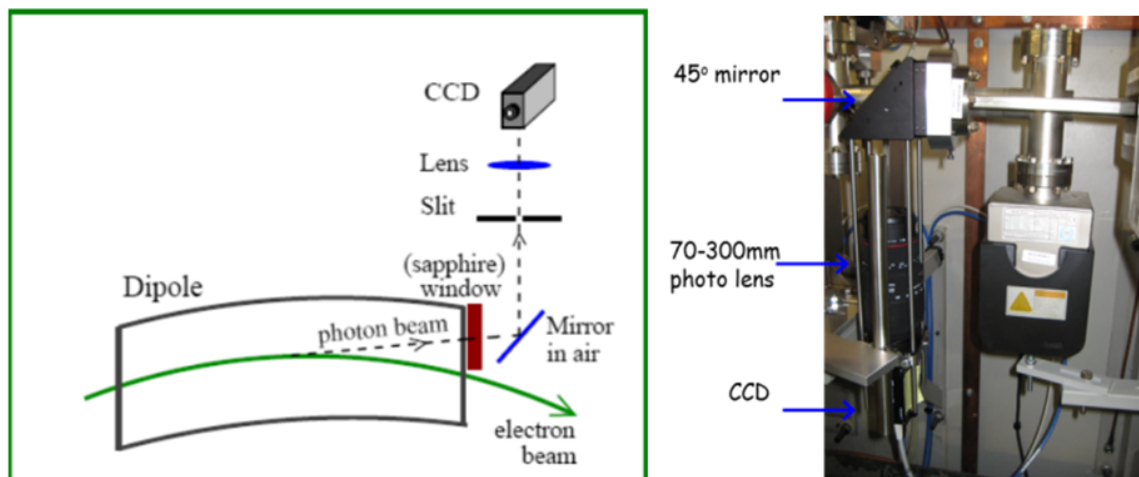


Fig. 12.7: Synchrotron radiation monitor for the booster of ALBA: schematic drawing (left) and photo of the ALBA installation (right) [12.6].

12.4.6 Striplines

One stripline will excite the betatron frequency and a second will serve as a receiver of the excitation, allowing the determination of the horizontal and vertical tunes. A signal generator (either a tracking generator, a swept-frequency generator, or a pink-noise source) will drive the orthogonal striplines in parallel, and a real-time spectrum analyser capable of processing the input through a bank of parallel digital filters creates a histogram of the response.

12.5 Storage ring diagnostics

The primary function of the beam diagnostics is to monitor the electron beam current, orbit position, orbit stability at the source points, and beam cross-section (emittance). Measurement of the betatron tunes is also required in order to maintain proper operation of the storage ring. More sophisticated measurements—such as beam-based alignment, response-matrix analysis to control beta functions and coupling, turn-by-turn pinger experiments, and measurement of the electron beam energy—are performed periodically.

This section describes the electron beam diagnostics and a system of diagnostic synchrotron light monitors. Although important for operation of the storage ring, measurements of the photon beam properties (beam position, beam stability, flux, etc.) are not covered. Also, beam loss monitors will be left as a possible upgrade [12.9].

12.5.1 Fluorescent screen (FS)

One fluorescent screen is located just after the injection septum to check the presence and position of the injected beam. The construction, operation, and display system are similar to those of the FS systems in the booster and transport lines. In addition, screens can be distributed along the ring, each quarter or half of the ring, to check injection parameters, mainly during commissioning and start-ups.

12.5.2 Fast current transformer (FCT)

The FCT measures the injected beam current on a pulse-to-pulse basis. Comparison with a similar monitor at the end of the transfer line allows direct determination of the injection efficiency. The FCTs and signal processing electronics will have the same design as in the booster synchrotron.

12.5.3 DC current monitor (DCCT)

The DCCT provides an absolute measure of the average beam current and is used to determine injection rates, loss rates, and beam lifetime. DCCTs are commercially available both as ‘off-the-shelf’ models

and as units custom-designed to meet special requirements (www.bergoz.com). Typical performance features include: 1) DC-to-100 kHz bandwidth, 2) dynamic range of up to 10^7 , and 3) absolute error less than 5×10^{-4} . High-quality shielded cables will connect the sensor to the front-end electronics and link the front-end electronics to the output chassis.

12.5.4 Beam position monitor (BPM)

A certain number of BPMs with high-precision measurement capability will measure the beam position in the storage ring [12.10]. The exact number will depend on the number of cells and the tune of the machine. It is recommended to have a minimum of four BPMs for each betatron oscillation. They will be of the button style and be installed in the main vacuum chambers. Extra BPMs will be installed in the diagnostic straight sections for tune measurement, turn-by-turn diagnostics, and potentially fast-feedback pick-ups. Insertion devices may include additional BPMs integrated into the ID vacuum chambers.

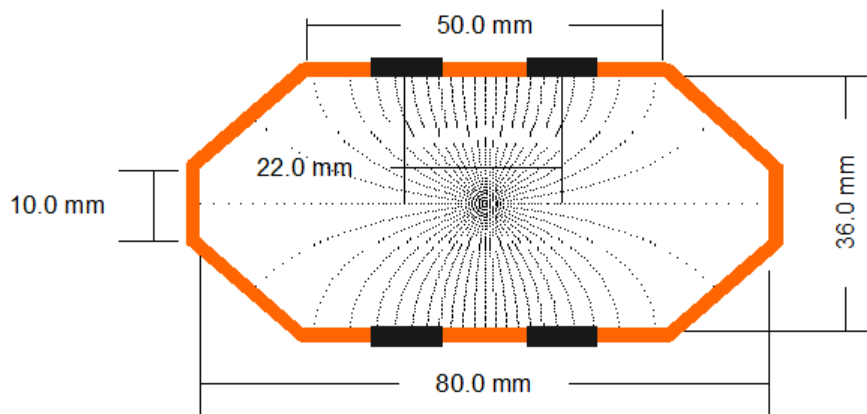


Fig. 12.8: Typical BPM geometry [12.10]

Leading candidates for the BPM receiver systems include ITech [12.17] and the newly developed system of NSLS-II. It is worth noting that when BPMs are used in the fast-orbit feedback system, both the corrector magnet currents and the BPM signals become important diagnostics for monitoring electron beam and power supply stability [12.11].

12.5.5 Beam-based alignment

The purpose of beam-based alignment is to calibrate the centre of each BPM to the magnetic centre of adjacent quadrupoles [12.13]. Individual quadrupole supplies are modulated by $\pm 1\text{--}2\%$ as the electron beam orbit is swept through the centre of the magnet. The BPM offset is determined by plotting the induced orbit shift as a function of beam position.

12.5.6 Scrapers

A horizontal and a vertical scraper will be installed to measure the dynamic acceptance and to function as a limiting aperture to protect the low-gap insertion devices.

With finite dispersion throughout the accelerator, the horizontal scraper can be used as an aperture-defining instrument for energy-acceptance measurements. The vertical scraper has the important function of measuring electron beam lifetime as a function of vertical chamber acceptance. The acceptance data is used in planning for future small-gap devices.

It is advisable to implement extra radiation protection around the scrapers, since they are the source of high radiation losses.

12.5.7 *Synchrotron radiation monitor (SRM)*

SRMs make a versatile diagnostic tool for longitudinal and transverse bunch measurements [12.8]. The system ideally consists of two beam lines with viewports accepting light from low-dispersion and high-dispersion emission points on a dipole magnet. For the diagnostics of the electron beam at the storage ring, we expect to use a minimum of two synchrotron light beam lines: 1) an X-ray pinhole beam line and 2) a visible light beam line.

12.5.7.1 *X-ray pinhole front end*

The X-ray pinhole beam line is intended for measuring the beam size and emittance of the electron beam. Due to the small vertical dimension of the electron beam, the use of X-rays is necessary in order to have a diffraction limit below the beam size.

The use of X-rays outside the shielding wall requires a shielded hutch, which will make the implementation of this beam line quite expensive, though it will of course provide greater flexibility.

Without completely relinquishing the flexibility and relying on motor-controlled positioning, one can foresee a beam line that is completely inside the shielding wall, so we can call it the X-ray pinhole front end. For it to be effective a long front end is needed (longer than 15 m).

12.5.7.2 *Visible light beam line*

The visible light beam line is intended for several types of measurements—bunch length, bunch purity, and instabilities—and for providing visually straightforward information about the beam spot (TV camera in the control room). To accommodate the kind of instrumentation to be placed in this beam line, the optical hutch has to be installed outside the shielding wall. No shielded hutch is required [12.7]. To have a large amplification factor, a short front end is desirable for this beam line.

To extract the visible light, two approaches can be taken: at 90° or at 0.5 m below the electron path. In both cases no beam shutter is required since no X-ray has to be stopped. A good candidate front end would be one that is short, not used by the experiments, and placed after the wall to locate the optical hutch.

A proposal is to use the first bending after the injection point in order to meet the above conditions, so that:

- at front end no. 1, coming from the first bending after the injection point, the visible light beam line can be placed;
- the light is extracted at 90° and at 0.5 m below the electron orbit, in order for the hutch to be placed in the area of the experimental hall that will not be used by the experiments (because it corresponds to the front end no. 33, occupied by the X-ray pinhole front end);
- the X-ray is not stopped, so an X-ray beam line can still be located in port 1.

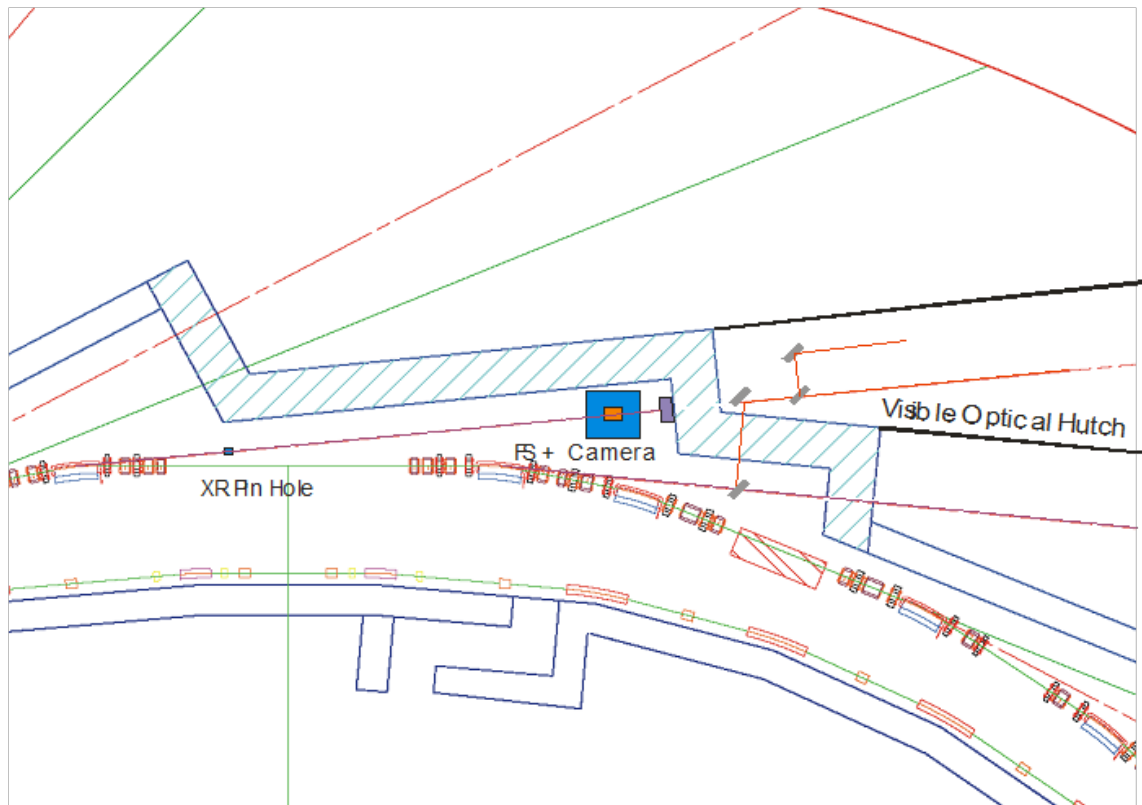


Fig. 12.9: Sketch of proposed combination of X-ray pinhole and visible light synchrotron radiation monitors

12.5.8 Stripline kicker and tune measurement

For the tune measurement, a four-electrode stripline can be used to excite the beam in the horizontal and vertical planes. Alternatively, transverse fast-feedback kickers can be used, but tune excitation increases the overall complexity of the feedback architecture and requires the system to be operational on day one of the machine commissioning phase.

The tune measurement can be processed on the signal generated at a single BPM button, thereby reducing the vacuum chamber complexity and impedance introduced by multiple striplines. Additional striplines may be required 90° from the fast-feedback kickers if the signal from individual BPM buttons is not sufficient for feedback applications.

12.5.9 Fast-feedback kickers

Two transverse feedback kickers, one horizontal and one vertical, will be installed for bunch-by-bunch feedback. As small-gap insertion devices are introduced into the vacuum chamber and the current is increased, resistive wall instabilities will manifest. Ideally, the kicker magnets will be approximately 90° from the pick-up electrodes (BPM or stripline). Examples of both transverse and longitudinal feedback systems are abundant, often developed by the high-energy physics community; see, for example, the transverse feedback systems installed at PEP-II, ALS, Daphne, etc. (reported in PAC and EPAC proceedings).

12.5.10 Pinger magnets for turn-by-turn beam dynamics

Turn-by-turn diagnostics for beam dynamics have become a popular means of analysing single-particle behaviour in simulations and measurements [12.15]. The single-turn pinger magnets kick charge that is stored in a single bunch in either the horizontal or the vertical direction. Turn-by-turn BPM measurements sample the ensuing bunch motion, and sophisticated analysis programs (NAFF, frequency-map analysis) decipher tune shift with amplitude. Based on the insight into beam dynamics, pinger magnets should be included to complement the storage ring diagnostic systems.

12.6 Summary of diagnostic system

The number of diagnostic elements used for the different parts of the accelerator complex are summarized in Table 12.1; $Q_{x,y}$ denotes the working point or tune in the horizontal and vertical directions.

Table 12.1: Diagnostic components used in the different parts of the accelerator

Component	Linac	LTB	Booster	BTS	SR	Total
Faraday cup	2					2
BCM	3					3
FCT		2	1	2	1	6
DCCT			1		1	2
Fluorescent screen	6	2	2	2	4	16
SRM	1		1		1	3
Pinhole X-ray					1	1
Stripline			2		1	3
Scraper		1		1	1+1	4
BPM	3	2	$4 \times Q_{x,y}$	4	$4 \times Q_{x,y}$	N
Exciter/kicker					2	2

References

- [12.1] A. Hofmann, Dynamics of beam diagnostics, CERN Accelerator School, Dourdan, France, CERN-2009-005 (CERN, Geneva, 2009), p. 65. <http://dx.doi.org/10.5170/CERN-2009-005.65>
- [12.2] J. Borer and R. Jung, Diagnostics, CERN Accelerator School: Antiprotons for Colliding-beam Facilities, Geneva, Switzerland, 11–21 October 1983, CERN-1984-015 (CERN, Geneva, 1984), p. 385. <https://doi.org/10.5170/CERN-1984-015.385>
- [12.3] U. Iriso, A. Olmos, and F. Pérez, Beam Diagnostics at the ALBA Linac, Proc. DIPAC2009, Basel, Switzerland (CERN, Geneva, 2009), p. 122. <https://accelconf.web.cern.ch/accelconf/d09/papers/mopd32.pdf>
- [12.4] G. Lambertson, Dynamic devices – pickups and kickers, *AIP Conf. Proc.* **153** (1985) 1413, <https://doi.org/10.1063/1.36380>
- [12.5] U. Iriso, A. Olmos, and F. Perez, Electron Beam Diagnostics for the ALBA Light Source, Proc. DIPAC 2007, Venice, Italy (CERN, Geneva, 2007), p. 27. <https://accelconf.web.cern.ch/accelconf/d07/papers/mod1a03.pdf>
- [12.6] U. Iriso and F. Pérez, Synchrotron Radiation Monitors at ALBA, Proc. EPAC2006, Edinburgh, Scotland (CERN, Geneva, 2006), p. 3410. <http://accelconf.web.cern.ch/AccelConf/e06/PAPERS/THPLS056.PDF>
- [12.7] Åke Anderson, Ph.D. thesis, Lund University, 1997. <http://lup.lub.lu.se/record/29536>
- [12.8] K. Hollmack *et al.*, Review of emittance and stability monitors using synchrotron radiation monitors, Proc. DIPAC2001, Grenoble, France (CERN, Geneva, 2001), p. . <http://accelconf.web.cern.ch/AccelConf/d01/papers/IT04.pdf>
- [12.9] K. Wittenburg, Beam loss monitoring and control, Proc. EPAC2002, Paris, France (CERN, Geneva, 2002), p. 109. <https://accelconf.web.cern.ch/accelconf/e02/PAPERS/THYGB001.pdf>
- [12.10] A. Olmos *et al.*, BPM design for the ALBA synchrotron, Proc. EPAC2006, Edinburgh, Scotland (CERN, Geneva, 2006), p. 1190. <https://accelconf.web.cern.ch/accelconf/e06/PAPERS/TUPCH078.PDF>
- [12.11] A. Olmos *et al.*, Commissioning of the ALBA Fast Orbit Feedback System, Proc. IBIC2014, Monterey, Calif., USA (CERN, Geneva, 2014), p. 691. <http://accelconf.web.cern.ch/AccelConf/IBIC2014/papers/wepd23.pdf>
- [12.12] M. Moszynski *et al.*, *Nucl. Instrum. Methods Phys. Res. A* **345** (1994) 461, [https://doi.org/10.1016/0168-9002\(94\)90500-2](https://doi.org/10.1016/0168-9002(94)90500-2)
- [12.13] P. Rojsel, *Nucl. Instrum. Methods Phys. Res. A* **343** (1994) 374, [https://doi.org/10.1016/0168-9002\(94\)90214-3](https://doi.org/10.1016/0168-9002(94)90214-3)

DIAGNOSTIC SYSTEM

- [12.14] K. Potter, Beam profiles, CAS-CERN Accelerator School: General Accelerator Physics, Gif-sur-Yvette, France, 3–14 September 1984, CERN-1985-019-V-I (CERN, Geneva, 1985), vol. 1, p. 301. <https://doi.org/10.5170/CERN-1985-019-V-1.301>
- [12.15] D. Robin *et al.*, *Phys. Rev. Lett.* **85** (2000) 558, <https://doi.org/10.1103/PhysRevLett.85.558>
- [12.16] Bergoz Instrumentation, <https://web.archive.org/web/20190506031406/https://www.bergoz.com/>, last accessed May 6th 2019.
- [12.17] Instrumentation Technologies, <https://web.archive.org/web/20170824173609/https://www.i-tech.si/accelerators-instrumentation/>, last accessed August 24th 2017.

13 Front end

D. Einfeld

The front ends (FEs) are essential parts of a synchrotron light source facility. They connect the vacuum system of the storage ring with that of the beam lines. The front ends serve the following objectives:

- (i) ensure radiation safety beyond the shielding wall during beam operation;
- (ii) maintain the vacuum in the storage ring and protect it from any accidents that might occur during the operation of the experimental beam lines.
- (iii) protect the optics and experimental stations from the synchrotron radiation power emitted from the bending magnet and insertion devices that are not used for the experiments;
- (iv) monitor the photon beam position as well as the characteristics of the photon beam.

To understand the specifications of different components in the front ends, the characteristics of different insertion devices (IDs) are summarized in Table 13.1. $P(\text{tot})$ is the overall emitted radiation power and $P(\text{dens})$ is the power density in the normal direction. These powers are needed for the layout of the second absorber and the photon shutter.

Table 13.1: Characteristics of the insertion devices that could be used for phase-I beam lines at SEE-LS

Source	$B(\text{max})$ (T)	Period (mm)	Length (m)	K	Gap	$P(\text{dens})$ (kW/mrad ²)	$P(\text{tot})$ kW
Bend	1.42					0.249	
MPW	1.782	80	1.07	13.32	12.5	7.61	6.87
IVU	0.805	21.3	2	1.6	5.5	26.57	2.95
EU (hor)	0.92	71.36	1.655	6.14	15.5	7.63	3.28
EU (vert)	0.73	71.36	1.655	4.69	15.5	5.8	1.92
EU (circ)	0.56	71.36	1.655	3.75	15.5	3.32	2.44

Table 13.2 shows the opening angles of the radiation cones coming from the insertion devices (X' and Y') and the opening requirements of users ($\Delta\theta$ and $\Delta\psi$) for the photon beams in the beam lines. In all cases X' and Y' are greater than $\Delta\theta$ and $\Delta\psi$. The radiation cone not needed for users has to be absorbed into the second absorber of the front end.

Table 13.2: Opening angles of the radiation cones (X' and Y') from different insertion devices and the user-required opening angles ($\Delta\theta$ and $\Delta\psi$).

Source	$X(\text{max})$ (μm)	X' (max) (μrad)	$Y(\text{max})$ (μm)	Y' (max) (μrad)	$\Delta\theta$ (μrad)	$\Delta\psi$ (μrad)
Bend					± 0.25	± 0.25
MPW	28.1	2.26	0.01	0.5	± 0.75	± 0.13
IVU	0.9	0.4	0.01	0.4	± 0.10	± 0.03
EU (hor)	11.9	1.13	0.01	0.45	± 0.15	± 0.15
EU (vert)	0.01	0.45	9.11	0.86	± 0.15	± 0.15
EU (circ)	7.3	0.9	7.28	0.9	± 0.15	± 0.15

13.1 General layout of a front end

The general layout of a front end showing the arrangement of its different elements is given in Figs. 13.1 and 13.2. In the following the different components and their functions are described; note that at different light sources one or more components could be missing [13.1, 13.2].

- 1) **Gate valve** at the end of the vacuum system (beam pipe) of the storage ring: this is a manual valve used only for maintenance.

- 2) **First fixed absorber** at the end of the beam pipe: this absorber is installed to protect the beam pipe against synchrotron radiation from the bending magnet, but it must have an opening through which all the radiation coming from the IDs can pass. This absorber is usually called the ‘crotch absorber’.
- 3) **Vacuum tube** with a length of up to 2 m and a diameter of 40 mm: this tube is needed to ensure enough space between the front end and the storage ring for the installation of front-end components. Also, a pumping unit has to be installed in this section to control the vacuum. The vacuum gauge of this unit controls the gate valve to the storage ring and is connected to the interlock system.
- 4) **Fluorescent screen** to monitor the radiation pattern from the IDs: this screen has to be inside the vacuum tube described above. Use of the fluorescent screen is possible only for small stored currents (around 5–10 mA) within the storage ring. The fluorescent screen will only be used for the commissioning of the beam line.
- 5) **First X-ray beam position monitor (XBPM)** to monitor the position of the radiation beam coming from the ID: this XBPM is at the end of the vacuum tube described in 3). In order to obtain a precise measurement of the position of the ID radiation, the whole radiation fan from the IDs has to reach the first XBPM. This means, again, that no ID radiation has to be stopped at the crotch absorber. During the commissioning of the beam line, the XBPM can be cross-checked against the fluorescent screen.
- 6) **Second fixed absorber and bellows**, which determine the aperture within the front end: the second fixed absorber more or less absorbs the main part of the radiation coming from the ID that is not needed for the experiments; it should be designed to absorb all the radiation coming from the IDs.
- 7) **Photon shutter**, which absorbs all the radiation coming from the IDs: the photon shutter completely intercepts the X-ray beam via a fast-acting mechanism in order to isolate the downstream components (beam line) from the source (storage ring). The photon shutter also acts as a safety device to protect the bremsstrahlung shutter from direct X-ray beam impingement. The photon shutter should be combined with the second fixed absorber, and both components should be combined with a pumping unit. The photon shutter is needed to protect subsequent valves from being irradiated with synchrotron radiation from the bending magnet and IDs. The time for closing the photon shutter is approximately 0.3–1 s.
- 8) **Second gate valve** in combination with a **fast valve**: this is the next unit in the arrangement. A pumping unit is also needed for both components, because the fast valve can be opened only if the pressure is roughly the same on both of its sides. This combination of gate and fast valve is needed to protect the storage ring against vacuum failures in the front end and beam line. The second gate valve should be as near as possible to the storage ring. The time for closing is approximately 8–10 ms for the fast valve and 1–2 s for the gate valve.
- 9) **Delay line** if needed: the aforementioned conductance pipe could be used as a delay line.
- 10) **Second XBPM** (if needed) to monitor the position of the radiation beam coming from the ID: the distance between the first and second XBPMs should be at least 4 m.
- 11) **Collimator** for absorbing some parts of the bremsstrahlung coming from the long straight sections. The transverse dimensions of the collimators are determined from ray-tracing calculations.
- 12) **Moveable aperture** to determine the aperture needed for special experiments.
- 13) Space for a **diaphragm** or **filter holder**.
- 14) **Bremsstrahlung shutter** in front of the shielding wall: the bremsstrahlung shutter is not cooled. The transverse dimensions of the bremsstrahlung shutter are determined from ray-tracing calculations.

FRONT END

- 15) **Gate valve** with pumping unit behind the shielding wall (inside the experimental hall): this unit must incorporate a fast pressure sensor for triggering the fast and gate valves as well as the photon and bremsstrahlung shutters.
- 16) **Beryllium window.**

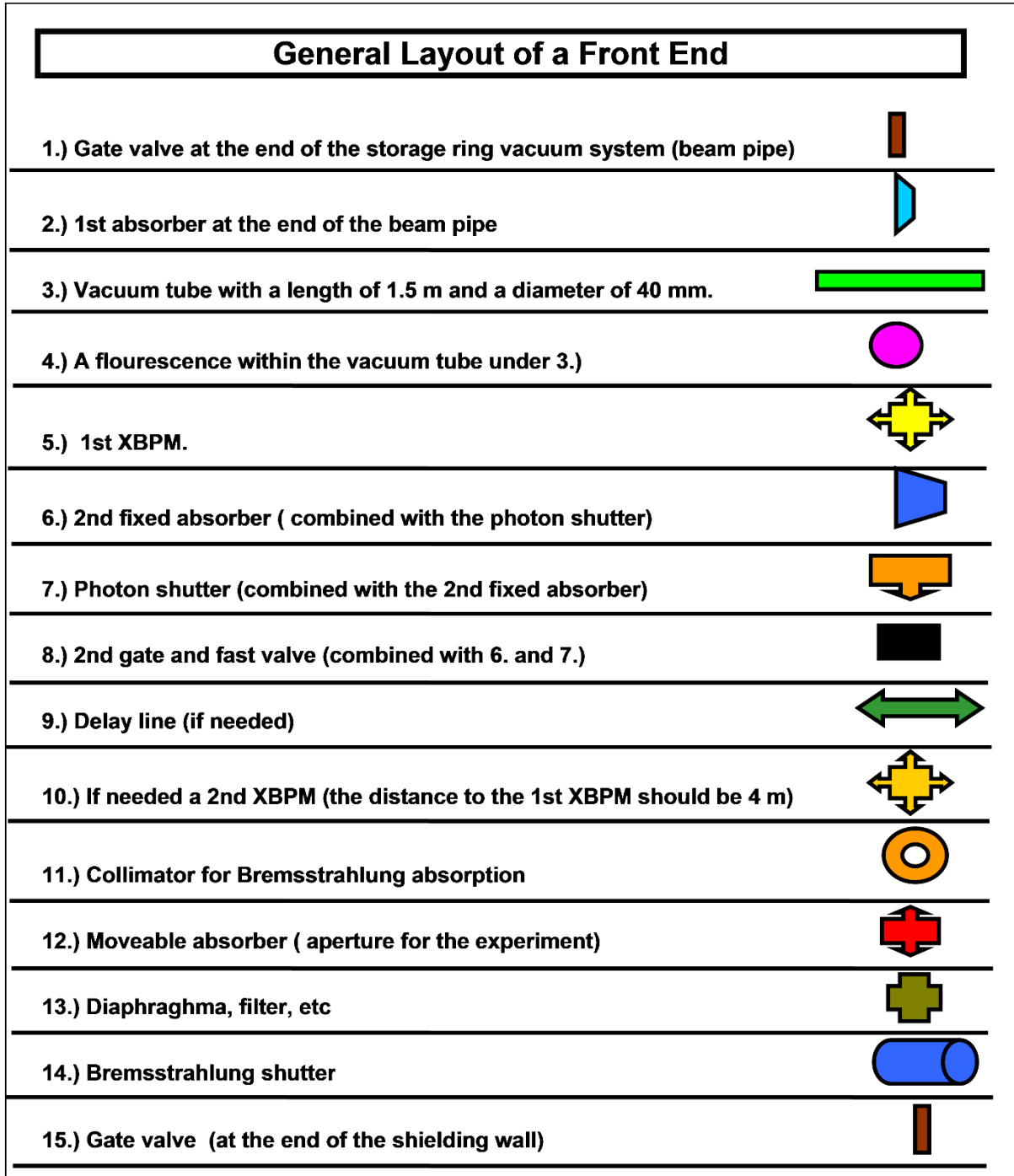


Fig. 13.1: Different elements used in front ends

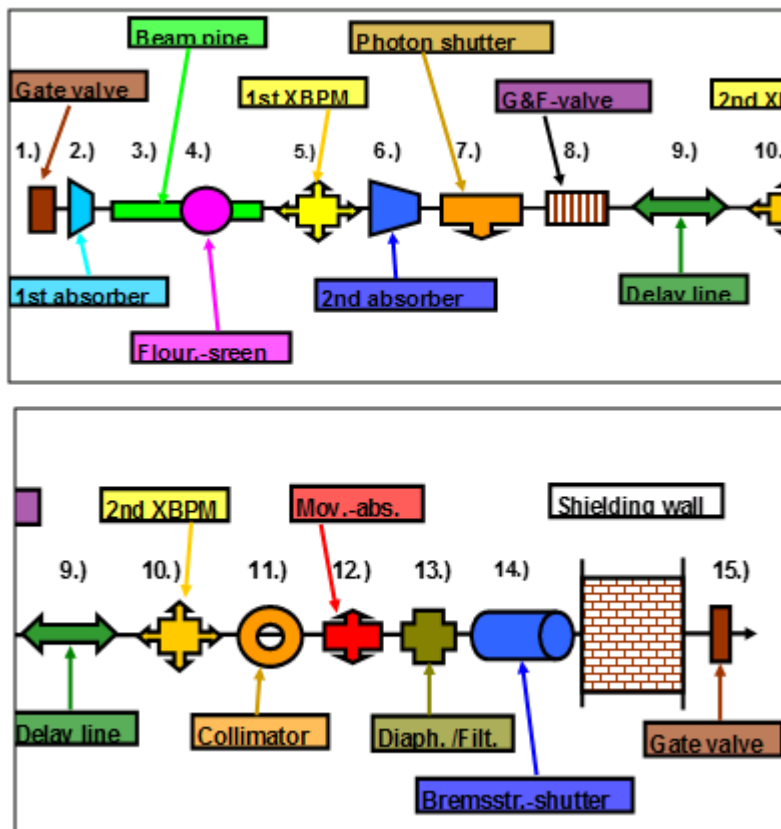


Fig. 13.2: Arrangements of elements in a front end

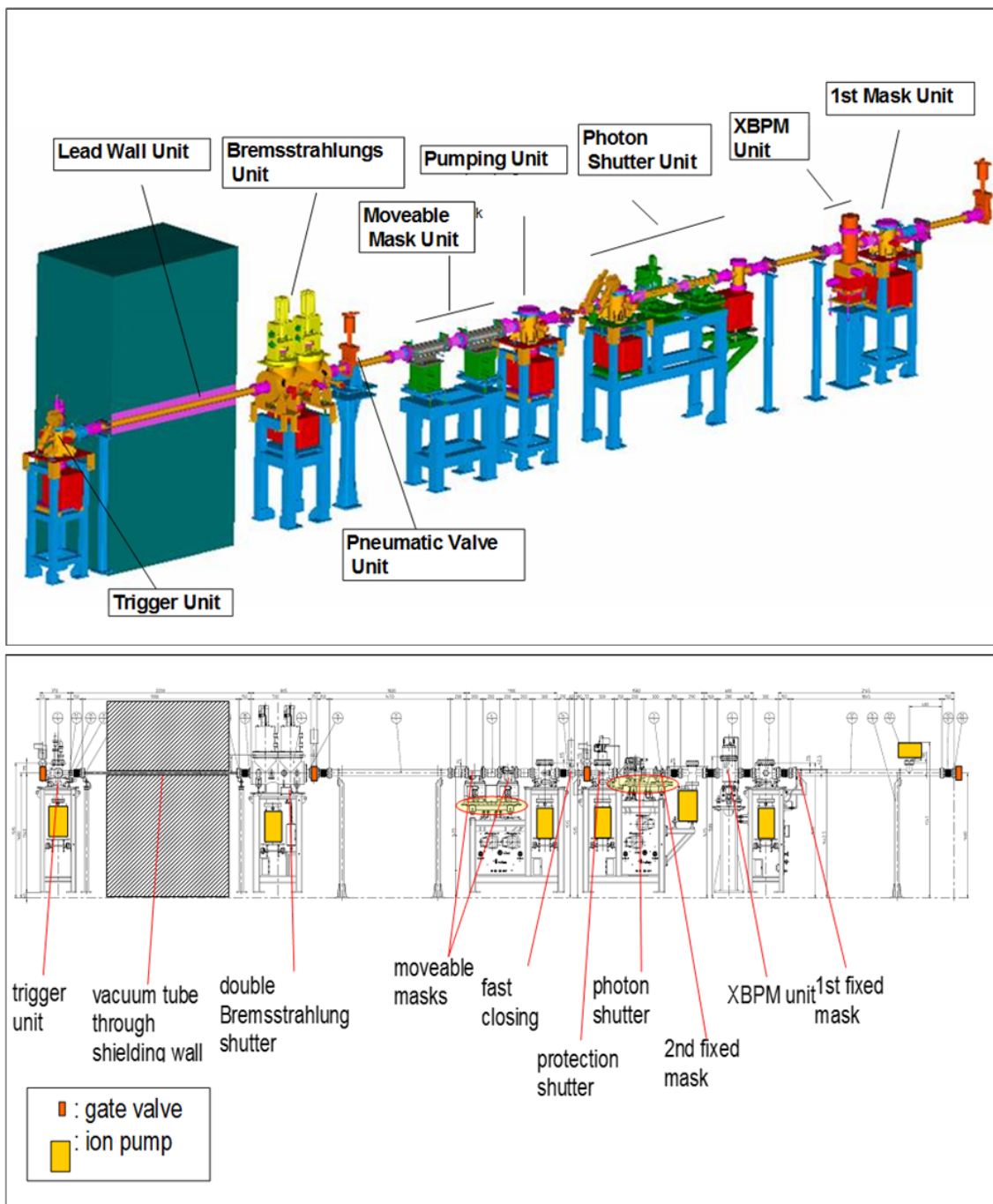


Fig. 13.3: Front-end components used in ALBA

13.2 A particular front-end layout

The layout of each individual FE has to be adapted to take into account the geometrical constraints defined by the available distance from the SR isolation valve to the front wall of the tunnel and by interference with adjacent elements (SR girders, RF cavities, cooling water pipes, etc.). Besides, radiation-absorbing elements have to be designed to meet the aperture and power load requirements imposed by both the characteristics of the photon source and the needs of users of the beam line. At the same time, an effort should be made to maintain a suitable degree of standardization between the components of different FEs. With these considerations, a modular design approach has been adopted.

The distance from the SR isolation valve to the front wall for phase-I FEs ranges from 7 to 9 m, but because of the proximity of the storage ring, the space available for the installation of FE

components inside the tunnel is effectively 5–7 m. A typical layout of phase-I FEs is shown in Fig. 13.3, with the following sequence of components going from the SR isolation valve to the beam line: (1) first fixed mask, (2) XBPM, (3) second fixed mask, (4) photon shutter, (5) protection shutter, (6) fast-closing shutter (FCS), (7) movable masks, (8) double bremsstrahlung shutter, (9) vacuum pipe through the front wall, and (10) trigger unit. These elements are described below.

- (1) **First fixed mask:** a first fixed mask is installed in all FEs with an ID as a source in order to protect downstream FE components from dipole radiation. This element consists of a 39 mm-thick copper block with internal water cooling, which is integrated into the first vacuum pipe connecting the SR isolation valve and the first pumping chamber of the FE. The copper block has an aperture that allows passage of the full ID radiation fan, taking into account the maximum allowed mis-steering of the e-beam.
- (2) **XBPM:** each FE is equipped with one XBPM to monitor the position of the photon beam at a distance of 7–10 m from the source point. Monitors have been produced according to the designs developed by K. Holldack from BESSY in collaboration with FMB [13.3]. Each XBPM makes use of four narrow negatively biased blades which intercept the edges of the photon beam distribution. The photoelectrical currents generated at each blade are measured using a low-current monitor, and after being combined they allow an on-line determination of the horizontal and vertical positions of the centre of the beam. Two different blade configurations have been employed depending on the characteristics of the source. In the case of bending magnet sources, four copper blades in the so-called staggered pair monitor configuration have been used. This configuration allows only the determination of the vertical position of the beam, but on the other hand it provides an internal calibration standard. In the case of ID sources, four tungsten blades arranged in an X shape have been used, providing information on both horizontal and vertical planes. This configuration requires a proper calibration for each setting of the ID source. The size and geometry (distances and angles) of the tungsten blades have been adapted to the beam characteristics of each ID in order to optimize the sensitivity of the system.
- (3) **Second fixed mask:** in all cases, second fixed masks consist of an out-of-vacuum copper body (either OFHC or Glidcop, depending on the situation) with an internal rectangular aperture defined by four inclined surfaces. Depending on the amount of power to be absorbed, different cooling schemes have been implemented. For small heat loads (less than 0.5 kW, bending magnet and IVU sources), a single cooling loop drilled around the aperture has been used. For medium heat loads (0.5–4 kW, such as EU and conventional wiggler sources) a ‘spiral cooling’ configuration has been used (Fig. 13.4, left), with a stainless steel cover (water box) brazed to the cylindrical body of the absorber, where a cooling channel in spiral form has been machined. For higher heat loads (greater than 4 kW, SCW source) a ‘side cooling’ configuration has been used (Fig. 13.4, right), with grooves machined next to each surface defining the aperture and a cover of the appropriate dimensions closing the machined cavity.
- (4) **Photon shutter:** the photon shutter is responsible for interrupting the photon beam when necessary, protecting all downstream components from synchrotron radiation. In the case of bending magnet sources with associated power of less than 100 W, an in-vacuum pneumatically actuated absorber has been used. The absorber consists of a water-cooled plate of OFHC copper positioned at an acute angle (30°) to the incident beam. In the case of FEs with an ID as source (between 1.5 and 13.5 kW), an out-of-vacuum design based on the high-power absorber of ESRF [13.4] has been used. In this design two brazed Glidcop blocks define an internal aperture whose profile depends on its vertical position. When in open position the aperture consists of two lateral straight surfaces that allow the passage of the full radiation fan as defined by the second fixed mask. When in the closed position, the two lateral surfaces are tapered and water-cooled according to the ‘side cooling’ scheme (see Fig. 13.4) and stop the photon beam completely. The vertical stroke required in order to go from one

position to the other is 16 mm, and the pneumatic actuator that drives the system takes approximately 200 ms to close the shutter.

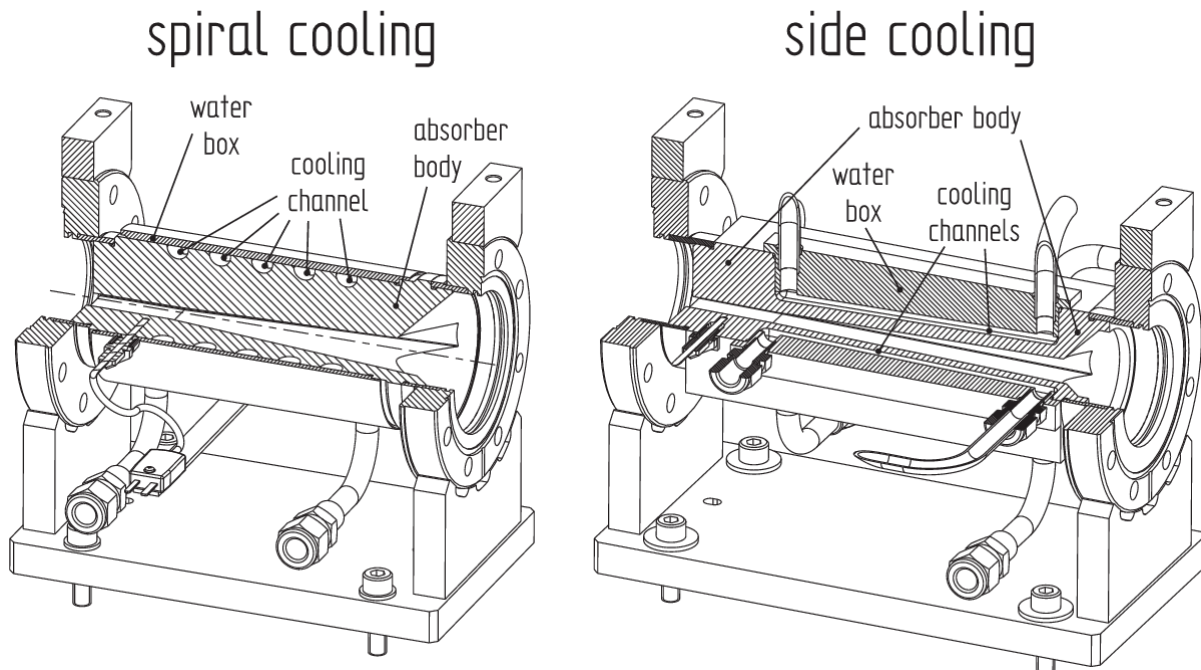


Figure 13.4: Second fixed masks for conventional wiggler sources (left) and superconducting wigglers (right), illustrating the ‘spiral cooling’ and ‘side cooling’ schemes.

- (5) **Protection shutter:** this element consists of a pneumatic cylinder and an in-vacuum 10 mm-thick copper plate. It does not have any water cooling and completely blocks the photon beam when in closed position. It is triggered together with the FCS and has a closing time of around 50 ms, thus protecting the FCS from synchrotron radiation during the time lapse required for the photon shutter to close.
- (6) **Fast-closing shutter (FCS):** this is a series 77 DN40 all-metal fast shutter which closes in less than 10 ms when triggered. The vacuum gauges providing the trigger signal for the FCS are located in the trigger unit, which is installed in the optics hutch of the beam line, thus protecting the SR against a vacuum failure in the beam line.
- (7) **Movable masks:** movable masks allow users to define the photon beam delivered to the beam line. They consist of a pair of Glidcop blocks, each having a rectangular aperture with two tapered surfaces (top-left surfaces for mask 1 and bottom-right surfaces for mask 2) that intercept part of the photon beam. All inclined surfaces are water-cooled using the ‘side cooling’ scheme. Each mask is mounted on a motorized X–Y stage, and when combined the two masks delimit a aperture with rectangular cross-section of customizable size and position within the maximum aperture defined by the second fixed mask.
- (8) **Double bremsstrahlung shutter:** this radiation safety element comprises two pneumatically actuated UHV-compatible tungsten-alloy blocks with a cross-section of 120 mm × 120 mm and a thickness of 200 mm. The two blocks are driven simultaneously but independently for redundancy reasons, and in combination with the photon shutter they provide users with safe access to the optics hutch of the beam line during operation.
- (9) **Vacuum pipe through front wall:** this pipe has a rectangular cross-section and provides the connection between the accelerator tunnel and the optics hutch; it has a standard length of 1.9 m and an internal opening of 41 mm × 20 mm for all FEs that have a larger vertical aperture requirement.
- (10) **Trigger unit:** the so-called trigger unit consists of a vacuum chamber where the two dedicated vacuum sensors that trigger the FCS are installed.

13.3 Cooling of front-end components

The design and validation of all power-absorbing elements have to be carried out in-house by means of finite-element analysis (FEA, ANSYS). As a rule of thumb, the incidence angle of the radiation on the cooled surfaces of the absorbers has to be decreased, reducing the maximum power density to 10–15 W/mm².

A cooling water velocity of 3 m/s has been considered in most of the cases, and it has been increased up to 4 m/s when required. The upper limits for the peak values of the different magnitudes considered within the FEA thermal analysis have been: (a) 100°C for the cooling water temperature; (b) 150°C for the temperature on the walls of the cooling channels; (c) 65–70 MPa stress and 0.1% strain in the case of OFHC copper absorber bodies; and (d) 250 MPa stress and 0.2% strain in the case of Glidcop absorber bodies.

References

- [13.1] ALBA, <https://web.archive.org/web/20160925132959/http://www.cells.es/en/about/welcome>, last accessed September 25th 2016.
- [13.2] *National Synchrotron Light Source II : Conceptual Design Report* (Brookhaven National Laboratory, Upton, New York, 2006).
<https://web.archive.org/web/20170705041358/https://www.bnl.gov/nsls2/project/CDR/>
- [13.3] K. Holldack, J. Feikes, and W. B. Peatman, *Nucl. Instrum. Methods Phys. Res., A* **467–468** (2001) 235, [https://doi.org/10.1016/S0168-9002\(01\)00555-1](https://doi.org/10.1016/S0168-9002(01)00555-1)
- [13.4] L. Zhang *et al.*, ESRF Thermal Absorbers: Temperature, Stress and Material Criteria, Proc. MEDSI02, 5–6 September 2002, Argonne National Laboratory, Argonne, Illinois, USA, p. 377. https://web.archive.org/web/20170128074927/http://www-eng.lbl.gov/~als/FEA/MEDSI_2002/High_Heat_Load_Comp/ESRF_Thermal_Absorbers.pdf

14 Injector

D. Einfeld

14.1 Booster synchrotron

The booster synchrotron should deliver a small beam size to the storage ring in order to minimize the beam losses during injection and accordingly the radiation dose. To minimize the emittance, a large number of bending magnets has to be installed, and this is possible if the booster synchrotron is placed in the same tunnel as the storage ring. This was first done at the Swiss light source [14.1] and after that at ALBA [14.2] as well as the TPS [14.3]. To minimize the number of magnets, the bending magnets will have a vertical focusing component. With this type of magnet the horizontal partition number J_x will be increased, which further reduces the emittance (see section 14.4).

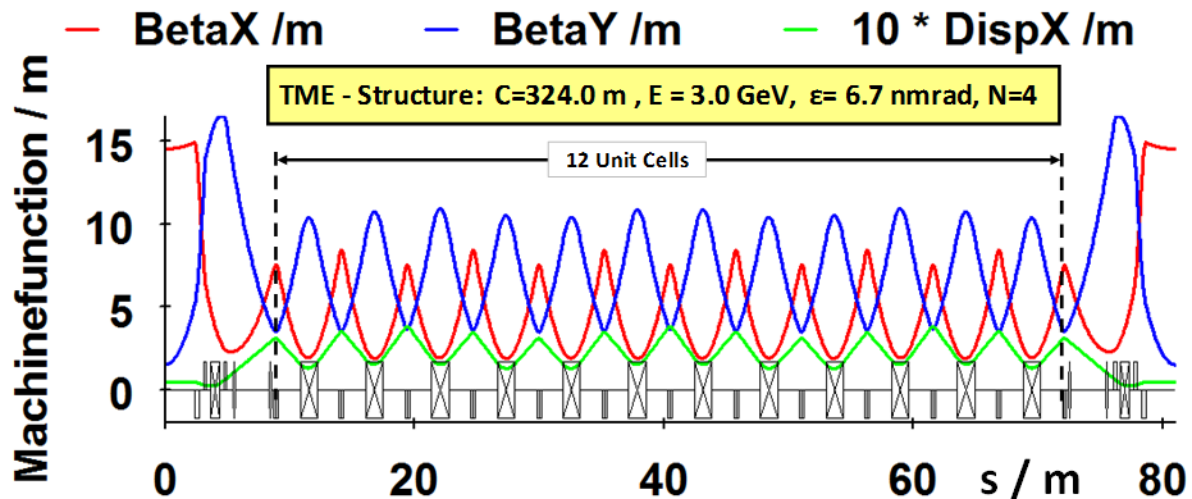


Fig. 14.1: The machine functions of the booster in one achromat (one quadrant of the ring)

For the booster synchrotron at least two straight sections are needed: one for the injection and one for the installation of the cavity. Like ALBA and the TPS, a four-fold symmetry with four straight sections was chosen. The circumference of the booster was chosen to be 324 m, which corresponds to a harmonic number of 108. The average distance between the storage ring and the booster is 3.82 m in this case. The machine functions within one achromat, shown in Fig. 14.1, are similar to those of ALBA and the TPS, yielding an emittance of 6.7 nrad at 3 GeV and 4.7 nrad at 2.5 GeV. The cross-sections of the beam are: $\sigma_x = 311 \mu\text{m}$ and $\sigma_y = 17 \mu\text{m}$. The lattice consists of the two matching sections at the beginning and end of the achromat (Fig. 14.3) along with 12 ‘unit cells’ (Fig. 14.2) forming the middle of the arc. The lattice functions have to be optimized further in order to achieve a sufficient dynamic aperture.

The specifications of the magnets are as follows.

- Bending: $L = 1.393 \text{ m}$, $\phi = 6.9231^\circ$, $\rho = 11.5286 \text{ m}$, $G = 3.1 \text{ T/m}$, $B_{\text{max}} = 0.868 \text{ T}$ (3 GeV).
- Quadrupole: $L = 0.36 \text{ m}$, $G = 15.01 \text{ T/m}$ (3 GeV).

These specifications are roughly the same as for the ALBA booster synchrotron (see Fig. 14.4).

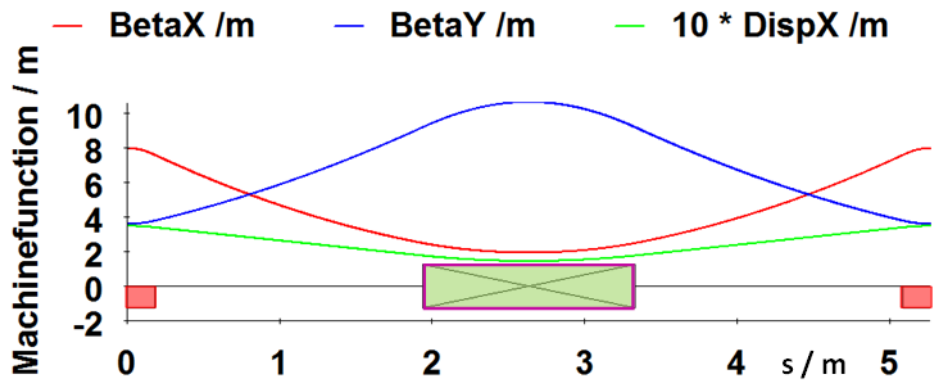


Fig. 14.2: The machine functions within the ‘unit cell’ of the booster synchrotron

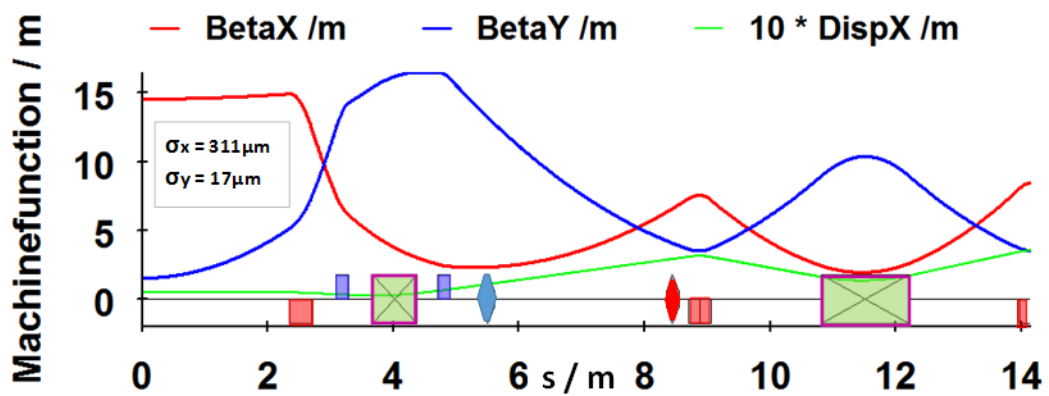
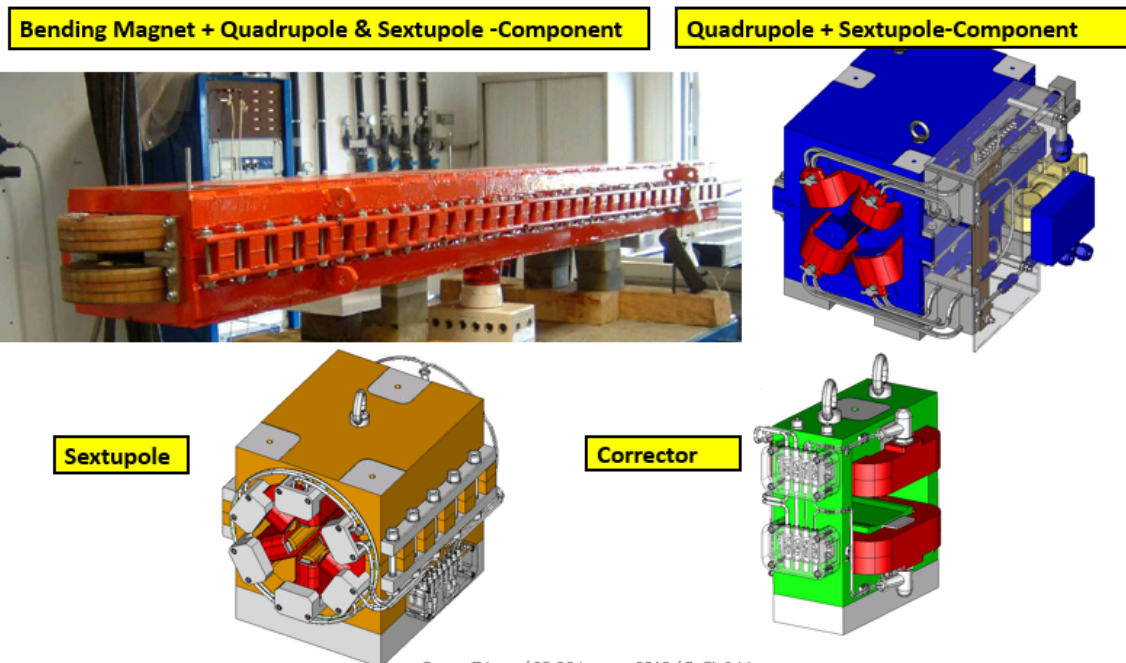


Fig. 14.3: The machine functions within the ‘matching cell’ of the booster synchrotron



Forum Trieste / 25-26 January 2018 / D. Einfeld

30

Fig. 14.4: The magnets used for the ALBA booster synchrotron

The magnetic layout of one achromat (one quadrant), together with the lattice data, is presented in Fig. 14.5. The compensation for the chromaticities will be done with some sextupole components in the bending magnets and in the quadrupoles and with some sextupoles in the matching region. The

INJECTOR

injection energy of the booster will be 100 MeV, and it will be ramped up with a frequency of around 1–3 Hz to 2.5 or 3 GeV.

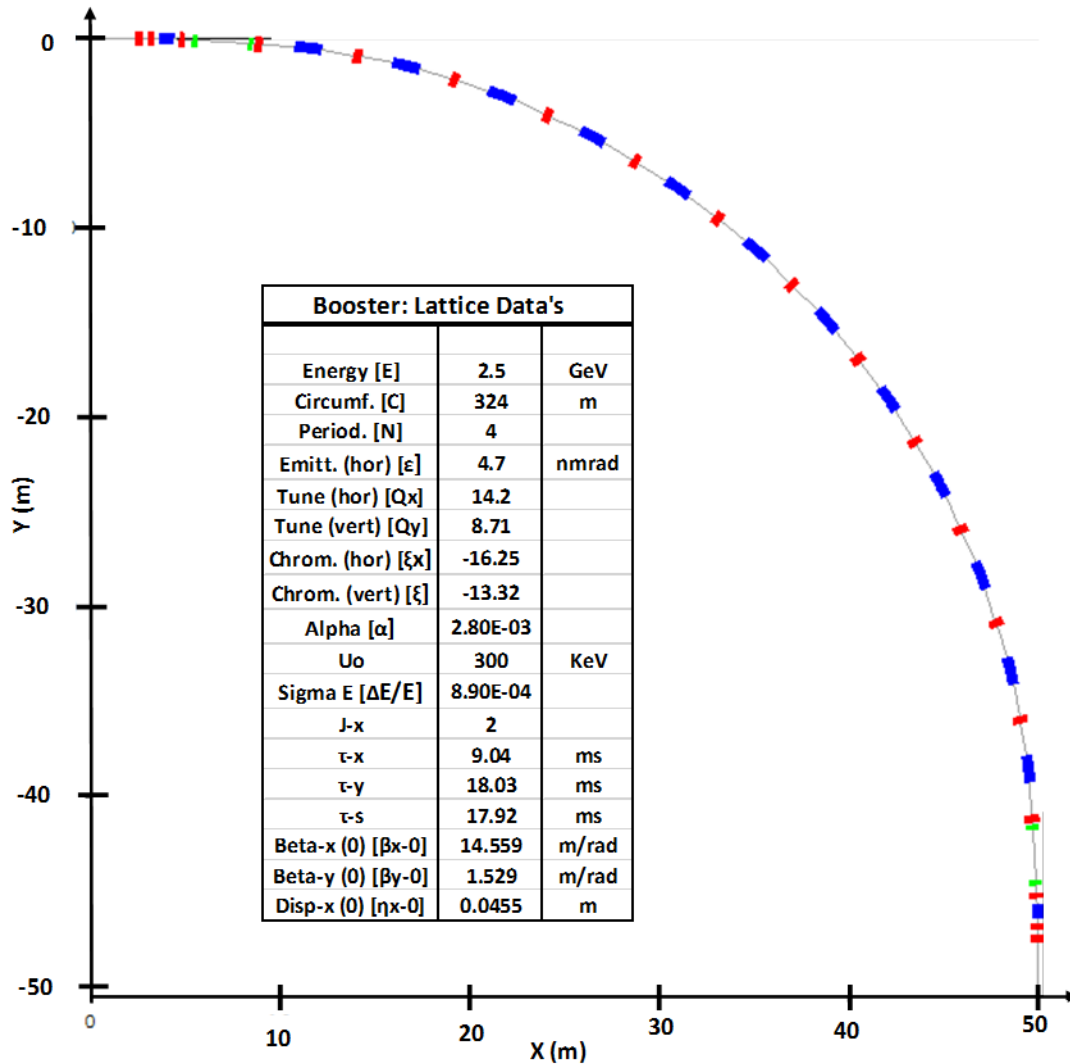


Fig. 14.5: The magnetic structure within one achromat (one quadrant) of the booster synchrotron, together with the lattice data.

The injection energy of the booster will be 100 MeV and it will be ramped up with a frequency around 1 to 3 Hz to 2.5 or 3 GeV.

14.2 Linac

The principal layout of the 100 MeV linac is presented in Fig. 14.6. The electron gun delivers a beam with an energy of 90 keV, which goes through a 500 MHz and a 3 GHz pre-buncher and then a buncher to reach an energy of 16 MeV. With two other accelerating sections, the final energy of the beam will be 110 MeV. The dimensions of the linac are shown in Fig. 14.7; the overall length is approximately 14 m.

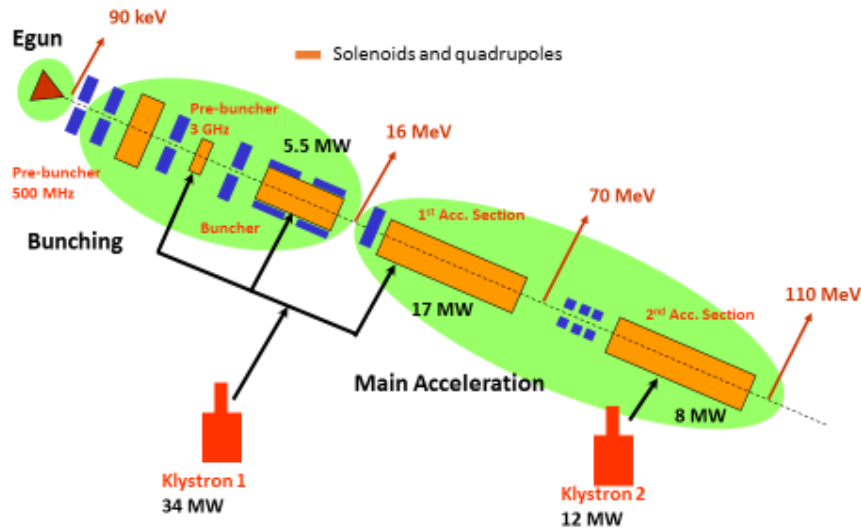


Fig. 14.6: The principal layout of the 10 MeV linac built by Thales for ALBA. The focusing coils and quadrupoles are in blue.

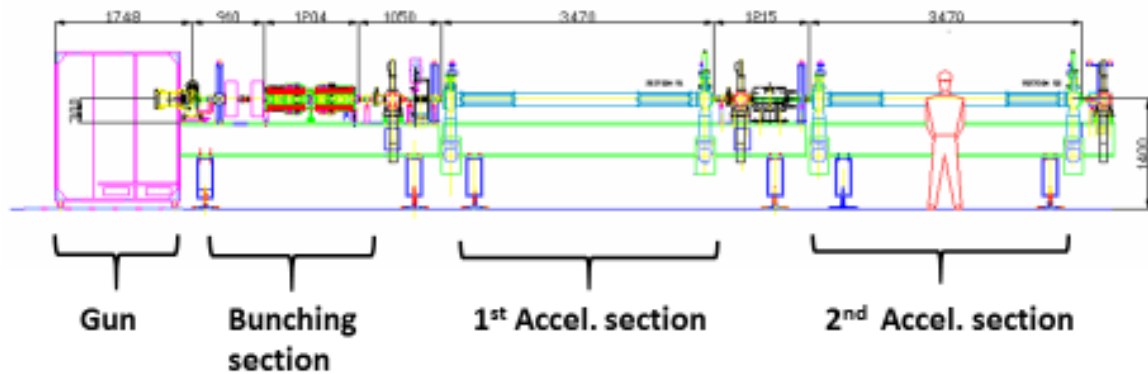


Fig. 14.7: The dimensions of the different linac components, leading to an overall length of 13.92 m

For the focusing of the beam, solenoids and quadrupoles are required, which are represented in Fig. 14.8 by blue boxes. The specifications of the 110 MeV beam are given in Table 14.1. The normalized emittance should be smaller than 30π mm rad with an energy spread of less than 0.25%. The linac has to be run in single- as well as multi-bunch mode.

For the diagnostics of the beam, six FCTs, three fluorescent screens, and one BPM are installed. The arrangements of the different components are presented in Fig. 14.8. A picture of the 110 MeV linac installed at ALBA is shown in Fig. 14.9.

Table 14.1: The specification of the 110 MeV electron beam delivered by the linac

Parameter	Single-bunch	Multi-bunch
Frequency	3 GHz	3 GHz
Bunch length	<1 ns (FWHM)	0.3–1 μ s
Charge	>2 nC	>4 nC
Energy	>100 MeV	>100 MeV
Pulse to pulse (δE)	<0.25% (r.m.s.)	<0.25% (r.m.s.)
Energy spread ($\Delta E/E$)	<0.5% (r.m.s.)	<0.5% (r.m.s.)
Normalized emittance ($1\sigma_{x,y}$)	< 30π mm mrad	< 30π mm mrad
Repetition rate	3–5 Hz	3–5 Hz

INJECTOR

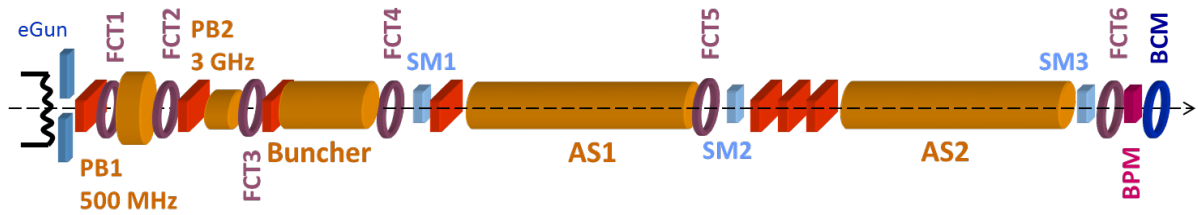


Fig. 14.8: The diagnostic elements for the linac and their locations

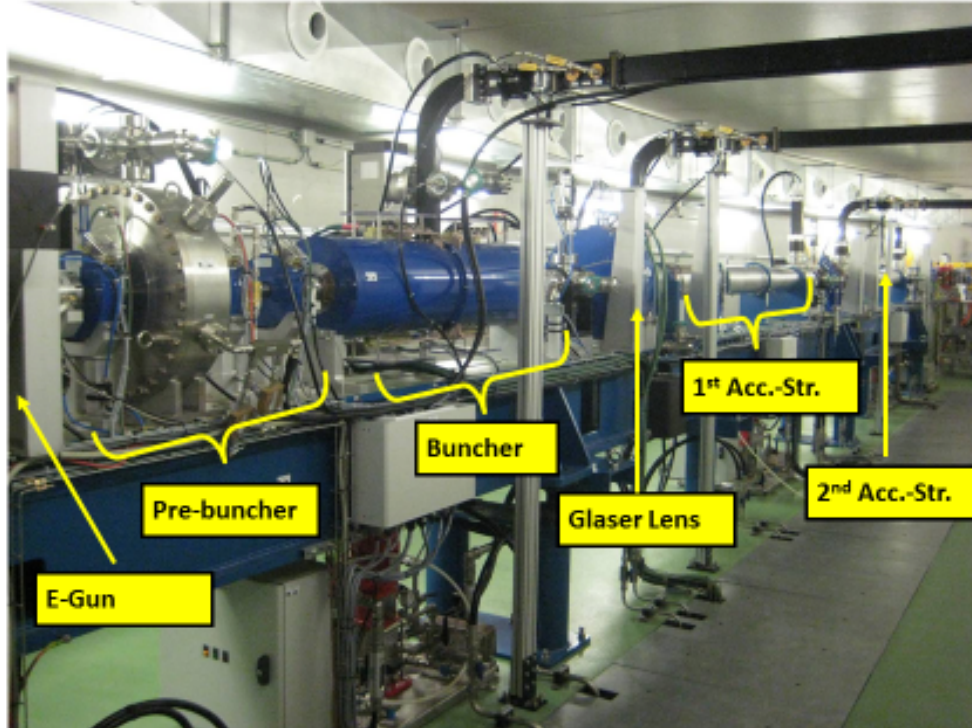


Fig. 14.9: Picture of the 110 MeV linac installed at ALBA

14.3 Diagnostic beam line

For the measurement and determination of the specification of the electron beam coming from the linac a special diagnostic line is needed. The set-up of this diagnostic line is shown in Fig. 14.10. The linac ends with a vacuum valve and the linac-to-booster transfer line (LTB) starts with two correctors, a quadrupole triplet, and a bending magnet. The bending magnet has two settings, one for the operation, bringing the beam to the booster, and one for the diagnostic, switching the beam into the diagnostic line. The diagnostic line is equipped with a scraper (SCR), a fluorescent monitor (FSOTR), a beam charge monitor (BCM2), a fast current transformer (FCT), and a Faraday cup (FCUP) for a beam dump.

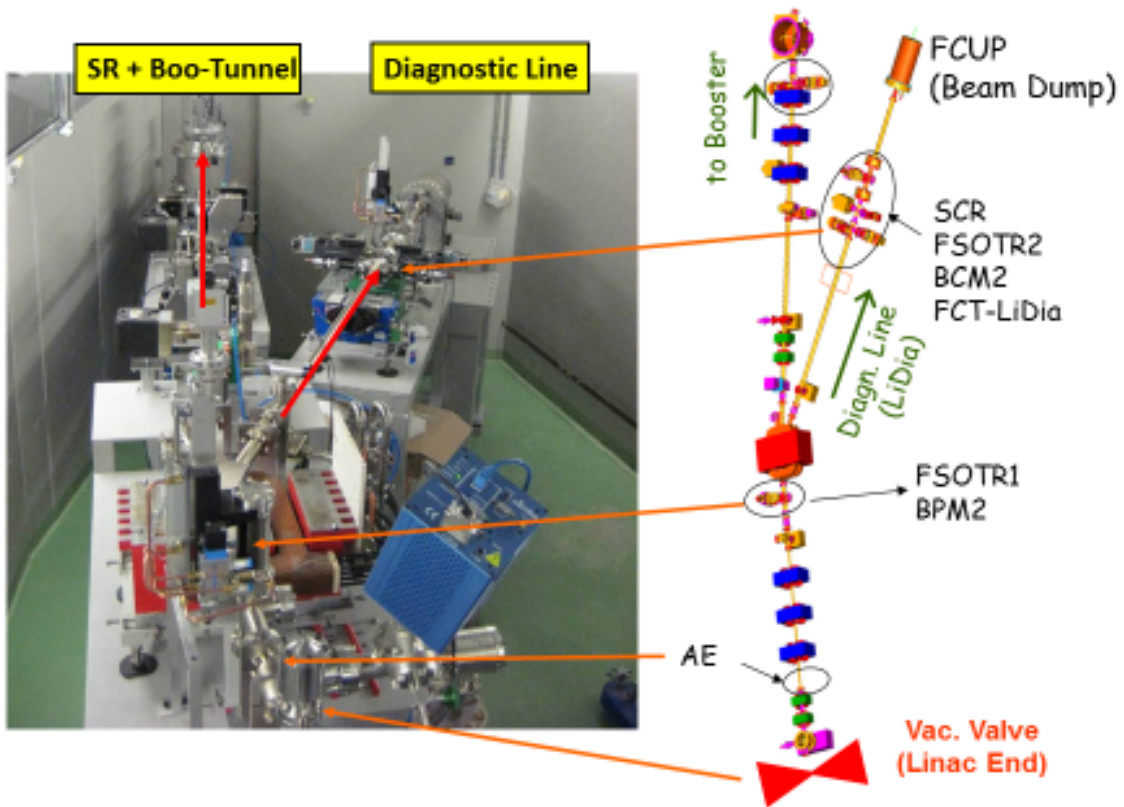


Fig. 14.10: The layout of the beginning of the LTB and the diagnostic line

The layout of such a diagnostic beam line installed at ALBA could also be used for the SEE-LS-project. A picture of the ALBA set-up is shown in Fig. 14.11.

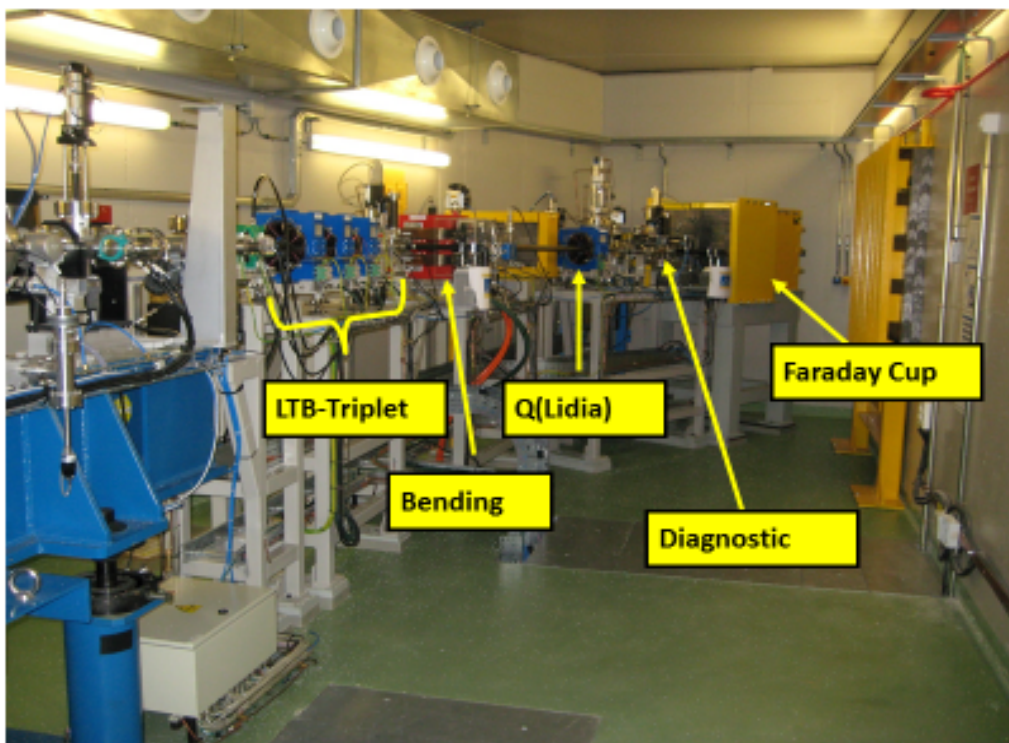


Fig. 14.11: A picture of the linac diagnostic beam line at ALBA

14.4 Linac-to-booster transfer line (LTB)

For optimization reasons the linac bunker has to be near the inner shielding wall of the machine tunnel; this means that the inner shielding wall should be the shielding wall for the machines in the tunnel and the linac. This arrangement is shown in Fig. 14.12.

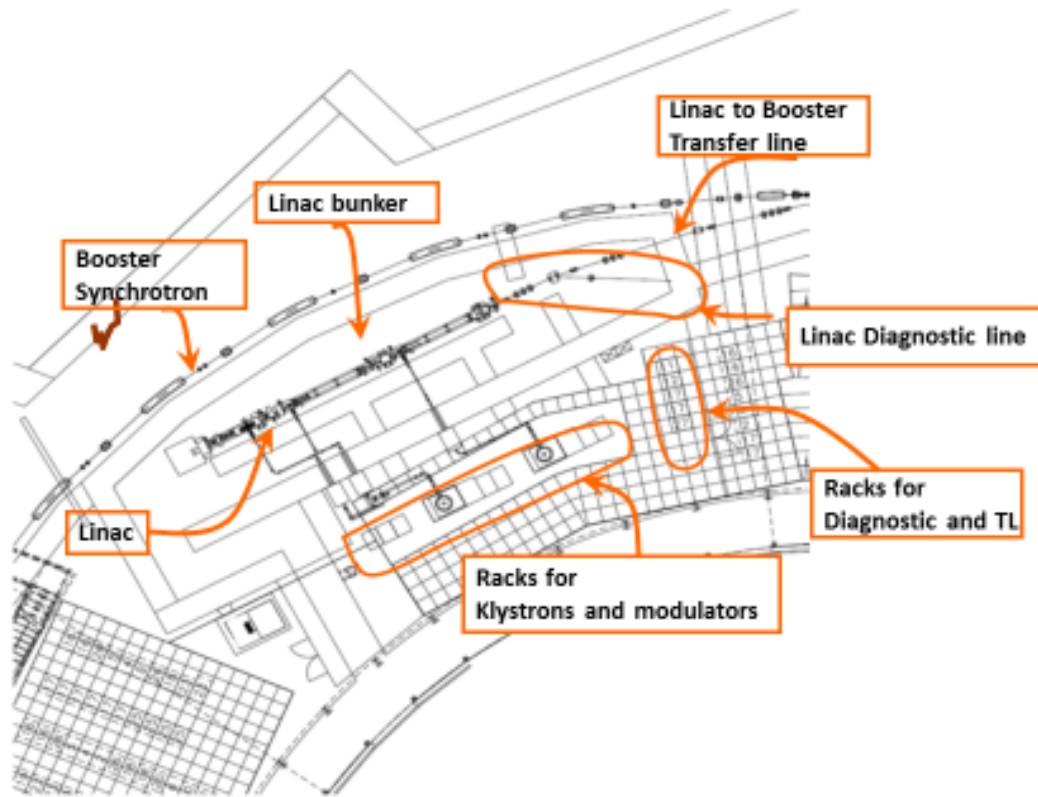


Fig. 14.12: The arrangement and layout of the linac bunker near the machine tunnel

With this arrangement the LTB needs a deflection angle for proper injection into the booster synchrotron. That is the reason for the bending magnet B1 at the beginning of the diagnostic beam line (see Fig. 14.10).

The LTB has to perform a matching of the beam parameters from the linac to the booster synchrotron. This can be done with an arrangement like the one in Fig. 14.13. In the middle of the transfer line is the shielding wall to the machine tunnel. In the linac bunker one bending magnet (B1) and two quadrupole triplets (Q1–Q3 and Q4–Q6) are needed. After the shielding wall another bending magnet (B2) and a quadrupole triplet (Q7–Q9) are required.

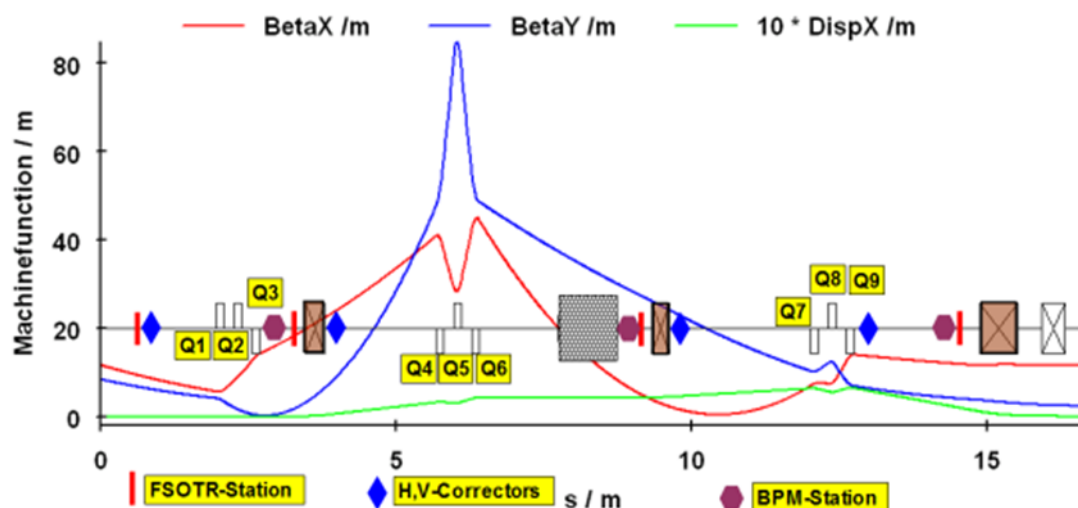


Fig. 14.13: The layout and machine functions of the LTB

14.5 Booster-to-storage ring transfer line (BTS)

The BTS has to perform a matching of the beam parameters from the booster synchrotron to the storage ring. A possible layout is presented in Fig. 14.14. The transfer line consists of (including septa and kicker) five bending magnets and seven quadrupoles. For the design it is important to have a magnet-free section in the middle of the transfer line, leaving space for transport in the machine tunnel.

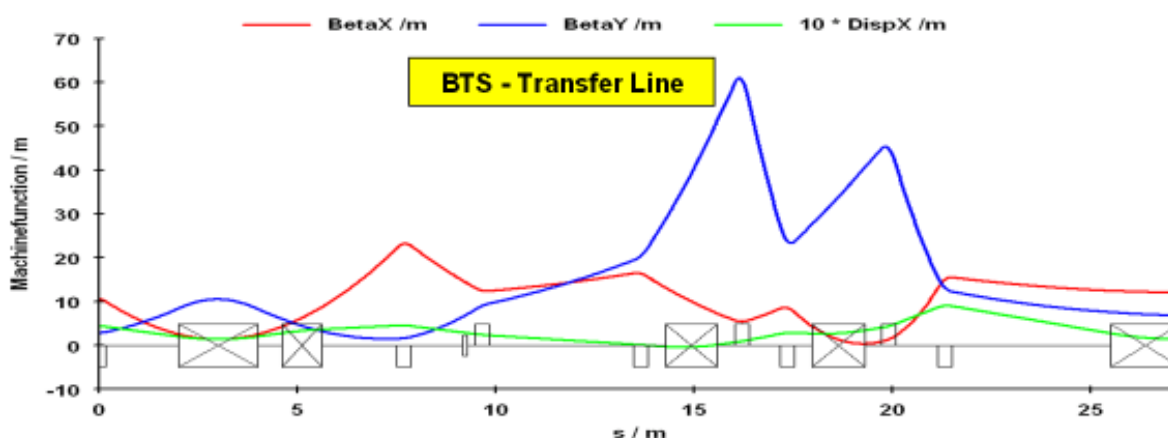


Fig. 14.14: The layout and machine functions of the BTS

References

- [14.1] W. Joho, M. Munoz, and A. Streun, *Nucl. Instrum. Methods Phys. Res. A* **562** (2006) 1, <https://doi.org/10.1016/j.nima.2006.01.129>
- [14.2] G. Benedetti *et al.*, Optics for the ALBA Booster Synchrotron, Proc. EPAC2008, Genoa, Italy, 23–27 June 2008 (CERN, Geneva, 2008), p. 2148. <https://inspirehep.net/record/795036/>
- [14.3] H. C. Chao *et al.*, Current Design Status of TPS 3 GeV Booster Synchrotron, Proc. PAC2009, Vancouver, Canada, 4–8 May 2009 (TRIUMF, Vancouver, 2011), p. 2258. <https://inspirehep.net/record/1378770>

15 Control system

D. Fernandez

15.1 Introduction

The control system refers to the hardware and software for the supervision, control, operation, protection, and data acquisition of the accelerators and beam lines. The main control system for the machine covers the linac, booster, storage ring (SR), and front ends (FEs) and includes the RF system, magnet power supplies, vacuum, diagnostics, insertion devices (IDs), etc. This distributed system uses several independent Ethernet networks, with dedicated servers in the computing room and particular databases. The term ‘control system’ also refers to independent (autonomous) hardware and software infrastructure for each beam line, including motion control, optics, diffractometers, sample environment, vacuum, etc.

The beam line control systems are independent from the logical point of view, having different databases and independent links with the central storage for data acquisition. At the same time they are very much interconnected with certain subsystems of the machine (control of IDs, FE diagnostics, etc.).

On the software side, building a system from scratch is no longer a cost-effective option and is not justified in most cases. A framework or toolkit and a middle layer are required. Tango[§] is a mature option, continuously growing and supported by other synchrotrons in the world. Tango is an object-oriented framework for building distributed control systems. The basic concept behind Tango is the device server model. A server is a program that manages one or several devices which are encapsulated in a piece of software (class).

This distributed control system runs on computers known as input/output controllers (IOCs) arranged around the technical areas in the accelerators and the controls racks in the beam lines. IOCs are typically compact PCI (cPCI) crates and are diskless, although industrial PCs (with disk) are also widely used. In modern designs, the number of IOCs can be reduced in favour of virtual servers in central data centres and extensive use of the Internet of Things (IoT), by means of pieces of equipment connected to the network. Figure 15.1 shows the generic architecture of a distributed control system like the one installed at ALBA [15.1, 15.2].

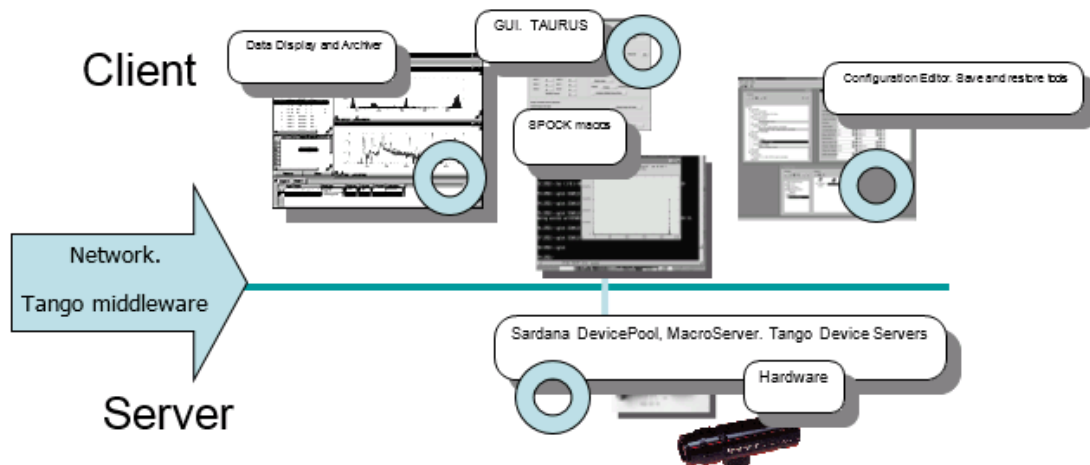


Fig. 15.1: Generic architecture of the software, similar to the control system at the ALBA synchrotron

15.2 Network

The overall architecture of the distributed control system is based on Ethernet. Ethernet is used for supervision and data communications and in most cases also as a fieldbus. There are two main reasons

[§]Tango Controls: <http://www.tango-controls.org>

for specifying Ethernet as the communications standard for both fieldbuses and supervision: cost and simplicity of maintenance.

All devices are by default required to have an Ethernet connection. But some of them, due to lack of availability in the market or other reasons (that is, convenience for other applications, since the control system must adapt to the market and customer needs), may specify different communication channels.

15.2.1 *Ethernet connected*

Ethernet is the preferred communication channel for:

- power supplies, except for eventually the correctors of the storage ring because of the very high bandwidth and short latencies that may be required for the fast-orbit feedback (FOFB), including power supplies of the booster and transfer lines, of the storage ring dipoles, quadrupoles, and sextupoles, and of the pulsed elements;
- oscilloscopes, spectrum analysers, and signal generators for diagnostics, which have an Ethernet link;
- Libera boxes for BPM controls, which communicate through Ethernet links;
- motor controllers;
- CCD cameras (gigabit Ethernet or GigE) for the fluorescence screens, optical transmission radiation monitors (OTRs)** , and other diagnostic cameras;
- input/output controllers, servers, archivers, etc.;
- radiation monitors, which use the independent VLAN for safety, and also the programmable logic controllers for the personnel safety systems, which are linked through the Ethernet for user interface and diagnostics;
- some vacuum devices, such as rest gas analysis (RGAs), and other vacuum components which may be linked by Ethernet or other channels such as serial lines that might be more convenient from the installation cost point of view.

15.2.2 *Not Ethernet connected*

Exceptionally, some devices may require another type of communication channel.

- Correctors for the storage ring: if Ethernet is not fast enough (the latency of the switches can be too high), there are other options such as the PSI interface [15.3]. As an example, the ALBA synchrotron installed PSI interfaces and not Ethernet, in order to meet the needs of the FOFB, which requires a closed loop in the 10 kHz range.
- Programmable logic controllers (PLCs): the connection between CPUs and the remote periphery of the PLCs often has a separate link due to performance and cost reasons. A deterministic Ethernet (such as the Ethernet or PowerLink) is also frequently required. It will be separated from the general network hardware because of high traffic, specific latency requirements, and the need to avoid unwanted interactions with the standard switches. The safety PLCs for the personnel safety system use a dedicated communication channel (Pilz SafetyBus, for example) for design reasons and to satisfy legal constraints (IEC 61508 compliance). Other PLCs can use other links such as ProfiNET, RS485, etc.
- Vacuum devices: pump controllers and gauge controllers may still be sold with other cheaper interfaces such as serial lines. In this case, serial-to-Ethernet adapters would be needed to

**An optical transmission radiation monitor is a device that emits light by transmission of radiation, which is monitored by a CCD or CMOS-type camera.

CONTROL SYSTEM

interface with the control system, which in practical terms would add extra points of failure (the Ethernet-to-serial converters). Nowadays, the range of Ethernet vacuum controllers on offer is much wider than a few years ago, and the prices should fit the budget.

- Other devices such as beam loss monitors: these may use different independent networks, such as different flavours of RS485.
- Other specific devices and detectors for the beam lines with particular hardware: these can be interfaced through different technologies, such as GPIB, serial line, dedicated fibre optics, etc.

The control networks must be separated from the offices and from the outside world by firewalls, specific network configurations, and demilitarized zones. The control system of the machine would need a number of different VLANs^{††} with private IPs, as shown in Fig. 15.2. Beam lines, most computing services, and the office networks often have public IPs. The network should use modern services and implement up-to-date cyber-security policies, assigning IP addresses by dynamic host configuration protocol (DHCP), with appropriate authentication and authorization protocols. In order to maintain consistency across the whole system, the IPs and MAC addresses are assigned when possible during the pre-installation of the equipment and are centralized in the general corporative equipment and cabling database (asset configuration). Network configuration files such as RADIUS, DHCP, and DNS can be generated from this central corporative equipment and cabling database.

^{††}VLAN stands for ‘virtual local area network’, defined by the standards IEEE 802.1D, 802.1p, 802.1Q, and 802.10.

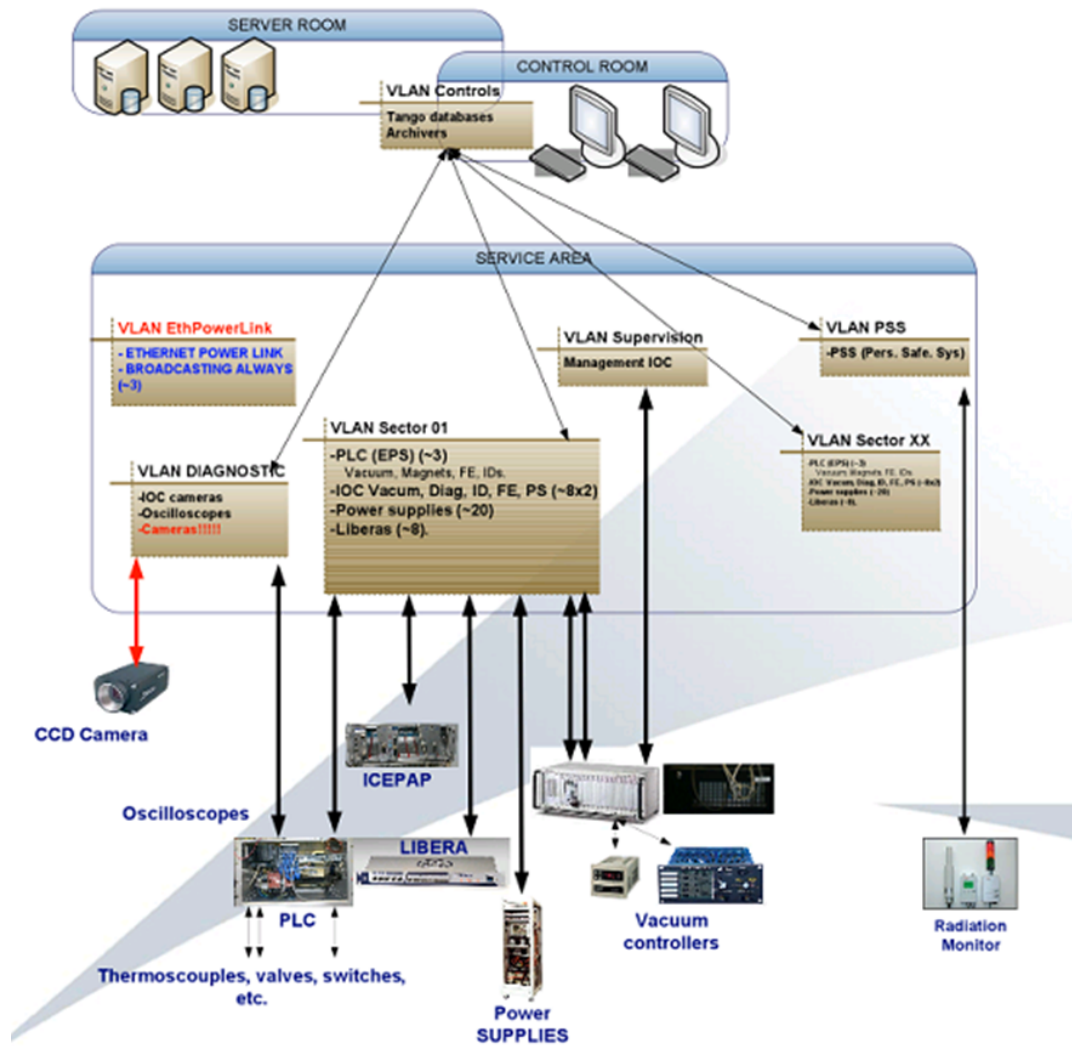


Fig. 15.2: Generic schema of the layout of the networks of a particle accelerator control system [15.1]

Several VLANs should be used for the machine controls: one general, one generic control network per sector, one for diagnostics, one for monitoring, one for protection and interlock systems, and one for safety systems, among others.

15.3 Controls administration

It is a common practice to have a generic control system account for administration. This has a few drawbacks from the security point of view but offers a number of advantages when organizing the installation and deploying software packages. The account has a predefined structure, in which packages, scripts, and configuration files are placed. This directory structure manages databases, servers, clients, graphical interfaces, scripts, remote booting, source files, and all the backups.

15.3.1 Development environment and collaborations

Version control tools need to be used. Subversion^{##} and Git^{##} are good choices, and both are well adapted to continuous integration/continuous delivery/continuous deployment tools and techniques. Keeping repositories in an external server enables collaborations between institutes, but for packaging and deployment an internal server would probably still be needed. On a second level, the Tango

^{##}Subversion or svn is a software version control tool: https://en.wikipedia.org/wiki/Apache_Subversion

^{##}Git is a version control system: <https://en.wikipedia.org/wiki/Git>

collaboration has a Git repository in Github^{***}. Tango runs on both Microsoft Windows and Linux. The main operating system is often Linux, but Windows is used in some particular cases where specific hardware is required. Tango supports C++, Java, and Python for both client and server sides. Pycharm, Eclipse, and Qt Designer^{†††} are tools commonly used by developers. Being multi-platform and compatible with multiple programming languages, Tango offers a lot of flexibility. In the particular case of ALBA, most computers run Linux although some devices run on Windows, such as the control system for DLLRF^{‡‡‡} and the interferometer for metrology measurements, and the preferred software programming language is Python [15.2]. In some facilities, such as the SOLEIL Synchrotron, use of Microsoft Windows operating systems and the Java programming language is more extensive.

A lot of work has already been done and is ready to be used free of charge. Other scientific installations—and in particular synchrotrons like the aforementioned ALBA, ESRF, SOLEIL, DESY, Max-IV, and Elettra—have actively contributed to the development of Tango, Sardana [15.4], and Taurus [15.5] on the software side, and the Electrometer [15.6] and IcePAP [15.7] motor controllers on the hardware side. Collaborations with these projects, though they would need to fulfil a few requirements and conditions depending on the project, are worth considering.

15.3.2 *Standard tool for maintaining versions of software packages installed*

A version control tool is not sufficient for keeping up-to-date an inventory of the versions installed in every machine. In addition, processes and tools for packaging, delivering, and deploying software are needed. The ESRF developed in the early 2000s a tool, blissinstaller, that was later used at the ALBA synchrotron as well. This tool keeps a central database with the software packages (RPM^{§§§}) built and the version of each package installed in every machine (beam line, accelerators, etc.). Other more recent approaches use the native package management systems provided by the operating system (in either a local or a remote repository); this is more complicated to set up in the first place but may become easier to maintain in the longer term. Continuous integration/continuous delivery/continuous deployment and the modern concepts of DevOps are also reaching the control systems. Tools such as Jenkins^{****} are common nowadays and becoming crucial in the software deployment automation process.

15.3.3 *Remote booting*

The physical computers in the service area will be *diskless*; they get their operating system from an external server in the computing room. This has proven to be an excellent solution for maintaining and keeping versions up to date, but it is probably not yet suitable for beam lines where every beam line has an ‘independent control’, making the gains of such a configuration less significant. As an example, the control system of the machine at ALBA initially installed 120 compact PCIs for the interfaces with timing, 16 industrial PCs for vacuum control, 10 industrial PCs for front ends, and another 6 for insertion devices, as well as a few others related to LLRF and fan-outs for timing, making a total of more than 160 industrial computers. The central services for the control system also require virtual machines and physical bare-metal servers in the data centre, for central databases, archiving, etc. These can be of the order of 50–100 servers, depending on the size of the installation.

***Tango Git repository: <https://github.com/tango-controls>

†††Pycharm: <https://www.jetbrains.com/pycharm/>; Eclipse: <https://www.eclipse.org/>; QT Designer: https://en.wikipedia.org/wiki/Qt_Creator

‡‡‡DLLRF stands for ‘digital low-level radio frequency’ and provides fast regulation for the RF phase and amplitude [15.8].

§§§RPM is the Red Hat Package Manager: [https://en.wikipedia.org/wiki/Rpm_\(software\)](https://en.wikipedia.org/wiki/Rpm_(software))

****Jenkins is a leading open-source software for DevOps automation: <https://jenkins.io/>

15.4 The control system centralized sequencer and hardware access manager: the Sardana ‘device pool’

The control systems of beam lines and accelerators might look very different, but they are actually not so distinct [15.1]. The control for the machine is closer to a commercial SCADA^{††††}, where the total number of elements to control is very large but the number of different types of elements remains constrained. The control for the beam lines, based on detectors data acquisition, sample environments, and synchronization with motor movements, is more ‘ad hoc’. The key point is the need to be able to easily add and remove new hardware from one experiment to the next or in the middle of an experiment, and to be able to configure scans with multiple motors, experimental channels, and on-line plotting and data visualization.

In some cases the machine also needs such capabilities as cycling magnets or scanning power supplies during the commissioning. The aim of the Sardana device pool is to provide an abstraction of the hardware with a simple and easy-to-use configuration tool and with a complete interface for configuring and executing scans and managing different user interfaces (graphical user interfaces or command line interfaces) at the same time. Figure 15.3 shows a snapshot of the initial main graphical user interface (GUI) of BL22 at ALBA, developed in Taurus and running Sardana and Tango [15.4, 15.5].

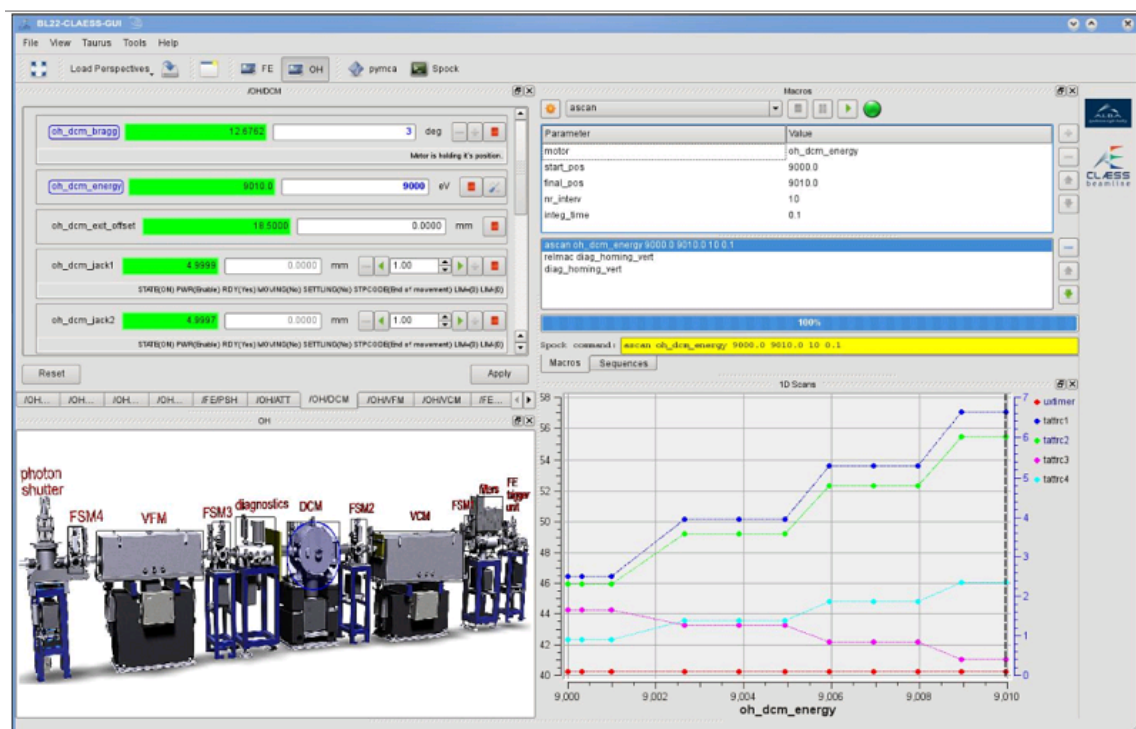


Fig. 15.3: Snapshot of a Sardana GUI based on Taurus at BL22 of ALBA

15.5 IT infrastructure: backups, storage, databases, central management information system, and system administration

There are a few areas of information technology (IT)^{††††} that are not covered in depth in this report but which are very relevant and critical to the control system. These include communications and network design and maintenance, cyber-security, system administration, databases, central storage, backup and archive services, and server hosting. Financial applications, project management tools, and service management infrastructure are other key IT disciplines that are not covered in this document.

††††SCADA, Supervision Control and Data Acquisition: <https://en.wikipedia.org/wiki/SCADA>

††††Information technology (IT): https://en.wikipedia.org/wiki/Information_technology

15.6 Naming conventions

Defining a naming convention at an early stage is crucial. A naming convention must exist for the engineering drawings and documents and must be compatible with the naming convention for the control system. These naming conventions, together with the equipment and cabling database [15.8], must be ready at an early stage.

15.7 Equipment, controls, and archiving databases

Databases are mandatory for the control system. Some facilities, such as SOLEIL or the ESRF, implement commercial databases (mostly Oracle or Microsoft SQLServer). ALBA has defined three main categories of databases, all of them running MySQL^{§§§§} (free of charge), which offer sufficient performance and features for most needs.

- (1) The **corporative equipment and cabling database** [15.8]: this has been developed early and made available to the electrical and electronic engineers. It is essential for the cabling definition and is intensively used during the cabling specifications, call for tenders, and installation. It has proven to be an excellent tool, which during operation became crucial for the maintenance. This database is used for pre-installing software in the IOCs, defining the network configuration (DNS, DHCP and RADIUS files, PLC variable definitions, etc.), and generating code automatically. The equipment protection system relies on it for defining PLC variables, Tango dynamic attributes, and GUI configuration files [15.9].
- (2) The **Tango database**: this is used, among other purposes, as a name service for Tango. It is the central point of the control system.
- (3) The **archiving database**: this is also a MySQL database running in separate hardware (much more powerful and adapted to the high workload of registering and making available to several clients of the order of 13,000 values last accessed in a few seconds). This archiving database records temperatures, setpoints, pressures, and many other process variables. The sampling rate can be further increased, up to the range of a few milliseconds, by using temporary archivers with dedicated databases.

Fast data loggers are purpose-specific systems that, depending on the requirements and on the hardware, can reach the micro/nanosecond or even faster ranges.

Signals can be visualized online in trending graphs and can also be recovered from the historical database. Data will typically be kept for few months and then removed and stored in permanent storage media.

The regular archivers define different triggering modes:

- regular intervals (user defined);
- on change (interval user defined);
- thresholds (greater/lower than a certain value);
- statistics, e.g. computation of minimum, maximum, average, r.m.s., full width half maximum (FWHM), etc. of the last X (user defined) samples.

15.8 Fast data logger

Although the fast data logger could be considered part of the archiver, the two are actually very different. The archiver is generic for any variable in the control system (in the case of Tango it can be considered part of the core services); this means that it collects data from device servers and saves the data to a database. The archiver provides tools for configuring the data to be archived, the signals, the

^{§§§§}MySQL is an open-source relational database management system (RDBMS): <https://en.wikipedia.org/wiki/MySQL>

frequency, and so on, as well as visualization tools for making trending graphs with on-line data and with historical data retrieved from the database.

The fast data logger is actually a set of subsystems, with independent hardware adapted to a particular purpose. There can be several fast data loggers for different applications and with different hardware. A fast data logger reads a reduced number of signals, which have to be stored in the microsecond/nanosecond range or faster. The aim is to have a record of the last few milliseconds for diagnostics and post-mortem analysis. Studying an arbitrary event means having a trace of relevant signals before and after the event. This is accomplished by means of one or several ring buffers, which can be configured with different sampling rates for different signals. In the ALBA synchrotron, for example, this is achieved by fast ADC cards (ADLINK2005; four ADC channels, 16 bits, simultaneous) running on cPCI crates or, in some cases, using specific hardware of a particular subsystem such as the Lyrtech hardware in the DLLRF system [15.10].

15.9 Equipment protection system

The equipment protection system (EPS) concerns the so-called interlocks and operation of components such as fluorescent screens, shutters, etc. It comprises the vacuum system, magnets, RF system, insertion devices, front ends, and beam lines. It is implemented using PLC technology. In the ALBA synchrotron the EPS is implemented with B&R PLCs that have the CPUs (around 50) in the service area and the remote peripherals (around 100) inside the tunnel interconnected by a X2S bus. PLC CPUs are connected by a deterministic network (Ethernet power link [15.11]). Every beam line has its independent EPS installation, with an independent CPU and dedicated peripherals. The PLC technology offers the reliability needed for the machine protection. Software interlocks managed by Tango with a potential risk of damaging components of the machine should be avoided.

Figure 15.4 shows the hardware layout of the vacuum system and the EPS. Racks with PLC CPUs are represented in red. The EPS of the machine manages thousands of signals that need to be processed and displayed in a comprehensive way. Figure 15.5 shows the main GUI of the EPS of the control system for the machine at ALBA.

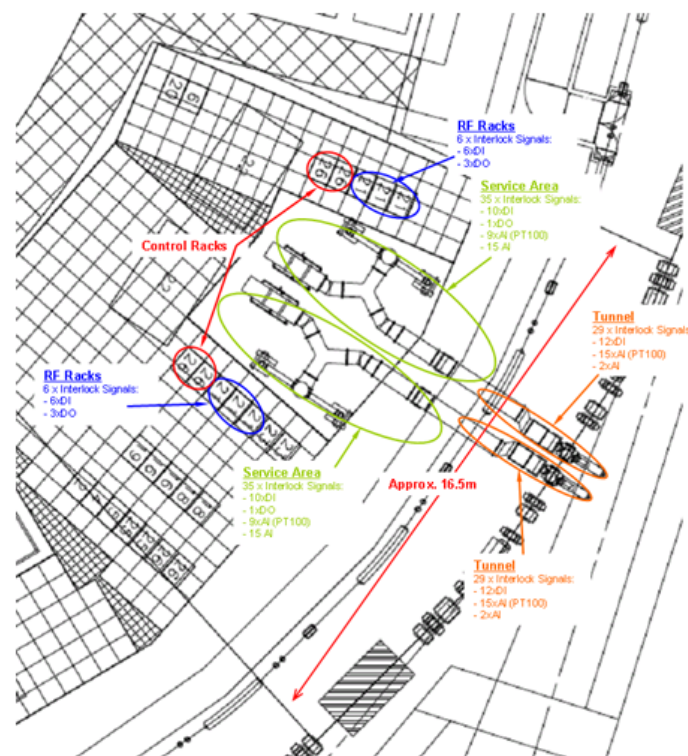


Fig. 15.4: Layout of the equipment protection system of an RF plant at ALBA

CONTROL SYSTEM

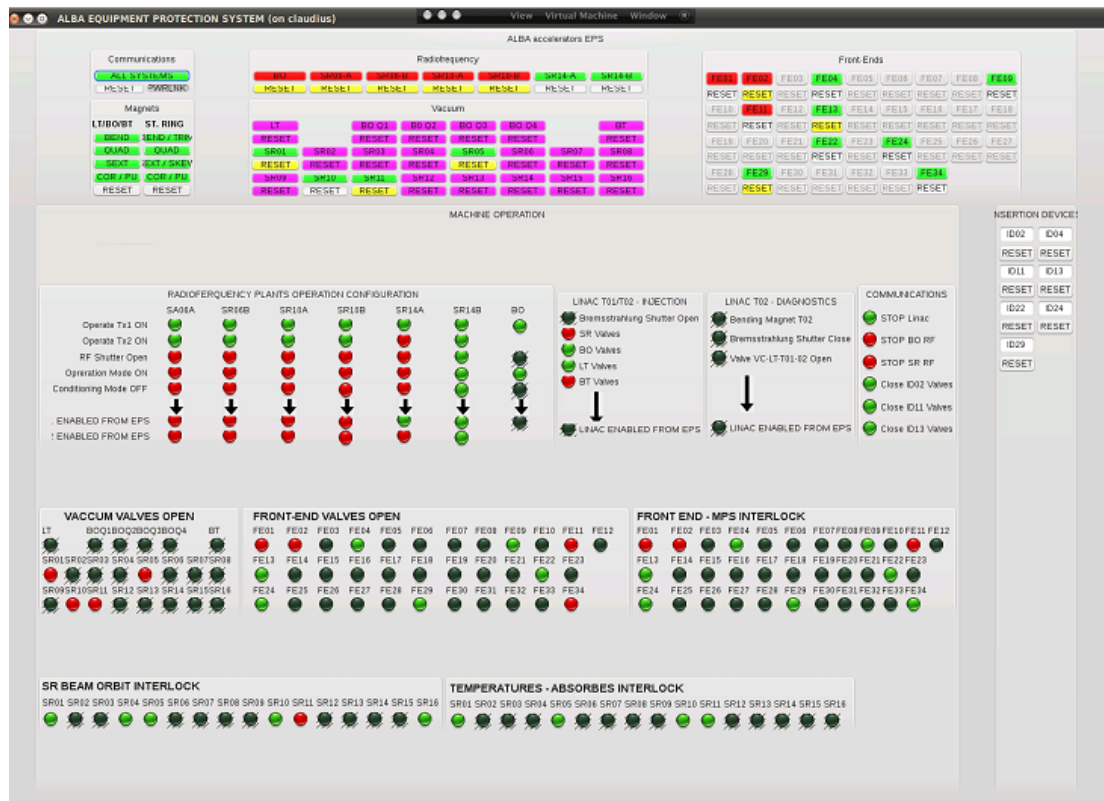


Fig. 15.5: Main GUI of the equipment protection system at ALBA

15.10 Machine controls

The software architecture is distributed. In a Tango-based control system, servers run in IOCs (Linux machines, PCI/cPCI computers), and human interfaces run on so-called workstations installed in the control room. IOCs and PLCs access field devices. Links between workstations, IOCs, and PLCs are based on Ethernet TCP/IP.

All software for the operation of the machine, user interfaces, device servers, archiving/restoring utilities, etc. communicate through Tango. User interfaces include those for monitoring settings and also archive/restore tools, tools for making trend graphs, etc. Two levels are defined:

- (1) the **server level**, which manages the hardware, runs on industrial PCs or cPCI racks, and comprises analogue input/output (AI/AO) cards, digital input/output (DI/DO) cards, connections to PLCs, and so on;
- (2) the **client level**, which includes user interfaces for monitoring, control, and setting values as well as recipes, archivers, etc. Fig. 15.6 shows the first version of the top-level synoptic of the booster synchrotron control system at ALBA.

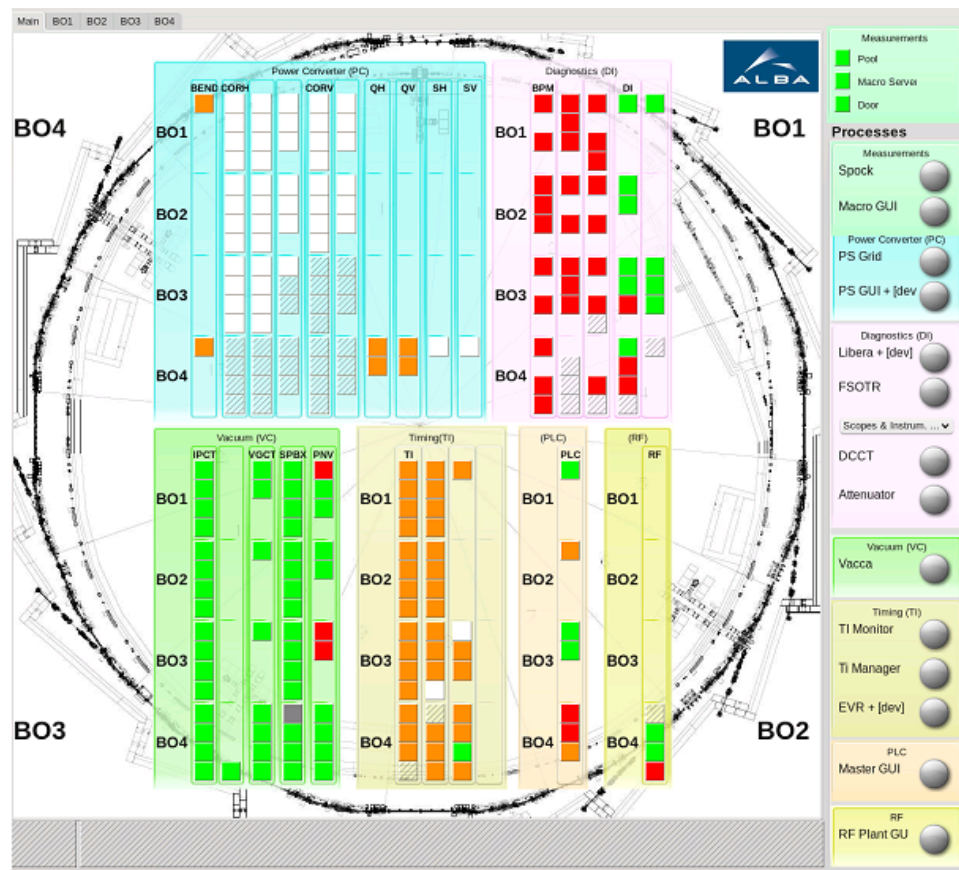


Fig. 15.6: Main GUI used for the booster control system at ALBA; it summarizes in a single view the state of all elements.

15.10.1 Subsystems

From the functional point of view, the control system can be divided into five parts (other divisions are possible, depending on the aim).

- **Supervisory control system** (Tango), including:
 - device servers, which control and get data from pieces of hardware called devices;
 - servers, which group low-level devices and implement sequences (e.g. Sardana device pool, macroserver);
 - generic graphical interfaces for monitoring, configuring, and operating the machine, which are used by operators, machine physicists, and beam line scientists; these interfaces are provided by Tango;
 - archiving tools for configuring signals to be stored long-term in the central databases and for archiving and restoring these signals;
 - alarm handling tools, which manage the configuration and operation of alarms and provide means of acknowledging and archiving alarms sorted by category, severity, and so on;
 - save/restore utilities, which save and restore the huge number of distributed parameters and set points of such complex machines as accelerators and beam lines, resulting in a sort of catalogue of recipes which are then available for restoring, consulting, comparing, etc.
- **Fast data logger** used to trace interlocks and problems in case of trips; typically it will run in the μ s range.
- **Timing and fast interlock system** used for synchronization of the machine and for propagation of fast interlocks along the accelerator.

CONTROL SYSTEM

- **Equipment protection system** responsible for the protection of all the equipment of the machine.
- **Personnel safety system (PSS)**, responsible for ensuring that any operation is done in safe conditions and sending any system to a safe state in case of failure.

Other subdivisions of the control system could be done by subsystems, such as vacuum system, radio-frequency system, timing system, diagnostic system, magnets and power supplies, insertion devices, and front ends.

15.11 Vacuum system

The vacuum control system is highly distributed as well. It deals with control, interlocks, and data acquisition. As an example, the machine at ALBA initially required around 170 ion pumps, 70 cold cathode gauges, 35 Pirani gauges, 45 gate valves, and more than 500 thermocouples—just for the vacuum subsystem. These numbers tend to increase after the commissioning to cover specific needs in different locations. Other devices, such as RGA and NEG pumps, may also be required (at ALBA, 16 were needed initially, one per sector). Figure 15.7(a) shows the main synoptic of the vacuum control system, VACCA, of the machine at ALBA [15.9]. Figure 15.7(b) shows an example of the definition and configuration of the instrumentation racks in the early stages of the project. These configurations of racks can be required at early stages during the hardware pre-installation.

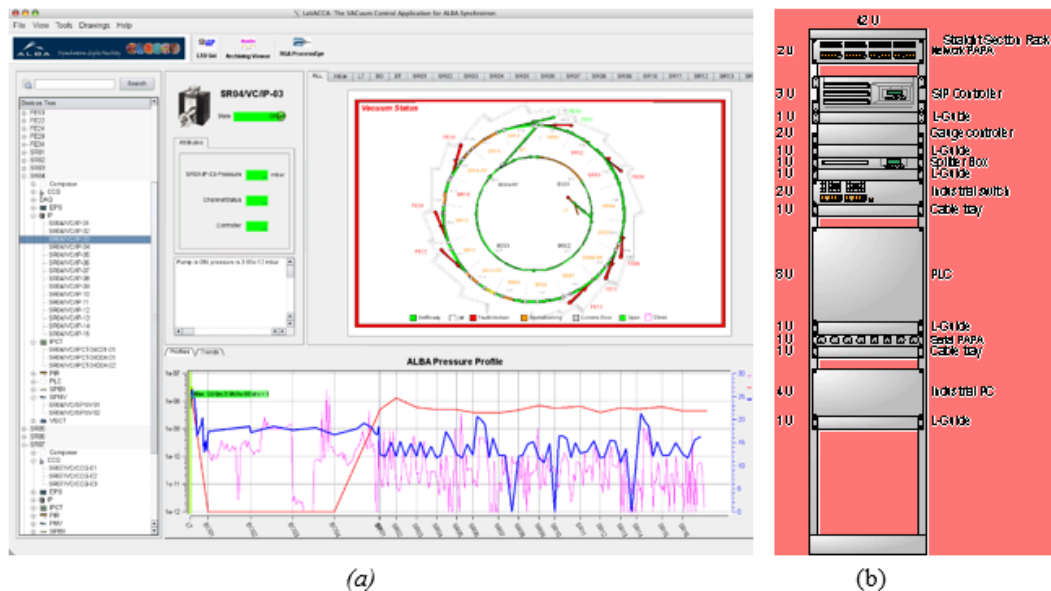


Fig. 15.7: (a) Synoptic of VACCA, the vacuum control system at ALBA [15.9, 15.1]; (b) first layout definition of a straight section instrumentation rack for the vacuum system.

15.12 Power supplies

All power supplies are interfaced by an Ethernet link, with the exception of those for the storage ring correctors, which may need a more deterministic interface. Figure 15.8 shows the generic electronic interface for monitoring and controlling setpoints and current measurements in all power supplies of the machine at ALBA.

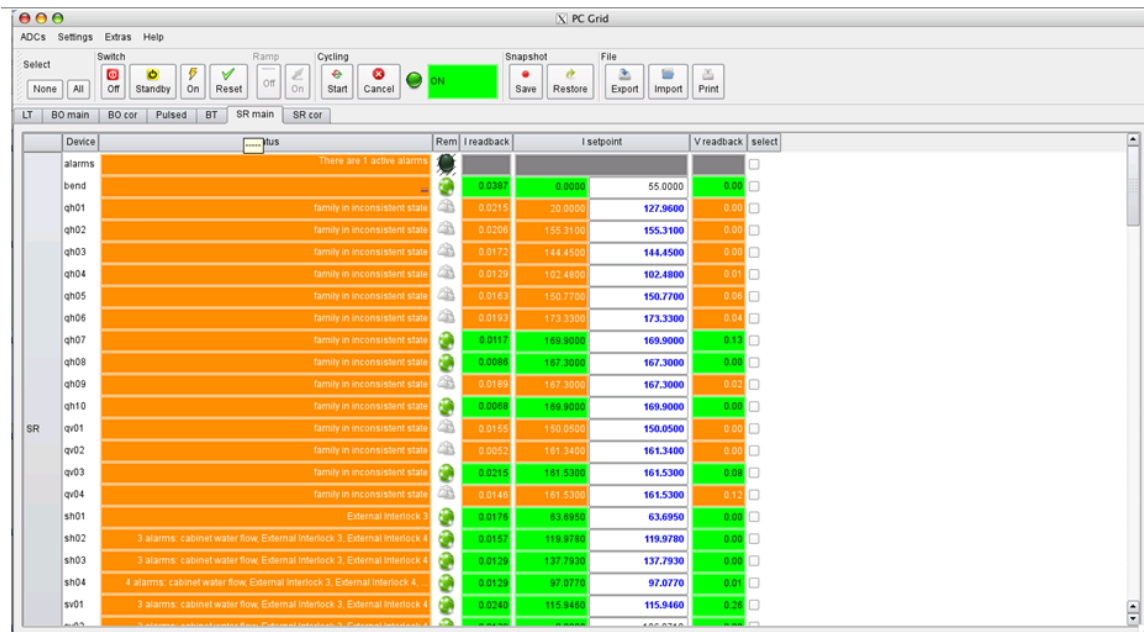


Fig. 15.8: Graphical interface for the power supplies at ALBA

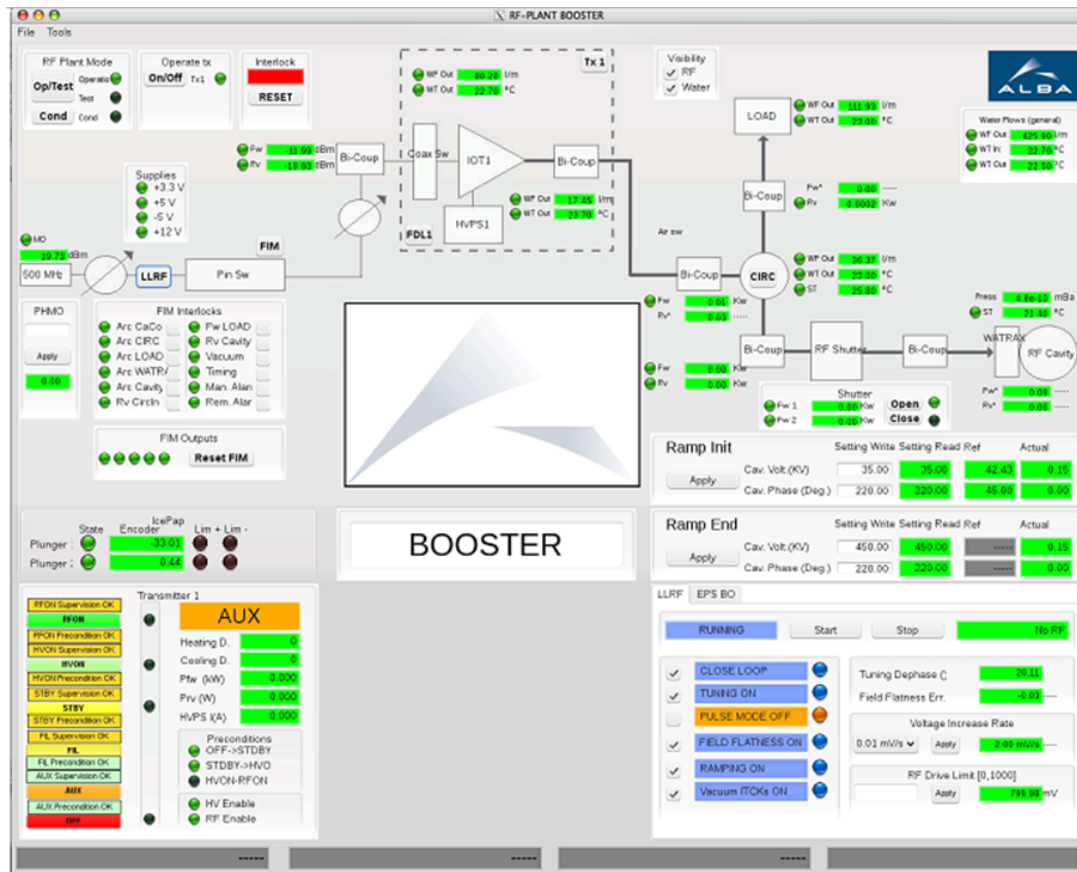


Fig. 15.9: Main synoptic of the GUI for the control system of the RF plant at ALBA

15.13 Radio-frequency (RF) system

The control system of the RF system has two levels. Most signals are managed by PLCs and the device servers running on dedicated IOCs. The fast control loops are performed on digital LLRF subsystems [15.10]. Slow loops, archiving, and control servers run on cPCI crates. The plungers are controlled by an IcePAP motor controller, the standard, configured in slave mode and receiving pulse and direction

from the LLRF system. Figure 15.9 shows the graphical user interface of the control system of the RF plant of the booster synchrotron at ALBA.

15.14 Diagnostic system

Beam position monitors and beam loss monitors are distributed along the ring. Other diagnostic devices may be concentrated in certain sectors. Remote desktops connected to oscilloscopes are widely used for readouts of fast current transformers, direct current–current transformers, etc.

15.14.1 Beam position monitors

The beam position monitors (BPMs) are managed by Libera^{****} boxes, which have dominated the market for the past 15 years and have evolved to adapt to newer needs. They need several timing signals: system clock (10 MHz), machine clock (which is the revolution clock, 1.1 MHz for the storage ring or 1.2 MHz for the booster), trigger (which is the injection trigger, 3 Hz), and post-mortem signal (a trigger signal generated by the interlock system).

15.14.2 Beam loss monitors

A number of BLMs need to be distributed across the storage ring (depending on the size of the machine). For example, the ALBA machine used 80–100 Bergoz detectors with a V2F converter handled by Cosylab signal conditioners daisy-chained by RS485 links. Four modules (reading eight beam loss monitors) are chained and read by an IOC.

15.14.3 Fluorescent screens

The fluorescent screens and OTRs can be implemented with CCD cameras, which need to be standardized for cost-efficiency reasons. At ALBA, the standardized model was the Basler SCA1000 30GM (readout by GigE Ethernet connection), although later other gigabit Ethernet models from Basler were also validated. They are usually triggered by the timing system and inserted and removed by the standard PLCs of the EPS.

15.14.4 Scrapers and other motions in the machine

Again, it is important to focus on the standardization of hardware and software in order to minimize installation costs and simplify the operation and maintenance. The scrapers of the machine are very similar to slits in the beam lines and movable masks in the front ends. All these are movable elements comprising motors, pseudo-motors (gap and offset), and graphical components. The hardware equipment and software should be reused and shared where possible to save on development costs and time.

15.14.5 Oscilloscopes

There are many signals for which the best interface is still an oscilloscope or a spectrum analyser. Providing an Ethernet connection to these devices (remote desktop for Windows-based devices) is cost-effective and solves quite a few problems. It also simplifies the cabling in the control room (i.e. only Ethernet connections). Special attention should be paid to Windows and other standard operating systems that may be vulnerable to cyber-attacks if not regularly updated and patched, which is not always possible and in any case a challenge in the case of oscilloscopes installed in the accelerators and beam line control networks.

****Instrumentation Technologies: <https://www.i-tech.si>

15.15 Insertion devices

In order to carry out state-of-the-art experiments and be prepared for future evolution, there needs to be flexible hardware synchronization between insertion devices and the beam line monochromator.

The standardization of the motor controllers can be extended to insertion devices. ALBA has successfully specified two-phase stepper motors for use with the standard IcePAP motor controller. These all have encoders configured in a closed loop, achieving precision better than a micron. Encoders typically have a precision of 0.1 micron, and the stepper motors move in closed loop with the encoders. Such configurations are also valid for big devices with large magnetic movement of the order of 1 mm/sec or more. Interlocks for the deviation of the taper (maximum 2 mm in 1 m length) with dedicated sensors, cables, hardware, and PLCs should be installed.

15.16 Orbit correction

The closed orbit correction involves two types of logical feedback loops that can be merged in the same system with the same hardware and software. The slow loop runs at speeds in the Hz range, stabilizes the static orbit, and also deals with energy drifts and radio frequencies. The fast loop (known as fast-orbit feedback, or FOFB) corrects for small deviations, reads at kHz frequencies, and acts on low frequencies below 100 Hz.

In the case of ALBA, the orbit feedback integrates up to 120 BPMs (the total number can be changed by enabling/disabling selected units) controlled by Libera boxes and 88 horizontal and 88 vertical corrector magnets along with their power supplies [15.12]. This system is very much dependent on the BPM electronics and on the interfaces of the correctors' power supplies with the control system (which must be fast and have a low enough latency to allow setpoints to be delivered to all correctors at deterministic rates of 5–10 kHz).

15.17 Motor controllers

A motor controller is a key hardware component in a synchrotron. It is very relevant for the beam lines; however, it turns out to be optimal to standardize motor controllers in the same way as for the machine. The ESRF developed the IcePAP motor controller in the 2000s and in 2006 commenced a collaboration with ALBA, joined a few years later by MAX IV. Both ALBA and MAX IV attained a high level of standardization on the motor controllers, with more than 95% of the axes, most of them in the beam lines, controlled by IcePAPs [15.7]. The IcePAP is a very cost-effective option to consider for future projects.

15.18 Timing system

The timing system provides all the trigger signals for synchronizing the process of injection of electrons from the linac to the booster and storage ring. The operations in this process include firing the linac (gun) and triggering the necessary injection kickers and septa in the booster transfer lines and storage ring, as well as all the diagnostic events, RF system, etc.

The timing system of the ALBA synchrotron is based on events and uses the hardware sold by Micro-Research Finland, which is used very extensively among recently constructed synchrotrons. The system has been extended and converted to be bi-directional in order to manage fast interlocks (in the μs range) as well [15.13].

Micro-Research Finland's system works as follows. The synchronization signals are distributed by events. Those events (132 user defined) and 8-bit distributed bus signals are generated by internal counters, triggers, or software. Events are distributed by fibre optics (multimode 850 nm). The aggregated jitter of the system is reduced to 25 ps r.m.s. Both transmitter and receivers are flexible enough to perform the final fine-tuning. Receivers have a time-stamp to use with each event. Figure 15.10 shows the schematic of the timing system, with the add-on feature of the fast interlocks, achieved by making the fibre-optic links bi-directional so that they can pass messages from any receiver

back to the transmitter and out again to the receivers. This timing system was first installed at ALBA and is now a standard feature of the control system.

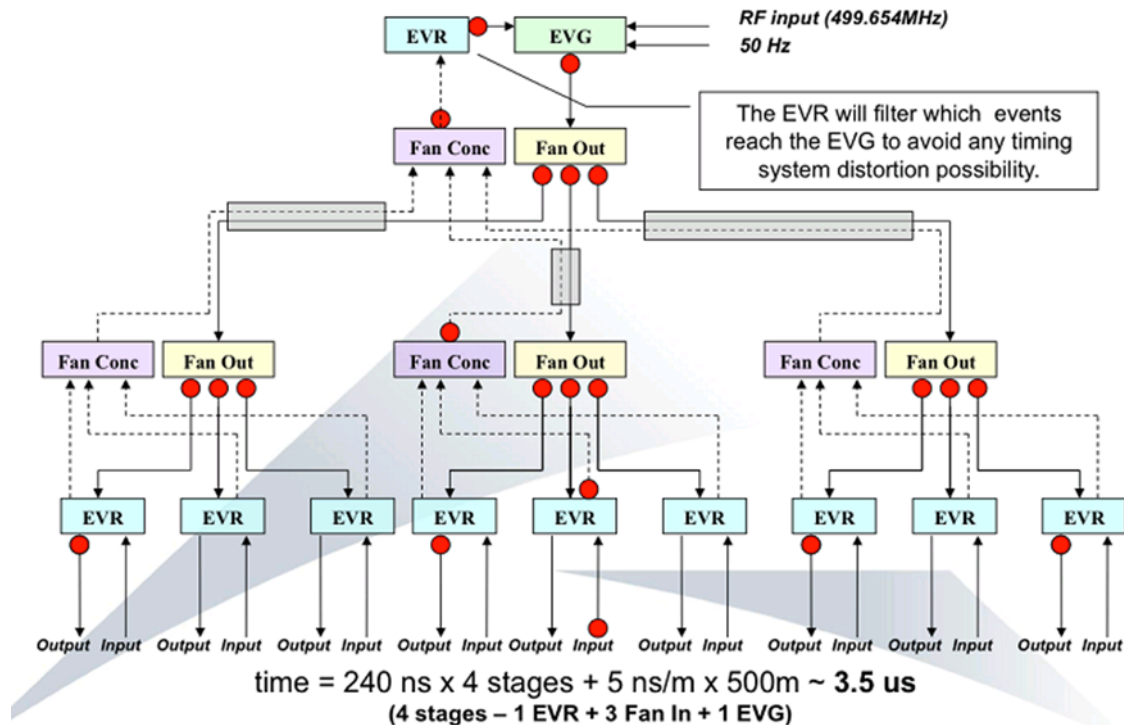


Fig. 15.10: Hardware layout of the timing system [15.13]

The most recent machines (the ESRF's being installed in December 2018) explored distributing the signals over PTP on deterministic networks, adapting the White Rabbit project⁺⁺⁺⁺ to this purpose. This approach is a good alternative to the Micro-Research Finland system for future installations.

15.19 Personnel safety system

The personnel safety system (PSS) monitors radiation levels and controls access to all the accelerator tunnels (linac, booster synchrotron, and storage ring) and beam line hutches. It prevents people from being exposed to a radiation dose higher than the limits established and specified by the competent authorities, ensuring that restricted areas are clear of personnel during machine operation and monitoring radiation levels outside the restricted areas (bunkers, tunnels, cabins, and hutches). It must be reliable and fail-safe.

Radiation hazards prevention involves technical aspects strictly regulated by different laws and always following the ALARA⁺⁺⁺⁺ principle. It is subject to ionizing radiation regulations and the authorities of the individual countries. It has to be independent from any other system. For example, ALBA's PSS was reviewed, validated and approved by the Spanish Nuclear Safety Council.

The system has a number of inputs and produces outputs. Outputs should be redundant and diverse. The whole design must follow norms such as the IEC 61508 [15.11].

- **Redundancy** is achieved by having two independent channels for every signal.
- **Diversity** means that any action is applied to two different components of the system; for example, disabling the RF system means dumping the RF driver and dumping the HV power

++++The White Rabbit project at the open hardware repository: <https://www.ohwr.org/projects/white-rabbit>

++++ALARA stands for 'as low as reasonably achievable'.

supplies. In other words, each individual action results in two redundant outputs (four signals in total).

Light panels that signal the state and show alarms or other major events must be installed in the relevant and appropriate places. The most cost-effective way of building the PSS is using safety PLCs. This has proven to be a good choice; it is very flexible and cost-effective.

15.20 Alarm handling

A generic alarm-handling system that is flexible, configurable, and transversal and which covers the whole control system is necessary from the initial phases of the project. The system provides mechanisms to configure the behaviour of the alarms, notifications, and databases for historical values; to monitor alarm activation, deactivation, severity, and traces; and to perform automatic actions and root cause analyses. The system should have adequate human-machine interfaces to correctly manage the large quantity of data [15.14].

15.21 Organization and economic aspects

The control system is critical for accelerators and beam lines. Its design needs to be considered from the beginning of the project and play a role in all phases of the development. The initial design and strategy for the installation must be ready at the early stages. Calls for tenders for the different components should include specifications for the interfaces with the control system. This includes specifications for standard hardware and software interfaces which can be applied generally to the many tenders involving the control system: linac, power supplies, diagnostics, motors, mechanical components, RF elements, insertion devices, monochromators, benders, mirrors, detectors, etc.

A project management system must be established from the beginning to share data between different subsystems and integrate the schedules for deliveries and installation of components. The goal is to have a central management system for the whole project, covering schedules, resources, risks, and the coordination of all sub-projects into the master baseline of the facility. The different sub-projects establish plans, organize resources, and define the delivery, installation, and commissioning of the different components. A model for project management could be Prince2, for example, which is the method followed at ALBA. It is well adapted to the needs of accelerators and beam lines, is easy to adapt to the scope of different projects, and can be combined with Agile methodologies for software development [15.15].

During the construction phase, different services will be built and some of them—such as vacuum chamber bake-outs, archivers, and other parts of the control system—will be turned on for operation during the installation. A system for tracking user requests and a central point of contact for the service desk would be required. ITIL best practices provide important guidelines for implementing service operation and support. This is particularly critical during the operation phase of the facility but would start already during the construction.

From the economic point of view, a good approach is to reserve a budget of 10% of the total project cost for the control system and computing services. This might vary depending on the strategy adopted in terms of software and hardware development and use of commercial off-the-shelf instrumentation. Writing software from scratch is money- and time-consuming. The right balance of in-house development and reuse of existing software (preferably free and open source or imported from existing institutes) is key to success. There will inevitably be some software to develop from scratch (e.g. for new hardware, new features, or new requirements), but there are many parts for which existing (and in some cases industrial) solutions are functional and fit to purpose. The use of industrial solutions (PLCs) and regular computers (industrial PCs) has worked very well in other synchrotrons, ALBA being a good example; it is cost-effective and reliable. Finally the manpower is very much dependent on the institute itself.

References

- [15.1] D. Fernández-Carreiras *et al.*, The design of the ALBA Control System: A cost-effective distributed hardware and software architecture, Proc. ICALEPCS2011, Grenoble, France, 10–14 October 2011, p. 1318.
<https://accelconf.web.cern.ch/accelconf/icalepcs2011/papers/frbhmust01.pdf>
- [15.2] D. Fernandez-Carreiras *et al.*, ALBA, a Tango based control system in Python, Proc. ICALEPCS2009, Kobe, Japan, 12–16 October 2009, p. 709.
<https://accelconf.web.cern.ch/accelconf/icalepcs2009/papers/thp016.pdf>
- [15.3] D. Beltran *et al.*, PCI/cPCI interface for the PSI power supply controller, Proc. ICALEPCS2009, Kobe, Japan, 12–16 October 2009, p. 471.
<https://accelconf.web.cern.ch/accelconf/icalepcs2009/papers/wep032.pdf>
- [15.4] T. Coutinho *et al.*, Sardana, the software for building SCADAS in scientific environments, Proc. ICALEPCS2011, Grenoble, France, 10–14 October 2011, p. 607.
<https://accelconf.web.cern.ch/accelconf/icalepcs2011/papers/weaaust01.pdf>
- [15.5] C. Pascual-Izarra *et al.*, Taurus big & small: from particle accelerators to desktop labs, Proc. ICALEPCS2017, Barcelona, Spain, 8–13 October 2017, p. 166.
<https://doi.org/10.18429/JACoW-ICALEPCS2017-TUBPL02>
- [15.6] J. Avil-Abellan *et al.*, Em# electrometer comes to light, Proc. ICALEPCS2017, Barcelona, Spain, 8–13 October 2017, p. 137. <https://doi.org/10.18429/JACoW-ICALEPCS2017-TUAPL04>
- [15.7] N. Janvier *et al.*, IcePAP, an advanced motor controller for scientific applications in large user facilities, Proc. ICALEPCS2013, San Francisco, Calif., USA, 6–11 October 2013, p.766.
<http://accelconf.web.cern.ch/AccelConf/ICALEPCS2013/papers/tuppc081.pdf>
- [15.8] D. Beltran *et al.* ALBA control and cabling database, Proc. ICALEPCS2009, Kobe, Japan, 12–16 October 2009, p. 423.
<https://accelconf.web.cern.ch/AccelConf/icalepcs2009/papers/wep009.pdf>
- [15.9] S. Rubio-Manrique *et al.*, Unifying all Tango control services in a customizable graphical user interface, Proc. ICALEPCS2015, Melbourne, Australia, 17–23 October 2015, p.1052.
<https://doi.org/10.18429/JACoW-ICALEPCS2015-WEPGF148>
- [15.10] A. Salom and F. Pérez, Digital LLRF for ALBA storage ring, Proc. EPAC2008, Genoa, Italy, 23–27 June 2008, p. 1419. <https://accelconf.web.cern.ch/AccelConf/e08/papers/tupc148.pdf>
- [15.11] D. Fernández-Carreiras *et al.*, Personnel protection, equipment protection and fast interlock systems. Three different technologies to provide protection at three different levels, Proc. ICALEPCS2011, Grenoble, France, 10–14 October 2011, p.1055.
<https://accelconf.web.cern.ch/accelconf/icalepcs2011/papers/wepmu005.pdf>
- [15.12] X. Serra-Gallifa *et al.*, Fast orbit feedback implementation at ALBA synchrotron, Proc. ICALEPCS2013, San Francisco, Calif., USA, 6–11 October 2013, p 1318.
<http://accelconf.web.cern.ch/AccelConf/ICALEPCS2013/papers/thppc115.pdf>
- [15.13] O. Matilla *et al.*, ALBA timing system. A known architecture with fast interlock system upgrade, Proc. ICALEPCS2011, Grenoble, France, 10–14 October 2011, p. 1024.
<http://accelconf.web.cern.ch/AccelConf/icalepcs2011/papers/wepms023.pdf>
- [15.14] S. Rubio-Manrique *et al.*, PANIC and the evolution of Tango alarm handlers, Proc. ICALEPCS2017, Barcelona, Spain, 8–13 October 2017, p.170.
<https://doi.org/10.18429/JACoW-ICALEPCS2017-TUBPL03>
- [15.15] D. Fernández-Carreiras *et al.*, Using Prince2 and ITIL practices for computing project and service management in a scientific installation, Proc. ICALEPCS2013, San Francisco, Calif., USA, 6–11 October 2013, p. 517.
<http://accelconf.web.cern.ch/AccelConf/ICALEPCS2013/papers/tumib01.pdf>

16 Building, infrastructure, and site

D. Einfeld

The layout of the building is determined by the circumference of the storage ring and the booster synchrotron. If both machines are operated with a 100 MHz RF system, the circumference must have a harmonic number corresponding to the wavelength of the RF system, which is 3 m. The circumference of the storage ring is 348 m and the circumference of the booster synchrotron is 324 m. The corresponding radii are 55.386 m for the storage ring and 51.566 m for the booster synchrotron; the difference between the two is 3.82 m. Around the storage ring is the outer shielding wall. The distance between the storage ring and the wall is determined by the required length of the front ends (roughly 16 m). The overall dimensions of the machine tunnel are presented in Fig. 16.1 for one quadrant. A cross-section of the tunnel with the locations of the storage ring and booster synchrotron is shown in Fig. 16.2.

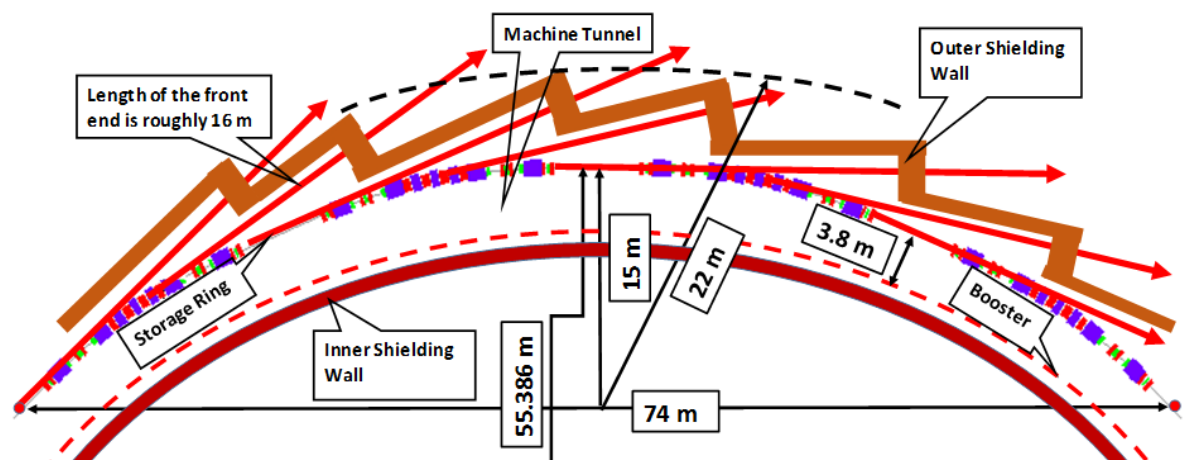


Fig. 16.1: The required dimensions for the machine tunnel and the shielding walls in one quadrant

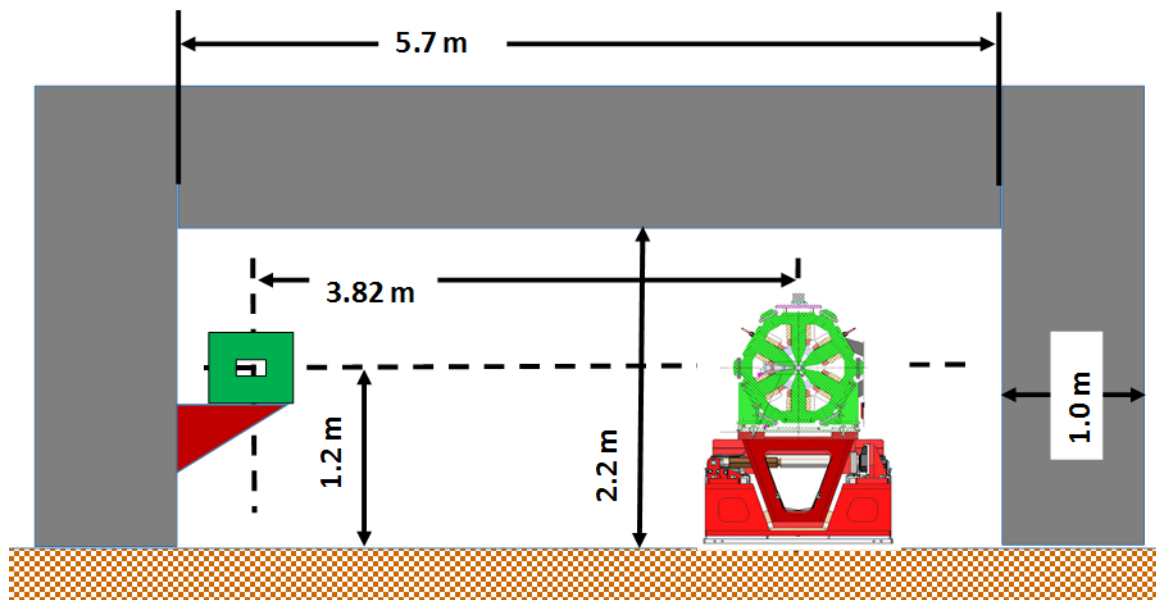


Fig. 16.2: Cross-section of the machine tunnel with the booster synchrotron on the left-hand side and the storage ring on the right-hand side.

The service area with a width of 10 m and a walking area of width 2.2 m around it must be added along the inner side of the machine tunnel. An area of diameter 74 m, called the courtyard, will remain

available in the middle of the main building. Part of this area can be used for laboratories and offices (as at the SLS). The overall layout of the inner part of the building is presented in Fig. 16.3.

On the outer side of the machine tunnel is the experimental area for setting up the beam lines; the radius of this area is 73 m and it has a walking area of width 2.2 m around it. The length of the beam lines from the shielding wall to the walking area is around 22 m. The arrangement of the linac bunker in the vicinity of the machine tunnel is presented in Fig. 16.4. The linac bunker has length 22 m and width 4 m. In front of the linac bunker is the service area for all the racks needed to operate the different components of the linac.

The cross-section of the main building is presented in Fig. 16.5, showing the experimental hall, the linac bunker, and the service and walking areas. A site walk is needed to cross the experimental hall. For the installation of the machines and beam lines, two cranes with a capacity of 15 tons are needed.

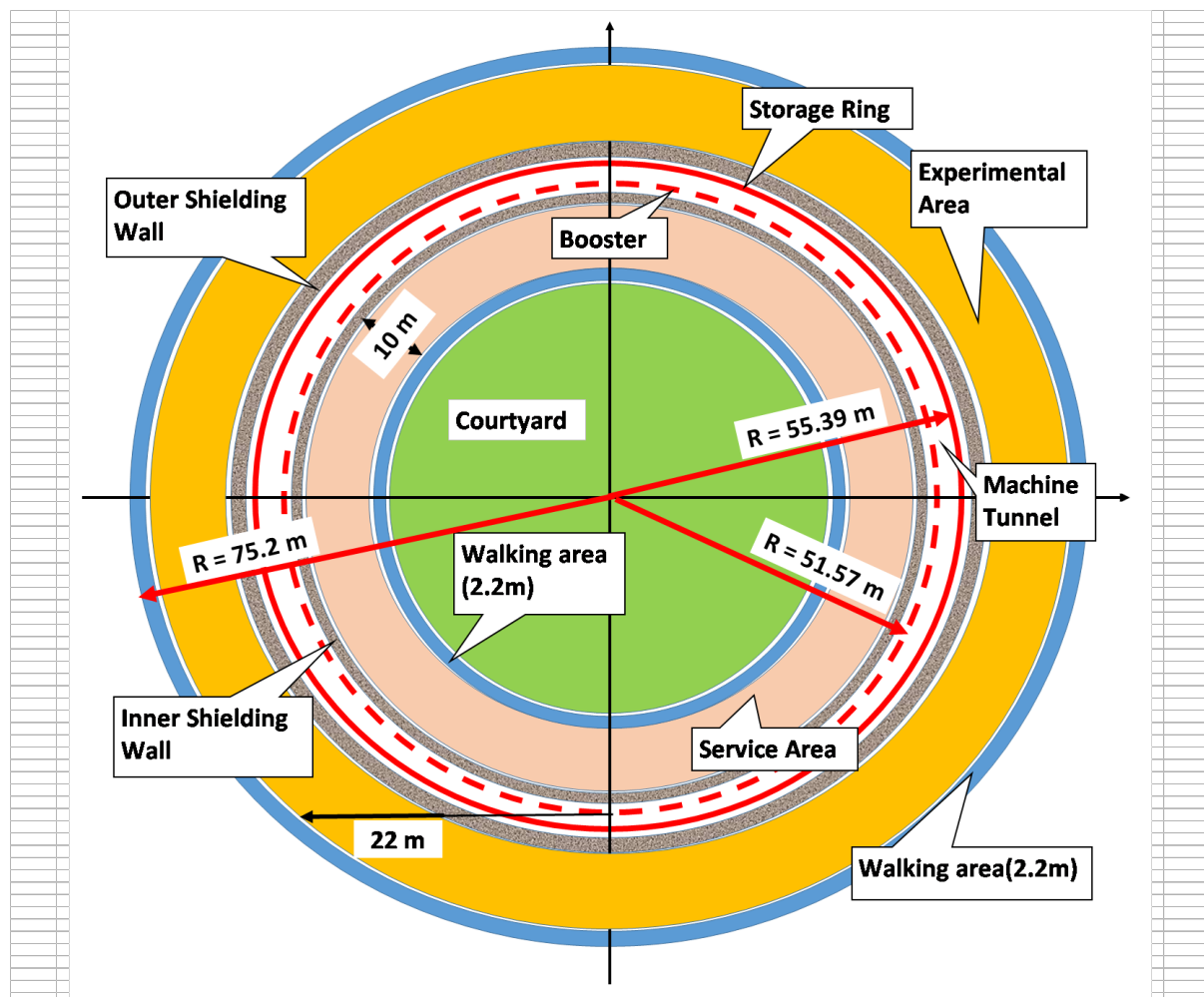


Fig. 16.3: The layout of the inner part of the main building

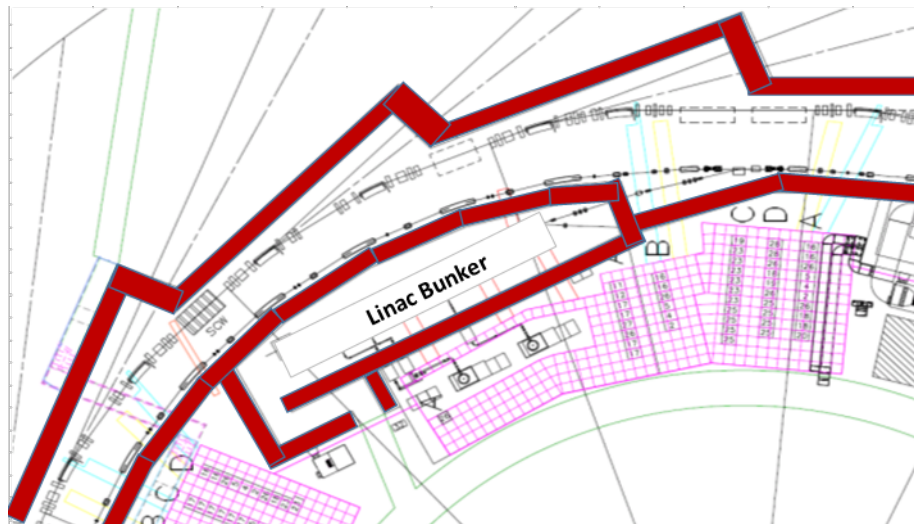


Fig. 16.4: The arrangement of the linac bunker near the machine tunnel

The cranes have to span the experimental hall, the machine tunnel, and the service area. Adjacent to the experimental hall are the laboratories and offices. As shown in Fig. 16.5, laboratories and offices can also be erected near the service area in the middle of the building.

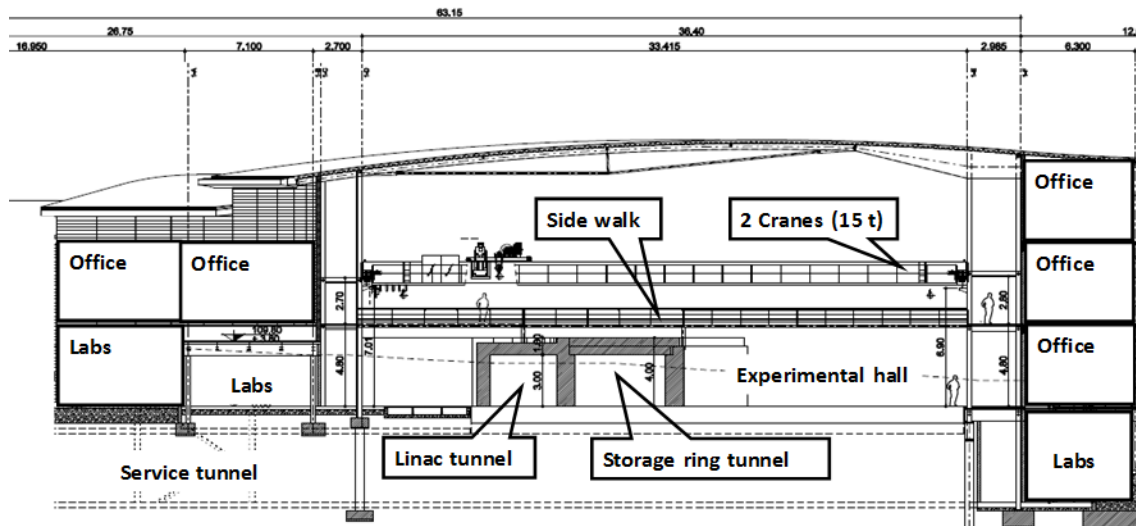


Fig. 16.5: Cross-section of the main building according to the layout of ALBA

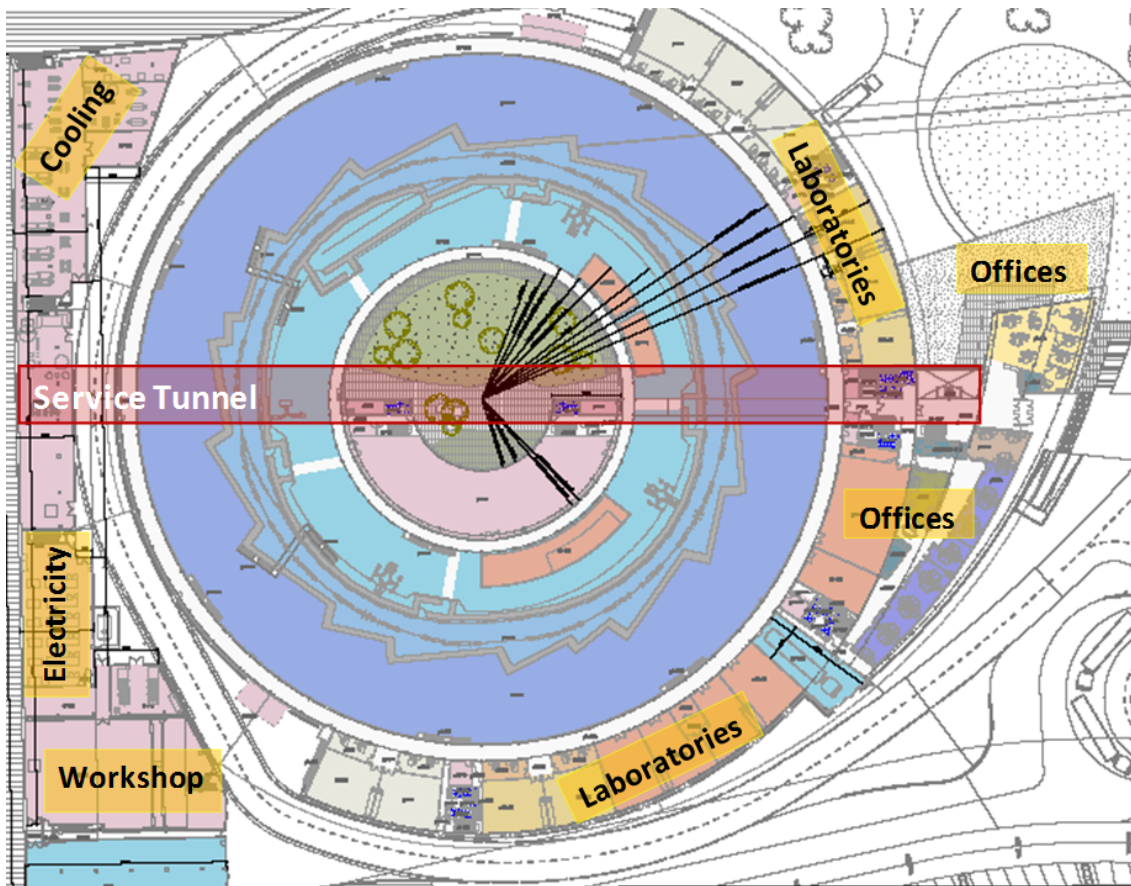


Fig. 16.6: Top view of the ALBA building, showing the spaces for the infrastructure, offices, and laboratories

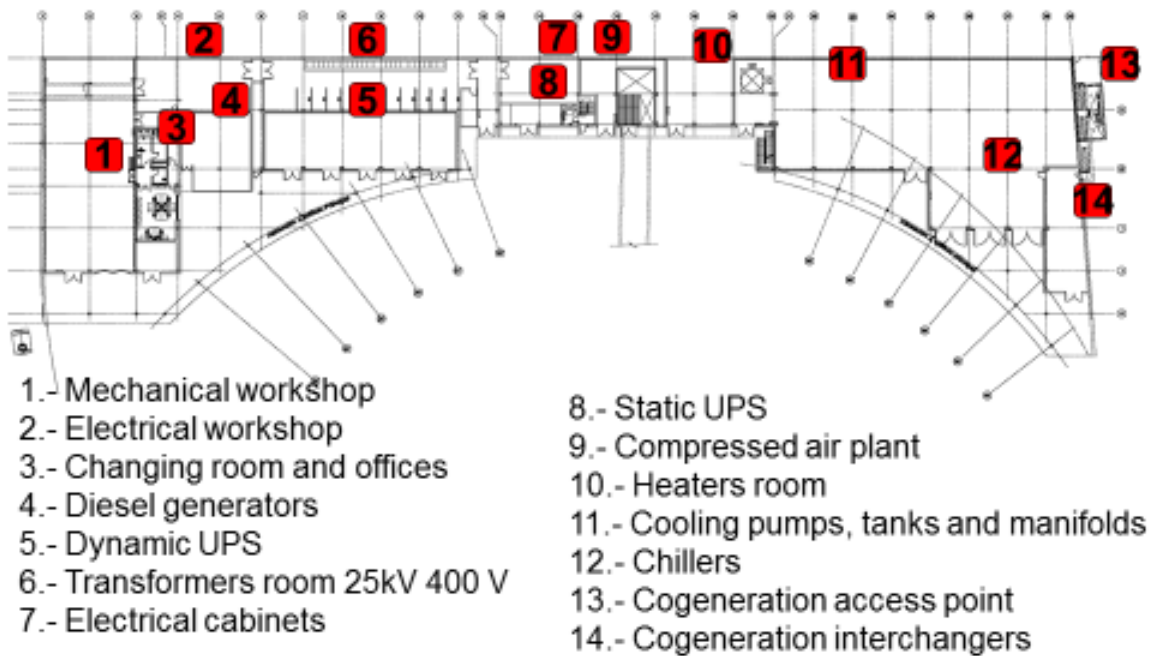


Fig. 16.7: The location of the different infrastructure components in the technical building of ALBA

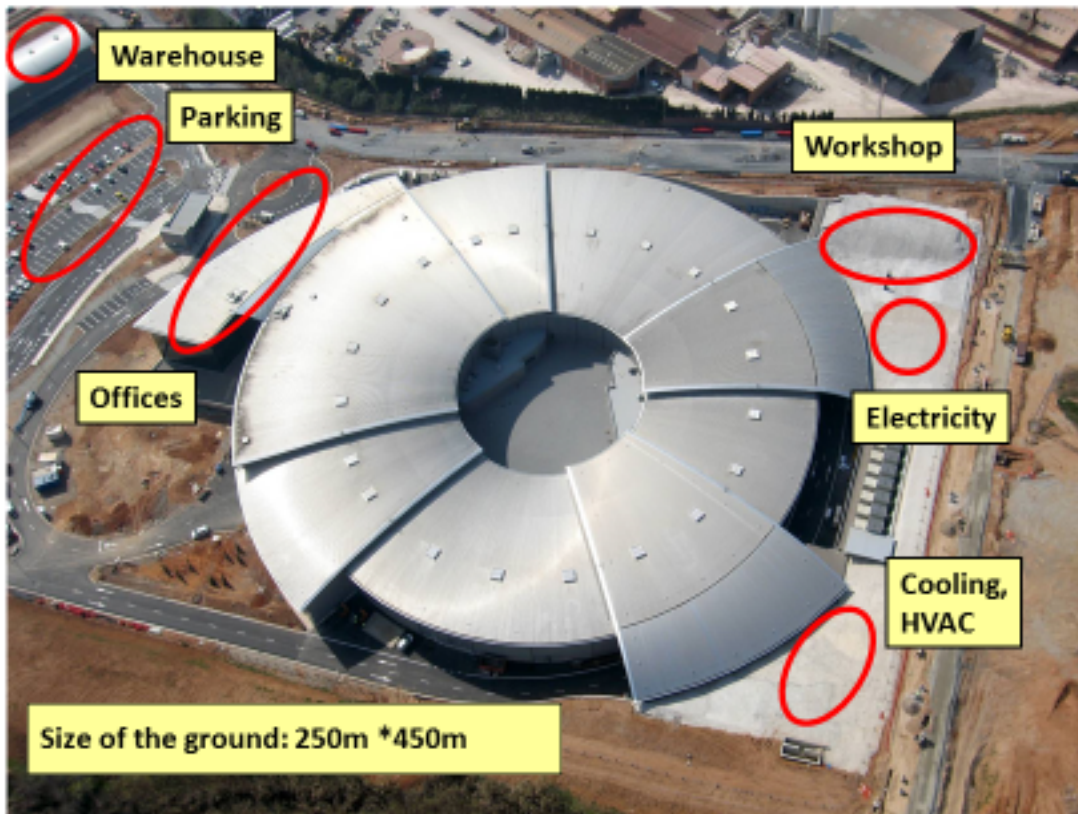


Fig. 16.8: Aerial view of the ALBA site, showing the spaces for the building, infrastructure, offices, parking, etc.



Buildings



Fig. 16.9: Aerial view of the SOLEIL site, showing the spaces for the building, infrastructure, offices, parking, etc.

The organization of the space near the experimental hall required for infrastructure such as cooling, electricity, and workshops is shown in Fig. 16.6. The connections for the machine, beam lines,

and offices go through a ‘service tunnel’ under the experimental hall. The arrangement of the different infrastructure components is presented in Fig. 16.7.

The arrangement of the experimental hall, technical building, offices, laboratories, etc. is different at the different light sources. Figure 16.8 shows the ALBA site and Fig. 16.9 the SOLEIL site. Figure 16.10 is a diagram of the overall ALBA site. With the greater circumference of the machine, an overall size of $300\text{ m} \times 500\text{ m}$ is required for the SEE-LS project.

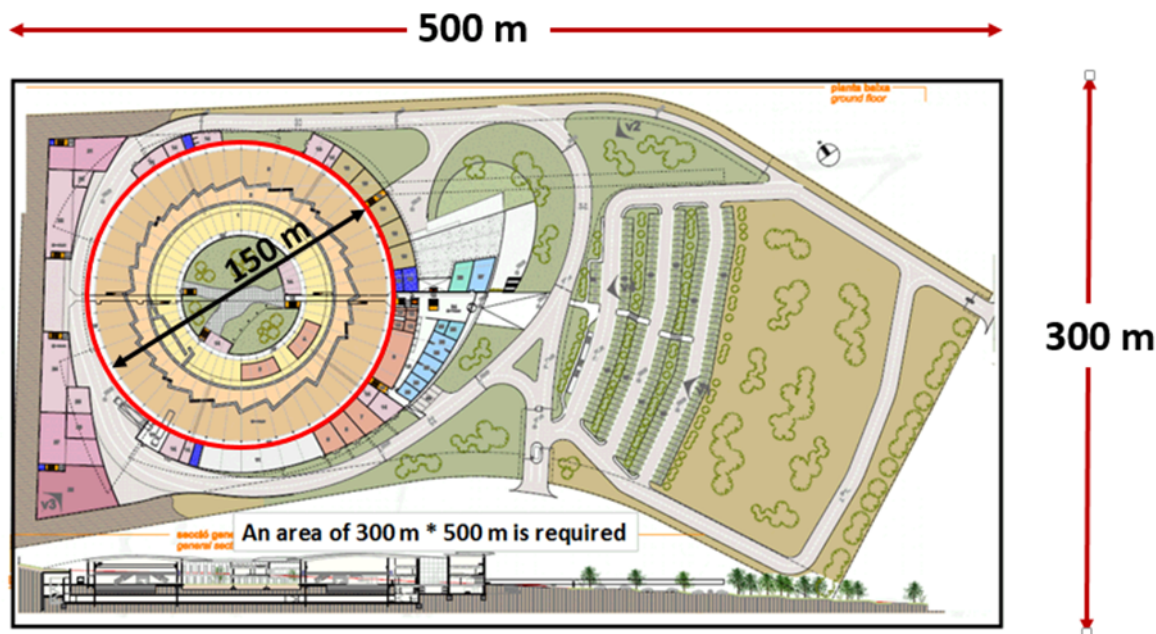


Fig. 16.10: ALBA site, showing the spaces for the building, infrastructure, offices, parking, etc. Overall an area of $300\text{ m} \times 500\text{ m}$ is needed.

The requirements for the site are the following.

- The overall size of the site should be about $300\text{ m} \times 500\text{ m}$.
- In view of potential future upgrades, and considering a lifetime of the facility of 30 years, the possibility of expanding the site by about 50% would be an advantage.
- The site should be very stable, and no vibrations (e.g. from nearby traffic) should disturb the stability of the building and the beam.
- A good connection to the electric power grid should exist.
- Easy access is important, including easy road access and a not-too-distant airport.
- A guest house, or at least hotel accommodation in the vicinity, should be available.

17 Organization

D. Einfeld

The organization of the SEE-LS should be close to that of similar facilities in Europe and of SESAME. The overall responsibility is with the Council of Delegates from the member states. The Council determines the budget and makes the general decisions concerning the beam lines and upgrade of the machine. The Director follows the decisions of the Council, is responsible for the day-to-day management of the facility, and has to make sure that a high-brilliance and stable photon beam is available to users. Generally, two advisory committees are nominated by the Council to follow up on the machine design and construction (Machine Advisory Committee) and the development of scientific activities (Science Advisory Committee). In general, the Director should follow the advice of both committees.

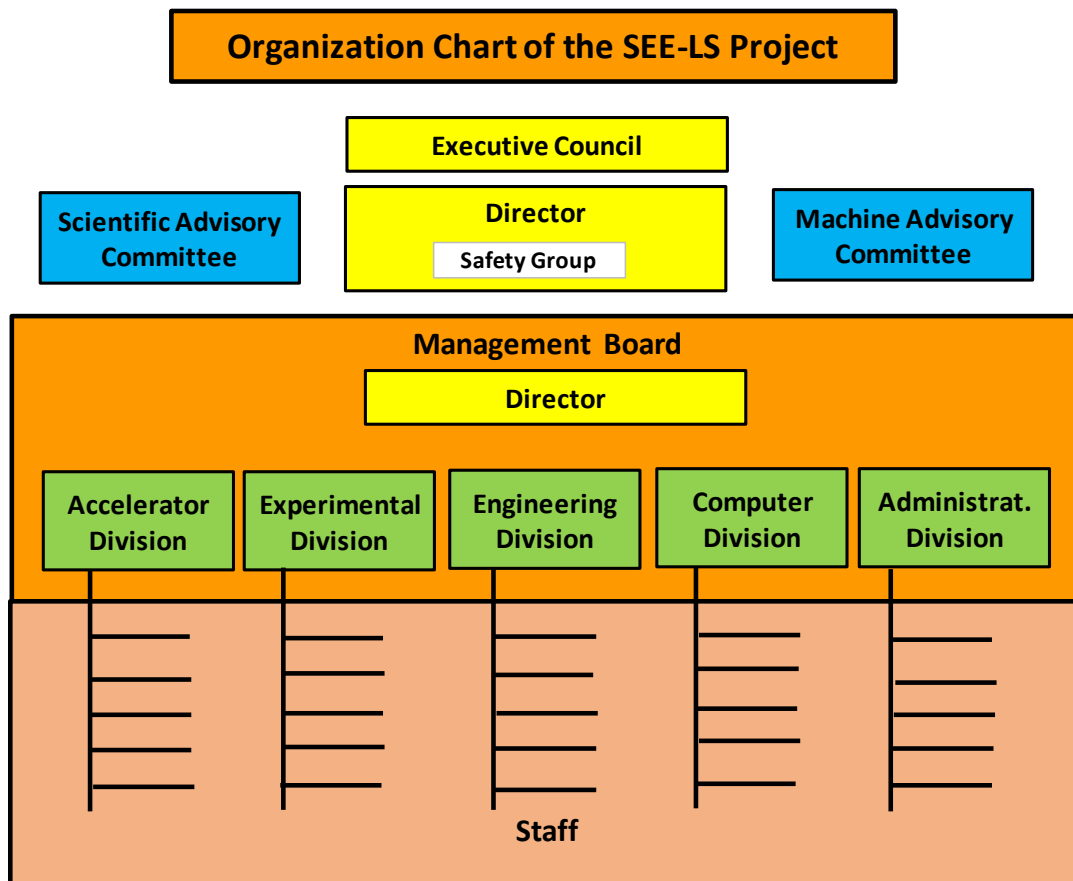


Fig. 17.1: Proposed organizational chart for the SEE-LS project

Under the Director are different divisions, including the accelerator division, experimental division, engineering division, computing division, and administrative division. The heads of the divisions and the Director together form the 'Management Board'. The Management Board should meet once per week to discuss all issues concerning the facility.

The accelerator division is in charge of the design of the lattice and the design and construction of the magnets and insertion devices, diagnostics, power supplies, RF systems, and all other components; it is of course in charge of the operation of the machine. The experimental division uses the beam lines to conduct scientific research and is responsible for the operation of the beam lines. The engineering division provides all the support needed by the accelerator and experimental divisions, such as electrical and cooling systems, civil engineering services, the vacuum system, and mechanical engineering services. The computing division will provide general informatics, software, and hardware controls for the accelerator and experimental divisions. Last but not least, the administrative division

will take care of personnel issues, contracts, finance, and accounts (see Fig. 17.2). The management board is composed of the heads of the five divisions, led by a general director. The security and safety group and the communication group are under the direct authority of the general director.

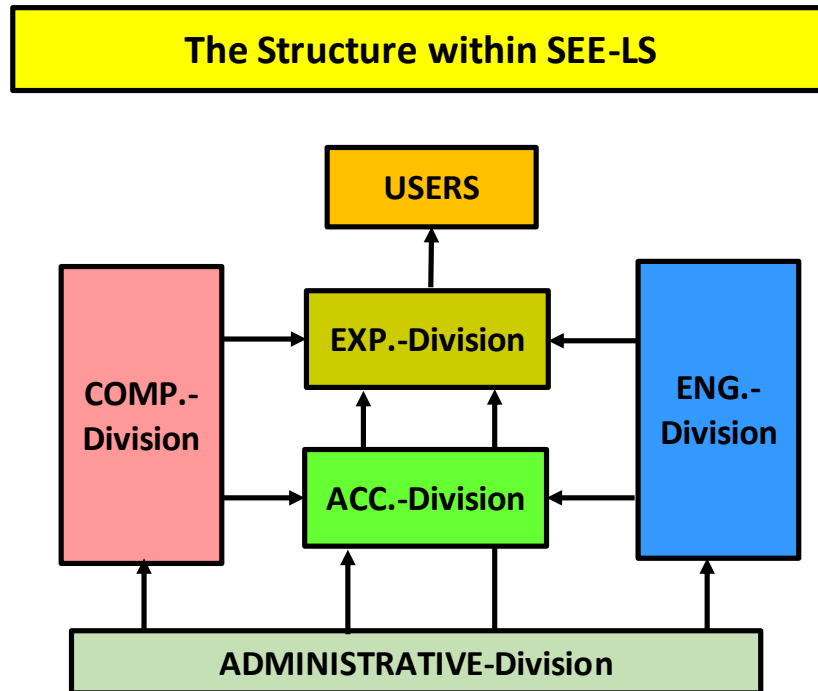


Fig. 17.2: The relationship between the different divisions of the SEE-LS

18 Project schedule

D. Einfeld

As far as the design of the machine is concerned, a considerable amount of work has already been done, which would be made available from the start. Therefore, once the requisite staff has been appointed, a detailed proposal could be submitted relatively quickly. The construction could be accelerated if, with the help of other laboratories, detailed drawings and other documents are prepared for the tendering process. The estimated time needed for the design period and the preparation of call-for-tender documents is roughly 1.5 years.

The production of the components of the machine and beam lines will take about three years: one year for the prototype or pre-series and two years for the series. The building containing the infrastructure (electricity, cooling, etc.) could be constructed in parallel and would take perhaps one year longer. The building could be built in stages to allow early installation of the 100 MeV pre-injector; this is also true of the 3 GeV booster synchrotron.

About one year would be needed for installation of the machine and beam lines. For the commissioning of the machine and the setting up of the beam lines, about six months are required. In conclusion (see Fig. 18.1), around six years in total would be required from approval of the project to production of the first light for synchrotron radiation experiments.



Fig. 18.1: Time schedule for the SEE-LS project

19 Training programme

A. Nadji

The training of scientists, engineers, and technicians must be treated as a priority from the beginning of the project, and great effort should be made to involve as many staff from the member countries of the project as possible. An international training committee made up of experts in the accelerator field could be established to help with the design and organization of the training programme. As different areas of expertise and different skills are needed to design, construct, and operate such a facility, the knowledge and connection of the members of the training committee with international facilities will be key to the success of the training programme. At the beginning, the most urgent need would be to gather experts who could help to design and construct the accelerator complex composed of a linac, a booster, and a storage ring. Although there is always a risk that some of the trainees sent abroad will stay there, the scheme implemented in the SESAME project was rather successful and could be emulated in this case. A large number of candidates (around 100) from the SEE region could be invited to participate in a school (approximately two weeks long) dedicated to particle accelerators and associated technology, and a group of them (20–25) could be selected to receive specialized long-term training in one of the European laboratories (for about 18 months).

It should be noted that the accelerator community is generally characterized by strong, supportive collaboration and honest competition between different laboratories in Europe and worldwide. All the institutions support each other to improve the specification of each light source and meet regularly in several networks, international conferences, and workshops.

During their training, the selected candidates can also deepen their knowledge by participating in well-known accelerator schools such as CAS (CERN accelerator school). The budget of this training programme is not negligible and should be planned for from the beginning.

If the proposal is selected for follow-up, then formal participation in the newly created LEAPS association will be sought.

20 Cost estimation

D. Einfeld

20.1 Investment cost

A firm cost estimate can be made only after the detailed design has been chosen, the site has been selected, and the environmental conditions are known. At this time it is only possible to give some global figures. The average investment cost for the machine, based on experience from the previous projects ALBA, SOLEIL, DIAMOND, and MAX IV, is roughly €0.25 million per metre. For a circumference of 350 m, this comes to €87.5 million. Included in this number are the costs for the 100 MeV linac, 3 GeV booster synchrotron, 2.5 GeV storage ring, transfer lines, and front ends.

The necessary investments for the first generation of beam lines can only be estimated when future users have expressed their interests. The cost of individual beam lines varies enormously and can range from less than €1 million (infrared beam line) to several millions of euros for sophisticated beams. Assuming that the facility starts with three beams, a minimum investment of about €18 million would be expected. However, at present it has not been determined whether funding for the experiments should be included in the investment costs of the facility, since at least part of it could be provided by future users, be it in kind or in money.

It is assumed that the site will be provided free by the host state (this should be taken into account when comparing the total cost estimate made here with the cost of existing facilities, as the cost of the land made up a large proportion of the total cost for some projects).

It is very difficult to make an estimation of the cost of the building without knowing its location, because civil engineering costs vary considerably from country to country. Experience from other countries suggests an upper limit of about €45 million.

The overall initial investment for the SEE-LS is estimated to be in the range of €150 million to €160 million, taking into account the aforementioned uncertainties. This does not include the cost of laboratory staff.

Table 20.1 Investment costs for initial set-up (not including additional laboratories)

Item	Investment cost (€ million)
Linac, booster, storage ring, front-end beams, controls	88.0
First 3 beam lines (average €6 million per beam)	18.0
Buildings and shielding	45.0
Laboratory staff during the construction	18.0
Total	169.0

For the design, following up the contracts, the installation, and the commissioning, around 40 people are needed (6 specialists from other SRLs for €110,000/year each, plus 15 engineers and 20 technicians for €66,000/year each). Overall it comes to €17.82 million for personnel during the construction period of six years, so that the total investment is estimated to be $150.5 + 17.82 \approx 168$ million euros (see Table 20.1).

The investments needed for the upgrades of the facility are presented in Table 20.2.

Table 20.2: Investments for possible upgrades (€ million)

Energy increase from 2.5 to 3 GeV	8
Additional beam lines: 10 (average €5 million per beam)	50
Total	58

20.2 Laboratory staff

The staff of the laboratory would have to be built up during the years of construction. At the beginning, a few top experts will be needed, meaning that internationally competitive salaries will have to be offered. Over time and after training, the staff could come from all over the region. To operate the facility at turn-on, about 50 to 60 staff members would be required.

Simultaneously with the employment of staff, the operating cost would increase. Staff costs will depend on the salary scales adopted, so no definite figures can be given at this time. In western European laboratories the average cost of staff per person–year is about €0.061 million. Assuming that around two-thirds of the personnel would be remunerated according to local salaries, one might assume an average cost per year of €0.037 million. At the start of the project, the cost of the laboratory staff would be about €3 million per year.

20.3 Operational budget

The operating budget of the facility has two components, one that depends on the number of operating hours and another part that is constant.

The experience of most scientific laboratories shows that about 50% of the total budget consists of personnel costs, estimates of which have been given in the previous section. For a synchrotron light source, the material budget is to a large extent dependent on the cost of electricity, which could be as high as 25% of the total operating budget. With a consumption of 4.5 MW, an operation time of 6,500 h/year, and an electricity price of €100/MWh (western European prices), the total amounts to €3 million per year.

The local cost of electricity should be considered during site selection. On the other hand, electricity cost considerations might encourage the development of a solar power project, not just for this facility but also for the benefit of the whole region.

Upon adding costs for maintenance and consumables, the total yearly operating budget is estimated to be about €9 million, which would have to be covered by the collaborating partners (see Table 20.3).

Table 20.3: Yearly operating cost

Item		€ million
Maintenance and consumables		3
Laboratory staff	60 to 70 staff	3
Energy	3.0 MW (western prices)	2–3
Total		8–9

Appendix A Synchrotron radiation characteristics

D. Einfeld

A.1 Introduction

Synchrotron radiation is characterized in general by the following attributes: spectral range, photon flux, photon flux density, brilliance, and polarization. The photon flux (photons per second and bandwidth) is the overall flux collected by an experiment and reaching the sample; the photon flux density is the flux per unit area at the sample; and the brilliance is the flux per unit area and opening angle. This appendix summarizes the formulas for the calculation of these quantities for the synchrotron radiation emitted from a stored beam in the bending magnet, wiggler, and undulator [A.1–A.9].

Establishing the theory of synchrotron radiation has been the work of many researchers. Today most of the calculations use the results of the Schwinger theory [A.6, A.2]. A relativistic electron moving around an orbit emits a radiation cone tangential to the orbit with a small opening cone, as shown in Fig. A.1. The aperture of the beam line of width B and height H at a distance D determines the flux that goes to the sample.

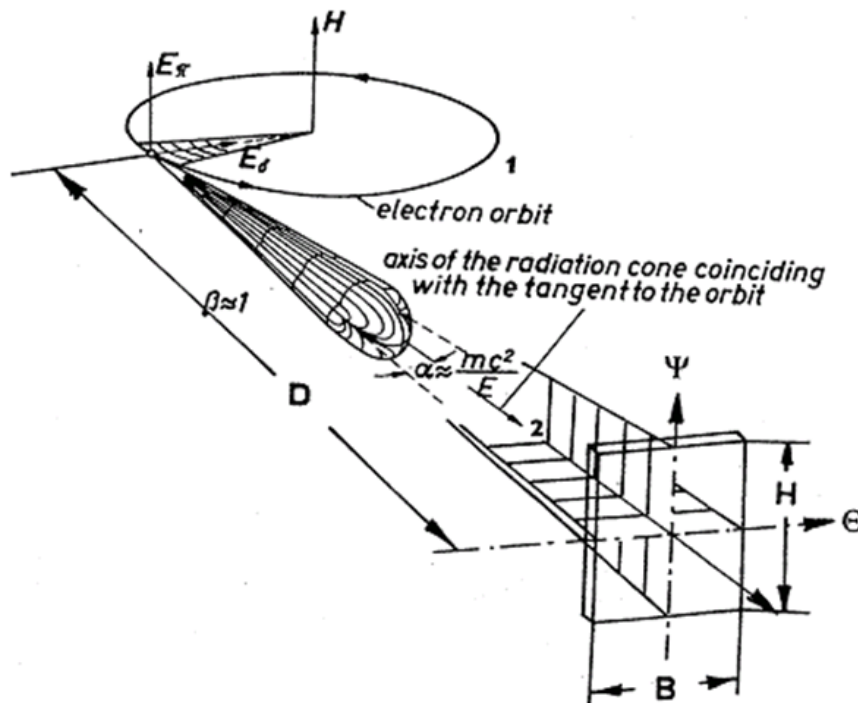


Fig. A.1: Characteristics of the synchrotron radiation emitted by a relativistic electron moving in a circle

The shape and intensity within the radiation cone, according to the Schwinger theory, is given by

$$\frac{d^2\Phi}{d\theta d\psi} = \frac{3\alpha}{4\pi^2} \gamma^2 \frac{\Delta\omega I}{\omega e} y^2 (1+X^2) \left[K_{2/3}^2(\xi) + \frac{X^2}{1+X^2} K_{1/3}^2(\xi) \right], \quad (\text{A.1})$$

where:

Φ is the photon flux (number of photons per second);

θ is the observation angle in the horizontal plane;

ψ is the observation angle in the vertical plane;

α is the fine structure constant (equal to $1/137$);

γ is the electron energy ($m_e c^2$ where m_e is the electron mass and c is the velocity of light);

ω is the angular frequency of photons ($h\omega = \text{photon energy} = \varepsilon$);

I is the beam current;

e is the electron charge (1.601×10^{-19} C);

$y = \omega/\omega_c = \varepsilon/\varepsilon_c$ (where ω_c is the critical frequency, $3\gamma^3 c/2\rho$);

E_c is the critical photon energy ($3hc\gamma^3/2\rho$);

ρ is the radius of instantaneous curvature of the electron trajectory (E/ecB in practical units, $\rho[\text{m}] = 3.3356 \times (E/\text{GeV})/(B/\text{T})$);

c is the speed of light (2.9979×10^8 m/s);

E is the electron beam energy;

B is the magnetic field strength;

$\varepsilon_c = h\omega_c$ ($\varepsilon_c[\text{keV}] = 0.665 \times (E/\text{GeV})^2 \times (B/\text{T})$);

$X = \gamma\psi$ (normalized angle in the vertical plane);

$\xi = y(1+X^2)^{3/2}/2$.

The subscripted K 's in equation (A.1) are modified Bessel functions of the second kind. Equation (A.1) is the basic formula for the calculation of synchrotron radiation characteristics. The polarization is given by the two terms within the square brackets.

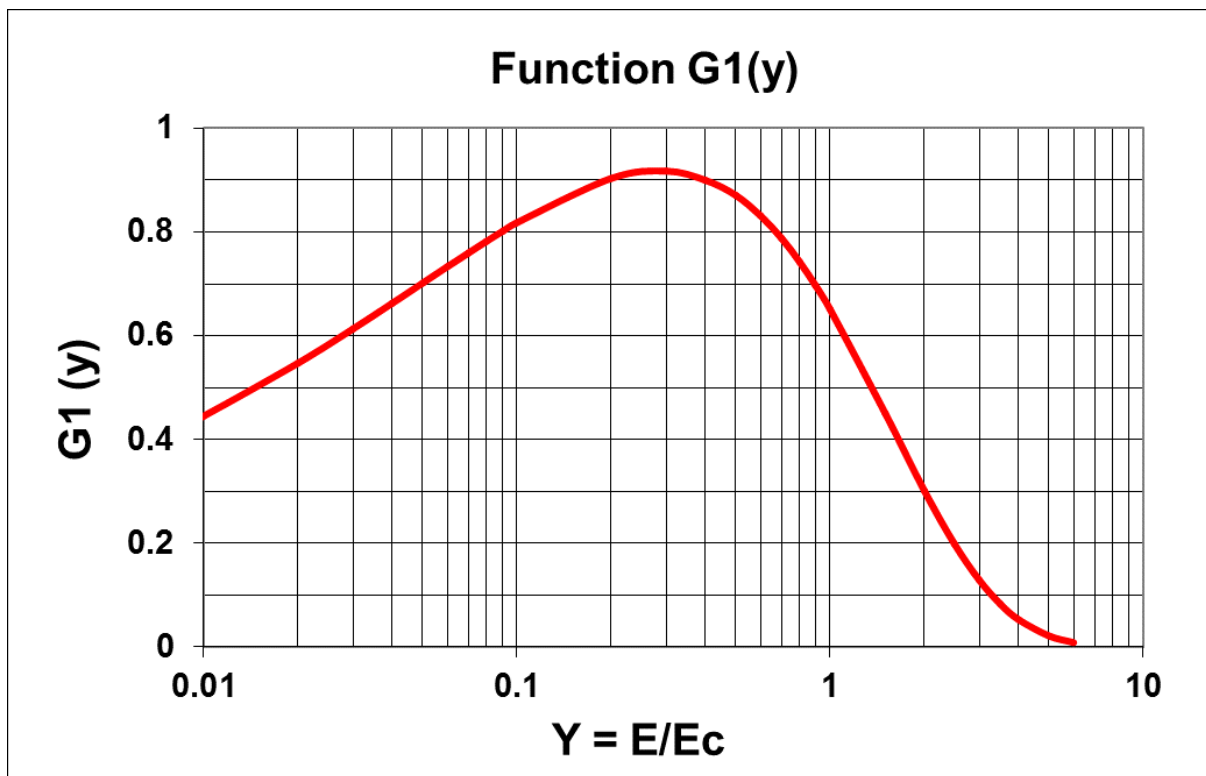


Fig. A.2: The parameter G_1 as a function of the normalized photon energy $\varepsilon/\varepsilon_c$

For synchrotron radiation users, three parameters are important (see Fig. A.1):

- the ‘photon flux’, i.e. the numbers of photons per second and per unit band width;
- the ‘photon flux density’, which is the photon flux divided by the beam cross-section, i.e. flux density = flux/ A_s [photons/(s mm² BW)].

APPENDIX A: SYNCHROTRON RADIATION CHARACTERISTICS

- the ‘brilliance’, which is the flux density divided by the opening angles $\Delta\theta$ and $\Delta\psi$, i.e. brilliance = flux density/ $(\Delta\theta\Delta\psi)$ [photons/(s mm² mrad² BW)].

A.2 Radiation from a bending magnet

The photon flux of the synchrotron radiation from the bending magnet as a function of the horizontal opening angle is given by

$$\frac{d\Phi(y)}{d\theta} = 2.458 \times 10^{13} \frac{\text{photons}}{\text{s} \cdot 0.1\% \text{BW} \cdot \text{mrad}} (E / \text{GeV})(I / \text{A})(\theta / \text{mrad}) \cdot G_1\left(\frac{\varepsilon}{\varepsilon_c}\right). \quad (\text{A.2})$$

According to Eq. (A.2), the photon flux is proportional to the beam current, the energy and the normalized function $G_1(\varepsilon/\varepsilon_c)$, which depends only on the critical photon energy (see Fig. A.2). The equation for the critical photon energy ε_c is

$$\varepsilon_c = 0.655 \text{ keV} \cdot (E / \text{GeV})^2 (B / \text{T}). \quad (\text{A.3})$$

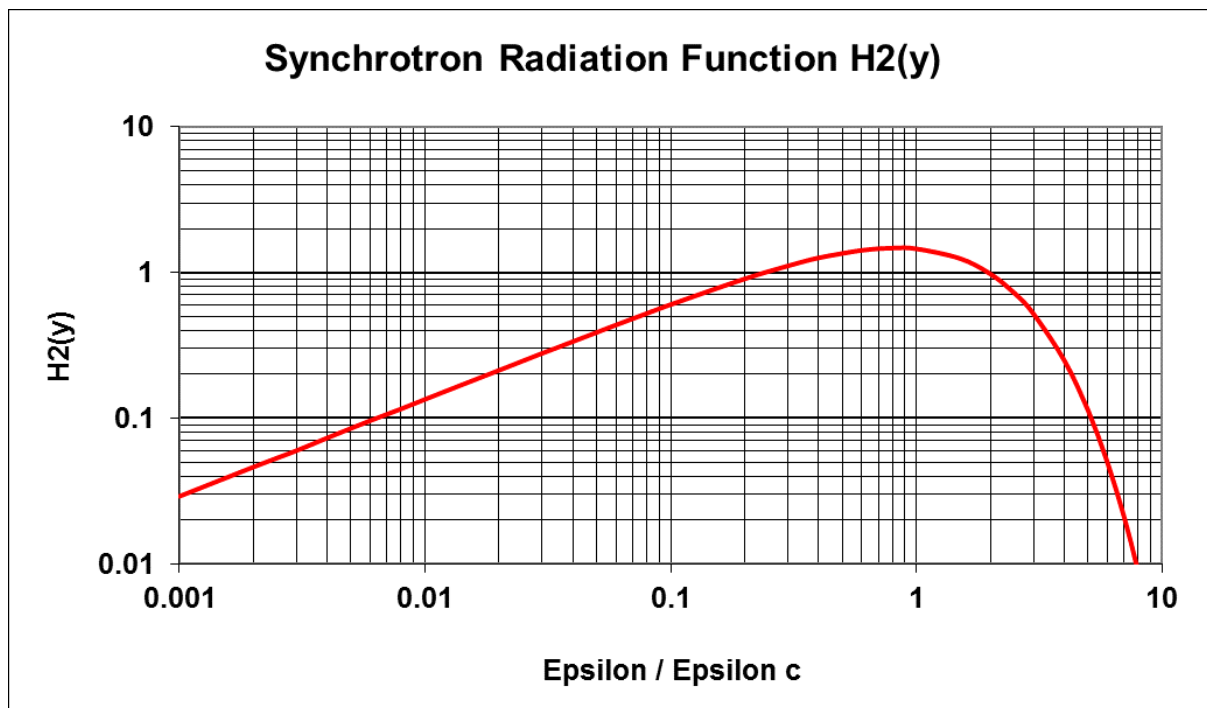


Fig. A.3: The parameter H_2 as a function of the normalized photon energy $\varepsilon/\varepsilon_c$

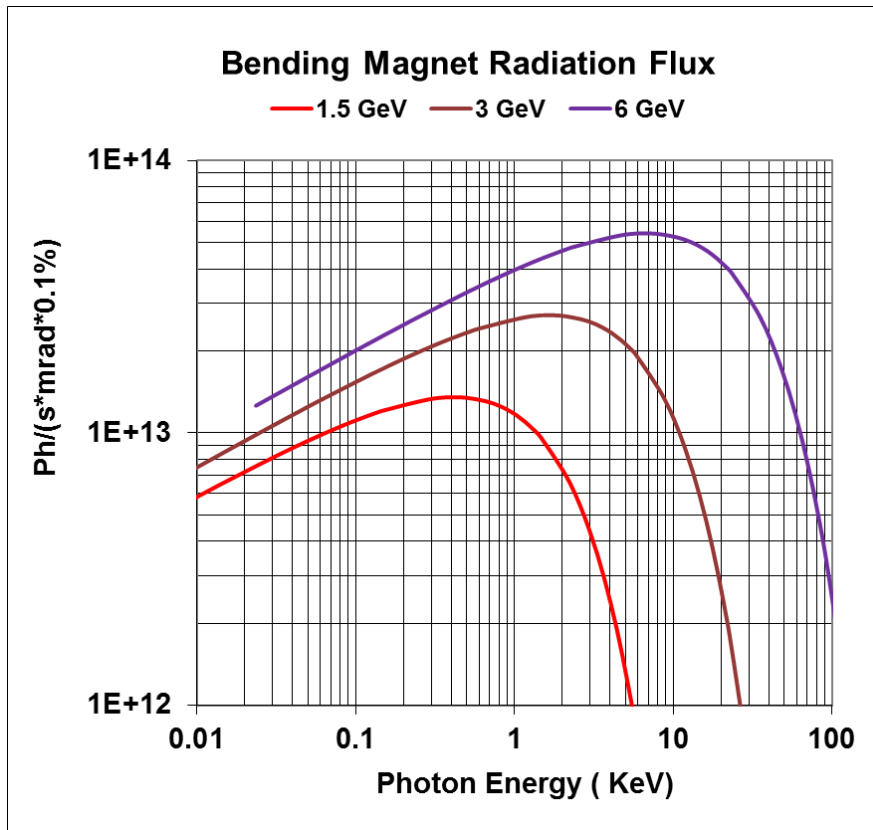


Fig. A.4: The photon flux emitted within the bending magnets for different electron energies (1.5 GeV, 3 GeV, and 6 GeV) and a current of 500 mA.

The intensity of the synchrotron radiation in the middle of the radiation cone ($\theta = 0$ and $\psi = 0$) is given by the following formula (central intensity):

$$\frac{d^2\Phi(y)}{d\theta d\psi} = 1.326 \times 10^{13} \frac{\text{photons}}{s \cdot 0.1\% \cdot \theta \text{ mrad} \cdot \psi \text{ mrad}} (E / \text{GeV})^2 (I / \text{A}) \cdot H_2 \left(\frac{\varepsilon}{\varepsilon_c} \right). \quad (\text{A.4})$$

The normalized function $H_2(\varepsilon/\varepsilon_c)$ is presented in Fig. A.3.

The photon flux as a function of the emitted photon energy for different beam energies (1.5 GeV, 3 GeV, and 6 GeV and a field of 1 T) is presented in Fig. A.4. The photon flux increases with the beam energy. In order to cover the soft-X-ray region (approximately 6–10 keV), beam energies of 1.5–2 GeV are needed. To reach the hard-X-ray region, the beam energy has to be 3–4 GeV. To reach photon energies of up to 100 keV, a beam energy of roughly 6 GeV is required.

Some users will be interested in the photon flux density (see Fig. A.5), which is the photon flux divided by the cross-section of the stored electron beam, because the cross-section of the beam will be imaged on the sample. With beam dimensions of $\sigma(x) = 11.3 \mu\text{m}$ and $\sigma(y) = 3.2 \mu\text{m}$ in the middle of the bending, the flux density should be around four orders of magnitudes higher than the flux, going from 10^{13} to 10^{17} – 10^{18} .

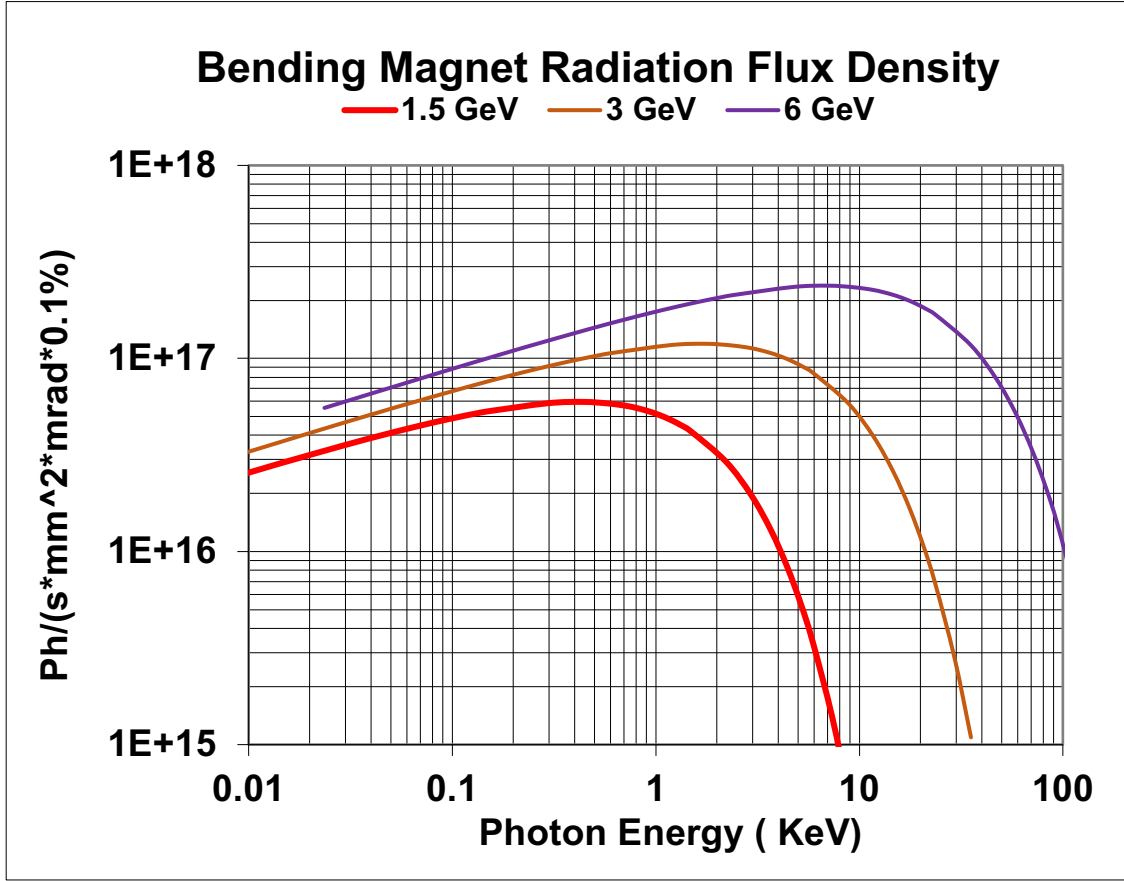


Fig. A.5: The photon flux density (for beam dimensions $\sigma(x) = 11.3 \mu\text{m}$ and $\sigma(y)=3.2 \mu\text{m}$) emitted from the bending magnet of SEE-LS at different energies and a current of 400 mA.

Because the radiation cone gets narrower with higher energy, the central intensity is proportional to the square of the energy. The spectral dependency is given by the normalized synchrotron function $H_2(y) = H_2(\varepsilon/\varepsilon_c)$. From the definition of the flux (Eq. (A.1)) and the central intensity (Eq. (A.4)), the vertical opening angle of the synchrotron radiation is given by

$$\sigma_\psi = \frac{1}{\sqrt{2\pi}} \cdot \frac{\left\langle \frac{d\Phi}{d\theta} \right\rangle}{\left\langle \frac{d^2\Phi}{d\theta d\psi} \right\rangle} (\psi = 0) = \sqrt{\frac{2\pi}{3}} \cdot \frac{1}{\gamma} \cdot \frac{G_1(y)}{H_2(y)} = 0.7395 \text{ mrad} \cdot \frac{1}{E / \text{GeV}} \cdot \frac{G_1(y)}{H_2(y)}. \quad (\text{A.5})$$

The opening angle of the synchrotron radiation from the bending magnet of SEE-LS for a stored beam with different energies is presented in Fig. A.6.

The opening angle at the critical photon energy ($y=1$ or $\varepsilon = \varepsilon_c$) is, according to Eq. (A.5),

$$\sigma_\psi (y=1) = 0.331 \text{ mrad} \cdot \frac{1}{E / \text{GeV}}. \quad (\text{A.6})$$

For a 3.0 GeV machine the corresponding angle is 0.11 mrad.

Most users would be interested in the photon brilliance. The brilliance of the synchrotron radiation from a bending magnet is given by the central intensity divided by the cross-section of the beam:

$$\text{Br} = \frac{\left\langle \frac{d^2\Phi}{d\theta d\psi} \right\rangle (\psi = 0)}{2\pi \Sigma_x \Sigma_y}, \quad (\text{A.7})$$

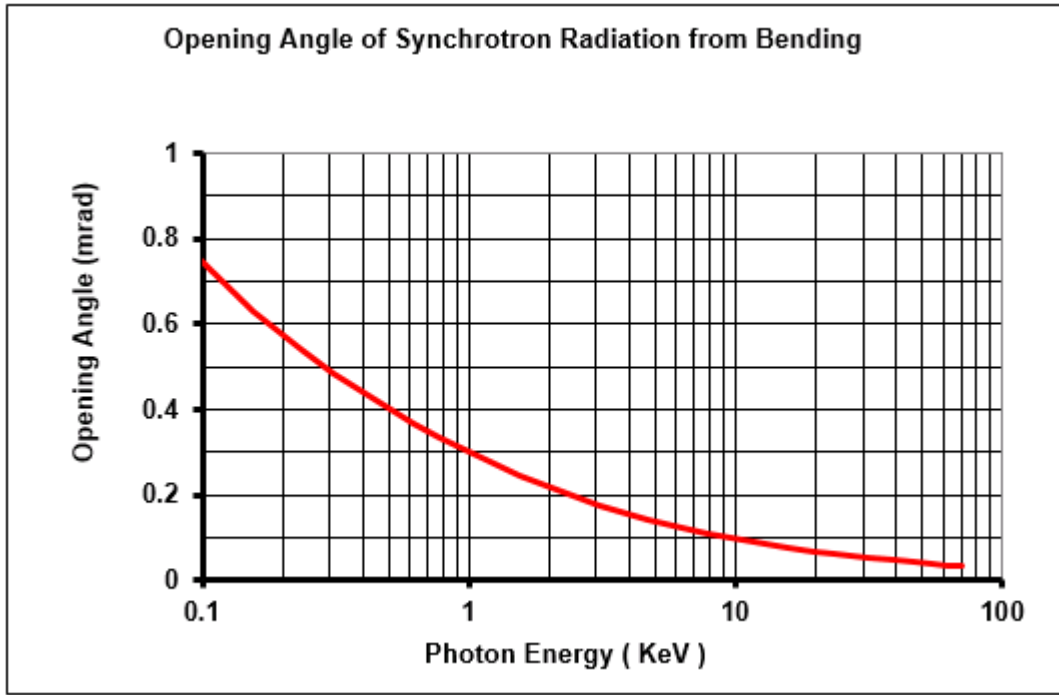


Fig. A.6: Opening angle of the synchrotron radiation from the bending magnet at 2.5 Ge.V

with

$$\Sigma_x = \left[\varepsilon_x \beta_x + \eta_x^2 \sigma_E^2 + \sigma_r^2 \right]^{1/2}, \quad \Sigma_y = \left[\varepsilon_y \beta_y + \sigma_r^2 + \frac{\varepsilon_y^2 + \varepsilon_y \gamma_y \sigma_r^2}{\sigma_\psi^2} \right]^{1/2}, \quad (\text{A.8})$$

where

ε_x (ε_y) is the electron beam emittance in the horizontal (vertical) plane;

β_x (β_y) is the electron beam beta function in the horizontal (vertical) plane;

η_x is the dispersion function in the horizontal plane;

σ_E : is the r.m.s. value of the relative energy spread;

γ_y is the Twiss parameter in the vertical plane;

σ_ψ is the r.m.s. value of the radiation opening angle;

$\sigma_r = \lambda / (4\pi\sigma_\psi)$ is the diffraction-limited source size;

λ is the observed photon wavelength.

At a photon energy of 10 keV the corresponding photon wavelength is 0.124 nm and the opening angle is smaller than 0.1 mrad (see Fig. A.6). This results in a diffraction-limited source size of $\sigma_r = 1.24 \mu\text{m}$. The term $\varepsilon_y / \sigma_\psi$ gives a cross-section of $2 \mu\text{m}$, and $\varepsilon_y \gamma_y / \sigma_\psi^2$ has a value between 1×10^{-3} and 4×10^{-3} . These factors are at least one order of magnitude smaller than the beam cross-section sizes σ_x and σ_y ; hence the overall cross-sections in Eq. (A.8) reduce to

$$\Sigma_x = \left[\varepsilon_x \beta_x + \eta_x^2 \sigma_E^2 \right]^{1/2}, \quad \Sigma_y = \left[\varepsilon_y \beta_y \right]^{1/2}, \quad (\text{A.9})$$

and the brilliance of the synchrotron radiation from the bending magnet of a non-diffraction-limited light source is given by

$$Br_{\text{Magnet}} = \frac{\left\langle \frac{d^2\Phi}{d\theta d\psi} \right\rangle(\psi=0)}{2\pi \left[\varepsilon_x \beta_x + \eta_x^2 \sigma_E^2 \right]^{1/2} \left[\varepsilon_y \beta_y \right]^{1/2}} = \frac{\left\langle \frac{d^2\Phi}{d\theta d\psi} \right\rangle(\psi=0)}{2\pi \sigma_x \sigma_y} . \quad (\text{A.10})$$

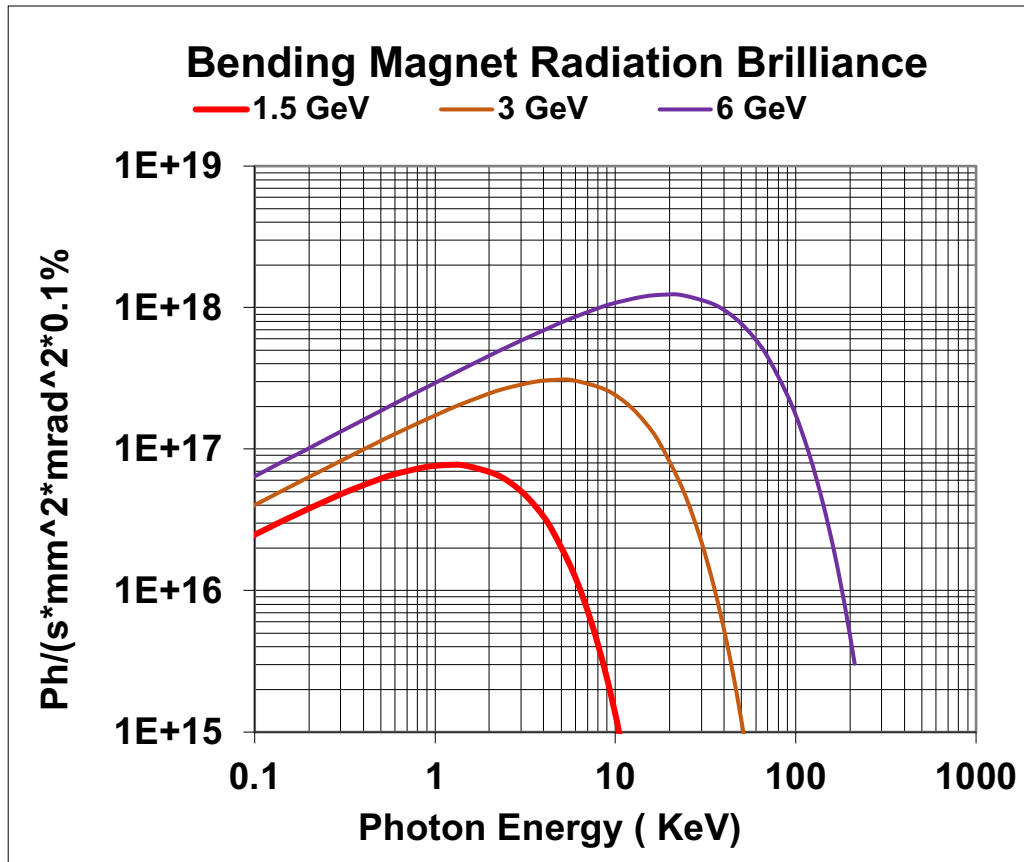


Fig. A.7: Radiation brilliance from the bending magnet at different energies, a current of 400 mA, and a field of 1 T.

Plots of the brilliance of the synchrotron radiation emitted from the bending magnets (for $I = 500$ mA and $B = 1$ T) at different energies are presented in Fig. A.7. The brilliance, as well the spectrum, increases with the energy of the beam.

A.3 Radiation from a wiggler

The wiggler is a special magnet with alternating directions of the magnetic field, and the trajectory of an electron beam through a wiggler is like a snake—a sinusoidal oscillation with the peak field in the middle of the magnets [A.4, A.5]. The arrangement of the magnets in a so-called ‘hybrid design’ (HYB) is shown in Fig. A.8. The arrows symbolize the direction of the magnetic field in the different materials. The green and yellow blocks are special permanent magnets, and the brown blocks are made of magnetic steel. The trajectory of the electron beam in such a wiggler is presented in Fig. A.9 (blue line). The red arrows symbolize the emitted radiation, and it follows that an overlapping of the radiation cone will occur. With this arrangement of magnets, the photon flux, flux density, and brilliance will increase approximately with the number of poles. The electron beam in the wiggler has a maximum amplitude X_0 and a maximum slope X'_0 .

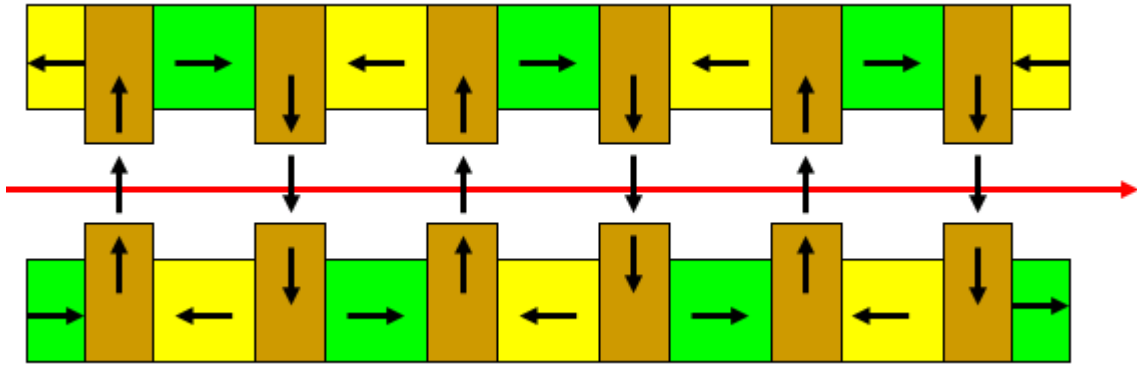


Fig. A.8: The arrangement of magnets within a wiggler; the green and yellow blocks represent permanent magnets, and the brown blocks are made of magnetic steel.

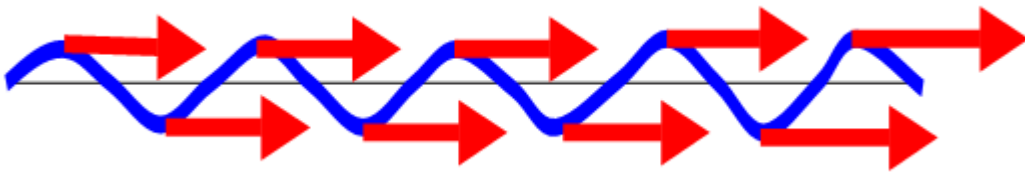


Fig. A.9: The trajectory of an electron beam within a wiggler (blue line); the red arrows symbolize the emitted synchrotron radiation in the horizontal direction.

The maximum slope X'_0 and the maximum amplitude X_0 characterize the trajectory of the electron beam. They are given by

$$X_0 = \frac{1}{2\pi} \cdot \frac{K}{\gamma} \cdot \lambda_p = \frac{8.13 \times 10^{-5}}{(E/\text{GeV})} K \lambda_p, \quad X'_0 = \frac{K}{\gamma}, \quad K = 0.934 (B/\text{T}) (\lambda_p / \text{cm}). \quad (\text{A.11})$$

The photon flux, as well as the central intensity of the radiation emitted by the wiggler, is the same as from the bending magnet but a factor of N_p more intense, where N_p is the number of poles within the wiggler. The value of N_p is, according to Table A.1, 86 (twice N_{per}). For the synchrotron radiation from the wigglers, the critical energy ε_c determines everything. To reach the same spectral range as from the bending magnets (given by ε_c ; see Eq. (A.3)), the magnetic flux density within the wigglers must be the same as within the bending magnets or—for shifting the spectrum to higher photon energies—even higher. At CCRL, Daresbury Laboratory, UK, fields of up to 2.5 T can be attained with ‘hybrid design’. Higher fields are possible with superconducting devices; at the MAX IV Laboratory, Lund, Sweden, fields of up to 3 T can be reached. In Table A.1 the data needed for calculation of the wiggler radiation characteristics at the different energies are summarized.

APPENDIX A: SYNCHROTRON RADIATION CHARACTERISTICS

Table A.1: Parameters for the calculation of the wiggler radiation characteristics

Energy	Unit	1.5 GeV	3 GeV	6 GeV
Current	mA	500	500	200
Field	T	3.7	3.7	3.7
L period	mm	46	46	46
N periods		43	43	43
K value		15.88	15.88	15.88
Emittance x	pmrad	64.1	251	1005
Emittance y	pmrad	5	5	5
σ_x	μm	31	62	124
σ_y	μm	4.7	4.7	4.7
β_x		15.16	15.16	15.16
β_y		4.44	4.44	4.44
Disp. x	m	0	0	0
Energy spread	1.0E-04	4.4	8.8	17.7
X_0	μm	39.6	19.8	9.9
X'_0	μrad	5.4	2.7	1.4

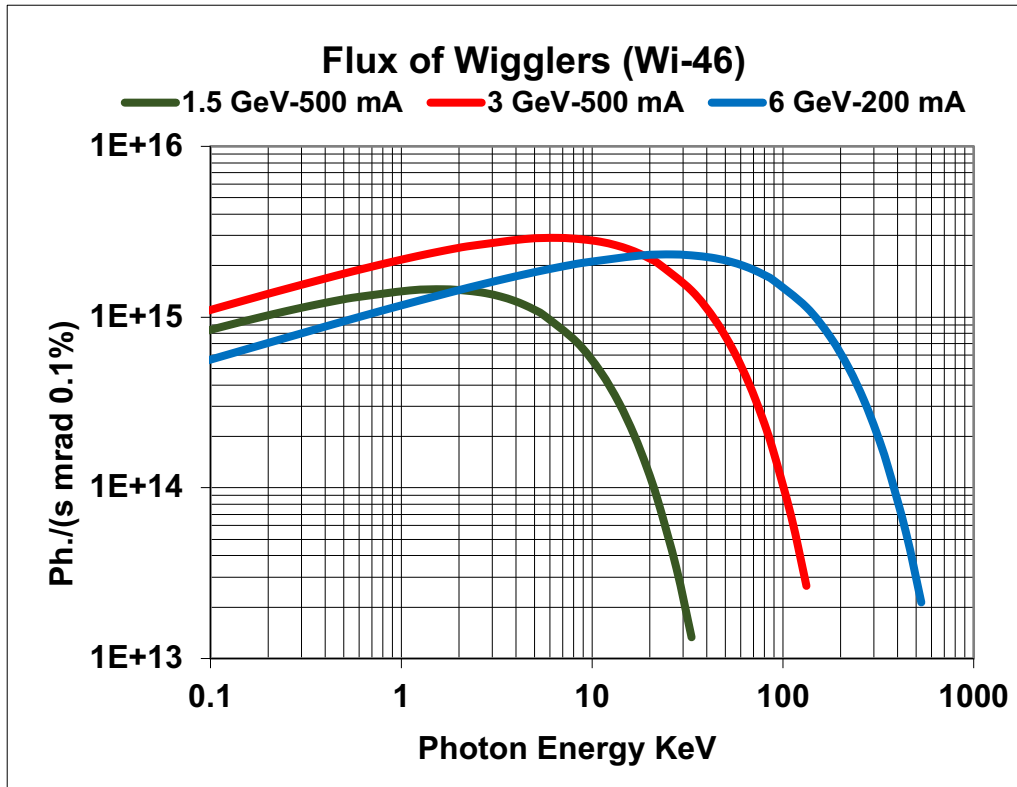


Figure A.10: The radiation flux of wiggler Wi-46 installed at SEE-LS for different energies and currents of 600 mA (1.5 GeV and 3 GeV) and 400 mA (6 GeV).

The wiggler radiation flux and flux density according to the parameters in Table A.1 are plotted in Figs. A.10 and A.11. The flux from the wiggler as a function of the photon energy has the beam characteristics of the bending magnet radiation, except that the intensity is higher by a factor 86 ($2 \times N_{\text{per}}$).

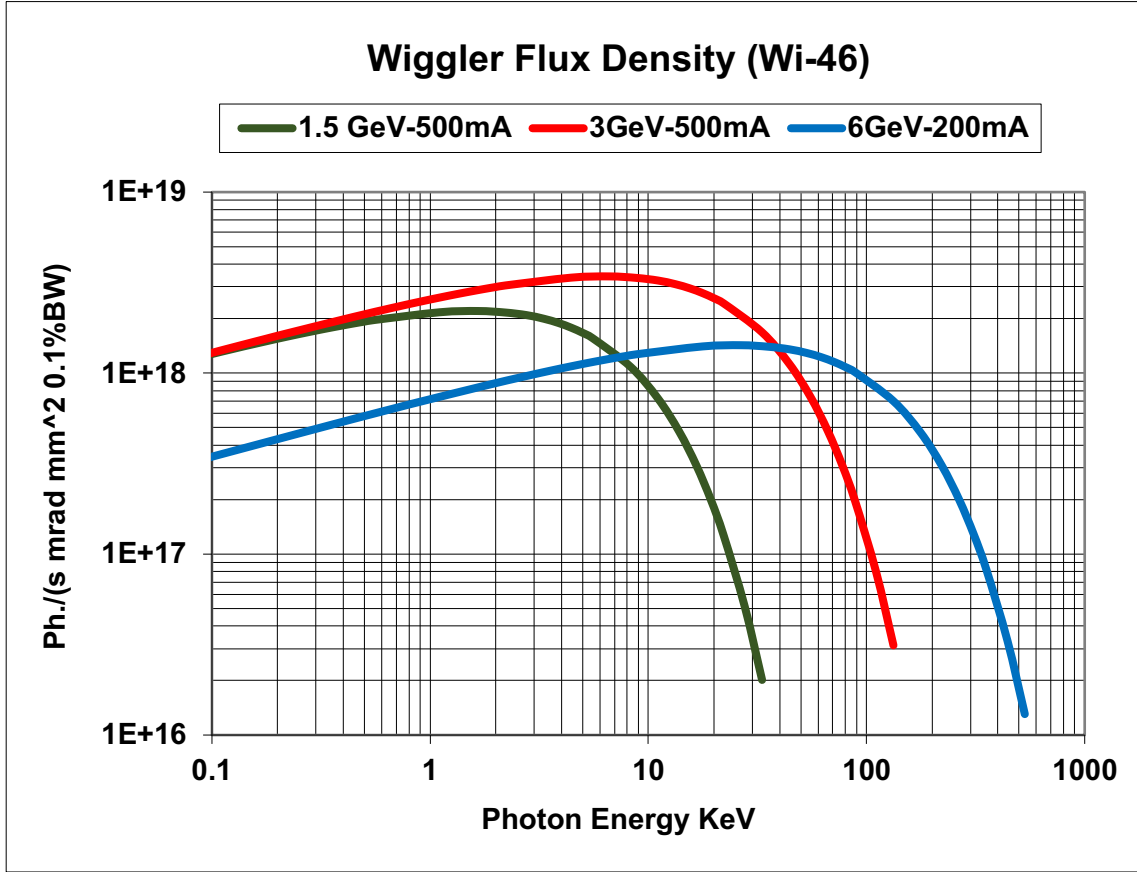


Fig. A.11: The radiation flux density of wiggler Wi-46 installed at SEE-LS for different energies and currents of 500 mA (1.5 GeV and 3 GeV) and 200 mA (6 GeV).

The wiggler flux density as a function of the photon energy is presented in Fig. A.11 for different electron beam energies. These characteristics are different from those of the bending magnet radiation because the emittance increases with the square of the beam energy and correspondingly the beam cross-section, as given in Table A.1.

The calculation of the brilliance of wigglers needs to take into account the depth of fields, i.e., the contribution to the apparent source size from different poles. The expression for the brilliance of the wigglers is

$$\text{Br}_{\text{Wiggler}} = \left\langle \frac{d^2\Phi}{d\theta d\psi} \right\rangle (\psi = 0) \cdot \sum_{-N/2}^{N/2} \frac{1}{2\pi} \cdot \frac{\exp\left\{-\frac{1}{2}\left(\frac{X_0^2}{\sigma_x^2 + z_n^2 \sigma_x'^2}\right)\right\}}{\left[\sigma_x^2 + z_n^2 \sigma_x'^2\right]^{1/2} \left[\frac{\varepsilon_y^2}{\sigma_\psi^2} + \sigma_y^2 + z_n^2 \sigma_y'^2\right]^{1/2}}. \quad (\text{A.12})$$

where:

$$z_n = \lambda_p \left(n + \frac{1}{4} \right). \quad (\text{A.13})$$

In Eq. (A.12) σ_x , σ_x' , σ_y , and σ_y' are the r.m.s. transverse sizes and angular divergences of the electron beam at the centre of an insertion straight section ($\alpha_x = \alpha_y = 0$). This means that the brilliance of the wiggler calculated according to Eq. (A.12) is normalized to the middle of the straight section.

The exponential factor in Eq. (A.12) arises because the wigglers have two points, separated by $2X_0$ with X_0 as in Eq. (A.11). The sum in Eq. (A.12) goes over all poles of the wiggler. As already discussed in the section on the radiation of the bending magnets, the term $\varepsilon_y/\sigma_\psi$ is at least a factor of 10

smaller than the cross-section σ_y and so can be neglected. The expression $z_n \sigma_y^2$ is the increase of the source size from the centre of the insertion device.

Instead of normalizing the brilliance to the centre of the straight section, the cross-sections of the beam at the positions of the poles, $\sigma_x(n)$ and $\sigma_y(n)$, can be used, yielding a simpler expression for the brilliance:

$$\text{Br}_{\text{Wiggler}} = \left\langle \frac{d^2\Phi}{d\theta d\psi} \right\rangle (\psi = 0) \cdot 2 \sum_{-N/2}^{N/2} \frac{1}{2\pi} \cdot \frac{\exp\left\{-\frac{1}{2}\left(\frac{X_0^2}{\sigma_x^2(n)}\right)\right\}}{\sigma_x(n) \sigma_y(n)}. \quad (\text{A.14})$$

The brilliances of the three types of wigglers in Table A.1 are presented in Fig. A.12. The brilliance is determined by the flux and the cross-sections of the beam; so because the cross-sections at the locations of the wigglers are three or four times larger than in the bending magnets, the brilliance of the wigglers is a factor of 20 more intense than that of the bending magnets.

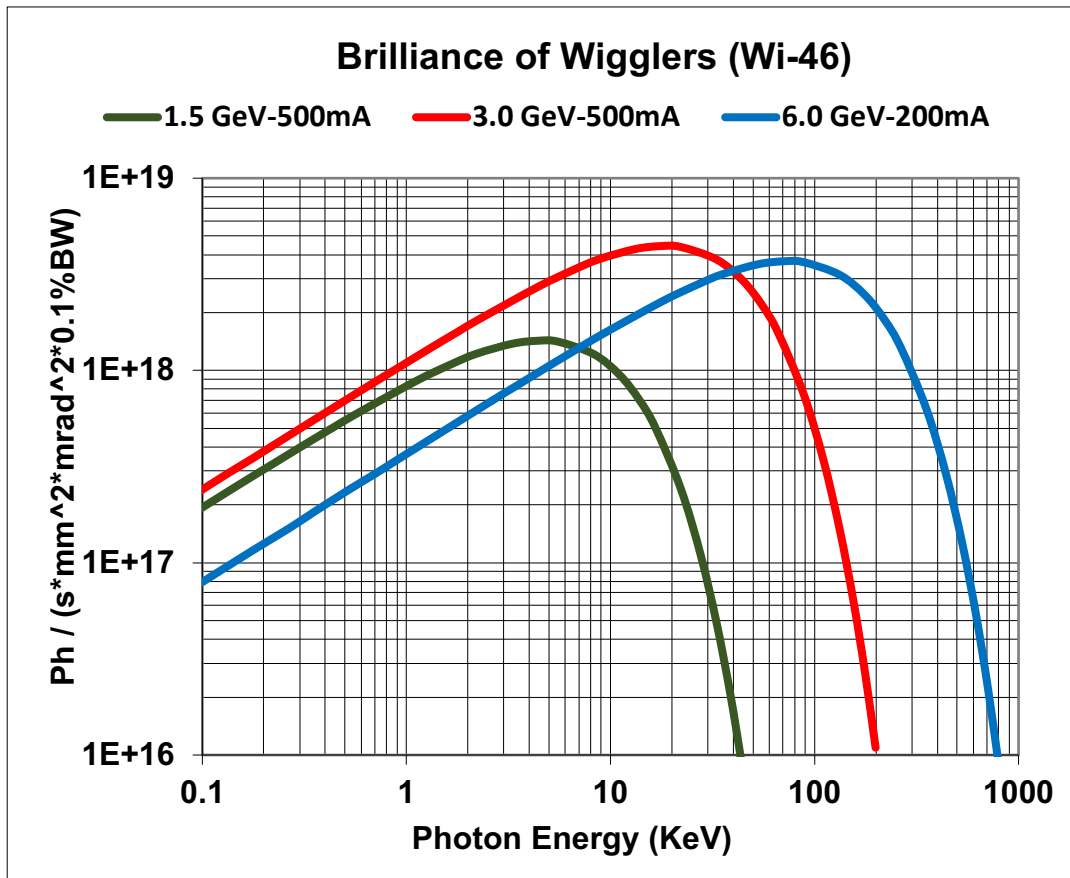


Fig. A.12: The radiation brilliance of the wiggler Wi-46 installed at SEE-LS for different energies and currents of 500 mA (1.5 GeV and 3 GeV) and 200 mA (6 GeV).

According to Eq. (A.14), the brilliance of a wiggler is inversely proportional to the cross-section of the beam and not to the emittance, because the amplitude X_0 of the beam oscillation has to be taken into account. In general the beam cross-section can be manipulated with the beta function in the storage ring. The dependence of the wiggler brilliance on the photon energy is shown in Fig. A.12 for different electron beam energies. The dependence on the beam energy is completely different from that of the bending radiation (cf. Fig. A.7), because the cross-sections are a function of the beam energy.

A.4 Radiation from an undulator

The opening angle σ_ψ of the synchrotron radiation from the bending magnet at the critical photon energy ε_c is, according to Eq. (A.5), about $0.655/\gamma$ or $1/\gamma$. The maximum slope of the electron trajectory in a wiggler is $X' = K/\gamma$. For values of K between 1 and 2, the deflection angle in a wiggler is within the opening angle of the synchrotron radiation [A.7–A.9]. In this special case the radiation from different periods interferes coherently, thus producing sharp peaks and resulting in completely different radiation characteristics. This radiation, as symbolized in Fig. A.13, is called undulator radiation, and the corresponding insertion devices are undulators. A photo of an insertion device is given in Fig. A.15.

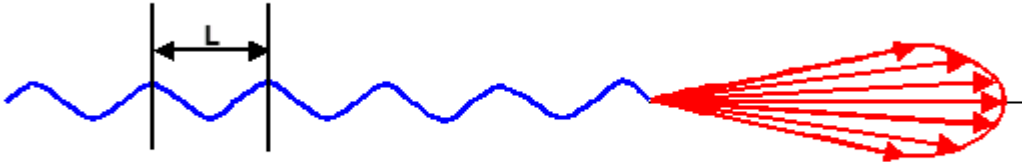


Fig. A.13: Characterization of the undulator radiation; L is the period length of the undulator

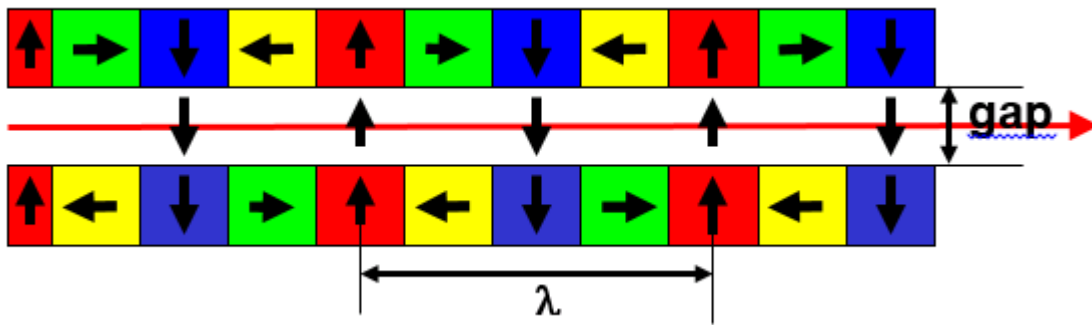


Fig. A.14: The arrangement of magnets within an undulator; the red, green, blue, and yellow blocks represent permanent magnets.

Undulators are insertion devices like the wigglers but with a smaller K values (between 1 and 2). The general set-up of an undulator is shown in Figs. A.14 and A.15. The blocks of different colours represent the permanent magnets, and the direction of the magnetic field is represented by arrows. The period length is denoted by λ .

The undulator emits radiation only at characteristic wavelengths:

$$\lambda_n = \frac{\lambda_{\text{Und}}}{2n\gamma^2} \left(1 + \frac{K^2}{2} + \gamma^2 \Theta^2 \right). \quad (\text{A.15})$$

The corresponding photon energies are

$$\varepsilon_n = 0.949 \text{ keV} \cdot (E / \text{GeV})^2 \frac{n}{(\lambda_{\text{Und}} / \text{cm}) (1 + (K^2 / 2) + \gamma^2 \Theta^2)}, \quad (\text{A.16})$$

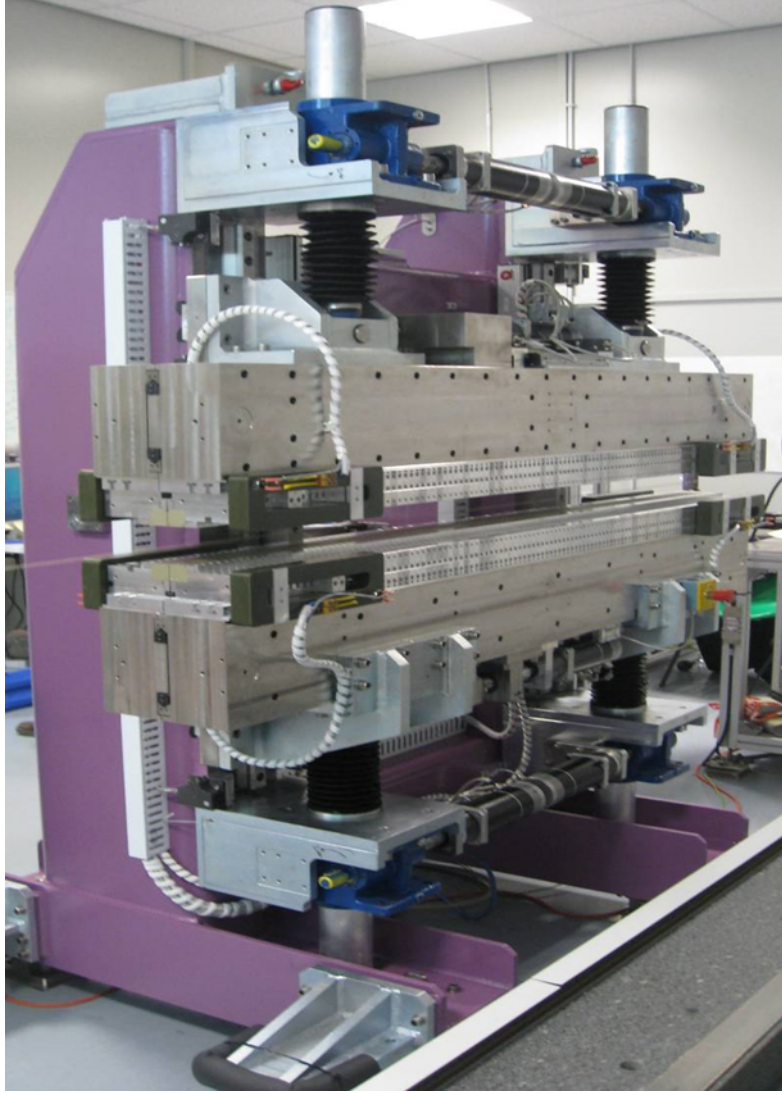


Figure A.15: Photo of an insertion device

with bandwidth

$$\frac{\Delta \varepsilon_n}{\varepsilon_n} = \frac{1}{n N_{\text{Und}}} , \quad (\text{A.17})$$

where:

n is the harmonic number ($n = 1, 3, 5, 7, \dots$);

N_{Und} is the number of periods;

λ_{Und} is the period length of the undulator;

K is the deflection parameter (see Eq. (A.11));

Θ is the observation angle in the horizontal direction.

The opening angle (σ'_γ) and the cross-section (σ_γ) of the undulator radiation are

$$\sigma_\gamma = \frac{\lambda_{\text{Und}}}{4\pi\gamma} \sqrt{\frac{(1+K^2/2)N}{2n}} , \quad \sigma'_\gamma = \frac{1}{\gamma} \sqrt{\frac{1+K^2/2}{2Nn}} . \quad (\text{A.18})$$

The maximum slope X'_0 and the amplitude X_0 characterizing the trajectory of the electron beam are

$$X_0 = \frac{1}{2\pi} \cdot \frac{K}{\gamma} \cdot \lambda_p = \frac{8.13 \times 10^{-5}}{(E/\text{GeV})} K \lambda_p, \quad X'_0 = \frac{K}{\gamma} = \frac{5.1 \times 10^{-4} K}{(E/\text{GeV})}. \quad (\text{A.19})$$

The K values for the undulators are roughly a factor of 10 smaller than for the wigglers; hence the amplitude X_0 and the divergence X'_0 for the undulators are around a factor of 10 smaller than for the wigglers.

$\Delta\varepsilon_n/\varepsilon_n$ is the energy resolution of the spectral line emitted from the undulator. To reach the required bandwidth of 0.1%, the product of n and N must be at least 1000.

The following example (in-vacuum undulator) illustrates the characteristics of the undulator radiation.

The flux of the undulator radiation within the cone of the harmonics is given by (in practical units)

$$\Phi_{\text{Und}}(n, K) = 1.432 \times 10^{14} N_{\text{Und}} \cdot (I/A) \cdot Q_n(K) [\text{photons}/(\text{s } 0.1\% \text{BW})]. \quad (\text{A.20})$$

According to Eq. (A.20), the flux of the undulator radiation is proportional to the number of periods, the current, and the function $Q_n(K)$ (see Fig. A.16). It is independent of the energy and the cross-section of the electron beam and is independent of the machine parameters. To reach a high photon flux (also for higher harmonics), the deflection parameter K should be in the range of 1 to 3. According to Eq. (A.16) the photon spectrum is proportional to the square of the energy and inversely proportional to the period length λ . In order to achieve X-ray radiation, the energy has to be in the range of 4–6 GeV with a period length of 40 mm. The gap would be 11 mm and the magnets of the undulator are outside the vacuum. Smaller period lengths can be attained only by reducing the gap, which is possible by putting the undulator inside the vacuum; so this type of undulator is called an ‘in-vacuum undulator’. The smallest period lengths can be reached with superconducting magnets. These types of undulator are called ‘mini-undulators’.

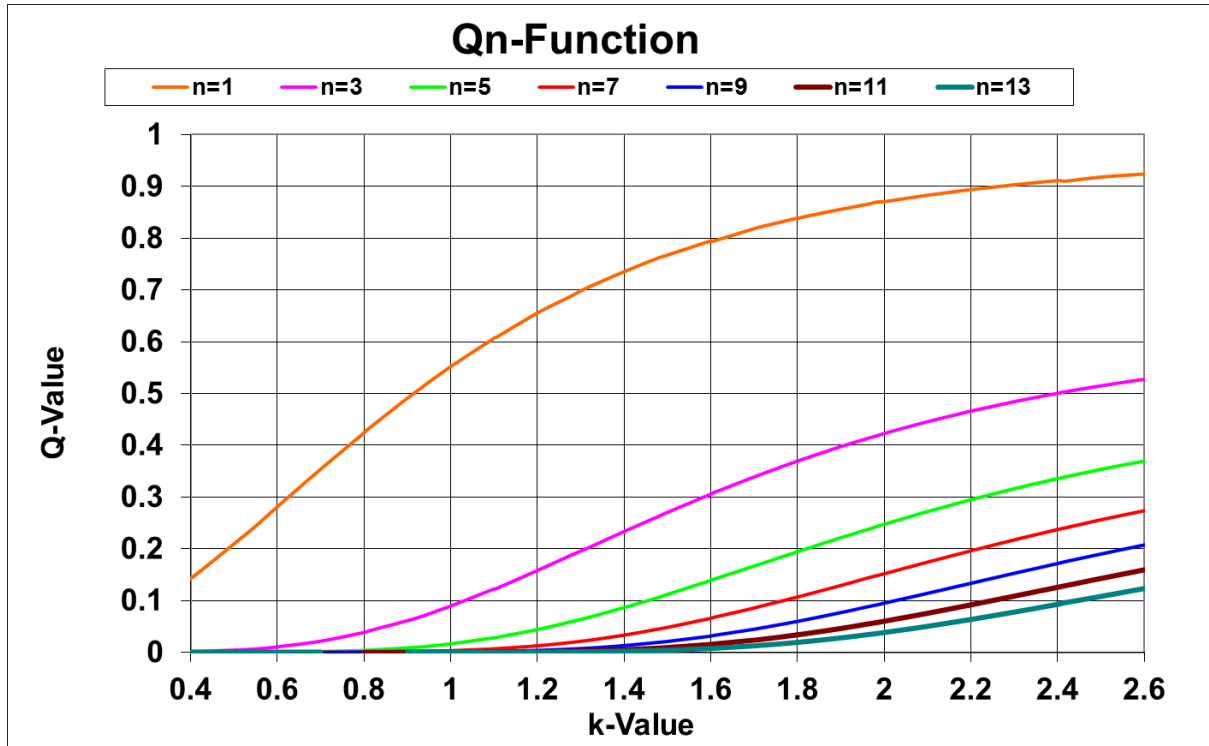


Fig. A.16: The dependence of the Q_n values on the K values

APPENDIX A: SYNCHROTRON RADIATION CHARACTERISTICS

The photon flux of the MAX IV undulator with the specifications $L = 2$ m, $\lambda = 15$ m, and $B_{\max} = 1.5$ T at an energy of 3 GeV and with a stored beam of 250 mA is presented in Fig. A.17.

The peak intensity on the axis of the n th harmonic of the undulator radiation is given by (in practical units of photons/(s mrad²0.1%BW))

$$\frac{d^2\Phi_{\text{Und}}}{d\theta d\psi}(\theta = \psi = 0) = 1.744 \times 10^{14} \cdot N_{\text{Und}}^2 \cdot (E / \text{GeV})^2 (I / \text{A}) \cdot F_n(K) . \quad (\text{A.21})$$

The peak intensity is proportional to the electron current, the radiation function $F_n(K)$ (see Fig. A.19), and the square of the period number. The opening angle of the radiation cone is inversely proportional to the energy, and therefore the peak intensity according to Eq. (A.21) is proportional to the square of the energy.

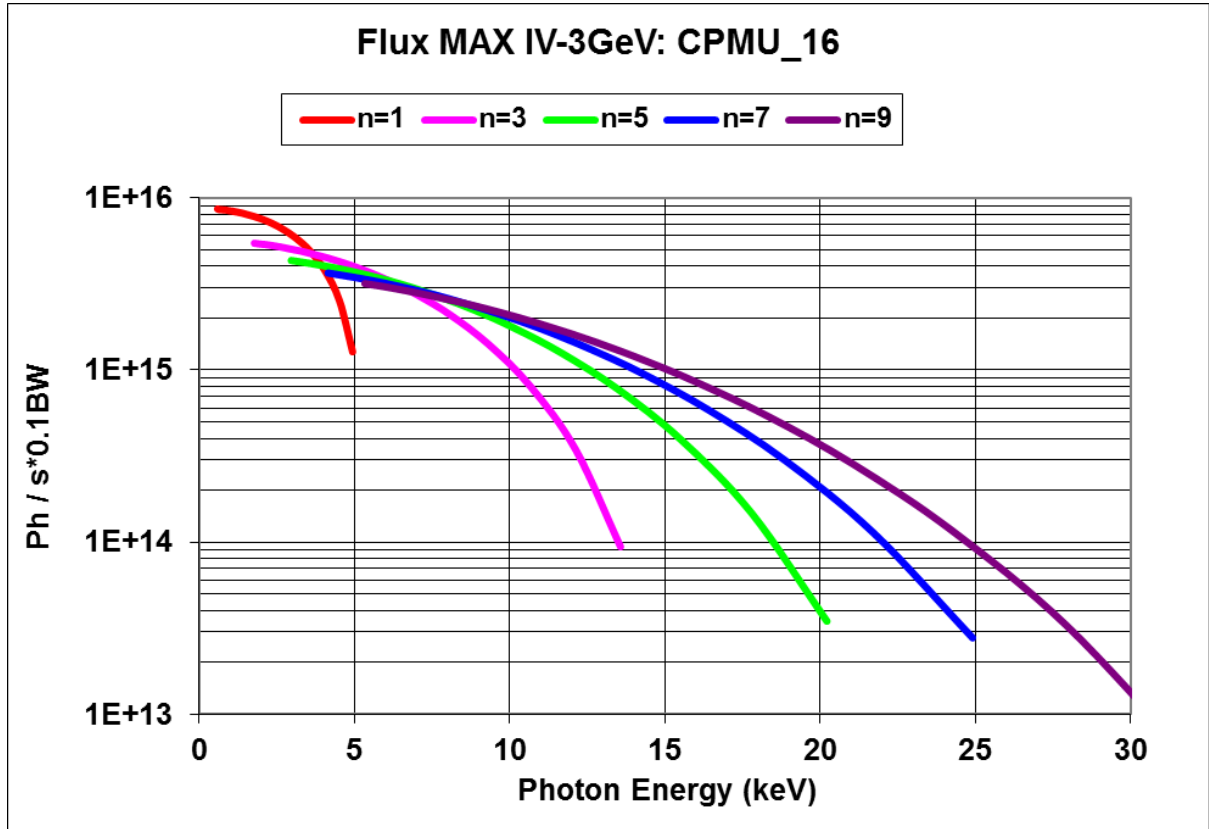


Fig. A.17: The radiation flux of the undulator CPMU_16 with an energy of 3 GeV and a stored beam of 500 mA calculated for the harmonics $n = 1, 3, 5, 7,$ and 9 . The period length of the undulator is 16 mm, the length is 2 m, and the maximum magnetic field is 1.5 T.

The brilliance of the undulator radiation is given by

$$\text{Br}_{\text{Und}} = \frac{\Phi_{\text{Und}}(n, K)}{\left(2\pi \sum_x \sigma \sum_y \sigma\right) \left(2\pi \sum_x \sigma' \sum_y \sigma'\right)} , \quad (\text{A.22})$$

with

$$\sum_x \sigma = \sqrt{\sigma_x^2 + \sigma_r^2}, \quad \sum_y \sigma = \sqrt{\sigma_y^2 + \sigma_r^2}, \quad \sum_x \sigma' = \sqrt{\sigma_x'^2 + \sigma_r'^2}, \quad \sum_y \sigma' = \sqrt{\sigma_y'^2 + \sigma_r'^2}, \quad (\text{A.23})$$

where

$$\sigma_{x,y} = \sqrt{\varepsilon_{x,y} \cdot \beta_{x,y}}, \quad \sigma'_{x,y} = \sqrt{\varepsilon_{x,y} / \beta_{x,y}}, \quad \sigma_r = \frac{1}{4\pi} \sqrt{\lambda L}, \quad \sigma'_r = \sqrt{\lambda / L} . \quad (\text{A.24})$$

Upon substituting λ from Eq. (A.15), σ_r and σ'_r are given by

$$\sigma_r = \frac{\lambda_{\text{Und}}}{4\pi\gamma} \sqrt{\frac{(1+K^2/2)N}{2n}}, \quad \sigma'_r = \frac{1}{\gamma} \sqrt{\frac{(1+K^2/2)}{2nN}}. \quad (\text{A.25})$$

For the aforementioned undulator the cross-sections σ_r and divergences σ'_r according to Eq. (A.24) are presented in Fig. A.18.

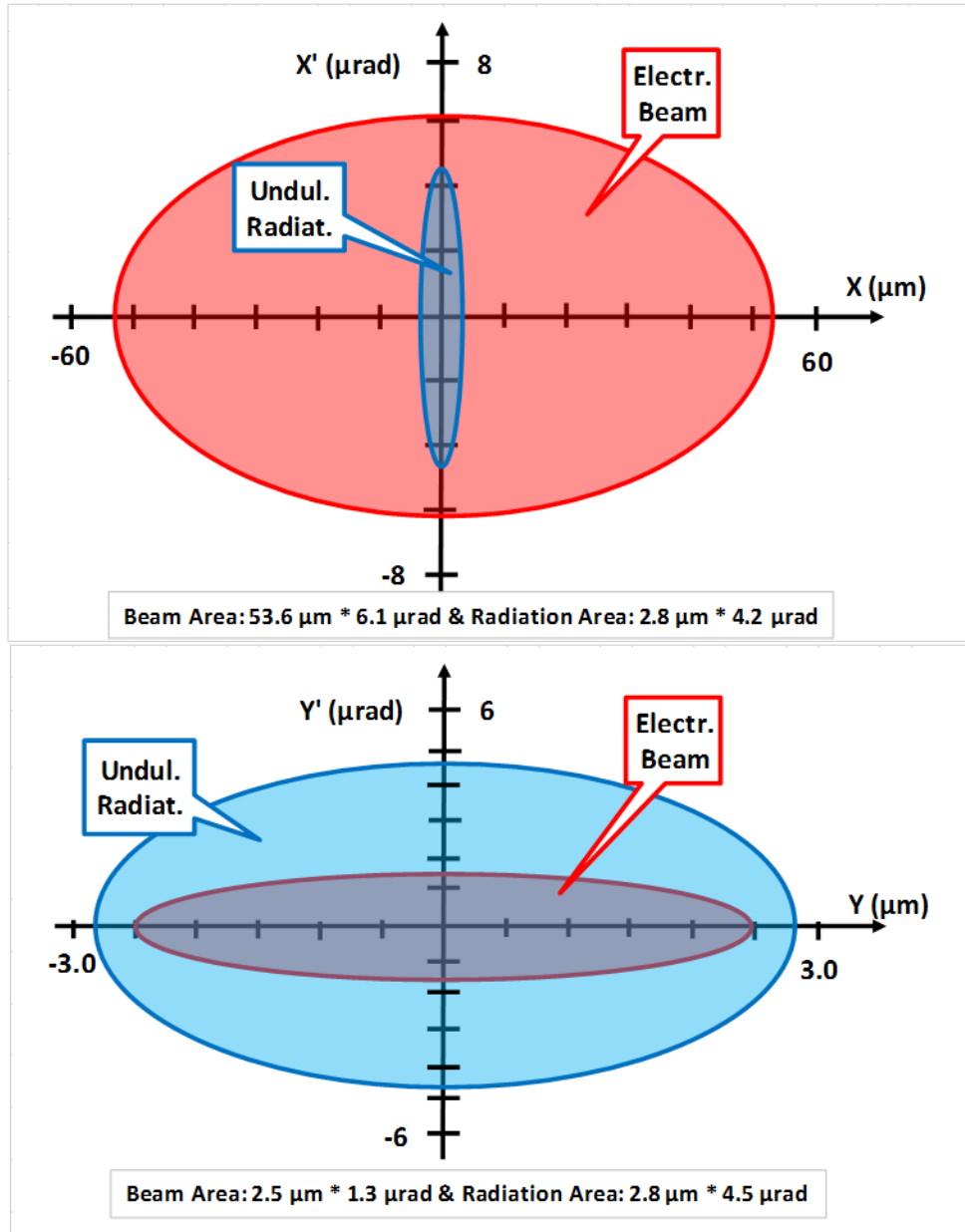


Fig. A.18: The phase space of the electron and radiation beam for the horizontal (upper diagram) and vertical (lower diagram) directions.

For the stored electron beam of 4th generation light sources such as MAX IV, the cross-sections and divergences are $\sigma_x \approx 54 \mu\text{m}$, $\sigma_y \approx 2.5 \mu\text{m}$, $\sigma'_x \approx 6.1 \mu\text{rad}$, $\sigma'_y \approx 1.3 \mu\text{rad}$, $\sigma_r \approx 2.8 \mu\text{m}$, and $\sigma'_r \approx 4.5 \mu\text{rad}$ (see Fig. A.18). For the calculation of the brilliance, in the horizontal direction the wiggler radiation cone can be neglected, but in the vertical direction it has to be taken into account.

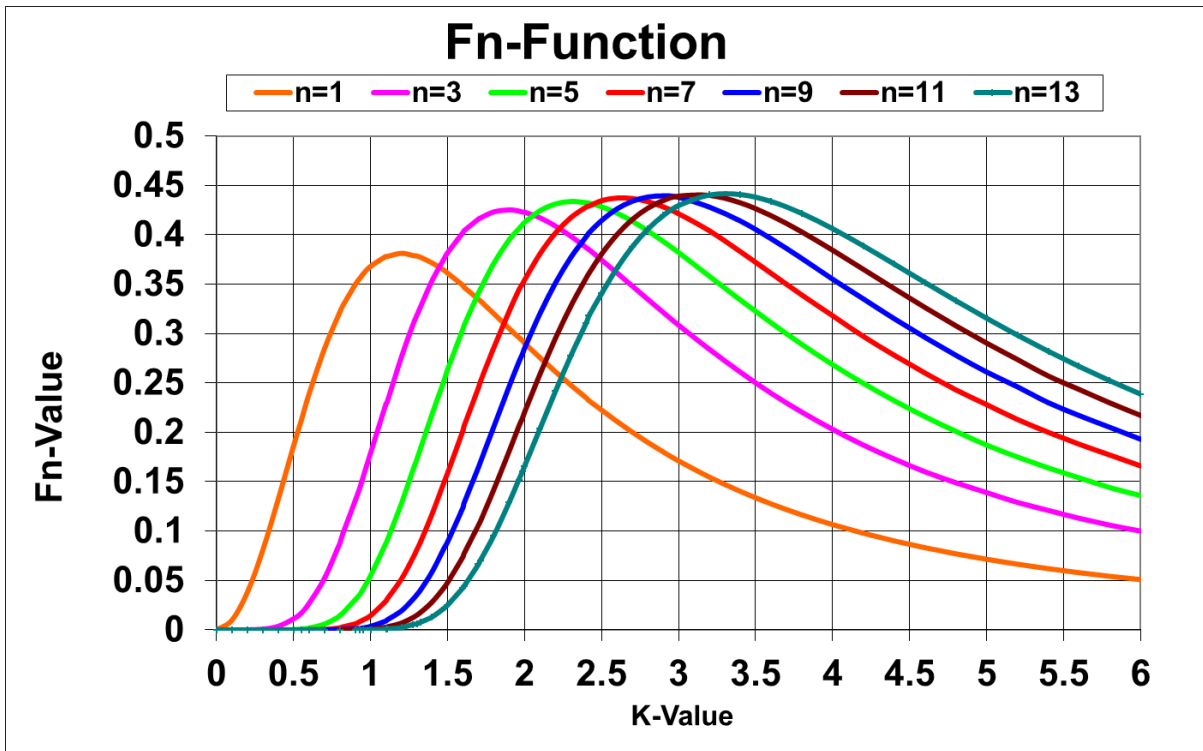


Fig. A.19: The dependence of the F_n values on the K values for the different harmonics

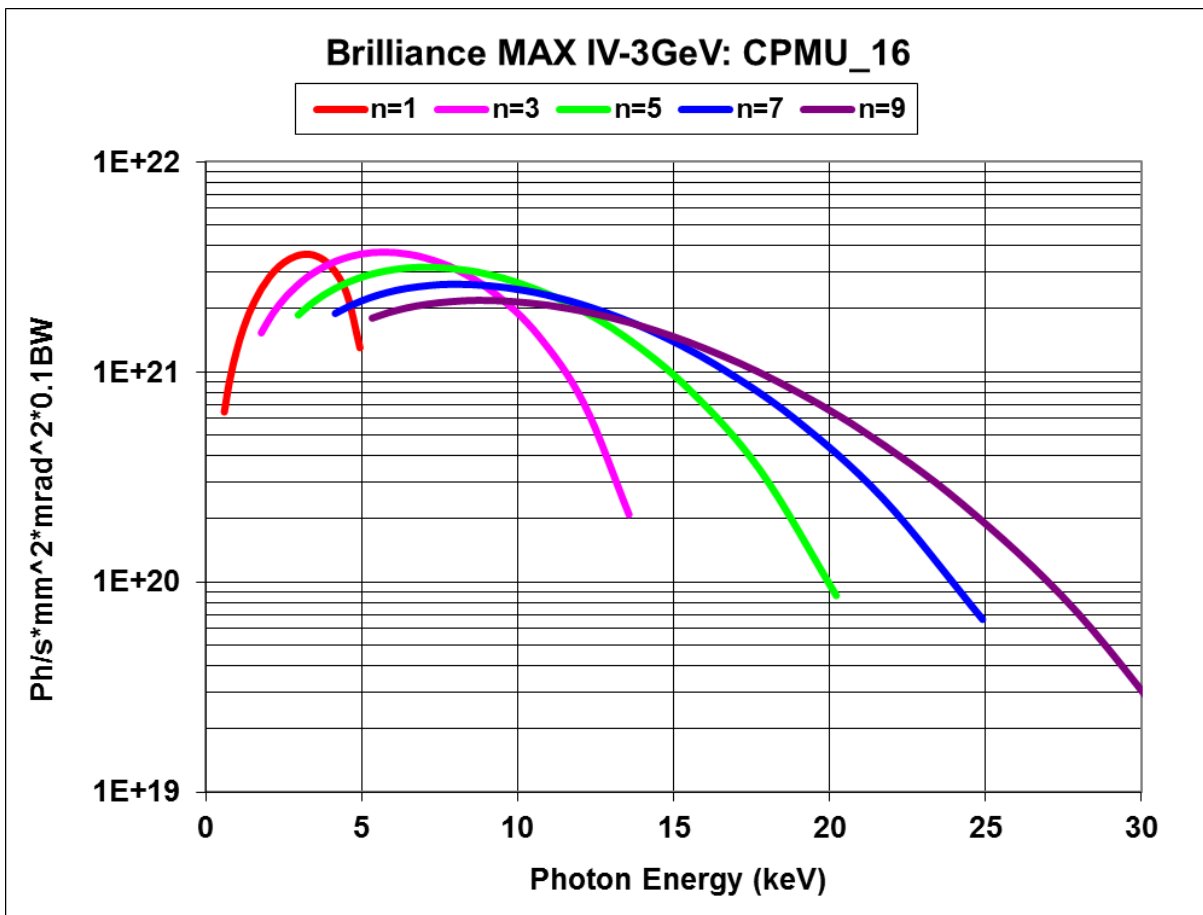


Fig. A.20: The radiation brilliance of the undulator CPMU_16 with an energy of 3 GeV

According to Fig. A.20, with a 4th generation light source such as MAX IV brilliances of up to 10^{22} photons/(s mm² mrad² 0.1BW) can be reached.

A.5 Influence of the beam energy spread on the spectral photon flux

The spectral photon flux is the number of photons per second per 0.1% bandwidth. The bandwidth of the undulator radiation is given by Eq. (A.17). The dependence of the emitted photon spectrum on the energy is described by Eq. (A.16). According to the energy spread of the stored electrons, the electrons emit light with different energies. The relative energy spread ($\delta E/E$) of the stored electron beam is in the range of 10^{-3} . This gives an energy spread for the undulator radiation of $\delta E/E = 2 \times 10^{-3}$. For the aforementioned example we have the following results.

- Natural photon energy spread of undulator radiation:
 $\Delta \varepsilon_1 = 16.74 \text{ eV}, \Delta \varepsilon_3 = 16.74 \text{ eV}, \Delta \varepsilon_5 = 16.74 \text{ eV}, \dots, \Delta \varepsilon_{11} = 16.74 \text{ eV}.$
- Photon energy spread according to variation of the beam energy:
 $\delta \varepsilon_1 = 3.2 \text{ eV}, \delta \varepsilon_3 = 9.6 \text{ eV}, \delta \varepsilon_5 = 16 \text{ eV}, \delta \varepsilon_7 = 22.6 \text{ eV}, \delta \varepsilon_9 = 29 \text{ eV}, \dots, \delta \varepsilon_{11} = 35.0 \text{ eV}.$

According to these results, the spectral photon fluxes of the higher harmonics of the undulator radiation are determined by the energy spread of the stored electron beam. With this example it starts at the 5th harmonic. This has to be taken into account.

References

- [A.1] H. Wiedemann, *Synchrotron Radiation* (Springer, Berlin, 2003), <https://doi.org/10.1007/978-3-662-05312-6>
- [A.2] R. Walker, Synchrotron radiation, CAS-CERN Accelerator School: 5th General Accelerator Physics Course, Jyväskylä, Finland, 7–18 September 1992, CERN-1994-001 (CERN, Geneva, 1994), p. 437. <https://doi.org/10.5170/CERN-1994-001>
- [A.3] CAS-CERN Accelerator School: Synchrotron Radiation and Free Electron Lasers, Grenoble, France, 22–27 April 1996, CERN-1998-004 (CERN, Geneva, 1998). <https://doi.org/10.5170/CERN-1998-004>
- [A.4] H. Onuki and P. Elleaume, *Undulators, Wigglers and Their Applications* (Taylor and Francis, London, 2003), <https://doi.org/10.4324/9780203218235>
- [A.5] J.A. Clarke, *The Science and Technology of Undulators and Wigglers* (Oxford University Press, Oxford, 2004), <https://doi.org/10.1093/acprof:oso/9780198508557.001.0001>
- [A.6] J. Schwinger, *Phys. Rev.* **75** (1949) 1912, <https://doi.org/10.1103/PhysRev.75.1912>
- [A.7] R. Walker, Insertion devices: undulators and wigglers, CAS-CERN Accelerator School: Synchrotron Radiation and Free Electron Lasers, Grenoble, France, 22–27 April 1996, CERN-1998-004 (CERN, Geneva, 1998), p. 129. <https://doi.org/10.5170/CERN-1998-004>
- [A.8] L. Rivkin, Synchrotron radiation, CAS-CERN Accelerator School: FELs and ERLs, Hamburg, Germany, June 2014. (Proceedings not published.)
 Lecture part I:
<https://web.archive.org/web/20190514093703/http://cas.web.cern.ch/sites/cas.web.cern.ch/files/lectures/hamburg-2016/rivkiniii.pdf>
 Lecture part II:
<https://web.archive.org/web/20190514093703/http://cas.web.cern.ch/sites/cas.web.cern.ch/files/lectures/hamburg-2016/rivkiniii.pdf>
- [A.9] J. Pflueger, Undulator technology, CAS-CERN Accelerator School: FELs and ERLs, Hamburg, Germany, June 2014. (Proceedings not published.)
 Lecture:
<https://web.archive.org/web/20190514094217/http://cas.web.cern.ch/sites/cas.web.cern.ch/files/lectures/hamburg-2016/pflueger.pdf>